

# Optoelectronic properties of the poly(3,4-ethylenedioxythiophene) : polystyrene sulphonate thin films in varied doping states

---

**Pathak, Gaurav**

**Doctoral thesis / Disertacija**

**2019**

*Degree Grantor / Ustanova koja je dodijelila akademski / stručni stupanj:* **University of Zagreb, Faculty of Science / Sveučilište u Zagrebu, Prirodoslovno-matematički fakultet**

*Permanent link / Trajna poveznica:* <https://um.nsk.hr/um:nbn:hr:217:372455>

*Rights / Prava:* [In copyright](#)/[Zaštićeno autorskim pravom.](#)

*Download date / Datum preuzimanja:* **2025-02-23**



*Repository / Repozitorij:*

[Repository of the Faculty of Science - University of Zagreb](#)





UNIVERSITY OF ZAGREB

FACULTY OF SCIENCE  
DEPARTMENT OF PHYSICS

Gaurav Pathak

Optoelectronic properties of the  
poly(3,4-ethylenedioxythiophene):  
polystyrene sulphonate thin films in varied  
doping states

DOCTORAL DISSERTATION

Zagreb, 2019



UNIVERSITY OF ZAGREB

FACULTY OF SCIENCE  
DEPARTMENT OF PHYSICS

Gaurav Pathak

Optoelectronic properties of the  
poly(3,4-ethylenedioxythiophene):  
polystyrene sulphonate thin films in varied  
doping states

DOCTORAL DISSERTATION

Supervisors:

Asst. Prof. Duško Čakara

Prof. George Malliaras

Zagreb, 2019



**UNIVERSITY OF ZAGREB**

PRIRODOSLOVNO-MATEMATIČKI FAKULTET  
FIZIČKI ODSJEK

Gaurav Pathak

**Optičko-elektronička svojstva tankih  
filmova poli(3,4-etilendioksitiofen):  
polistiren sulfonata pri variranim stanjima  
dopiranosti**

DOKTORSKI RAD

Mentori:

Doc. dr. sc. Duško Čakara

Prof. dr. sc. George Malliaras

Zagreb, 2019

# Declaration of Authorship

I, GAURAV PATHAK, declare that this thesis titled, '**Optoelectronic properties of the poly(3,4-ethylenedioxythiophene):polystyrene sulphonate thin films in varied doping states**' and the work presented in it are my own.

I confirm that:

- This work was done wholly or mainly while in candidature for a research degree at this University.
- Where any part of this thesis has previously been submitted for a degree or any other qualification at this University or any other institution, this has been clearly stated.
- Where I have consulted the published work of others, this is always clearly attributed.
- Where I have quoted from the work of others, the source is always given. With the exception of such quotations, this thesis is entirely my own work.
- I have acknowledged all main sources of help.
- Where the thesis is based on work done by myself jointly with others, I have made clear exactly what was done by others and what I have contributed myself.

Signed:

---

Date:

---

## Supervisor information

**Dr. Duško Čakara** received the PhD degree in chemistry from the University of Geneva (2004) after graduating from the University of Zagreb, Faculty of Science (MSc in chemistry, 1999). He has spent several years as postdoc at the École Supérieure de Physique et de Chimie Industrielles (ESPCI) in Paris (2004-2006), Bayer Schering Pharma in Berlin (2006-2007) and Universities in Maribor and Graz (2007-2008). He was appointed as lecturer at the University of Rijeka, Faculty of Medicine (2008). Currently he holds the position of assistant professor within the Department of Biotechnology (since 2011) at the same university, and leads the Laboratory for Colloids, Polyelectrolytes and Interfaces within the Centre for Micro and Nanosciences and Technologies (since 2012). Dr. Čakara received the Swiss National Science Foundation Fellowship for prospective researchers (2004) as well as several other smaller research projects and fellowships in Croatia and Switzerland. He was attributed as the primary investigator and work package leader within the FP7 Marie Curie ITN project "Organic bioelectronics - OrgBio" (2013-17). The research of Dr. Čakara is focused on the physicochemical properties and modelling of polyelectrolytes and interfaces in aqueous medium, in which field he is author or coauthor of thirteen scientific papers (which received 536 citations according to WOS CC) and a number of conference contributions.

**Prof. George Malliaras** received a BS in Physics from the Aristotle University (Greece) in 1991, and a PhD in Mathematics and Physical Sciences, cum laude, from the University of Groningen (the Netherlands) in 1995. After postdocs at the University of Groningen and at the IBM Almaden Research Center (California), he joined the faculty in the Department of Materials Science and Engineering at Cornell University (New York) in 1999. From 2006 to 2009 he served as the Lester B. Knight Director of the Cornell NanoScale Science Technology Facility. He moved to the Ecole des Mines de St. Etienne (France) in 2009, where he started the Department of Bioelectronics and served as Department Head. He joined the University of Cambridge as the Prince Philip Professor of Technology in 2017. His research on organic electronics and bioelectronics has been recognized with awards from the New York Academy of Sciences (Blavatnik Award), the US National Science Foundation, and DuPont. He is a Fellow of the Materials Research Society and of the Royal Society of Chemistry, and serves as an Associate Editor of Science Advances. He is a co-author of 200+ publications in peer-reviewed journals that have received over 23,000 citations. His h-index is 84 (google scholar, 2/19).

*“Respect is to be earned, not demanded”*

Late Shri L.K. Pathak

UNIVERSITY OF ZAGREB

# *Abstract*

FACULTY OF SCIENCE  
DEPARTMENT OF PHYSICS

Doctoral thesis

**Optoelectronic properties of the  
poly(3,4-ethylenedioxythiophene):polystyrene sulphonate thin films in  
varied doping states**

by [Gaurav Pathak](#)

Poly(3,4-ethylenedioxythiophene): polystyrene sulfonate (PEDOT:PSS) has gained considerable attention in the past decade due to its novel applications in the field of flexible electronics. PEDOT:PSS is the leading candidate for the channel material in the organic electrochemical transistor (OECT) devices. While PEDOT:PSS has been reported to provide high values of transconductance in transistor devices, the fundamental physical understanding of electrochemical gating of conducting polymers is still unclear. Whether the effect of gating is electrostatic, electrochemical or both, and how to distinguish them, is still a topic of debate. In this thesis, the optoelectronic properties of PEDOT:PSS thin films are studied using variable angle spectroscopic ellipsometry (VASE). The electrochemical characterization of PEDOT:PSS films is performed in combination with VASE measurements, which is termed as electrochemical variable angle ellipsometry (EVASE). The EVASE measurements were able to successfully differentiate the electrostatic effects on the PEDOT:PSS film from that of the redox effects due to the application of an electrochemical bias. In addition, ellipsometric techniques take into account the anisotropy and the increase in film thickness upon swelling of the film (when immersed in an electrolyte); which are usually neglected in state of the art electrical characterization. The above study was extended to the OECT devices, which provided an optical and electrochemical characterization of OECTs. For the electrical characterization, the drain and transfer characteristics of the device were obtained. A highest transconductance value of the device was found to be  $0.8 \mu\text{S}/\text{cm}$ . X-ray reflectivity (XRR) and near edge X-ray absorption fine structure (NEXAFS) studies were performed to investigate if the origin of anisotropy in these systems could be due to the molecular orientation of their crystalline constituents. No such anisotropy was detected from the above measurements on PEDOT:PSS films. Indicating that the origin of anisotropy in such films could solely be due to the morphological reasons, where the sub-micrometer sized PEDOT-rich domains are separated by PSS lamellae in the horizontal direction.



**Keywords** : *PEDOT, ellipsometry, VASE, flexible, electronics, bioelectronics, organic, transistors, anisotropy*

SVEUČILIŠTE U ZAGREBU

# *Prošireni sažetak na hrvatskom jeziku*

PRIRODOSLOVNO-MATEMATIČKI FAKULTET

FIZIČKI ODSJEK

Doktorski rad

## **Optičko-elektronička svojstva tankih filmova poli(3,4-etilendioksitiofen):polistiren sulfonata pri variranim stanjima dopiranosti**

by [Gaurav Pathak](#)

Polimerni kompleks poli(3,4-etilendioksitiofen):polistiren sulfonata (PEDOT:PSS) stekao je značajnu pozornost u proteklom desetljeću zbog njegovih novih primjena u vrlo brzo napredujućem području fleksibilne elektronike. PEDOT:PSS je vodeći kandidat za materijal kanala u uređajima kao što su organski elektrokemijski tranzistori (eng. organic electrochemical transistor, OECT). Dok se u literaturi navodi da PEDOT:PSS pruža visoke vrijednosti transvodljivosti (eng. transconductance) u tranzistorima, osnovni fizikalni princip mehanizma elektrokemijskog upravljanja vratima tranzistora (eng. electrochemical gating) vodljivih polimera još uvijek je nejasan. Da li je utjecaj upravljanja vratima tranzistora elektrostatski, elektrokemijski ili oboje, i kako ih razlikovati, još uvijek je predmet rasprave. Razlog tomu je što, za razliku od čvrstih tranzistora, potpuno razumijevanje OECT uređaja zahtijeva poznavanje elektrokemije i fizike kondenzirane materije.

U ovoj disertaciji, optoelektronička svojstva PEDOT:PSS tankih filmova su proučavana tehnikom spektroskopske elipsometrije pri variranom kutu refleksije (eng. variable angle spectroscopic ellipsometry, VASE). Kretschmannova elektrokemijska ćelija konfigurirana je na način da proučava modulaciju vodljivosti primenom elektrokemijskog potencijala. Elektrokemijska karakterizacija PEDOT:PSS filmova provedena je u kombinaciji s VASE mjerenjima, i u ovoj disertaciji se naziva

elektrokemijska elipsometrija pri variranom kutu refleksije (eng. electrochemical variable angle ellipsometry, EVASE). EVASE mjerenja su uspješno razlikovala elektrostatski utjecaj na PEDOT:PSS filmove od redoks utjecaja zbog primjene elektrokemijskog potencijala. Osim toga, elipsometrijske tehnike uzimaju u obzir anizotropiju i debljinu filma do koje dolazi zbog bubrenja filma (kad je film uronjen u elektrolit), koji se inače zanemaruju pri električnoj karakterizaciji.

PEDOT:PSS tanki filmovi nanošeni su metodom vrtnje (eng. spin-coating) vodene suspenzije PEDOT:PSS-a na kvarcne i Si/SiO<sub>2</sub> supstrate koristeći vodenu suspenziju koja sadrži dimetil sulfoksid kao kootapalo i (3-glicidoksi)propil)trimetoksisilan kao umreživač (cross-linker). VASE i EVASE mjerenja provedena su na svim uzorcima, dok se je za fitanje (eng. fitting) izmjerenih elipsometrijskih podataka koristio uniaksijalni anizotropni Tauc-Lorentz-Drude-ov model. Iz fitanog optičkog modela dobivene su in-situ i ex-situ dielektrične funkcije za PEDOT:PSS. Parametri Tauc-Lorentz funkcije ukazuju na promjenjivu elektronsku konfiguraciju za PEDOT pod utjecajem elektrokemijskog stresa. Za razliku od toga, Drude-ovi parametri pružaju informaciju o DC vodljivosti sustava. Vodljivost suhog filma koja je izračunata iz Drude-ovih parametara iznosi 258.6 S/cm. Ovaj rezultat je u skladu s vrijednošću od 283.9 S/cm, koja je izračunata Van-der-Pauw metodom iz električnih mjerenja. Opaženo je da se u tekućem elektrolitu debljina filma poveća za 20 %, dok se DC vodljivost se također smanjila na vrijednost od 107.5 S/cm. zbog bubrenja filma. Ova pojava popraćena je promijenom oksidacijskog stanja, zbog čega se opaža i promjena u dielektričnoj funkciji, i to u oba smjera napredovanja zrake: redovitom i izvanrednom.

Iz cikličkih voltamograma (CV), pri čemu je elektrokemijski potencijal variran u rasponu između valentne i vodljive elektronske vrpce, opaženo je poluvodičko ponašanje PEDOT:PSS filma. Oksidacija (iznad +0.2V s obzirom na Ag/AgCl referentnu elektrodu), redukcija (ispod -0.2V) i razdvajanje naboja (između -0.2 i 0.2 V) opaženi su u CV i EVASE mjerenjima. EVASE mjerenja provedena su u sva tri režima. Energija elektronskih prijelaza, dobivena iz redovite dielektrične funkcije za napone u režimu razdvajanja naboja iz CV-a, je gotovo konstantna, što ukazuje da se Fermijev nivo nalazi u području energijskog procijepa PEDOT:PSS poluvodiča. Stoga, promjena u vodljivosti u ovom rasponu el. potencijala je posljedica

isključivo efekta polja uzrokovanog ubacivanjem iona u matricu polimera, prilikom čega ne dolazi do redoks dopiranja. Za razliku od toga, u oksidacijskom režimu CV-a, opaža se plavi pomak u energiji prijelaza, zbog čega DC vodljivost izračunata iz Drudeovih parametara pokazuje značajan porast. Ovo ukazuje na oksidacijsko dopiranje PEDOT-a, tj. Fermijev nivo pada u valentnu vrpću što uzrokuje dopiranje p-tipa u PEDOT-u.

Elektrokemijska priroda PEDOT:PSS elektroda proučavana je metodom elektrokemijske impedancijske spektroskopije (EIS) pri variranom ravnotežnom potencijalu. Obrada eksperimentalnih podataka EIS mjerenja sastojala se od fitanja primjenom modela dvaju serijskih Randles-ovih petlji, pri čemu je jedna od tih petlji ukazivala na formaciju električkog dvosloja s minimalnom vrijednošću kapaciteta kondenzatora. Međutim, drugi Randlesov krug ukazao je na superkapacitivno ponašanje elektrode odn. PEDOT:PSS tankih filmova, slično ponašanju opaženom u CV-u. Pokazalo se da je superkapacitivno ponašanje PEDOT:PSS filmova gotovo jednako u cijelom rasponu primijenjenih el. potencijala. Međutim, prijenos naboja pratio je ponašanje opaženo u EVASE i CV mjerenjima, gdje je uočeno da se vodljivost povećava u oksidacijskom i redukcijskom režimu u odnosu na režim razdvajanja naboja.

Pomoću opisanih mjerenja, utvrđeno je postojanje dvaju različitih elektrokemijskih režima za PEDOT:PSS filmove. U režimu razdvajanja naboja, vodljivost se može podešavati pomoću isključivo kapacitivnog efekta koji je uzrokovan ubacivanjem iona u matricu polimera, a u redoks režimu polimer može biti dopiran ili dedopiran čime se mijenja koncentracija nosilaca naboja a time i vodljivost.

Opisano istraživanje prošireno je na organske elektrokemijske tranzistore (OECT), koji su proizvedeni tehnikom optičke litografije. Proces je uključivao primjenu maske s uzorkom i naknadnu depoziciju metala (elektroda), parilena (nevodljivi sloj elektrode) i PEDOT:PSS (kanal). PEDOT:PSS vodena disperzija koja sadrži etilen-glikol, dodecilbenzensulfonsku kiselinu i (3-glicidiloksi)propil)trimetoksisilan (GOPS) pripremljena je za nanošenje kao materijala za kanal u uređaju metodom vrtnje. Etilen-glikol se upotrebljava za povećavanje električke vodljivosti, dodecilbenzensulfonska kiselina je površinski aktivna tvar koja smanjuje napetost

površine između suspenzije PEDOT:PSS suspenzije i staklenog supstrata kako bi se formirali uniformni filmovi, dok GOPS služi kako crosslinker u PEDOT:PSS disperziji. Pripremljeni uzorci su analizirani tehnikama VASE i EVASE. Pokušano je naći veza između rezultata EVASE mjerenja i električne karakterizacije pripremljenih uređaja. Suhi filmovi električki su karakterizirani četverkontaktnim mjerenjem otpora (eng. four-probe measurement), prilikom čega je konstantna struja ISD u iznosu 0.1 mA puštena kroz kanal, a mjerena je razlika potencijala između dva kontakta (eng. voltage probes). Izmjereno je da vodljivost materijala kanala iznosi 205.4 S/cm u suhim uvjetima, međutim u dodiru s vodenom otopinom elektrolita pada na vrijednost od 82.6 S/cm. CV uređaja je snimljen u kapacitivnom rasponu napona kanala iz čega je izračunat volumetrijski kapacitet materijala kanala koji iznosi 44 F/cm<sup>3</sup>. Taj rezultat je u skladu s podacima dostupnim u literaturi. Izvan kapacitivnog područja CV-a, je opažen faradejski odziv uređaja. EVASE je proveden u svim naponskim režimima, i jasno razlikuje različite kapacitivne i redoks režime, a time i efekt polja od procesa elektrokemijskog dopiranja u OECT-u.

Karakteristike odvoda (eng. drain) i prijenosa (eng. transfer) pripremljenih uređaja dobivena su električnom karakterizacijom. U karakteristikama odvoda, kada se na upravljačkoj elektrodi (eng. gate) ne primjenjuje potencijal, I-V karakteristika kanala pokazuje linearno ohmsko ponašanje. Međutim, pri određenom narinutom naponu na upravljačkoj elektrodi (tzv. 'pinch-off' napon), struja izvora-odvoda (eng. source-drain current) pokazuje zasićenje. Pri narinutom naponu od 0.6 V na upravljačkoj elektrodi, gotovo nikakva struja ne prolazi kroz kanal, zbog čega se uređaj prebacuje u „OFF“ stanje. Prilikom skeniranja napona upravljačke elektrode za konstantni napon na kanalu, moguće je mjeriti struju odvoda kao karakteristiku prijenosa naboja u pripremljenom uređaju. Prva derivacija krivulje prijenosa naziva se „transvodljivost“ uređaja i može se koristiti za procjenu kvalitete uređaja. Najveća vrijednost transvodljivosti od 0.8 S/cm izmjerena je pri 0.2 V s obzirom na el. potencijal Zemlje. Iako su rezultati dobiveni električnom i EVASE karakterizacijom kvalitativno usporedivi, jasna razlika između kapacitivnog i redoks režima uređaja mogla je biti opažena jedino iz EVASE mjerenja. Također, referentni potencijali u tim dvjema tehnikama su različiti (Ag/AgCl odn. zemlja),

zbog čega je kvantitativna usporedba rezultata dobivenih u ovim eksperimentima praktički nemoguća.

Prilikom EVASE mjerenja tankih filmova PEDOT:PSS-a ili PEDOT:PSS-a u pri - pre - mlje - nim uređajima, pokazano je da je on uniaksijalno anizotropan, s elektronički vodljivim ponašanjem u redovitom smjeru (paralelno sa supstratom) i nevodljivim tipom ponašanja u izvanrednom smjeru (okomito na supstrat). Međutim, EVASE mjerenje ne daje odgovore o izvoru anizotropije u filmovima. Stoga, reflektivnost rentgenskog zračenja pri malom kutu (eng. X-ray reflectivity, XRR) i spektroskopska metoda fine strukture apsorpcije rentgenskih zraka blizu rubova ljuski (eng. near edge X-Ray absorption fine structure, NEXAFS) upotrebljene su da bi se proučilo da li je izvor anizotropije u ovim sistemima posljedica molekularne orijentacije u kristalima od kojih se sastoje. XRR i NEXAFS mjerenja provedena su na sinkrotronu Elettra u Trstu na liniji BEAR. Analizirani su tanki PEDOT:PSS filmovi nanošeni metodom vrtnje na Si/SiO<sub>2</sub> nosače. XRR i NEXAFS spektri snimljeni su oko K-ruba ugljika (270-320 eV) u s- i p- polarizaciji elektromagnetskog zračenja pri upadnom kutu od 5°. Intenzitet reflektirane zrake prati se kao fotostruja generirana na fotodiodi. NEXAFS spektri dobiveni su mjerenjem struje koju stvaraju Augerovi elektroni pobuđeni apsorpcijom polariziranih rendgenskih zraka. Ekstinkcijski koeficijent za film u danom rasponu energija izračunat je iz NEXAFS eksperimentalnih podataka te je odgovarajući realni dio indeksa loma izračunat je primjenom Kramers-Kronig-ove transformacije za obje, p- i s-, polarizacije. Pokazano je da se kompleksni indeksi loma izračunati za p- i s-polarizaciju upadne zrake, gotovo međusobno podudaraju. Ovaj rezultat ukazao je da nema anizotropije koja bi proizlazila iz kristalnih domena monomera. Nadalje, dobiveni indeksi loma upotrebljeni su za modeliranje reflektancija PEDOT:PSS filmova u području energija K-ruba ugljika, primjenom izotropnog Fresnelovog optičkog modela. Debljina PEDOT:PSS filmova dobivena prilagodbom tog modela u skladu je s vrijednostima debljina filmova izmjerenih mikroskopijom atomskih sila (eng. atomic force microscope, AFM). Također, modelirane reflektancije u dobrom su slaganju s eksperimentalnim vrijednostima XRR.

# *Acknowledgements*

The research included in this dissertation could not have been performed if not for the assistance, patience, and support of many individuals. I would like to extend my gratitude first and foremost to my thesis advisor Dr. Duško Čakara, Asst. Professor, Dept. of Biotechnology, University of Rijeka, for mentoring me over the course of my PhD program. His insight lead to the original proposal of my thesis. He has helped me through extremely difficult times over the course of the analysis and the writing of the dissertation and for that I sincerely thank him for his confidence in me.

I would additionally like to thank Prof. George Malliaras for his support in both the research and especially for allowing me to visit his lab at École des Mines de Saint-Étienne, Gardanne, France. It lead me to the development of the OECT devices and extend my research in a positive direction. His knowledge and understanding of the written word has allowed me to fully express the concepts behind this research.

I would also like to extend my appreciation to Prof. Mladen Petravić for allowing me to use his lab facilities, whenever I required them.

I'm extremely grateful to Prof. Saša Zelenika for his help in the AFM measurements and for being available for discussions and clarifying my doubts.

This research would not have been possible without the experimental collaboration of Prof. Lilianna Szyk-Warszyńska and Zofia Krasińska-Krawet who performed the QCM-D measurements on my samples.

I would like to extend my sincere thanks to Dr. Aleš Omerzu for the discussions about the behaviour of semiconducting electrodes in electrochemical environment.

I'm extremely grateful to Prof. Nenad Pavin for for helping me throughout my PhD studies, I couldn't have gone through it without his support.

A special thanks to Ms. Marina Kavur and Mr. Marko Hum for always being available to explain me each every procedure and paper work required for my coursework.

I am also grateful to Dr. Iva Šarić and Dr. Robert Peter for being excellent colleagues and friends, who were always there for me in good and bad.

I would like to extend my deepest gratitude to Prof. Ratnamala Chatterjee who has served as a voice of quiet wisdom in matters ranging from the most basic aspects of science, to the paths that my career has eventually taken.

I would like to extend my special thanks to Dr. Vivek Pachauri, first and foremostly for being a great friend and for the scientific discussions that we had.

I can't thank enough Vedrana, Tomislav, Kamelija and Karla for the friends they have been and for those endless discussion that we had. I find myself lucky to have made such lifelong friends.

I wish to thank my best friend Kristina, basically for being what she is, a great friend and a beautiful person at heart.

A big THANK YOU!! to Mom, Dad, Di and Jij, you have been so supreme, You have nurtured my learning, supported my dreams!

And at last to my better half Nagma, This wouldn't have been possible without your love, support and understanding.

This research was funded by the project MARIE SKŁODOWSKA-CURIE FP7-PEOLPLE-ITN-2013 (PITN-GA-2013-607896) "Organic bioelectronics".

This research was supported by the European Fund for Regional Development and the Ministry of Science, Education and Sports of the Republic of Croatia under the project Research Infrastructure for Campus-based Laboratories at the University of Rijeka (grant number RC.2.2.06-0001).



# Contents

<b>Declaration of Authorship</b>	<b>i</b>
<b>Abstract</b>	<b>iv</b>
<b>Extended abstract in Croatian</b>	<b>vi</b>
<b>Acknowledgements</b>	<b>xi</b>
<b>List of Figures</b>	<b>xvi</b>
<b>List of Tables</b>	<b>xxv</b>
<b>Abbreviations</b>	<b>xxvii</b>
<b>Physical Constants</b>	<b>xxix</b>
<b>Symbols</b>	<b>xxx</b>
<b>1 Introduction</b>	<b>1</b>
<b>2 Theoretical background</b>	<b>6</b>
2.1 Conducting polymers . . . . .	6
2.2 Doping in conducting polymers . . . . .	7
2.3 Poly(3,4-ethylenedioxythiophene):polystyrene sulphonate (PEDOT:PSS) . . . . .	14
2.3.1 Electrochemical doping in PEDOT:PSS . . . . .	15
2.4 Organic electrochemical transistors . . . . .	16
2.5 Ellipsometry . . . . .	19
2.5.1 Propagation of light in a medium . . . . .	19
2.5.2 Reflection of a polarized light . . . . .	21
2.5.3 Measurement principle of ellipsometry . . . . .	24

---

<b>3</b>	<b>Doping of poly(3,4-ethylenedioxythiophene):poly(styrene- sulfonate) films studied by means of electrochemical variable angle spectroscopic ellipsometry</b>	<b>29</b>
3.1	Experimental part . . . . .	31
3.1.1	Sample preparation . . . . .	31
3.1.2	Atomic force microscopy . . . . .	32
3.1.3	Electrical measurements . . . . .	34
3.1.4	Transmission measurements . . . . .	34
3.1.5	Variable angle spectroscopic ellipsometry . . . . .	35
3.1.6	Electrochemical variable angle spectroscopic ellipsometry . .	36
3.1.7	Electrochemical impedance spectroscopy . . . . .	38
3.2	Tauc-Lorentz-Drude model . . . . .	38
3.3	Results and discussions . . . . .	40
3.3.1	Van Der Pauw measurements . . . . .	40
3.3.2	Optical Transmission . . . . .	41
3.3.3	Variable angle spectroscopic ellipsometry . . . . .	42
3.3.4	Electrochemical variable angle spectroscopic ellipsometry . .	48
3.4	Electrochemical impedance spectroscopy . . . . .	57
3.5	Summary and conclusion . . . . .	61
<b>4</b>	<b>Understanding the transport mechanism in poly(3,4-ethylenedioxythiophene): poly(styrene- sulfonate) based organic electrochemical transistors</b>	<b>63</b>
4.1	Experimental part . . . . .	66
4.1.1	Sample preparation . . . . .	66
4.1.2	Device fabrication . . . . .	66
4.1.3	Variable angle spectroscopic ellipsometry . . . . .	68
4.1.4	Electrical resistivity measurements . . . . .	69
4.1.5	Cyclic voltametry . . . . .	70
4.1.6	Electrochemical variable angle spectroscopic ellipsometry and electrical conductivity measurement . . . . .	70
4.1.7	Device characterization . . . . .	72
4.2	Results and discussions . . . . .	73
4.2.1	Variable angle spectroscopic ellipsometry . . . . .	73
4.2.2	Electrical Measurements . . . . .	75
4.2.3	Cyclic voltammetry and capacitance measurements . . . . .	78
4.2.4	Electrochemical variable angle spectroscopic ellipsometry . .	81
4.2.5	Device characteristics . . . . .	85
4.3	Summary and conclusions . . . . .	90
<b>5</b>	<b>X-Ray reflectivity and near edge X-ray absorption fine structure</b>	<b>93</b>
5.1	Experimental . . . . .	96
5.1.1	Sample preparation . . . . .	96
5.1.2	X-ray reflectivity and NEXAFS . . . . .	96
5.2	Results and discussion . . . . .	98

---

5.3 Summary and conclusions . . . . .	102
<b>6 Conclusions</b>	<b>103</b>
<b>Bibliography</b>	<b>105</b>
<b>A Measurement of ellipsometric parameters <math>\Psi</math> and <math>\Delta</math></b>	<b>138</b>
<b>B <math>\Psi</math> and <math>\Delta</math> fitting of EVASE measurements</b>	<b>141</b>
B.1 $\Psi$ and $\Delta$ fits of EVASE measurements of PEDOT:PSS thin films used in chapter 3 . . . . .	143
B.2 $\Psi$ and $\Delta$ fits of EVASE measurements of PEDOT:PSS channel used in chapter 4 . . . . .	152
<b>C Ion beam deposition</b>	<b>157</b>
C.1 Experimental part . . . . .	158

# List of Figures

2.1	Double bonding in an ethylene molecule . . . . .	7
2.2	Electronic configuration in a $sp^2$ hybridized system, where the outer shell $2s^2 2p^2$ of carbon hybridizes to form three $sp^2$ orbitals leaving one $2p$ orbital unhybridized . . . . .	7
2.3	Evolution of a polaron in a neutral poly(alkylthiophene) chain by p-doping (oxidation) . . . . .	8
2.4	Evolution of polaron, polaron* (P,P*) and bipolaron, bipolaron* (BP, BP*) band upon the p-doping(oxidation). The arrows are the allowed electronic transitions. (a) the schematic of the band structure of PEDOT molecule in its pristine state. (b) the evolved band structure with polaron bands upon the oxidation of the pristine PEDOT. (C) the evolved band structure with bipolaron bands upon further oxidation of PEDOT. . . . .	9
2.5	Primary, secondary and tertiary structure of PEDOT:PSS. Image reproduced from [47] . . . . .	15
2.6	A typical structure of an OECT device. S, D and G represent the source drain and gate electrodes respectively. $d$ is the thickness of the CP film. $V_G$ is the applied gate-source voltage. $V_D$ represents the applied source-drain voltage and $I_D$ is the corresponding current for the same. Image reproduced from [74] . . . . .	17
2.7	Representation of the ionic and electronic circuits used in the modelling of OECT devices. $R_{ch}$ represents the electronic resistance of the channel in the electronic circuit of the model. $R_E$ and $C_{ch}$ represents electrolyte resistance and channel capacitance in the ionic circuit. . . . .	18
2.8	Schematic representation of the reflection of light from the interface of two media. . . . .	23
2.9	Schematic representation of the reflection of light from from a system with two interfaces. . . . .	24
2.10	A 2D projection of an polarized light beam at normal incidence, where the angle $\psi$ represents the ellipticity of the polarized light. $a_x$ and $a_y$ are the amplitudes of the light beam in X and Y directions of the cartesian co-ordinates . . . . .	25
2.11	A flowchart explaining the steps taken for fitting the ellipsometric data to a model for the determination of optical constants. Adapted from [81] . . . . .	27

3.1	The scanning atomic force micrograph of the PEDOT:PSS film spin-coated at the Si/SiO <sub>2</sub> substrate. . . . .	32
3.2	Height profile diagram of the sample spun at the rate of 4000 rpm for 30 sec , determined along the three lines indicated in the micrograph (fig.3.1). The micrograph was recorded in air medium, approximately at the same spot as VASE. . . . .	33
3.3	The thickness of the PEDOT:PSS thin film measured with AFM vs the spin speed (all for 30 sec). . . . .	33
3.4	Image of PEDOT:PSS thin film sample on quartz substrate with the tungsten probes in electrical contact with the sample in Van-der-Pauw geometry . . . . .	35
3.5	Scheme of Kretschmann electrochemical cell, which facilitates VASE measurements in the NIR range for the PEDOT:PSS film is in contact with the electrolyte . . . . .	36
3.6	Scheme of sample in a Kretschmann cell, connected to a potentiostat. Where, the Au/PEDOT:PSS film serves as W.E, a Pt rod electrode is used as a C.E and an Ag/AgCl wire in 0.1 M KCl (aq)(or 0.1 M LiClO <sub>4</sub> in acetonitlire) is used as a R.E . . . . .	37
3.7	Four probe Van-der-Pauw <i>I-V</i> curves for eight different pairwise combinations of current vs voltage probes, The inset in the figure represents the assigned numbers to the contact points and the legends indicate the measurements performed for different combination of current and voltage probes. Red line is a linear fit to the measurements, whereby the slope provides the resistance. (a) Van-der-Pauw measurements of PEDOT:PSS film on quartz substrate. (b)Van-der-Pauw measurements of PEDOT:PSS film on Si/SiO <sub>2</sub> substrate . . . . .	40
3.8	(a) UV-VIS-IR spectra of PEDOT:PSS thin film spin coated on a quartz substrate, the legends denote the sample of different thickness (cf. table 3.1). (b) Lambert-Beer's law fit (eq: 3.6) to the measured absorption spectra, the legends denote the fitted parameters . . . . .	41
3.9	VASE spectra of the PEDOT:PSS sample spin coated on Si/SiO <sub>2</sub> substrate at room temperature in air ambient. The scatter points represent the measured data at varied angle of incidence (AOI50 to AOI64) and the solid lines represent the best fit of the TLD model. (a) Ellipsometric angle $\Delta$ ,(b) Ellipsometric angle $\Psi$ . . . . .	44
3.10	VASE spectra of the PEDOT:PSS sample spin coated on quartz substrate at room temperature in air ambient. The scatter points represent the measured data at varied angle of incidence (AOI50 to AOI64) and the solid lines represent the best fit of the TLD model. (a) Ellipsometric angle $\Delta$ ,(b) Ellipsometric angle $\Psi$ . . . . .	44
3.11	Complex ordinary and extraordinary dielectric dispersion derived from the uniaxially anisotropic TLD model simultaneously fitted to the ellipsometric data presented in fig 3.9 and 3.10 . . . . .	45

- 3.12 VASE spectra of the PEDOT:PSS sample spin coated on quartz substrate at room temperature in 0.1 M KCl aqueous solution. The scatter points represent the measured data at varied angle of incidence (AOI, from 50 to 64 degrees) and the solid lines represent the best fit of the TLD model. (a) Ellipsometric angle  $\Delta$ , (b) Ellipsometric angle  $\psi$ . . . . . 46
- 3.13 TLD dielectric model fitted to the ellipsometric angles  $\psi$  and  $\Delta$  measured for the PEDOT:PSS film exposed to 0.1 M KCl (aq) electrolyte. (a) The fitted ordinary and extraordinary dielectric function. (b) comparison of the ordinary dielectric function of the dry and electrolyte exposed PEDOT:PSS film. The arrows represent the parallel shift in the real part ( $\epsilon_1$ ) of the dielectric function and the rise of the oscillator at 1.24 eV when exposed to the electrolyte 47
- 3.14 Scheme depicting the change in position of Fermi level in the band structure of PEDOT, when brought in contact with the electrolyte. 48
- 3.15 Cyclic voltammogram measured for the PEDOT:PSS WE vs. Ag/AgCl in 0.1 M KCl, in the three-electrode cell (cf. fig. 3.6), at scan rate 0.01 Vs<sup>-1</sup>. The horizontal arrows denotes the direction of potential sweep, the vertical arrow denotes the temporal evolution of cycles. 49
- 3.16 Uniaxially anisotropic complex TLD dielectric function model fitted to the ellipsometric angles  $\psi$  and  $\Delta$  measured for the PEDOT:PSS film exposed to 0.1 M KCl (aq) electrolyte at varied electrochemical bias. (a) The fitted complex ordinary dielectric function. The arrows represent the rising TL oscillator and decreasing Drude tail with decreasing electrochemical bias (b) The fitted complex extraordinary dielectric function. . . . . 51
- 3.17 . (a) The DC conductivity calculated from the Drude parameters (left axis) fitted from the EVASE data under varied equilibrium electric potentials at the PEDOT:PSS electrode, in the range +0.6 to -0.2 V vs Ag/AgCl in 0.1 M KCl (pH $\approx$ 7), and the corresponding Tauc-Lorentz resonance energy (right axis). The error bars represent the confidence of the fitted parameters, lines serve to guide the eye. (b) The scheme representing the evolution of the electronic structure of PEDOT:PSS upon increase of the positive electric bias (redox doping). . . . . 51
- 3.18 Cyclic voltammogram measured for the PEDOT:PSS WE vs. Ag/AgCl in 0.1 M LiClO<sub>4</sub>, in acetonitrile, at scan rate 0.01 Vs<sup>-1</sup>. . . . . 56
- 3.19 Uniaxially anisotropic complex TLD dielectric function model fitted to the ellipsometric angles  $\psi$  and  $\Delta$  measured for the PEDOT:PSS film exposed to 0.1 M LiClO<sub>4</sub> in acetonitrile electrolyte at varied electrochemical bias. (a) The fitted complex ordinary dielectric function. The arrows represent the lowering TL oscillator value and increasing Drude tail with increasing electrochemical bias (b) The fitted complex extraordinary dielectric function. . . . . 56

3.20	(a) Nyquist plots for the from the EIS measurements performed on PEDOT:PSS electrodes at varied electrochemical potentials, the solid lines are the equivalent circuit fitted to individual measurements (b) Bode and phase pots of the same as above. . . . .	58
3.21	Equivalent circuit fitted to the Nyquist , Bode and phase plots. The corresponding values of the parameters are presented in Table 3.5 . . . . .	59
4.1	Scheme of the device fabrication steps with photolithography technique. (a) Photoresist layer is coated on the substrate with spin coating, (b)the photoresist is etched using photolithography (c) Cr/Au metal is deposited using a thermal evaporator (d) lift off is performed (e) Paralyne insulation and sacrificial layers are deposited (f) Channel is patterned by depositing another photoresist and performing another lithography step and reactive ion etching (g) PEDOT:PSS is spin coated (h) the sacrificial paralyne-C layer is removed . . . . .	67
4.2	Photograph of the the device with electrodes . . . . .	68
4.3	Scheme of four point probe measurement . . . . .	69
4.4	Scheme of the Krestchmann cell setup where four point probe electrical measurements are performed when the device is in contact with the electrolyte (0.1 M KCl). The source and drain electrode are connected to a current source through an ammeter and the voltage probes are connected to a voltmeter . . . . .	70
4.5	Scheme of the Krestchmann electrochemical cell where EVASE and electrical measurements (under electrochemical bias) are performed. The source electrode of the device is connected as a working electrode of the potentiostat, the Pt counter electrode immersed in the electrolyte is used as gate to the device, the drain electrode is connected to the ground of the potentiostat through an ammeter and the $V_A$ and $V_B$ electrodes of the device are connected to a voltmeter. . . . .	71
4.6	Schematic of the setup for device characterization measurements. The gate electrode used is Ag.AgCl wire 0.1 M KCl electrolyte. The source and drain electrodes are connected to a voltage source through an ammeter and an additional voltage source is connected to the gate electrode. . . . .	73
4.7	Ordinary, real ( $\epsilon_1$ ) and imaginary( $\epsilon_2$ ) dielectric dispersion of the dry PEDOT:PSS channel of the device obtained by fitting the ellipsometric angles $\Psi$ and $\Delta$ measured by VASE. The dashed line are the Ordinary, real ( $\epsilon_1$ ) and imaginary( $\epsilon_2$ ) dielectric dispersion of the dry PEDOT:PSS used in Chapter 3 and the solid line is from the PEDOT:PSS channel in the current study . . . . .	74
4.8	Schematic representation of the thin PEDOT:PSS channel representing the dimensions of the film. The length and width of the channel are know from the dimensions of the channel slot defined in the lithography process. The thickness is determined from AFM measurements. . . . .	76

4.9	(Left) Photograph of the scratch on the channel where the AFM scan is performed.(Right) Scanning atomic force micrograph of the PEDOT:PSS channel of device across the scratch. The height profile is measured at three distinct points and the average is considered	77
4.10	Cyclic voltammogram of the device. The PEDOT:PSS channel is used as a W.E and Pt rod electrode as an C.E and Ag/AgCl wire is used as a R.E in 0.1 M KCl aqueous solution. the black line is the raw data and the red line (eye guide) represents the 10 point average of the same.	79
4.11	EVASE spectra of the PEDOT:PSS channel in the OECT device at room temperature in 0.1 M KCl aqueous solution at an electrochemical bias of 0.024 V vs Ag/AgCl. The scatter points represent the measured data at varied angle of incidence (AOI, from 50 to 64 degrees with the step size of 2 degrees) and the solid lines represent the best fit of the TLD model. (a) Ellipsometric angle $\Delta$ ,(b) Ellipsometric angle $\Psi$ .	81
4.12	Ordinary, (a) real ( $\epsilon_1$ ) and (b) imaginary( $\epsilon_2$ ) dielectric dispersion of the PEDOT:PSS channel of the device obtained by fitting the ellipsometric angles $\Psi$ and $\Delta$ measured from EVASE. The arrows in the real and imaginary plots represent that the strength of the main optical transition decreases with a parallel increase in Drude tail when the potential is applied from negative to positive Vs Ag/AgCl in 0.1 M KCl at room temperature conditions.	83
4.13	Drain characteristics of the OECT device at varied gate voltage. The scatter points represent the measured data points and the Solid line is the linear fit in the Ohmic region of the plot	86
4.14	Sketch of the voltage profile through the channel length.	87
4.15	Gate voltage vs conductance of the OECT device in the ohmic range of the drain characteristics, obtain by calculating the slope of the linear region of the drain characteristics at varied gate voltage	88
4.16	Transfer characteristics of the OECT device at the source to drain voltage of -0.6V. Left Y axis is the drain current measured at different gate potentials, the right y axis is the transconductance measured by calculating the first derivative of $I_D$ VS $V_G$ plot using eq.4.5	89
5.1	Schematic representation of the structural arrangement of thiophene molecules in P3HT polymer. (i) lamella oriented perpendicular to the substrate(ii) lamella oriented parallel to the substrate[173]	94
5.2	Sketch of the cross section morphology of a PEDOT:PSS film. The PEDOT rich clusters (dark) are separated by PSS lamellae (light). Image reproduced from [174]	95
5.3	Schematic diagram of the X-ray reflectivity measurement, the beam of polarized X-ray is incident on the sample and the reflected beam is monitored by the photodiode detector inside the spectroscopy chamber. Image reproduced from [182]	97



5.4	The normalized XAS spectrum, measured for both p and s polarization, around the C1s edge of the 120nm thick PEDOT:PSS + 10% DMSO film. . . . .	99
5.5	The complex refractive index dispersion, for both p- and s- polarizations, calculated from the measured XAS data in the C1s edge energy range. The imaginary part ( $k$ ) of the refractive index is calculated from scaling the XAS signal to the molecular (EDOT:SS) scattering cross sections values, whereas the real part ( $n$ ) is calculated using the Kramers-Kronig transformations. . . . .	100
5.6	Measured(dots/thick line) and modeled (solid thin line) XRR signal for p polarization. The model curve was obtained using Fresnel's equations by using the calculated refractive index as shown in fig.5.5. . . . .	101
5.7	Measured(dots/thick line) and modeled (solid thin line) XRR signal for s polarization. The model curve was obtained using Fresnel's equations by using the calculated refractive index as shown in fig.5.5. . . . .	101
A.1	Schematic illustration of a typical nulling ellipsometer with their optical elements. . . . .	139
B.1	Schematic representation of the optical model used in (a)EVASE and (b) VASE measurements . . . . .	141
B.2	EVASE spectra of the PEDOT:PSS sample spin coated on quartz substrate at room temperature in 0.1 M KCl aqueous solution at an electrochemical bias of 0.6 V vs Ag/AgCl. The scatter points represent the measured data at varied angle of incidence (AOI, from 50 to 64 degrees with the step size of 2 degrees) and the solid lines represent the best fit of the TLD model. (a) Ellipsometric angle $\Delta$ , (b) Ellipsometric angle $\Psi$ . . . . .	143
B.3	EVASE spectra of the PEDOT:PSS sample spin coated on quartz substrate at room temperature in 0.1 M KCl aqueous solution at an electrochemical bias of 0.5 V vs Ag/AgCl. The scatter points represent the measured data at varied angle of incidence (AOI, from 50 to 64 degrees with the step size of 2 degrees) and the solid lines represent the best fit of the TLD model. (a) Ellipsometric angle $\Delta$ , (b) Ellipsometric angle $\Psi$ . . . . .	144
B.4	EVASE spectra of the PEDOT:PSS sample spin coated on quartz substrate at room temperature in 0.1 M KCl aqueous solution at an electrochemical bias of 0.4 V vs Ag/AgCl. The scatter points represent the measured data at varied angle of incidence (AOI, from 50 to 64 degrees with the step size of 2 degrees) and the solid lines represent the best fit of the TLD model. (a) Ellipsometric angle $\Delta$ , (b) Ellipsometric angle $\Psi$ . . . . .	145

- B.5 EVASE spectra of the PEDOT:PSS sample spin coated on quartz substrate at room temperature in 0.1 M KCl aqueous solution at an electrochemical bias of 0.3 V vs Ag/AgCl. The scatter points represent the measured data at varied angle of incidence (AOI, from 50 to 64 degrees with the step size of 2 degrees) and the solid lines represent the best fit of the TLD model. (a) Ellipsometric angle  $\Delta$ , (b) Ellipsometric angle  $\Psi$ . . . . . 146
- B.6 EVASE spectra of the PEDOT:PSS sample spin coated on quartz substrate at room temperature in 0.1 M KCl aqueous solution at an electrochemical bias of 0.2 V vs Ag/AgCl. The scatter points represent the measured data at varied angle of incidence (AOI, from 50 to 64 degrees with the step size of 2 degrees) and the solid lines represent the best fit of the TLD model. (a) Ellipsometric angle  $\Delta$ , (b) Ellipsometric angle  $\Psi$ . . . . . 147
- B.7 EVASE spectra of the PEDOT:PSS sample spin coated on quartz substrate at room temperature in 0.1 M KCl aqueous solution at an electrochemical bias of 0.08 V vs Ag/AgCl. The scatter points represent the measured data at varied angle of incidence (AOI, from 50 to 64 degrees with the step size of 2 degrees) and the solid lines represent the best fit of the TLD model. (a) Ellipsometric angle  $\Delta$ , (b) Ellipsometric angle  $\Psi$ . . . . . 148
- B.8 EVASE spectra of the PEDOT:PSS sample spin coated on quartz substrate at room temperature in 0.1 M KCl aqueous solution at an electrochemical bias of 0.0 V vs Ag/AgCl. The scatter points represent the measured data at varied angle of incidence (AOI, from 50 to 64 degrees with the step size of 2 degrees) and the solid lines represent the best fit of the TLD model. (a) Ellipsometric angle  $\Delta$ , (b) Ellipsometric angle  $\Psi$ . . . . . 149
- B.9 EVASE spectra of the PEDOT:PSS sample spin coated on quartz substrate at room temperature in 0.1 M KCl aqueous solution at an electrochemical bias of -0.1 V vs Ag/AgCl. The scatter points represent the measured data at varied angle of incidence (AOI, from 50 to 64 degrees with the step size of 2 degrees) and the solid lines represent the best fit of the TLD model. (a) Ellipsometric angle  $\Delta$ , (b) Ellipsometric angle  $\Psi$ . . . . . 150
- B.10 EVASE spectra of the PEDOT:PSS sample spin coated on quartz substrate at room temperature in 0.1 M KCl aqueous solution at an electrochemical bias of -0.2 V vs Ag/AgCl. The scatter points represent the measured data at varied angle of incidence (AOI, from 50 to 64 degrees with the step size of 2 degrees) and the solid lines represent the best fit of the TLD model. (a) Ellipsometric angle  $\Delta$ , (b) Ellipsometric angle  $\Psi$ . . . . . 151

B.11	EVASE spectra of the PEDOT:PSS channel in the OECT device at room temperature in 0.1 M KCl aqueous solution at an electrochemical bias of -0.1 V vs Ag/AgCl. The scatter points represent the measured data at varied angle of incidence (AOI, from 50 to 64 degrees with the step size of 2 degrees) and the solid lines represent the best fit of the TLD model. (a) Ellipsometric angle $\Delta$ , (b) Ellipsometric angle $\Psi$ . . . . .	152
B.12	EVASE spectra of the PEDOT:PSS channel in the OECT device at room temperature in 0.1 M KCl aqueous solution at an electrochemical bias of 0.1 V vs Ag/AgCl. The scatter points represent the measured data at varied angle of incidence (AOI, from 50 to 64 degrees with the step size of 2 degrees) and the solid lines represent the best fit of the TLD model. (a) Ellipsometric angle $\Delta$ , (b) Ellipsometric angle $\Psi$ . . . . .	153
B.13	EVASE spectra of the PEDOT:PSS channel in the OECT device at room temperature in 0.1 M KCl aqueous solution at an electrochemical bias of 0.2 V vs Ag/AgCl. The scatter points represent the measured data at varied angle of incidence (AOI, from 50 to 64 degrees with the step size of 2 degrees) and the solid lines represent the best fit of the TLD model. (a) Ellipsometric angle $\Delta$ , (b) Ellipsometric angle $\Psi$ . . . . .	154
B.14	EVASE spectra of the PEDOT:PSS channel in the OECT device at room temperature in 0.1 M KCl aqueous solution at an electrochemical bias of 0.4 V vs Ag/AgCl. The scatter points represent the measured data at varied angle of incidence (AOI, from 50 to 64 degrees with the step size of 2 degrees) and the solid lines represent the best fit of the TLD model. (a) Ellipsometric angle $\Delta$ , (b) Ellipsometric angle $\Psi$ . . . . .	155
B.15	EVASE spectra of the PEDOT:PSS channel in the OECT device at room temperature in 0.1 M KCl aqueous solution at an electrochemical bias of 0.75 V vs Ag/AgCl. The scatter points represent the measured data at varied angle of incidence (AOI, from 50 to 64 degrees with the step size of 2 degrees) and the solid lines represent the best fit of the TLD model. (a) Ellipsometric angle $\Delta$ , (b) Ellipsometric angle $\Psi$ . . . . .	156
C.1	Schematic illustration of a ion beam deposition system. A high energy ion beam strikes the material to be deposited. The material sputters out from the source and gets deposited on the substrate fixed on the rotating sample holder. . . . .	157
C.2	Schematic illustration of masking of a quartz substrate. (1) bare quartz substrate. (2) Quartz substrate masked with Carbon tape. . . . .	158
C.3	Photograph of the sample transfer device. (1) Sample holder is placed in the transfer device. (2) Sample is attached to the transfer device. (3) Sample is lifted to perform the transfer to the IBD chamber. . . . .	159

C.4 Schematic representation of the sample as taken out from the IBD chamber after deposition. (1) Sample with carbon tape. (2) Sample after removing carbon tape. . . . . 160

# List of Tables

3.1	Thicknesses of the samples used for UV-VIS-NIR transmission measurements, measured using an AFM. . . . .	41
3.2	The best fit parameters of the ordinary TLD of the uniaxially anisotropic dielectric function (cf. eqs.3.3-3.5); DC conductivity ( $\sigma_{DC}$ ) calculated from the Drude term (cf. eq.3.6) ; film thickness ( $d$ ) obtained from the fit and measured from AFM . All fit parameters are obtained by fitting the VASE spectra ( $\Psi, \Delta$ vs $E$ ) in air. . . . .	45
3.3	The best fit parameters of the ordinary TLD and extraordinary Drude term parameters of the uniaxially anisotropic dielectric function (cf. eqs. 3.3-3.5); and DC conductivity ( $\sigma_{DC}$ ) calculated from the Drude term (cf. eq. 3.6) ; film thickness ( $d$ ) obtained from the fit. All fit parameters are obtained by fitting the measured VASE spectra ( $\Psi, \Delta$ vs $E$ ) when PEDOT:PSS film is in contact with the electrolyte (0.1 M KCl aqueous solution). . . . .	47
3.4	The best fit parameters of the ordinary TLD and extraordinary Drude term parameters of the uniaxially anisotropic dielectric function (cf. eqs.3.3-3.5); and DC conductivity ( $\sigma_{DC}$ ) calculated from the Drude term (cf. eq.3.6) ; film thickness ( $d$ ) obtained from the fit . All fit parameters are obtained by fitting the EVASE spectra ( $\psi, \Delta$ vs Photon energy) , under varied equilibrium electric potentials (EMF) at the PEDOT:PSS electrode, in the range +0.6 to -0.2 V vs Ag/AgCl in 0.1 M KCl (pH $\approx$ 7). . . . .	52
3.5	The best fit parameters of the ordinary TLD and extraordinary Drude term parameters of the uniaxially anisotropic dielectric function (cf. eqs.3.3-3.5); and DC conductivity ( $\sigma_{DC}$ ) calculated from the Drude term (cf. eq.3.6) ; film thickness ( $d$ ) obtained from the fit . All fit parameters are obtained by fitting the EVASE spectra ( $\psi, \Delta$ vs Photon energy), under varied electromotive force (EMF) at the PEDOT:PSS electrode, in the range +0.0 V to 1.0 V vs Ag/AgCl in 0.1 M LiClO <sub>4</sub> . . . . .	55
3.6	Fit parameters of the equivalent circuit fitted to the EIS measurements at varied applied potential . . . . .	59

- 
- 4.1 The best fit parameters of the ordinary TLD parameters of the ordinary dielectric function (cf. eqs.3.3-3.5); and DC conductivity ( $\sigma_{DC}$ ) calculated from the Drude term (cf. eq.3.6) ; film thickness (d) obtained from the fit; the electrical conductivity measured by means of the four probe measurements . All fit parameters are obtained by fitting the EVASE spectra ( $\Psi, \Delta$  vs  $E$ ) , under varied equilibrium electric potentials at the PEDOT:PSS electrode, in the range -0.1 to +0.75 V vs Ag/AgCl in 0.1 M KCl (pH  $\approx$ 7). . . . . 82
- 5.1 Samples prepared for XRR and NEXAFS measurements at varied spin speeds to obtain different thickness as measured by AFM. . . . . 96

# Abbreviations

<b>PEDOT:PSS</b>	<b>Poly(3,4-EthyleneDiOxyThiophene) PolyStyrene Sulfonate</b>
<b>DMSO</b>	<b>DiMethyl SulfOxide</b>
<b>DBSA</b>	<b>Dodecyl Benzene Sulfonic Acid</b>
<b>GOPS</b>	<b>(3-GlycidylOxyPropyl) trimethoxySilane</b>
<b>PDMS</b>	<b>Poly(DiMethylSiloxane)</b>
<b>CP</b>	<b>Conducting Polymer</b>
<b>PEC</b>	<b>PolyElectrolyte Complex</b>
<b>SE</b>	<b>Spectroscopic Ellipsometry</b>
<b>VASE</b>	<b>Variable Angle Spectroscopic Ellipsometry</b>
<b>RAE</b>	<b>Rotating Analyzer Ellipsomete</b>
<b>RCE</b>	<b>Rotating Compensator Ellipsometer</b>
<b>PME</b>	<b>Phase Modulation Ellipsomete</b>
<b>EVASE</b>	<b>Electrochemical Variable Angle Spectroscopic Ellipsometry</b>
<b>FCC</b>	<b>Free Charge Career</b>
<b>VB</b>	<b>Valance Band</b>
<b>CB</b>	<b>Conduction Band</b>
<b>HOMO</b>	<b>Highest Occupied Molecular Orbital</b>
<b>LUMO</b>	<b>Lowest Unoccupied Molecular Orbital</b>
<b>DOS</b>	<b>Density Of States</b>
<b>BLA</b>	<b>Bond Length Alternation</b>
<b>DC</b>	<b>Direct Current</b>
<b>AFM</b>	<b>Atomic Force Microscopy</b>
<b>SPM</b>	<b>Scanning Probe Microscopy</b>
<b>IBD</b>	<b>Ion Beam Deposition</b>

---

<b>VRH</b>	<b>V</b> ariable <b>R</b> ange <b>H</b> opping
<b>EC</b>	<b>E</b> lectro <b>C</b> hemical
<b>CV</b>	<b>C</b> yclic <b>V</b> oltammogram
<b>W.E</b>	<b>W</b> orking <b>E</b> lectrode
<b>C.E</b>	<b>C</b> ounter <b>E</b> lectrode
<b>R.E</b>	<b>R</b> eference <b>E</b> lectrode
<b>UV-VIS</b>	<b>U</b> ltra <b>V</b> iolet - <b>VIS</b> ible
<b>NIR</b>	<b>N</b> ear <b>I</b> nfra <b>R</b> ed
<b>EM</b>	<b>E</b> lectro <b>M</b> agnetic
<b>QCM-D</b>	<b>Q</b> uartz <b>C</b> rystal <b>M</b> icrobalance- with <b>D</b> issipation
<b>EIS</b>	<b>E</b> lectrochemical <b>I</b> mpedance <b>S</b> pectroscopy
<b>CPE</b>	<b>C</b> onstant <b>P</b> hase <b>E</b> lement
<b>TLD</b>	<b>T</b> auc <b>L</b> orentz <b>D</b> rude
<b>FET</b>	<b>F</b> ield <b>E</b> ffect <b>T</b> ransistor
<b>OFET</b>	<b>O</b> rganic <b>F</b> ield <b>E</b> ffect <b>T</b> ransistor
<b>OTFT</b>	<b>O</b> rganic <b>T</b> hin <b>F</b> ilm <b>T</b> ransistor
<b>MOSFET</b>	<b>M</b> etal <b>O</b> xide <b>S</b> emiconductor <b>F</b> ield <b>E</b> ffect <b>T</b> ransistor
<b>OECT</b>	<b>O</b> rganic <b>E</b> lectro- <b>C</b> hemical <b>T</b> ransistor
<b>EGOFET</b>	<b>E</b> lectrolyte <b>G</b> ated <b>O</b> rganic <b>F</b> ield <b>E</b> ffect <b>T</b> ransistor
<b>OLED</b>	<b>O</b> rganic <b>L</b> ight <b>E</b> mitting <b>D</b> iode
<b>XPS</b>	<b>X</b> - <b>R</b> ay <b>P</b> hotoelectron <b>S</b> pectroscopy
<b>XRR</b>	<b>X</b> - <b>R</b> ay <b>R</b> eflectivity
<b>XRD</b>	<b>X</b> - <b>R</b> ay <b>D</b> iffraction
<b>NEXAFS</b>	<b>N</b> ear <b>E</b> dge <b>X</b> - <b>R</b> ay <b>A</b> bsorption <b>F</b> ine <b>S</b> tructure
<b>XAS</b>	<b>X</b> - <b>R</b> ay <b>A</b> bsorption <b>S</b> pectroscopy
<b>BEAR</b>	<b>B</b> ending <b>M</b> agnet for <b>E</b> mission, <b>A</b> bsorption and <b>R</b> eflectivity



# Physical Constants

Speed of Light	$c$	=	$2.997\,924\,58 \times 10^8 \text{ ms}^{-1}$
Permittivity of free space	$\epsilon_0$	=	$8.854\,187\,817 \times 10^{-12} \text{ Fm}^{-1}$
Planck's constant	$h$	=	$4.135\,667\,70 \times 10^{-15} \text{ eV} \cdot \text{s}$
Reduced Planck's constant/Dirac's constant	$\hbar = \frac{h}{2\pi}$	=	$6.582\,119\,57 \times 10^{-16} \text{ eV} \cdot \text{s}$
Elementary charge	$e$	=	$1.602\,176\,634 \times 10^{-19} \text{ C}$
Electron mass	$m_e$	=	$9.109\,382\,616 \times 10^{-31} \text{ Kg}$
Avogadro constant	$N_A$	=	$6.022\,141\,510 \times 10^{23} \text{ mol}^{-1}$
Faraday constant	$F$	=	$96\,485.338\,383 \text{ Cmol}^{-1}$
Boltzmann constant	$k$	=	$8.617\,343\,15 \times 10^{-5} \text{ eVK}^{-1}$

# Symbols

$\Psi$	ellipsometric angle Psi	°
$\Delta$	ellipsometric angle Delta	°
$\rho$	resistivity	$\Omega\text{cm}$
$\sigma$	conductivity	S/cm
$\tilde{\epsilon}$	complex dielectric function	
$\epsilon_1$	real dielectric function	
$\epsilon_2$	imaginary dielectric function	
$\epsilon_\infty$	high frequency dielectric	
$n$	refractive index	
$k$	extinction coefficient	
$\lambda$	wavelength	nm
$E$	energy	eV
$\Gamma$	damping	eV
$\alpha$	absorption coefficient	
$A$	strength of oscillator	$\text{eV}^2$
$d$	thickness	nm
$E_0$	resonance energy of oscillator	eV
$E_g$	band gap	(eV)

*Dedicated to my Grandfather...*

# Chapter 1

## Introduction

Intrinsically conducting polymers have provided a breakthrough in the field of organic electronics. These organic polymers can possess the electrical, electronic, magnetic and optical properties of metals while retaining the mechanical flexibility of a polymer. Chiang *et al.* and Shirakawa *et al.* demonstrated the capability to dope some of these polymers in a rich spectrum of conductivities, ranging from an insulator to a metal-like behaviour[1, 2] . With such flexibility, both in mechanical and electrical properties, conducting polymers (CP) have opened a new field of electronics which is flexible [3-5]. Solution-processed polymers are easily printable and coatable. Hence they provide ease of fabrication at meager costs. Due to their wide range of doping capabilities, CPs can be easily tuned to serve the required purpose *e.g.* in photovoltaics, light emitting diodes, organic field effect transistors, biosensors etc.[4, 6-9]. In the field of bioelectronics, the techniques of incorporating enzymes into electro-depositable conducting polymeric films permit the localization of biologically active molecules on electrodes of any size or geometry and are particularly appropriate for the fabrication of multi-analyte micro-amperometric biosensors [10, 11]. Conducting polymers are also known to be compatible with biological molecules in aqueous solution and can be used to sense the binding of these molecules on CP surfaces by using electrical or spectroscopic techniques [12, 13]. CPs are reported to change their intrinsic

conductivity by several orders of magnitude with the change in the pH value or redox potential of their environment[14].

Poly(3,4-ethylenedioxythiophene): poly(styrenesulfonate) (PEDOT:PSS) is one of the most promising CP material to be used as a channel material in transistor devices and is the subject of study in the presented work. PEDOT, unlike most of the charged conjugated polymer, is insoluble in polar solvents. Therefore the synthesis of PEDOT polycation is performed in the presence of PSS to form the PEDOT:PSS polyelectrolyte complex (PEC) [15]. PEDOT:PSS is highly water stable *i.e.* it can retain its electronic properties if kept in aqueous solutions for a longer period. This makes it very useful for biosensing applications, flexible electrochemical electrodes, and organic electrochemical transistors (OECTs) [16, 17]. Moreover, PEDOT:PSS dispersed in water can be easily coated on substrates by all commonly known thin film deposition techniques *e.g.* spray deposition, roll to roll gravure coating, dip coating, spin coating, inkjet printing etc. The most frequently used method is spin coating, as it is a readily available technique to obtain uniform films in the thickness range of 10-500 nm [18]. Another significant advantage of PEDOT:PSS is its thermal stability. After spin coating, it can be quickly baked on a hot plate at temperatures between 100°C - 200°C for few seconds without any degradation of its conducting properties [19]. This is done to remove any water content that might be present in the spin coated film. However, due to the presence of sulfonic acid groups in PEDOT:PSS, it is highly hygroscopic. Thus, it can take up high amount of moisture when kept at room temperature conditions [20]. Due to this, PEDOT:PSS films tend to swell and increase their thickness when kept in humid conditions [21]. This swelling behaviour of most CP films makes them a non-ideal channel material for electronic devices. The change in thickness due to swelling can cause a change in their conductivity, doping state and optical properties [22, 23]. In particular, for organic electrochemical transistors, where the channel is brought in direct contact with the electrolyte, the swelling of the channel can bring a significant shift in the device performance. However, these details are usually neglected while using CPs in electronic switching devices and biosensing applications [24, 25] causing inaccuracies in measurements. Another vital process

in organic electrochemical devices is the influx and efflux of ions in the polymer matrix by application of electrochemical bias, which in turn can dope or de-dope the CP film [26]. It must be noted that the influx and efflux of ions can again cause the film to swell and shrink [27]. Therefore, it becomes essential to perform an *in-situ* characterization of such devices. The electrochemical doping/de-doping in CPs is described by Alan J. Heeger in his Nobel lecture [28] as the oxidation or reduction of the conducting polymer, thereby increasing/decreasing the number of electronic charge carriers in the CP. Thus, application of an electrochemical bias to a CP can change its conductivity by oxidizing/reducing it. While PEDOT:PSS is an electrochemically active polymer, its conductivity can also be varied by the formation of a capacitive double layer at its surface. At the application of electrochemical bias, ions in the electrolyte migrate and accumulate at the electrolyte-CP surface. As a result, a capacitive (electrical) double layer is formed. Due to its porous nature, PEDOT:PSS has a large surface area and therefore has an ability to store a large amount of ionic charge at its 3D interface with the electrolyte. These infused ionic charges in the porous CP do not exchange electrons/holes with the CP, but rather form a capacitive double layer in the volume of the thin film [29]. The charging of this capacitive double layer is similar to the gating action in a field effect transistor *i.e.* accumulation of ions in the porous CP film produces a large electric field which in turn causes the accumulation (depletion) of electronic charge carriers in the semiconducting thin film [30, 31]. Thus, affecting the conductivity of the conducting polymer by a electrostatic field effect. Although, in the available literature the distinction between field effect and doping/de-doping in OECT devices is seldom made. Chapter 3 of this thesis presents an extensive study aimed to enable distinguishing the field effect mechanism from that of redox doping in a PEDOT:PSS thin film.

Spectro-electrochemical measurements of thin CP films are a useful tool for studying the *in-situ* evolution of electronic band structure of CPs [32–34]. Electrochemical doping/de-doping gives rise to the formation of polaron and bi-polaron electronic states in the band structure of CPs [35] and causes a shift in the absorption

spectra at varied applied electrochemical biases. By carefully modelling the absorption spectra of CP at varied applied electrochemical biases, the evolution in the optoelectronic properties of the CP film can be extracted [36]. On the other hand, no information about the optical anisotropy of CPs can be deduced from these studies. Depending on the processing procedure of CPs, preferential orientation of the polymer chains takes place, rendering CPs a complex anisotropic structures [37, 38]. Therefore, to have a complete understanding, it is essential to study the anisotropy in these materials. Spectroscopic ellipsometry is an efficient tool for studying the order of anisotropy and thickness of the CP film, simultaneously [39–41]. Petterson *et al.* reported the dielectric function of a PEDOT film by fitting a uniaxially anisotropic Lorentz-Drude model to their ellipsometric data [42]. The thickness of the film and the electronic transition in PEDOT along with its DC conductivity (extracted from the Drude parameters) were reported. Lasakarakis *et al.* also employed ellipsometry to study the optoelectronic properties of PEDOT:PSS film, however, an isotropic model was fitted to the measured ellipsometric data in this case [43]. The anisotropy found in the ellipsometry measurements of Petterson *et al.* indicates a possibility of a preferential orientation of PEDOT molecules in the PEDOT:PSS film. Nardes *et al.* [44], however, report a macroscopic reasoning of the observed anisotropy in PEDOT:PSS films. According to them, the anisotropy originates due to the stacking of PEDOT particles in the PEDOT:PSS matrix, into a lamellae parallel to the substrate separated by a thick PSS barrier. Therefore, the charge carrier hopping in the direction perpendicular to the substrate is reduced. While this can be a valid explanation for the reported anisotropy, the possibility of the anisotropic orientation of PEDOT molecules deserves a experimental examination.

In this work, we explore the optoelectronic properties of PEDOT:PSS films using variable angle spectroscopic ellipsometry (VASE). The use of VASE over other optical techniques serves two purposes, (i) since VASE presents a model dependent measurement technique, one can study the degree of anisotropy by employing an anisotropic dielectric function model for fitting the measured data. (ii) The dielectric functions can be extracted *in-situ* in parallel with electrochemically doping

---

the polymer film. The details of the *in-situ* electrochemical VASE (EVASE) technique are described in chapter 3 of this thesis. Further, the EVASE technique is used to characterize the OECT devices fabricated on quartz substrates. Chapters 3 and 4 explain the conduction mechanism of the PEDOT:PSS films on a macro level. Chapter 4 focuses on describing the charge transport mechanism of these devices from the optical, electrochemical and electrical measurements. Chapter 5 focuses on studying the anisotropy at the molecular level by exploring the molecular orientation of the constituents of the films under study.



# Chapter 2

## Theoretical background

### 2.1 Conducting polymers

Conducting polymers are organic macromolecules with  $sp^2$  hybridized carbon atoms along the backbone, connected with alternating single and double bonds [45, 46]. The electronic configuration of carbon atoms is  $1s^2 2s^2 2p^2$ . When making bonds with other carbon atoms, the four valence electrons in the  $2^{nd}$  shell form covalent bonds with neighbouring carbon atoms. In the case of conjugated polymers, the  $2s$  orbital mixes with two of the three available  $2p$  orbitals to form three  $sp^2$  hybrid orbitals leaving one  $2p$  orbital unhybridized (fig.2.2). Two of the  $sp^2$  orbitals form a covalent bond with a hydrogen atom (or a side group), one of them covalently binds with one  $sp^2$  orbital of the neighboring carbon, to form a sigma bond. The unhybridized  $p$  orbital overlaps with an unhybridized  $p$  orbital of the neighboring carbon to form a  $\pi$  bond. Since  $\pi$  bonds are bound weakly compared to the sigma bond, electrons in  $\pi$  bonds can be easily delocalized. These delocalized electrons (or holes) become the conducting charge carriers in conjugated polymers [47].

As per Bloch theory, conjugated polymers formed from atoms or molecules with half filled shells must have partially filled bands and should show metallic transport properties [48]. However, due to the bond length alternation (BLA) in conjugated polymers, Peierls instability occurs, which opens a gap in the band structure of

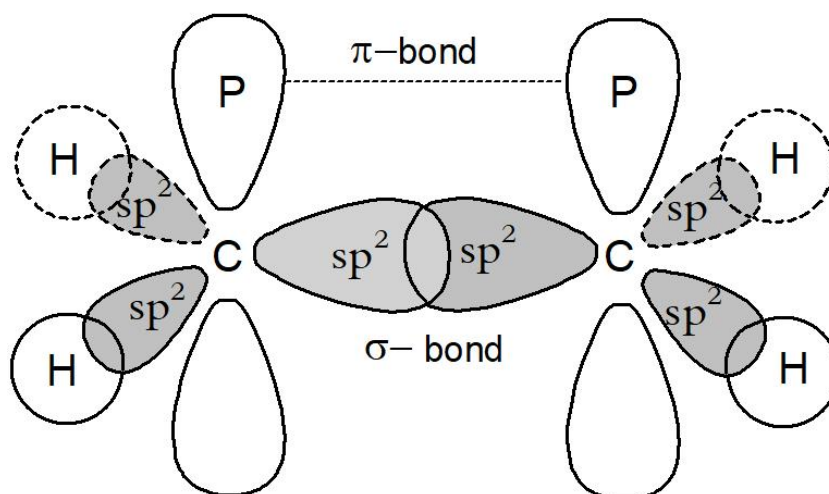
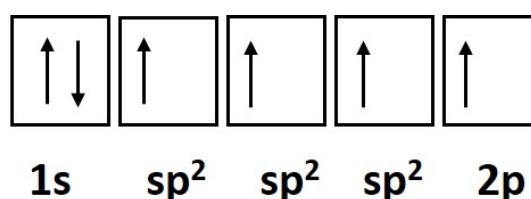


FIGURE 2.1: Double bonding in an ethylene molecule

FIGURE 2.2: Electronic configuration in a  $sp^2$  hybridized system, where the outer shell  $2s^2 2p^2$  of carbon hybridizes to form three  $sp^2$  orbitals leaving one  $2p$  orbital unhybridized

conjugated polymers, rendering them to behave as a semiconductor instead of a metal [49, 50]. The conductivity of a conjugated polymer can be enhanced from semiconducting to metallic by the process of doping. While the term “doping” had been picked directly from the inorganic solid-state physics, the process of doping in case of conjugated polymers can be viewed merely as a redox process, where the charge carriers are added or replaced by a chemical processes.

## 2.2 Doping in conducting polymers

Unlike conventional inorganic semiconductor, the doping process in conducting polymers is not done by mere element substitution. In the doping process of conducting polymers, the pristine polymer is transformed into an ionic complex. The

polymer is oxidized/reduced using an oxidizing/reducing agent [51]. A counterion is used to balance the excess charge produced in the pristine polymer due to oxidation/reduction. To stick to the terminology used in conventional semiconductors, the oxidized state of CP is called p-doped and the reduced state is called n-doped. The electronic configuration of CPs changes upon ionisation, this also effects the geometry of the polymer. Fig. 2.3 shows that the equilibrium geometry of the ionised state of poly(alkylthiophene) is quinoid-like and that of the neutral poly(alkylthiophene) is benzoid-like. Thus, the neutral polymer has a different energy state in comparison to the ionised (oxidized/reduced) one. Near the doped charges, strong coupling of electrons and phonons produces a distortion in the polymer lattice and bond lengths. In case of non-degenerate ground states, like in polythiophene, doped charges are stored as polarons and bipolarons [52].

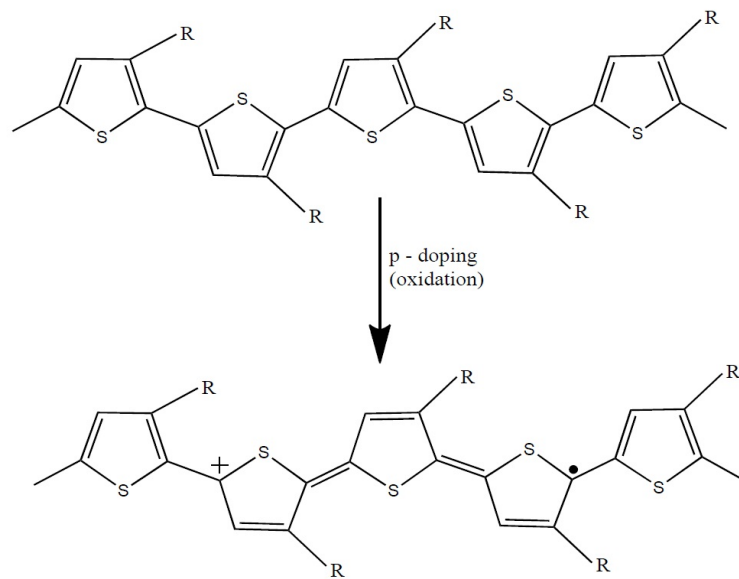


FIGURE 2.3: Evolution of a polaron in a neutral poly(alkylthiophene) chain by p-doping (oxidation)

In high doping conditions, these polarons interact with other polarons to form electrically conducting partially filled energy bands. On the other hand, for degenerated ground state CPs, the charge can move without dissipation and deformation. Therefore it has the property of a solitary wave and is referred to as a soliton[35, 53].

The quantum mechanical description of the non-degenerate system can be expressed by the band diagram in fig. 2.4. Just like in a crystal, the interaction of the delocalized electrons among the neighbouring monomeric units in a polymer leads to the formation of electronic bands. The highest occupied molecular orbital is the top of the valence band and the lowest unoccupied molecular orbital is the bottom of the conduction band. The difference in the energy level of the conduction and valence bands is called the forbidden energy gap or band gap. For most of the organic conjugated polymers, the band gap is above 1.5 eV, rendering them intrinsically insulating. In case of ionisation of such molecule, however, it can be energetically favorable to localize the charge by causing a local distortion around the lattice [35], which in turn results in pushing the highest occupied energy level (HOMO) upward and the lowest unoccupied molecular orbital (LUMO) downwards.

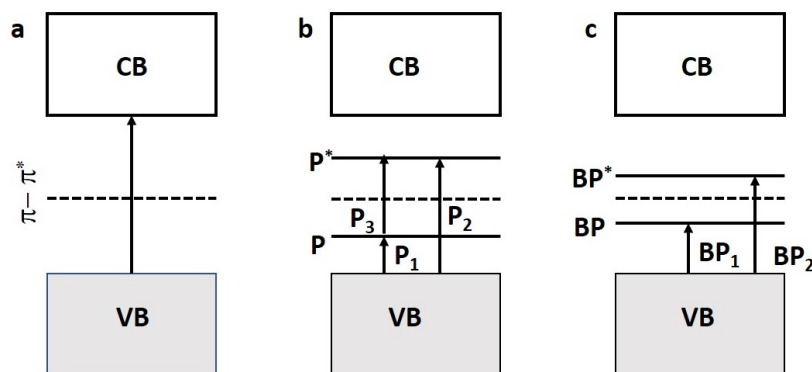


FIGURE 2.4: Evolution of polaron, polaron\* (P,P\*) and bipolaron, bipolaron\* (BP, BP\*) band upon the p-doping(oxidation). The arrows are the allowed electronic transitions. (a) the schematic of the band structure of PEDOT molecule in its pristine state. (b) the evolved band structure with polaron bands upon the oxidation of the pristine PEDOT. (c) the evolved band structure with bipolaron bands upon further oxidation of PEDOT.

Now if the energy level shift of  $\Delta E$  is larger than the distortion energy ( $E_{dis}$ ), it is favorable for the molecule to attain the distorted (quinoid) structure in comparison to relaxing into the benzoid ground state. In such conditions, new bands are formed within the forbidden gap, which are termed as "polarons" in condensed matter physics. Removal of two electrons from such molecules, however, results in a new states in the forbidden gap, these are termed as bipolaron states. The

formation of a bipolaron is thermodynamically more favourable in comparison to the formation of two polarons by 0.26 eV [54]. Fig.2.4 depicts the formation of polaron bands when a neutral conjugated polymer is oxidized by taking an electron out of the molecular configuration. Two new states appear in the  $\pi - \pi^*$  band gap of the neutral polymer upon oxidation. In this new system, only the electronic transitions as per the symmetry selection rules are allowed. In the above case, the allowed transitions are the ones represented by arrows *i.e.* P<sub>1</sub>, P<sub>2</sub> and P<sub>3</sub> for polaronic transitions and BP<sub>1</sub> and BP<sub>2</sub> for bipolarons [33, 55].

While the above explains about the intramolecular electronic transitions in CPs, the charge transport in CPs is not limited only to the intramolecular conduction, but also is intermolecular. Charged carriers in CPs can hop from one polymer chain to another via the Mott hopping conduction mechanism for amorphous materials[44, 56]. Keeping this in mind it shall be noticed that the polymer films do not dope uniformly during the doping process, so the conductivity of different regions of polymer film can differ, and the resulting conductivity of the whole thin polymer films will depend on how uniformly the doping is spread throughout the film.

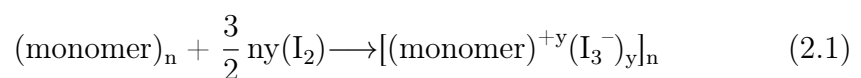
In their pristine state, CPs such as polythiophenes show poor conducting behavior, with the conductivity of the order of 0.1-10 S/cm [35, 57, 58]. However, it has been reported that the conductivity of such CPs can be increased up to 3-4 orders of magnitude upon doping, compared to their pristine counterparts[59, 60]. The process of doping is reversible, and the CP can be de-doped to its original state with little or no degradation of the polymer backbone. Unlike inorganic semiconductors, where doping of semiconductors is achieved by the addition of electron donating or electron acceptor impurity into the crystal lattice, for CPs doping leads to the formation of conjugation defects, viz. solitons, polarons or bipolarons in the polymer chain [35]. The ultimate conductivity in polymeric semiconductors depends on many factors, *e.g.* nature, and concentration of dopants, homogeneity of doping, carrier mobility, crystallinity and morphology of polymers[61, 62]. By adjusting the above parameters, the conductivity of CPs can be tuned from insulating to metal like conduction.

Since every repeating unit in a conducting polymer is a potential redox site, doping can be easily achieved in CPs by chemical routes. The most widely used methods described by Alan J. Heeger, in his Nobel lecture[28] are:

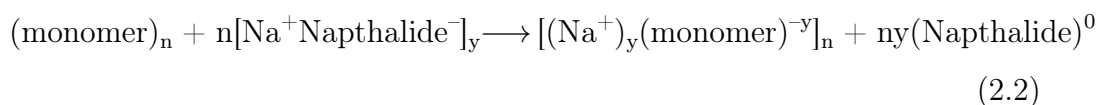
- Chemical doping
- Electrochemical doping
- Photochemical doping
- Interfacial doping

In the process of chemical doping, the conducting polymer is exposed to an oxidizing or reducing agent. Oxidation extracts an electron from the polymer backbone and provides it with a positive charge, which in analogy to the inorganic semiconductor can be referred to as p-doping. In case of reduction, an electron is introduced in the polymer matrix, and the process is called n-doping. With chemical doping process, organic materials can reach a very high conductivity which can be as high as that of copper. An example of such a process is explained through the chemical reaction below[28, 63]:

- *p-type*



- *n-type*



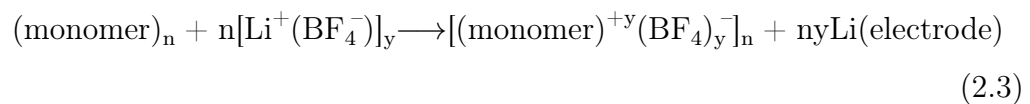
where, (monomer) represents the repeat unit of a  $\pi$ -conjugated polymer (monomer)<sub>n</sub>.

In the above reaction 2.1 the polymer is exposed to an iodine solution, which acts as an oxidizing agent that p-dopes the polymers and a tri-iodide ion compensates the positive charge of the polymer. Oppositely, in reaction 2.2, the polymer is

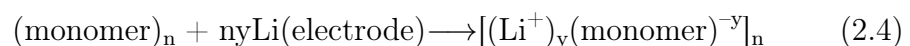
exposed to a sodium naphthalide solution. The polymer gains an electron from the naphthalide ion and the positive  $\text{Na}^+$  ion compensates the negatively charged polymer.

While chemical doping serves the purpose of doping the CPs to a large extent, whereby in many cases conductivity comparable to metals can be achieved, the intermediate doping, becomes hard to achieve by that route. This is because chemical doping is hard to control, since the chemical reaction continues until it reaches saturation. To remedy this issue, electrochemical doping is introduced by Nigrey *et al.* [64]. As the name suggests, electrochemical doping works on the principles of electrochemical reactions. One of the electrode (working electrode) in the electrochemical cell supplies charge to the electrode of opposite polarity (counterelectrode). One or both these electrodes can be the CP film to be doped. The ions from the electrolyte can be exchanged with the conducting polymer to balance the lost (or gained) electronic charge. The reaction can be controlled by the applied potentials at the electrode, and the doping level of the CP is determined by the applied potential for a given time until the redox reaction reaches an equilibrium. Electrochemical doping can be explained in the example below [28] :

- *p-type*



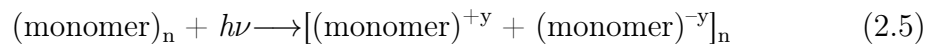
- *n-type*



The reaction 2.3 describes the p-type electrochemical doping of a pi-conjugated polymer. In the given reaction a pi-conjugated polymer electrode gives an electron to the  $\text{Li}^+$  ion in the  $\text{Li}^+\text{BF}_4^-$  electrolyte, producing a Li metal. The positive charge on the polymer is compensated by the  $\text{BF}_4^-$  ion from the electrolyte, leaving the

polymer to be p-doped. In reaction 2.4, on the other hand, n-type doping is performed. The polymer gains an electron from the Li counter electrode, producing a  $\text{Li}^+$  ion, which compensates the negative polymer charge. This leaves the polymer with an additional negative charge, which is counter balanced by a  $\text{Li}^+$  ion from the electrode.

Absorption of photons from a light source creates an electron-hole pair in the conducting polymers, creating free charge carriers. This process can also be seen as the local oxidation and reduction of the polymer by photoexcitation. The photoreaction describing the doping mechanism is explained below [28]:



where  $y$  is the number of electrons/holes in the excited state.

In a semiconductor device, when the semiconducting channel is connected through a source and drain electrodes on the two ends, the contact points of the channel can be doped due to the injection of charge carriers in the valance or conduction bands of a semiconductor [65, 66]. This process is known as interfacial doping. For a  $\pi$ -conjugated polymer channel,  $n$ -type interfacial doping occurs by the injection of electron from a metal electrode with low work function to the  $\pi^*$  band of the CP. Oppositely,  $p$ -type interfacial doping takes place when a high work function metal injects a hole in the  $\pi$  band of the CP. The interfacial doping mechanism for hole and electron injection is explained by the example below [28]:

- Hole injection



- Electron injection





This mechanism differs from the above described chemical and electrochemical processes, as there is no counterion in the equation to balance the charged polymer [65, 67].

## 2.3 Poly(3,4-ethylenedioxythiophene):polystyrene sulphonate (PEDOT:PSS)

PEDOT:PSS is a relatively new member of the conducting polymer group of materials. PEDOT was developed by Bayer corporate research laboratories by electrochemical polymerization of the EDOT monomer [47]. The benefits of PEDOT over other thiophene derivatives are that it is very stable at room conditions and is highly conductive in its cationic (doped) state. However, it is tough to process PEDOT into a coating or flexible thin films, as it is insoluble in most polar solvents. To make use of the extensive properties of PEDOT in industrial application, EDOT monomer can be polymerized in the presence of polystyrene sulfonate (PSS). PSS acts as a template polymer for PEDOT oligomers [8]. Synthesis of PEDOT:PSS in the presence of an oxidant such as sodium peroxodisulfate renders PEDOT in its conductive cationic state [68]. Whereas, anionic PSS has two functions in the PEDOT:PSS complex. Firstly, it acts as an electrostatic charge balancing counter-ion in the PEDOT:PSS structure [69], without the PSS counterion in the oxidation process, 3,4-ethylenedioxy-2(5H)-thiophene is formed instead of PEDOT:PSS [70]. Secondly, it makes the polymer complex dispersible in water, forming a deep blue microdispersion of polymer gel particles. PSS is often referred to as the "dopant" in the PEDOT:PSS complex.

The proposed structure of PEDOT:PSS complex is represented in fig. 2.5. The repeating units of the ionic pair  $\text{EDOT}^+$  and  $\text{SS}^-$  in the PEDOT:PSS complex are represented in the primary structure of the fig. 2.5. In the secondary structure the PEDOT oligomers are attached to the PSS chain forming a PEDOT:PSS complex. When this polyionic complex is dispersed in water it becomes highly swollen with up to 95% water and only 5% solid content and at higher concentration it is

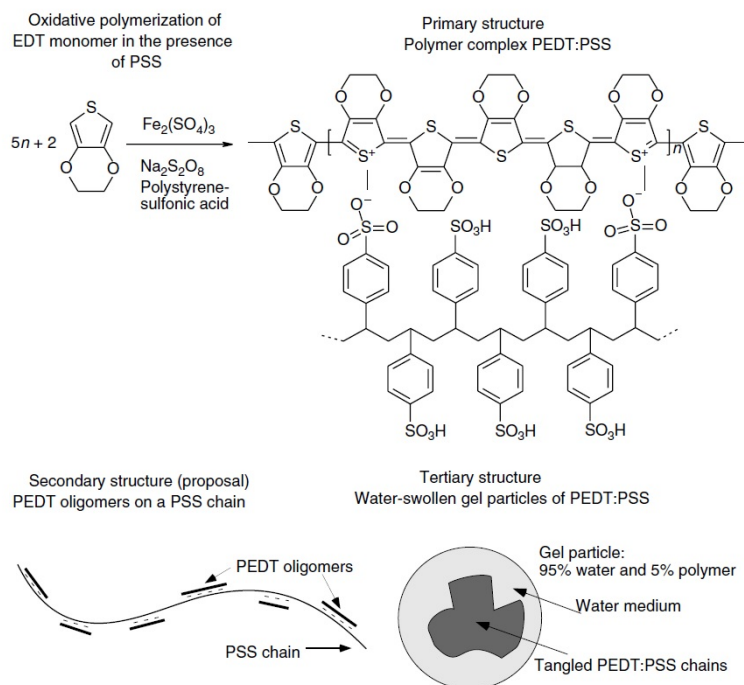


FIGURE 2.5: Primary, secondary and tertiary structure of PEDOT:PSS. Image reproduced from [47]

present as a hydrogel [71], which is highly processable for depositing films through wet coating techniques. The conductivity of PEDOT:PSS films depends on several factors like the oxidation state of PEDOT, PEDOT to PSS ratio, PEDOT particle size, etc.. The larger PEDOT to PSS ratio increases the conductivity [72], but at the same time decreases the solubility of the complex. Decreasing the particle size of PEDOT increases the distance between the PEDOT oligomers causing a longer hopping distances [73], resulting with a decreased conductivity of the film. In the present work the commercially purchased high conductivity grade PEDOT:PSS is used with 1:2.5 (Clevios, PH1000) PEDOT to PSS ratio.

### 2.3.1 Electrochemical doping in PEDOT:PSS

As explained above, PEDOT:PSS can be doped electrochemically, like all CPs. This property of PEDOT:PSS is explored in this thesis and is used to understand the functioning of organic electrochemical transistors (OECTs). Commercially available PEDOT:PSS (Clevios PH1000 PEDOT:PSS purchased from Heraeus

Deutschland GmbH and Co. KG was used in this work, c.f. sec. 3.1.1) is usually comprised of a doped state of PEDOT, which is electrostatically compensated with PSS. The details of the synthesis process are explained in the section above. Electrochemical doping may be used to de-dope PEDOT:PSS, such that it turns from its pristine conducting state to an insulating state. With the application of an opposite electrochemical bias, the process can be reversed, such that PEDOT:PSS is re-doped to its conductive state. The electrochemical process of doping can be understood by the following reaction[26]:



The left-hand side of equation 2.8 has a doped or oxidized state of the EDOT monomer, which is counter-balanced by a  $\text{SS}^-$  monomer. When  $\text{EDOT}_n^+ \cdot \text{SS}^-$  is provided with an electron and a cation from the electrolyte, the product on the right-hand side of the equation is a neutral or de-doped  $\text{EDOT}^0$  monomer while the negatively charged  $\text{SS}^-$  is counter-balanced by the cation.

## 2.4 Organic electrochemical transistors

The property of reversible switching of CPs from conducting to insulating and vice-versa by using electrochemical doping is utilized in organic electrochemical transistors (OECTs) [74–76]. The functioning principle of OECTs differs from that of traditional inorganic field effect transistors (FETs) and metal-oxide-semiconductor field-effect transistor (MOSFETs). While the latter devices employ the electrostatic field for controlling the channel current (a process called "gating"), OECT devices exploit a combination of electrostatic and electrochemical processes to modulate the conductivity of the channel material. An OECT consists of a conducting polymer film as a channel material, deposited in between and in contact with the source and drain electrodes, which is in contact with an electrolyte. Another electrode is dipped in the electrolyte, which is termed as the "gate" electrode,

in analogy to solid state transistors electrodes. A typical OEET structure is presented in fig. 2.6. A constant current is passed through the channel, which can be manipulated by applying an electrochemical voltage bias between gate and source electrode.

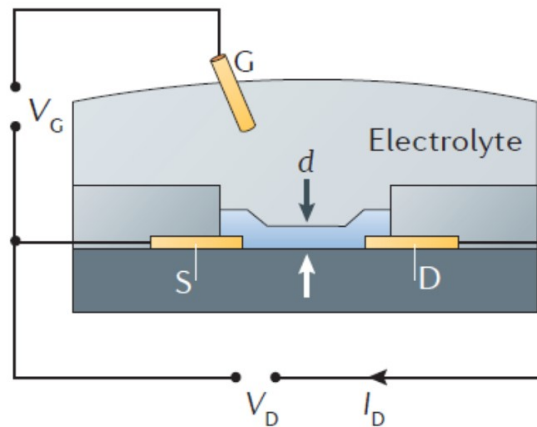


FIGURE 2.6: A typical structure of an OEET device. S, D and G represent the source drain and gate electrodes respectively.  $d$  is the thickness of the CP film.  $V_G$  is the applied gate-source voltage.  $V_D$  represents the applied source-drain voltage and  $I_D$  is the corresponding current for the same. Image reproduced from [74]

The transduction of the drain current by the application of a small gate voltage can be studied by the transfer curves of OEETs, *i.e.*  $I_D$  vs  $V_G$  [74]. The figure of merit of a OEET is defined by the change in drain with respect to the applied gate voltage and is can be calculated from the first derivative of the transfer curve,  $\Delta I_D / \Delta V_G$  [75, 76]. This is termed as the transconductance of the device. At a given gate voltage, the drain characteristics of a OEET can be defined as the change in drain current with changing source to drain voltage ( $V_D$ ). When  $V_D$  is varied the drain current,  $I_D$ , varies with it as per Ohm's law. A parallel change in gate to drain voltage ( $V_{GD}$ ) also takes place in this process, causing a influx of ions towards the drain electrode from the electrolyte. When the total density of the infused ions is equal to the intrinsic dopant density of the channel material, the source to drain current saturates. The voltage ( $V_D$ ) at which  $I_D$  saturates is called the pinch off voltage [75]. By increasing the gate voltage the pinch off

voltage can be manipulated and the device can be switched from OFF to ON state or vice-versa.

A model for the functioning of an OECT device is described by Bernardis *et al.* [77], where it is assumed that at an application of a gate potential, ions from the electrolyte infuse into the volume of the channel and thereby affecting the electronic conductivity.

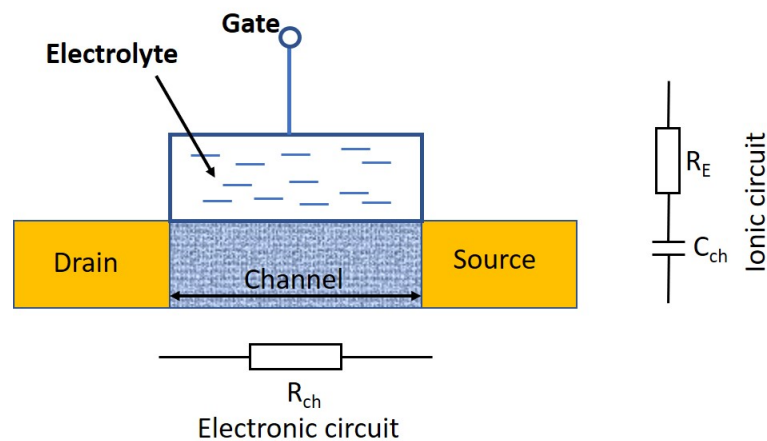


FIGURE 2.7: Representation of the ionic and electronic circuits used in the modelling of OECT devices.  $R_{ch}$  represents the electronic resistance of the channel in the electronic circuit of the model.  $R_E$  and  $C_{ch}$  represents electrolyte resistance and channel capacitance in the ionic circuit.

In this model, the device is divided in two circuits (c.f. fig.2.7). One is an ionic circuit, which describes the gate-electrolyte-channel architecture of the device. Other is an electronic circuit, represented as a resistor ( $R_{ch}$ ), which describes the flow of electronic charge from source to drain electrode. The electronic circuit is treated according to Ohm's law, where the electronic charge carriers drift under the influence of externally applied potential. The ionic circuit however, is described with a resistor ( $R_E$ ) in series with a capacitor ( $C_{ch}$ ). The resistor represent the electrolyte resistance and the capacitor represents the capacity of the channel to store ionic charge. According to the ionic circuit of this model, the process of gating *i.e.* the application gate potential is purely a capacitive process and no electrochemical reaction takes place between the electrolyte and channel [74, 78].

While this model provides a good fit for the output characteristics of the OECT, this theoretical treatment does not assume the possibility of redox doping (c.f. section 2.2) in the CP films. Therefore, in chapter 3 and 4 of this thesis an *in-situ* optical and electrochemical characterization of CPs are performed. This enables the differentiation between electrostatic and redox effects in an OECT.

## 2.5 Ellipsometry

### 2.5.1 Propagation of light in a medium

The interaction of electromagnetic (EM) waves with the matter in which it propagates were described by Maxwell's equations as [79, 80]:

$$\nabla \cdot \mathbf{E} = \frac{1}{\hat{\epsilon}_p} \cdot \rho \quad (2.9)$$

$$\nabla \cdot \mathbf{B} = 0 \quad (2.10)$$

$$\nabla \times \mathbf{E} = -\frac{\partial \mathbf{B}}{\partial t} \quad (2.11)$$

$$\nabla \times \mathbf{B} = \hat{\mu}_p \cdot \mathbf{J} + \hat{\epsilon}_p \hat{\mu}_p \frac{\partial \mathbf{E}}{\partial t} \quad (2.12)$$

where,  $\mathbf{E}$  is the electric field vector,  $\mathbf{B}$  is the magnetic field vector,  $\rho$  is the charge density,  $\mathbf{J}$  is the current density,  $\hat{\mu}_p$  and  $\hat{\epsilon}_p$  are the permeability and permittivity of the material.

Remarkably, the magnetic and electric field vectors are coupled in equation 2.11 and 2.12. To obtain a purely electric field equation, a curl operator is applied to equation 2.11 and the current density is assumed to be constant:

$$\nabla \times (\nabla \times \mathbf{E}) = \nabla \times -\frac{\partial \mathbf{B}}{\partial t} \quad (2.13)$$

$$\nabla^2 \mathbf{E} = \hat{\epsilon}_p \hat{\mu}_p \frac{\partial^2 \mathbf{E}}{\partial t^2} \quad (2.14)$$

Equation 2.14 shows that the propagation of the electric field vector in a three dimensional material depends on the permeability ( $\hat{\boldsymbol{\mu}}_p$ ) and the permittivity ( $\hat{\boldsymbol{\epsilon}}_p$ ) tensors of the material. In a material with homogeneous distribution of  $\hat{\boldsymbol{\mu}}_p$  and  $\hat{\boldsymbol{\epsilon}}_p$ , the EM wave propagates with a velocity:

$$\hat{\boldsymbol{v}} = \frac{1}{\sqrt{\hat{\boldsymbol{\epsilon}}_p \hat{\boldsymbol{\mu}}_p}} = \frac{c}{\hat{\boldsymbol{n}}} \quad (2.15)$$

where,  $c$  is the speed of light in vacuum and  $\hat{\boldsymbol{n}}$  is the refractive index tensor of the material,

$$\hat{\boldsymbol{n}} = \sqrt{\frac{\hat{\boldsymbol{\epsilon}}_p \hat{\boldsymbol{\mu}}_p}{\epsilon_0 \mu_0}} = \begin{bmatrix} \tilde{n}_{xx} & 0 & 0 \\ 0 & \tilde{n}_{yy} & 0 \\ 0 & 0 & \tilde{n}_{zz} \end{bmatrix} \quad (2.16)$$

where  $\tilde{n}_{xx}$ ,  $\tilde{n}_{yy}$  and  $\tilde{n}_{zz}$  are the complex refractive indices in the x, y, and z components of the refractive index tensor.  $\epsilon_0$  and  $\mu_0$  are the permittivity and permeability of free space respectively. For most materials  $\mu_p = \mu_0$ , therefore,

$$\hat{\boldsymbol{n}} \approx \sqrt{\frac{\hat{\boldsymbol{\epsilon}}_p}{\epsilon_0}} = \sqrt{\hat{\boldsymbol{\epsilon}}} \quad (2.17)$$

where,  $\hat{\boldsymbol{\epsilon}}$  is the dielectric tensor of the material and can be represented as:

$$\hat{\boldsymbol{\epsilon}} = \begin{bmatrix} \tilde{\epsilon}_{xx} & 0 & 0 \\ 0 & \tilde{\epsilon}_{yy} & 0 \\ 0 & 0 & \tilde{\epsilon}_{zz} \end{bmatrix} \quad (2.18)$$

where  $\tilde{\epsilon}_{xx}$ ,  $\tilde{\epsilon}_{yy}$  and  $\tilde{\epsilon}_{zz}$  are the complex dielectric functions in the x, y, and z components of the dielectric tensor. If all the three components of a dielectric tensor are equal, then the medium is called isotropic. In the other case, the medium is termed as anisotropic or birefringent. If two of the three components

are equal, the medium is termed as uniaxially anisotropic, and if all the three components are distinct, it is called biaxial.

### 2.5.2 Reflection of a polarized light

When a polarized beam of light reflects from the interface of two surfaces, the light-matter interaction changes the polarization of the reflected light. By studying the changed polarization of reflected light beam, with respect to the incident light, the dielectric properties of the reflecting sample can be determined. This measurement of change in the polarization state of light is called “ellipsometry” [81]. By resolving the incident and reflected light along the p- and s- polarization, the reflection of light can be mathematically described as follows [82]:

$$\mathbf{E}_r = \mathbf{R} \cdot \mathbf{E}_i \quad (2.19)$$

or,

$$\begin{bmatrix} \tilde{E}_p^r \\ \tilde{E}_s^r \end{bmatrix} = \begin{bmatrix} \tilde{R}_{pp} & \tilde{R}_{sp} \\ \tilde{R}_{ps} & \tilde{R}_{ss} \end{bmatrix} \begin{bmatrix} \tilde{E}_p^i \\ \tilde{E}_s^i \end{bmatrix} \quad (2.20)$$

Here,  $\mathbf{E}_r$  represents the electric field vector of reflected light,  $\mathbf{E}_i$  represents the electric field vector of the incident light, and  $\mathbf{R}$  represents the Fresnel’s reflection coefficient matrix.  $\tilde{E}_p^i$  and  $\tilde{E}_s^i$  are the orthogonal components of the incident polarized light (p and s polarized components). The Fresnel’s reflection coefficient is a 2x2 matrix representing the optical properties of the reflecting material. In simple terms, the above equation explains that when an incident light interact with a surface of a material, depending on the reflection coefficient matrix of the material the outcome polarization of the reflected light will change. If the optical axis of the reflecting material is parallel to the sample plane then a p or s polarized incident beam can have both p and s polarized components in its reflected counterpart, invoking the  $\tilde{R}_{ps}$  and  $\tilde{R}_{sp}$  components of the reflection coefficients. On the other hand, if the optical axis of the reflecting material is normal to the



sample plane then the off-diagonal components of the reflection coefficient,  $\tilde{R}_{ps}$  and  $\tilde{R}_{sp}$  become zero. Such is the case of uniaxially anisotropic materials, where the reflection coefficients can be represented as:

$$\mathbf{R} = \begin{bmatrix} \tilde{R}_{pp} & 0 \\ 0 & \tilde{R}_{ss} \end{bmatrix} \quad (2.21)$$

In the special case of an isotropic medium, where the dielectric function of the medium is equal in all three co-ordinates (c.f. sec 2.5.1), the light-matter interaction is equal in all directions. Therefore the p and s components of the reflected light are equal. In this case,  $|\tilde{R}_{pp}| = |\tilde{R}_{ss}|$ .

When a beam of polarized light reflects from the interface of an isotropic ambient and an uniaxially anisotropic substrate (fig.2.8), the reflection coefficient can be represented as [81]:

$$\tilde{R}_{pp} = \frac{\tilde{n}_{1o}\tilde{n}_{1e}\cos(\theta_0) - \tilde{n}_0\sqrt{(\tilde{n}_{1e}^2 - \tilde{n}_0^2\sin^2\theta_0)}}{\tilde{n}_{1o}\tilde{n}_{1e}\cos(\theta_0) + \tilde{n}_0\sqrt{(\tilde{n}_{1e}^2 - \tilde{n}_0^2\sin^2\theta_0)}} \quad (2.22)$$

$$\tilde{R}_{ss} = \frac{\tilde{n}_0\cos(\theta_0) - \sqrt{(\tilde{n}_{1o}^2 - \tilde{n}_0^2\sin^2\theta_0)}}{\tilde{n}_0\cos(\theta_0) + \sqrt{(\tilde{n}_{1o}^2 - \tilde{n}_0^2\sin^2\theta_0)}} \quad (2.23)$$

where,  $\tilde{n}_{1o}$  and  $\tilde{n}_{1e}$  are the complex ordinary ( $\tilde{n}_{xx} = \tilde{n}_{yy}$ ) and extraordinary ( $\tilde{n}_{zz}$ ) refractive indices of the uniaxially anisotropic material.  $\tilde{n}_0$  is the complex refractive index of the isotropic ambient.  $\theta_0$  is the angle of incidence.

The reflection coefficients for the interface of isotropic ambient and isotropic substrate can be obtained by substituting  $\tilde{n}_{1o} = \tilde{n}_{1e} = \tilde{n}_1$  in the above equations,

$$\tilde{R}_{pp} = \frac{\tilde{n}_1^2\cos(\theta_0) - \tilde{n}_0\sqrt{(\tilde{n}_1^2 - \tilde{n}_0^2\sin^2\theta_0)}}{\tilde{n}_1^2\cos(\theta_0) + \tilde{n}_0\sqrt{(\tilde{n}_1^2 - \tilde{n}_0^2\sin^2\theta_0)}} \quad (2.24)$$

$$\tilde{R}_{ss} = \frac{\tilde{n}_0\cos(\theta_0) - \sqrt{(\tilde{n}_1^2 - \tilde{n}_0^2\sin^2\theta_0)}}{\tilde{n}_0\cos(\theta_0) + \sqrt{(\tilde{n}_1^2 - \tilde{n}_0^2\sin^2\theta_0)}} \quad (2.25)$$

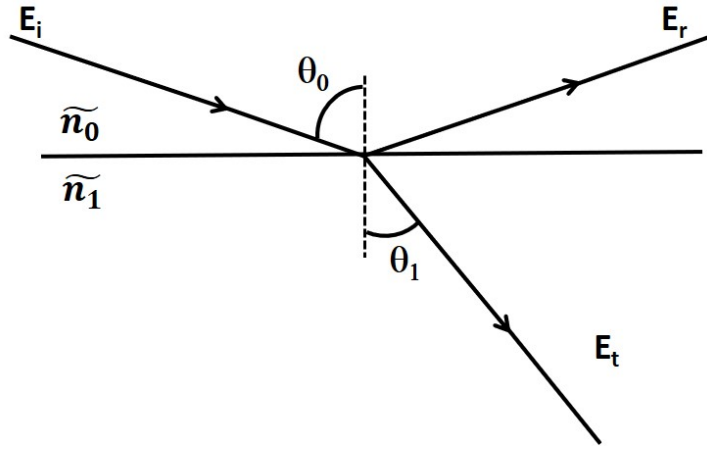


FIGURE 2.8: Schematic representation of the reflection of light from the interface of two media.

The Fresnel's equations can be extended for stratified multilayer systems. Specifically in the presented study, where a thin uniaxially anisotropic polymer film on an isotropic substrate in an isotropic ambient is studied using ellipsometry. Fig. 2.9 is an illustration of a three phase optical system, where the incident light  $E_i$  strikes the thin film ( $\tilde{n}_1$ ) of thickness  $d$ , through the ambient ( $\tilde{n}_0$ ). The polarized light ray is reflected from the ambient-film interface at the angle same as the angle of incidence ( $\theta_0$ ). The light refracted from the ambient-film interface, strikes the substrate ( $\tilde{n}_2$ ) and reflect back towards the film-ambient interface and transmits in the ambient. Due to the interaction of light with two different interfaces as compared to only one interface in the two phase optical system (fig. 2.8), the reflection coefficients in this scenario are different. For the sake of differentiation, the reflection coefficients for p and s polarizations in a three phase system are denoted as,  $\rho_{pp}$  and  $\rho_{ss}$  respectively.

$$\tilde{\rho}_{pp} = \frac{R_{pp01}^{\sim} + R_{pp12}^{\sim} \cdot e^{-i2\beta}}{1 + R_{pp01}^{\sim} \cdot R_{pp12}^{\sim} \cdot e^{-i2\beta}} \quad (2.26)$$

$$\tilde{\rho}_{ss} = \frac{R_{ss01}^{\sim} + R_{ss12}^{\sim} \cdot e^{-i2\beta}}{1 + R_{ss01}^{\sim} \cdot R_{ss12}^{\sim} \cdot e^{-i2\beta}} \quad (2.27)$$

Where,  $\rho_p$  and  $\rho_s$  are the total reflection coefficients of p and s polarized light in a three phase optical system.  $R_{pp01}$  and  $R_{pp12}$  are the reflection coefficients of p

polarized light at ambient-film and film-substrate interfaces respectively. Accordingly, the notation is extended for s polarized light. The term  $\beta$  is derived from the phase change that occurs due to the propagation of light in the film ( $\tilde{n}_1$ ) medium [83].

$$\beta = 2\pi \frac{d}{\lambda} \sqrt{\tilde{n}_1^2 - \tilde{n}_0^2 \sin^2 \theta_0} \quad (2.28)$$

where,  $\lambda$  is the wavelength on incident light and  $d$  is the film thickness.

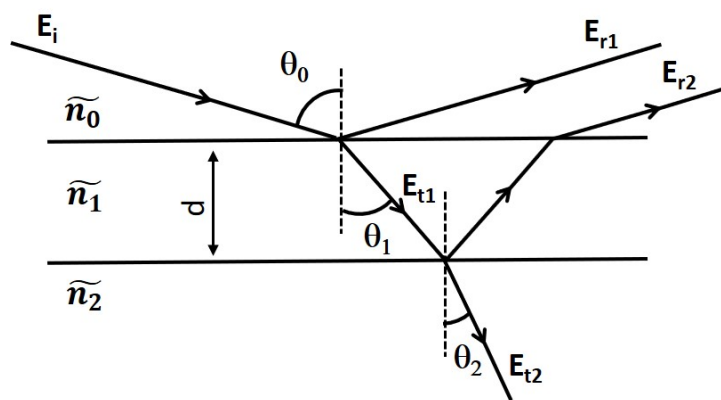


FIGURE 2.9: Schematic representation of the reflection of light from a system with two interfaces.

### 2.5.3 Measurement principle of ellipsometry

The polarization state of any light beam can be obtained by dividing the electric field vector into two components, which are parallel (p) and perpendicular (s) to the direction of propagation of the light beam. The electric field vector of the p and s polarized component of the EM wave can be represented by the plane wave equation as: :

$$\tilde{E}_p = a_p e^{i\delta_p} \quad (2.29)$$

$$\tilde{E}_s = a_s e^{i\delta_s} \quad (2.30)$$

Therefore, the polarization state of a light beam can be defined by the ration of eq. 2.5 and 2.6, *i.e.*,

$$\frac{\tilde{E}_p}{\tilde{E}_s} = \frac{a_p}{a_s} \cdot e^{i(\delta_p - \delta_s)} \quad (2.31)$$

While eq. 2.7 describes the polarization state of an electric field vector. The two main parameters that summarize the given polarization state are  $\psi$  and  $\Delta$ , which are defined as:

$$\Psi = \arctan\left(\frac{a_p}{a_s}\right) \quad (2.32)$$

$$\Delta = \delta_p - \delta_s \quad (2.33)$$

The term  $\Psi$  represents the ratio of the amplitudes of the p (x direction) and s (y direction) components of the light beam, and  $\Delta$  represents the phase difference between them. Fig. 2.10 represents a 2D projection of a polarized light beam at normal incidence, the X and Y components of the amplitude of light are presented in the Cartesian co-ordinates.

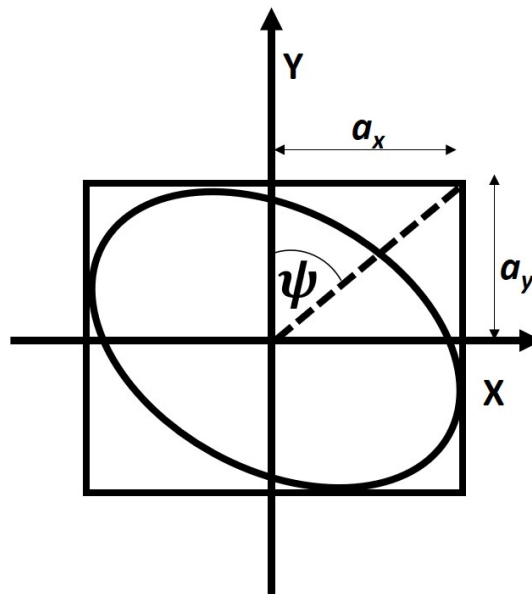


FIGURE 2.10: A 2D projection of an polarized light beam at normal incidence, where the angle  $\psi$  represents the ellipticity of the polarized light.  $a_x$  and  $a_y$  are the amplitudes of the light beam in X and Y directions of the cartesian co-ordinates

To obtain the change in polarization by interaction at the interface of a medium, the ratio between the reflection coefficients of p and s polarized light is to be analyzed [83]. The Fresnel's reflection coefficient for the reflected polarized electric field vector can be written in terms of electric field amplitude 'a' and phase  $\delta$  as :

$$\boxed{\frac{\tilde{R}_{pp}}{\tilde{R}_{ss}} = \frac{\frac{a_p^r}{a_p^i} e^{i(\delta_p^r - \delta_p^i)}}{\frac{a_s^r}{a_s^i} e^{i(\delta_s^r - \delta_s^i)}} = \tan(\Psi e^{i\Delta})} \quad (2.34)$$

By introducing equations 2.24, 2.25 and 2.34, a direct relation between the ellipsometric angles  $\Psi$  and  $\Delta$  and the refractive index of the reflecting material can be established as follows:

$$\tan(\Psi e^{i\Delta}) = \frac{\tilde{R}_{pp}}{\tilde{R}_{ss}} = \frac{\tilde{n}_1^2 \cos(\theta_0) - \tilde{n}_0 \sqrt{(n_1^2 - n_0^2 \sin^2 \theta_0)}}{\tilde{n}_1^2 \cos(\theta_0) + \tilde{n}_0 \sqrt{(n_1^2 - n_0^2 \sin^2 \theta_0)}} \cdot \frac{\tilde{n}_0 \cos(\theta_0) + \sqrt{(n_1^2 - n_0^2 \sin^2 \theta_0)}}{\tilde{n}_0 \cos(\theta_0) - \sqrt{(n_1^2 - n_0^2 \sin^2 \theta_0)}} \quad (2.35)$$

By inversion of equation 2.35, the complex refractive index  $\tilde{n}_1$  can be calculated from eq. 2.35 from the measured or known values of the ellipsometric angles ( $\Psi$  and  $\Delta$ ), the angle of incidence and the known refractive index of the ambient ( $\tilde{n}_0$ ).

The above equation holds for the reflection coefficients of an isotropic system. To obtain the values of  $\Psi$  and  $\Delta$  for an uniaxially anisotropic film on a isotropic substrate, the reflection coefficient described in eq. 2.26 and 2.27 must be substituted in eq. 2.34.

$$\frac{\rho_p}{\rho_s} = \tan(\Psi e^{i\Delta}) \quad (2.36)$$

In eq. 2.36 two ellipsometric angles  $\Psi$  and  $\Delta$  are equated to nine p and s reflection coefficient parameters. These parameters consist of the real and imaginary parts of complex refractive indices,  $\tilde{n}_0$  (ambient),  $\tilde{n}_1$  (film)  $\tilde{n}_2$  (substrate), angle of incidence, film thickness ( $d$ ) and the wavelength of the incident light beam ( $\lambda$ ). The values of parameters like, angle of incidence and wavelength, are known from the

design of experiment. The complex dielectric function of the substrate and ambient can be obtained from the literature or a separate ellipsometry measurement for the substrate can be conducted. The real and imaginary part of refractive index and the thickness of the thin film are the unknown parameters that must be determined using ellipsometry. Since there are more unknown parameters in the L.H.S compared to the two ellipsometric angles of R.H.S of eq. 2.36, the solution must be determined by fitting a model to the ellipsometric angles. A flowchart explaining the fitting process is presented in fig. 2.11.

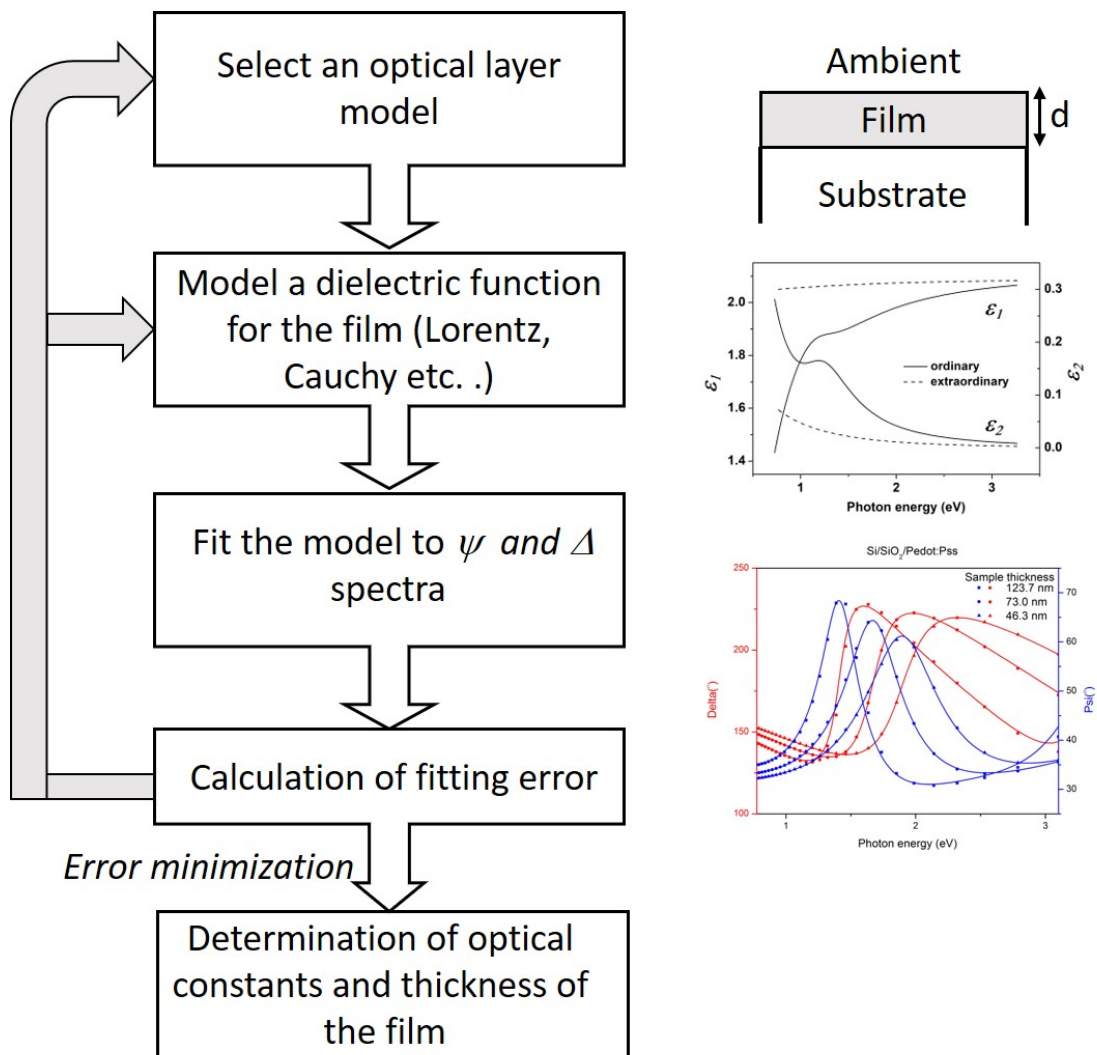


FIGURE 2.11: A flowchart explaining the steps taken for fitting the ellipsometric data to a model for the determination of optical constants. Adapted from [81]

Where a stratified layer optical model based on Fresnel equations is built. The values of the complex refractive indices of the substrate and ambient are obtained

from the literature. A model of a complex dielectric function (or refractive index) of the film is plugged into in the Fresnel's equations for the optical model. To reduce the cross correlations of the parameters, multiple ellipsometric measurements at varied angle of incidence and varied wavelength can be performed and fitted to the same model. This measurement is known as variable angle spectroscopic ellipsometry (VASE). Several iterations of the fitting procedure are performed to reduce the fitting error. When the fitting error is below the allowed limit, the optical constants and the thickness of the film can be extracted from the model. In this thesis, two different stratified optical layer models were used to fit the measured ellipsometric angles. For samples in air ambient

The detailed explanation of how the ellipsometric angles ( $\Psi$  and  $\Delta$ ) are measured are explained in Appendix A.

## Chapter 3

# Doping of poly(3,4-ethylenedioxythiophene):poly(styrene-sulfonate) films studied by means of electrochemical variable angle spectroscopic ellipsometry

<sup>1</sup>The use of liquid electrolytes as a gate dielectric has been practiced in the area of inorganic solid-state transistors for past few decades [84, 85]. Due to the formation of an electrical double layer at the solid-liquid (channel-electrolyte) interface, liquid electrolytes can modulate the conductivity of the channel material at very low gate voltages. This is fundamentally advantageous for producing high-efficiency devices with low power consumption [75, 86]. However, the electrochemical gating in the field of CP electronics is a somewhat new and more complex concept in comparison to inorganic transistors. While many extensive studies have been reported regarding the practical application of such systems [87–89], the underlying principles of charge transfer by the application of electrochemical bias to

---

<sup>1</sup>Parts of this chapter have been published in an elsevier journal , "Thin solid films" DOI: <https://doi.org/10.1016/j.tsf.2018.01.049>



CPs remains to be fully explored [77, 90, 91]. Due to the porosity of conducting polymers, liquid electrolytes can significantly affect the electronic mobility and therefore the conductivity of the channel material. This is due to the formation of electrical double layer at the electrolyte-CP interface [92–94], where the double layer acts as a electrical dipole, thus disrupting the flow of free charge carriers in the CP by a field effect. However, because the CPs are electrochemically active, it's been discussed that the electronic/hole charge carrier densities in CPs can be controlled by reversible electrochemical doping [26, 28, 95], where due to the reversible oxidation/reduction of the polymer channel the charge carrier concentration is modulated to switch the polymer film from insulating to conducting or vice-versa. In this chapter, the focus is to explore the electrochemical-doping mechanism of conducting polymers. By using optical techniques in combination with electrochemistry, an attempt is made to distinguish the effects of electrochemical doping from that of an electrostatic field effect.

CP chains prefer to orient themselves in particular directions depending on the processing procedure, rendering them complex anisotropic structures [37, 38]. Such anisotropies are critical for device functionality for specific applications such as charge transport in lateral (OTFTs) or perpendicular (OLED) directions with respect to the substrate. Thereby, studying electrical and optical anisotropies of CP films are of specific interest and require precise methods of characterization. Spectroscopic ellipsometry (SE) is an advantageous technique to characterize such complex polymer systems in a non-invasive manner. SE is able to provide multiple sets of information such as transition energy, optical band-gap, DC conductivity and degree of anisotropy [81]. Dry Polymer films at room temperature conditions have already been studied via SE, and descriptive electrodynamic models have been suggested to understand the conducting/semiconducting nature of the CPs depending on their optical anisotropy [42, 43]. The effect of electrolyte gating on conducting polymers, however, has not been explored so far by SE. Although standard optical transmission/absorption measurements have been used to study the effect of electrolyte gating in CPs, critical influence of anisotropy in CPs cannot be accounted for using such techniques. Moreover, the effect of external influences

on chemical and physical properties of polymer films, such as swelling when immersed in an electrolyte, has mostly been ignored in both optical and electrical measurements [17].

For a better understanding of these relatively new electronic/electrochemical polymer systems, much broader characterization methods and techniques are required. In this chapter, we explore the optoelectronic properties of conducting polymer poly(3,4-ethylenedioxythiophene):poly(styrene-sulfonate) or PEDOT:PSS by using SE techniques. In order to investigate the mechanism of electrochemical doping in PEDOT:PSS, electrochemical VASE (EVASE) technique is introduced, where VASE measurements are conducted at varied electrochemical load applied to the PEDOT:PSS film. An appropriate anisotropic Tauc-Lorentz-Drude model is used to fit the ellipsometry data at different electrochemical (EC) potentials. This enables studying the electronic properties of PEDOT:PSS films while tuning the Fermi level with respect to a reference electrode. Swelling of the CP thin-films in electrolyte solution was taken into account while fitting the data using this model. Electrochemical impedance measurements (EIS) are conducted to compare the trend in conductivity measured by the optical method. EIS measurements also enables to differentiate between the different electrochemical processes, that occur simultaneously on PEDOT:PSS electrode. In this chapter, a non-invasive benchmark technique is established to characterize electrochemically active conducting polymers.

## 3.1 Experimental part

### 3.1.1 Sample preparation

A suspension containing 0.8 % (w/w) PEDOT:PSS (Clevios PH-1000), 10 % DMSO (Acros Organics) and 0.1 % GOPS (Sigma Aldrich) in water, was spin-coated for 30 sec at varied spin speeds onto quartz or Si/SiO<sub>2</sub> substrates to produce films of varied thickness (fig. 3.1). The film thickness of ca. 80-100 nm was

found appropriate for VASE/EVASE measurements, and to produce such samples the spin speed of 4000 RPM was used. While spin coating provided a smooth deposition of the PEDOT:PSS films, the orientation of the polymer chains could not be controlled with this method. However, one should note that the secondary and tertiary structures of PEDOT:PSS (as shown in fig. 2.5) are present in the suspension, These gel particles spread out on the substrate due to the centrifugal force of the spin, forming a thin film. The distance between these particles is controlled by spin speed and the concentration of PEDOT:PSS in the suspension [96, 97]. The films were then annealed on a hot plate at 150°C for 10 minutes, rinsed thoroughly with deionized water (resistivity 18.2 MΩcm) and dried. Samples were subject to atomic force microscopy (AFM), VASE, electrochemical impedance spectroscopy(EIS) and EVASE measurements at room temperature (25°C).For Evase measurements, the same procedure was performed on Quartz substrates with previously coated Cr/Au contact pads (only for EVASE, c.f Appendix C).

### 3.1.2 Atomic force microscopy

Atomic force microscopy (AFM) was performed using a Bruker Nanoscope atomic force microscope to measure the thickness of the spin-coated film and to measure the uniformity of the film. On both the substrate, PEDOT:PSS film was scratched with a sharp tweezer to create a step. The scans were performed in the contact mode configuration using a silicon tip on a nitride lever (scanasyst-air). A 20X20 micron scan was conducted across the step at three

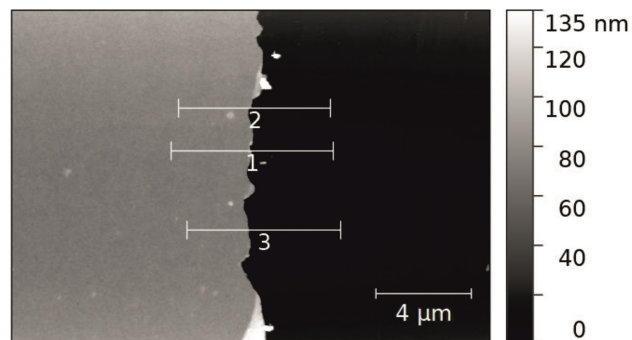


FIGURE 3.1: The scanning atomic force micrograph of the PEDOT:PSS film spin-coated at the Si/SiO<sub>2</sub> substrate.

different regions. The height profile was measured from the  $z$  (height) vs  $x$  AFM data at all the three regions from which the average thickness of the film was calculated (fig. 3.2). Thicknesses of samples prepared at different spin speeds is plotted in fig.3.3

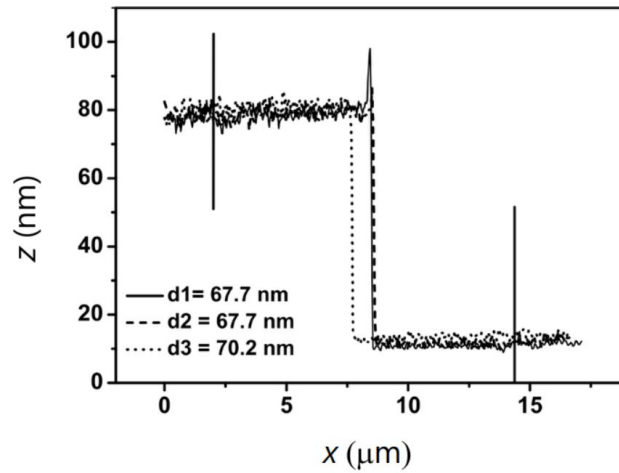


FIGURE 3.2: Height profile diagram of the sample spun at the rate of 4000 rpm for 30 sec, determined along the three lines indicated in the micrograph (fig.3.1). The micrograph was recorded in air medium, approximately at the same spot as VASE.

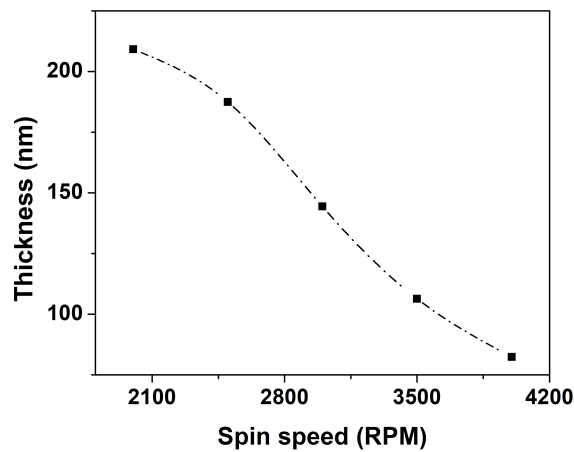


FIGURE 3.3: The thickness of the PEDOT:PSS thin film measured with AFM vs the spin speed (all for 30 sec).

### 3.1.3 Electrical measurements

Van der Pauw contact geometry was used for four probe resistivity measurement. This is a fine experimental technique to accurately calculate the resistivity of a thin film [98]. A home build probe station was used with four tungsten probes mounted on four micro-aligners (Everbeing intl. corp). The probe tips were mounted with a conducting glue to avoid piercing the soft PEDOT:PSS film when in contact. The probes were placed at four corners of a nearly square sample. Current is passed through one edge of the sample (*e.g.*,  $I_{12}$ ), and voltage drop is measured across the other edge (*e.g.*,  $V_{34}$ ). The current is swept from 0-1 mA, and a corresponding voltage ramp is recorded. The slope of the  $I - V$  curve is taken as the resistance. The process was repeated for 8 combinations of voltage to current probes, and the average horizontal and vertical resistance ( $R_{hor}$  and  $R_{ver}$ ) were calculated. The sheet resistance ( $R_s$ ) is then calculated using the Van der Pauw formula:

$$\exp^{-\pi R_{hor}/R_s} + \exp^{-\pi R_{ver}/R_s} = 1 \quad (3.1)$$

Resistivity can be equated to sheet resistance as per definition ( $\rho = R_s \cdot d$ ). The thickness  $d$  is measured using AFM, as explained above.

Fig. 3.4 shows the Van der Pauw measurement (c.f sec. 3.1.3) setup, where the four contacts are marked 1,2,3 and 4. Four measurements are performed in horizontal dimensions, where the current is passed through one horizontal side (*e.g.*,  $I_{12}$ ), and the voltage is measured through the other (*e.g.*,  $V_{34}$ ). The same is repeated for the four combinations in the vertical dimension.

### 3.1.4 Transmission measurements

To examine the optical behavior of dry PEDOT:PSS thin films spin-coated on quartz substrates, UV-VIS-NIR spectroscopy was performed. An Agilent UV-VIS spectrophotometer was used to record the absorption spectra of films on the UV-VIS range. A Metrohm near infra-red spectrophotometer (NIRS rapid liquid

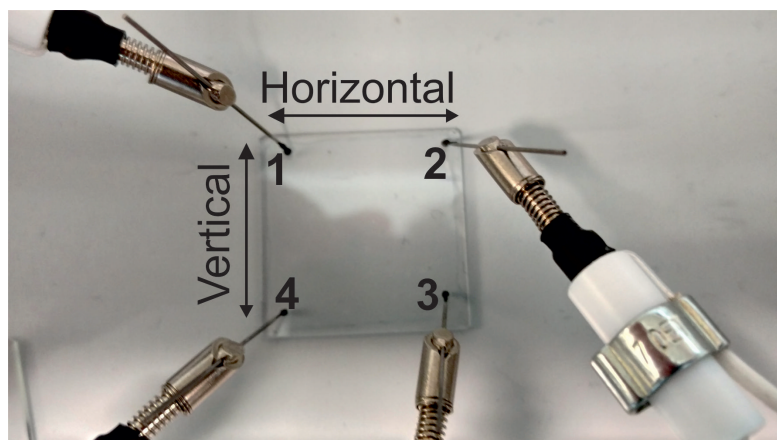


FIGURE 3.4: Image of PEDOT:PSS thin film sample on quartz substrate with the tungsten probes in electrical contact with the sample in Van-der-Pauw geometry

analyzer) was used to record the absorption spectra in the VIS-NIR range. Firstly a bare quartz substrate was placed perpendicular to the incoming beam in the spectrophotometer, and a background spectrum was recorded. Similarly, the measurement was repeated for the PEDOT:PSS thin film on a quartz substrate. The background spectrum was subtracted from the spectrum measured from the sample, such that the absorption coming from the substrate is eliminated and only the PEDOT:PSS thin film spectrum is observed. The UV-VIS and VIS-NIR measurements were stitched together to observe the spectrum in the full UV-VIS-NIR range.

### 3.1.5 Variable angle spectroscopic ellipsometry

The VASE measurements were performed with Accurion EP4 spectroscopic nulling ellipsometer at room temperature. The first set of measurements was performed in air ambient for both Si/SiO<sub>2</sub> and quartz substrates. The angle of incidence was varied in the range of 50-64 degrees with a 2-degree step. For each spectrum, 30 data points were measured in the wavelength range of 400-1700 nm. The EP4 Model software by Accurion GmbH was used for fitting the uniaxially anisotropic

dielectric function and film thickness from the VASE data (ellipsometric angles  $\Psi$  and  $\Delta$ ), by solving the Fresnel's equations for a stack of stratified optical layers.

Similar VASE measurements were conducted only on a quartz substrate, where instead of air, the PEDOT:PSS layer was kept in contact an electrolyte (0.1 M KCl). To perform the measurement in the VIS-NIR range such that the NIR radiation is not absorbed by the electrolyte, a Kretschmann cell is used (fig. 3.5). The PEDOT:PSS film was sealed between the quartz prism on top of the quartz substrate and the electrolyte cell on the bottom. Change in incident angle due to refraction through the prism was taken into account. No electrochemical bias was applied in this experiment.

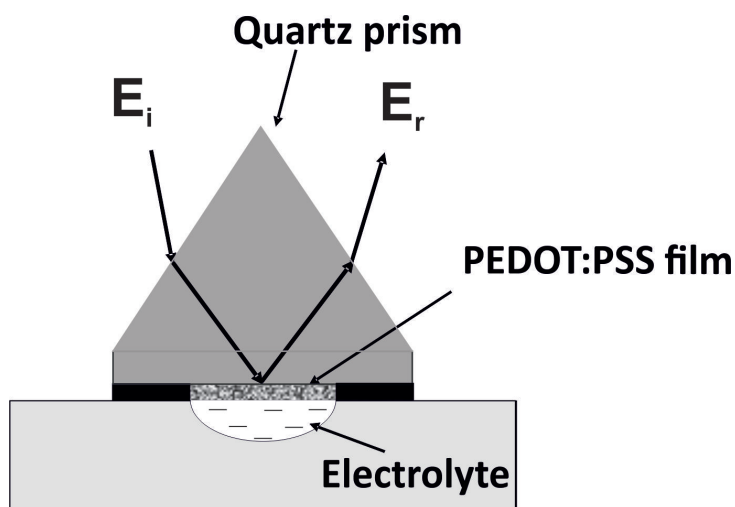


FIGURE 3.5: Scheme of Kretschmann electrochemical cell, which facilitates VASE measurements in the NIR range for the PEDOT:PSS film is in contact with the electrolyte

### 3.1.6 Electrochemical variable angle spectroscopic ellipsometry

The *in-situ* electrochemical VASE (EVASE) measurements were performed in the Kretschmann optical geometry as explained above. Autolab PGSTAT128 potentiostat was used for the electrochemical measurements in the three-electrode setup, with Au/PEDOT:PSS film connected as the working electrode (WE), a Pt-rod as a counter electrode (CE), and an Ag/AgCl wire as a reference electrode in

0.1 M aqueous solution of KCl (RE). First, the WE-RE potential was cycled in the range -0.45 V to +0.8 V vs. Ag/AgCl (in 0.1 M KCl), at a sweep rate of 10 mV/s, and cyclic voltammograms (CV) were recorded during several cycles. The EVASE measurements were performed in the potential range from 0.6 V to -0.2 V with -0.1 V step, by pausing the CV at a particular potential, and after the current dropped to nearly zero, which was achieved within ca. 2-3 min. In this situation, the film is in (electro)chemical equilibrium, and the EVASE measurements were performed in the same manner as above described. This procedure is repeated for all the voltage values. The EP4 model software is used to fit the EVASE measurements, separately for all potential values. The detailed process and the steps taken to achieve the best fit parameters is described in appendix B. The experiment is repeated in 0.1 M LiClO<sub>4</sub> in acetonitrile to extend the range of the electrochemical scan, as in aqueous electrolytes one is limited the potential range below  $\pm 0.8$  V to avoid parasite reactions such as hydrogen evolution. Also, due to the inert nature of LiClO<sub>4</sub> in acetonitrile, it is assured that the redox reactions are occurring at the PEDOT:PSS electrode and not in the electrolyte itself.

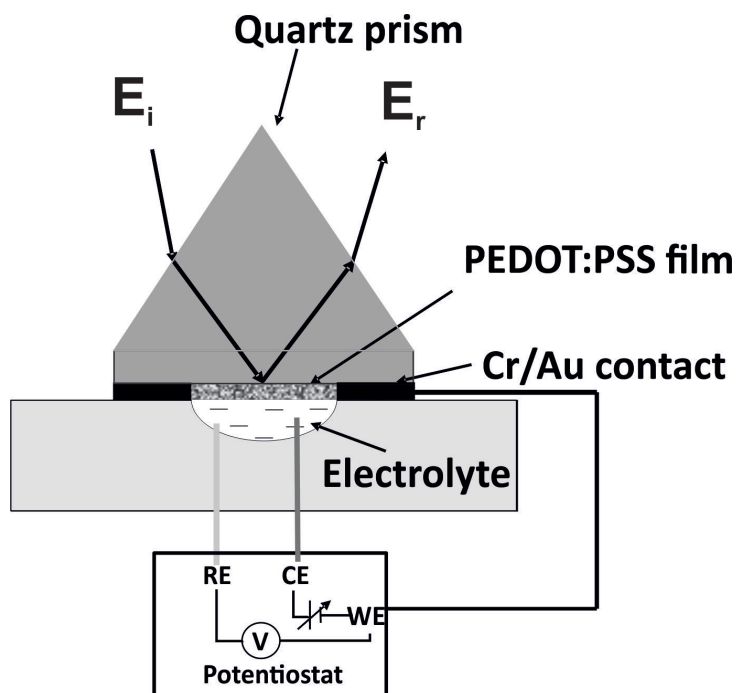


FIGURE 3.6: Scheme of sample in a Kretschmann cell, connected to a potentiostat. Where, the Au/PEDOT:PSS film serves as W.E, a Pt rod electrode is used as a C.E and an Ag/AgCl wire in 0.1 M KCl (aq)(or 0.1 M LiClO<sub>4</sub> in acetonitrile) is used as a R.E



### 3.1.7 Electrochemical impedance spectroscopy

Electrochemical impedance spectroscopy (EIS) measurements were conducted using the FRA module of the Autolab PGSTAT128 potentiostat, in the same setup as explained above. Multiple measurements were conducted for a given sample around voltages adjusted to the same values as in the case of EVASE. The scans were conducted between the frequency range from 0.1 Hz to  $10^5$  Hz with the amplitude value of 1 mV. For each EIS measurement at given voltages, Nyquist and Bode plots were recorded, and an equivalent circuit was fitted using the Autolab NOVA 2.0 software.

## 3.2 Tauc-Lorentz-Drude model

To solve the Fresnel equations (cf. sec. 2.5) for the stratified layers of the sample, one needs to know the dielectric properties of all the layers. While the dielectric function of the substrate and the ambient are known, the dielectric function of the polymer layer must be modeled using an electrodynamic function. Therefore a model function is introduced in the Fresnel's equation to fit the ellipsometric angles.

The dielectric function of PEDOT:PSS thin films was modeled using a uniaxially anisotropic Tauc-Lorentz-Drude model. Within the Tauc-Lorentz-Drude (TLD) model, the complex dielectric function  $\epsilon_{TLD} = \epsilon_1 + i\epsilon_2$  is a sum of three terms:

$$\tilde{\epsilon}_{TLD}(E) = \epsilon_{\infty} + \tilde{\epsilon}_{TL}(E) + \tilde{\epsilon}_D(E) \quad (3.2)$$

where  $E$  is the photon energy,  $\epsilon_{\infty}$  is the purely real high frequency dielectric constant.  $\tilde{\epsilon}_{TL}(E)$  is the Tauc-Lorentz (TL) oscillator, for which the imaginary part is given as:

$$\epsilon_{TL}^{im}(E) = \begin{cases} 0, & E \leq E_g \\ \frac{E-E_g}{E^2} \cdot \frac{A_{TL}E_0\Gamma_{TL}E}{(E_0^2-E^2)^2+\Gamma_{TL}^2E^2}, & E > E_g \end{cases} \quad (3.3)$$

where  $A_{TL}$  is the strength,  $E_g$  is the Tauc gap,  $E_0$  is the resonance energy, and  $\Gamma_{TL}$  is the damping (or "broadening"). The real part of  $\tilde{\epsilon}_{TL}$  is derived from  $\epsilon_{TL}^{im}$  using the Kramers-Kronig transformation. This model is frequently used for the inter-band electronic transitions in amorphous semiconductor thin films, where both the valence and conduction bands (VB, CB, respectively) are approximated by a single asymmetrical density of states (DOS) functions [81, 99–101]. The reader is referred to the above-cited authors for a detailed description of the TLD model, while for further discussion, the meaning of the three parameters defining the TL oscillator is underlined: the strength is proportional to the overlap integral of the ground and excited states taking part in the transition, the resonance energy is the energy of the most probable transition, while the Tauc (or "optical") gap is the energy difference between the LUMO and HOMO, irrespective of their electron densities. The intra-band absorption by the free charge carriers (FCC) is described by the Drude oscillator, which is evidenced as a tail at the low energy end in the dielectric function [102].

$$\tilde{\epsilon}_D(E) = \frac{A_D}{E^2 + i\Gamma_D E} \quad (3.4)$$

where  $A_D$  is the oscillator strength proportional to the hole concentration in the unfilled VB of PEDOT, and  $\Gamma_D$  is the damping. From the Drude parameters  $A_D$  and  $\Gamma_D$ , the low frequency conductivity of the film can be calculated as:

$$\sigma_{DC} = \frac{\epsilon_0}{\epsilon_\infty \cdot \hbar} \cdot \frac{A_D}{\Gamma_D} \quad (3.5)$$

where  $\epsilon_0$  is the permittivity of free space and  $\epsilon_\infty$  is the high frequency dielectric constant.

### 3.3 Results and discussions

#### 3.3.1 Van Der Pauw measurements

The measured  $I - V$  curves for all eight combinations of electrodes on dry PEDOT:PSS films deposited on Si/SiO<sub>2</sub> and quartz substrates are presented in fig. 3.7 a,b. It can be noticed that vertical and horizontal resistances are very slightly different in value. This could be because the PEDOT:PSS sheet may not be an exact square. Therefore the length of the sides may cause a difference in resistance values. The sheet resistance is calculated using eq. 3.1 and was found to be 429.5  $\Omega/\text{cm}$  and 233.12  $\Omega/\text{cm}$  for quartz/PEDOT:PSS and Si/SiO<sub>2</sub>/PEDOT:PSS samples respectively. The thickness values measured by AFM were found to be 82 nm and 160 nm for the respective samples. The resistivity values calculated from Eq. 3.2 are found to be 283.9 S/cm and 266.4 S/cm on quartz and Si/SiO<sub>2</sub> samples respectively. The linear response of  $I-V$  curves represents the Ohmic contact of PEDOT:PSS films to the Au electrodes, *i.e.*, no potential barrier is present at the contact, and the resistive flow of charge carriers is observed in the measured voltage range.

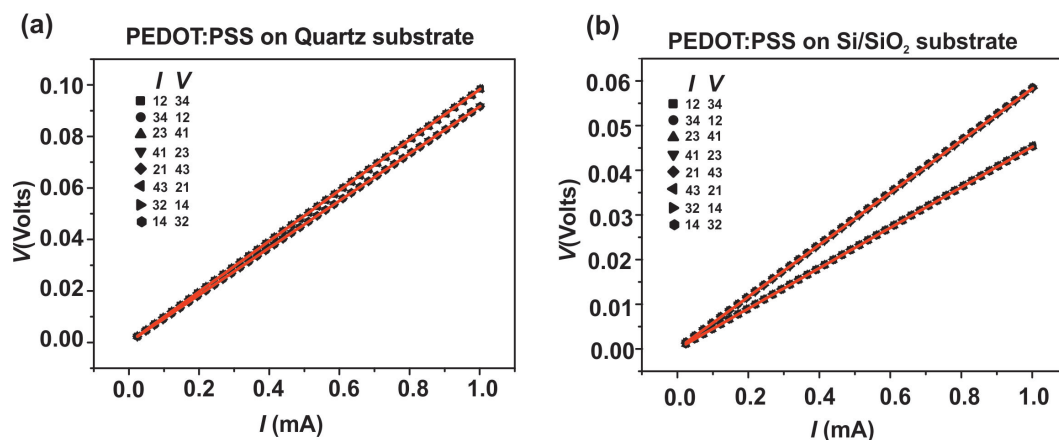


FIGURE 3.7: Four probe Van-der-Pauw  $I-V$  curves for eight different pairwise combinations of current vs voltage probes, The inset in the figure represents the assigned numbers to the contact points and the legends indicate the measurements performed for different combination of current and voltage probes. Red line is a linear fit to the measurements, whereby the slope provides the resistance. (a) Van-der-Pauw measurements of PEDOT:PSS film on quartz substrate. (b) Van-der-Pauw measurements of PEDOT:PSS film on Si/SiO<sub>2</sub> substrate

### 3.3.2 Optical Transmission

Transmission measurements recorded for five different sample of varied thicknesses (table 3.1) in the UV-VIS-NIR range is presented in fig. 3.8 (a). One can clearly observe the PSS  $\pi - \pi^*$  transition peak at 5.5 and 6.2 eV in the UV range of the spectra, as reported in various literature[102–105]. The PEDOT:PSS films seem almost transparent in the visible range, and the increasing absorbance in the NIR range indicates the presence of free charge carriers (FCC).

TABLE 3.1: Thicknesses of the samples used for UV-VIS-NIR transmission measurements, measured using an AFM.

Sample no.	Thickness (nm)
1	575
2	170
3	69
4	53
5	30

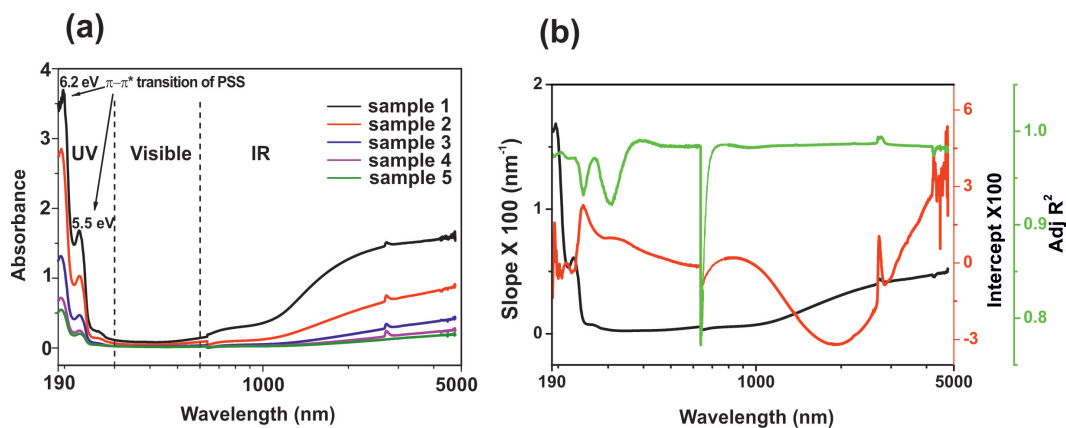


FIGURE 3.8: (a) UV-VIS-IR spectra of PEDOT:PSS thin film spin coated on a quartz substrate, the legends denote the sample of different thickness (cf. table 3.1). (b) Lambert-Beer's law fit (eq: 3.6) to the measured absorption spectra, the legends denote the fitted parameters

The increasing absorbance with increasing film thickness can be noticed in fig.3.8a. This is in accordance with the Lambert-Beer's law:

$$Abs = \alpha \cdot d + C \quad (3.6)$$

$$\alpha = \frac{4\pi k}{\lambda} \quad (3.7)$$

$$Abs = \frac{4\pi k \cdot d}{\lambda} + C \quad (3.8)$$

where,  $Abs$  is the measured absorbance,  $\alpha$  is the absorption coefficient,  $d$  is the film thickness,  $C$  is a constant for a given wavelength,  $k$  is the extinction coefficient and  $\lambda$  is the wavelength.

Since absorbance is wavelength-dependent and equation 3.7 is a linear equation for a given wavelength. Therefore, a linear regression between the absorbance and thickness was performed for each wavelength data point. This is to extract the absorption coefficient  $\alpha$  from the slope and the constant element  $C$  from the intercept of the linear fit. The Adj  $R^2$  for all wavelength point is close to 1, implying that the fit is linear for all wavelengths and the sample obeys Lambert-Beer's law.

### 3.3.3 Variable angle spectroscopic ellipsometry

Three stratified layers were used for modeling the ellipsometric data obtained for the dry PEDOT:PSS films on both quartz and Si/SiO<sub>2</sub> substrate, in air ambient. Beforehand, an effective dielectric dispersion of the substrate was calculated by performing a VASE measurement on the bare substrates. The measured  $\Psi$  and  $\Delta$  of the effective substrate were converted to complex dielectric parameters by mathematical inversion of eq. 2.35 (see section 2.5.3) and used as the dielectric function of the substrate. The top layer is the PEDOT:PSS thin film, for which the dielectric function is unknown and shall be modeled using the uniaxially anisotropic model. The ambient layer is air, dielectric function of which can be obtained from the literature.

Tauc-Lorentz-Drude ( $\tilde{\epsilon}_{TLD}$ ) model (eq. 3.3) was used for ordinary orientation of the dielectric tensor, where the Tauc-Lorentz oscillator is responsible for the interband electronic transitions, and the Drude term for the intraband transition of free charge carriers. A Drude model ( $\tilde{\epsilon}_D$ ) (eq. 3.5) was employed for the extraordinary orientation, as adding additional parameters in the extraordinary

direction did not improve the fit significantly. To reduce the cross-correlation of multiple parameters in the fit, the VASE data of PEDOT:PSS films on Si/SO<sub>2</sub> and quartz substrates for eight angle of incidences was simultaneously fitted with the same anisotropic TLD model. The thickness of the two samples was taken as two different fit parameters in the model, while all other parameters were kept the same for the samples on both substrates.

Fig. 3.9 and 3.10 represent the best simultaneous fit for the ellipsometric angles  $\Psi$  and  $\Delta$  for eight angles of incidences obtained on Si/SiO<sub>2</sub> and quartz substrates, respectively. Fig. 3.11 represents the TLD function fitted to the measured ellipsometric angles. The ordinary and extraordinary fitted parameters of the TLD model and the conductivity calculated from Eq. 3.6 are listed in table 3.2. An RMSE value close to 1 indicates a good fit of the parameters. The fitted thickness on Si/SiO<sub>2</sub> is in a close match with the thickness measured by AFM, which confirms the validity of the model. A little deviation in the thickness can be expected due to the non-uniformity of the spin-coated polymer film. It can be observed from fig. 3.11 that in the low-frequency range, the ordinary dielectric function of PEDOT:PSS in air represents a steep drop and steep increase in the values of  $\epsilon_1$  and  $\epsilon_2$  respectively. This behavior is termed as the "Drude tail". Which is evidence of the presence of free charge carriers in highly doped semiconducting materials[106]. In the high-frequency range, the variation in the values of real and imaginary dielectric function is almost negligible. These observations indicate that the ordinary dielectric function of PEDOT:PSS shows similar features to that of a semi-metal. On the other hand, the extraordinary dielectric function does not exhibit any variation with photon energy. Thus it does not contain TL or Drude terms, but just a high-frequency dielectric constant of 1.47 eV. This shows that PEDOT:PSS behaves as a bulk dielectric in the extraordinary direction. The degree of anisotropy ( $\frac{\epsilon_{1,o}}{\epsilon_{1,e}}$ ) ranges from 0.5-1.2 from low to high frequency, according to which PEDOT:PSS is significantly anisotropic in its dry state. The DC conductivity of 258.56 Scm<sup>-1</sup> is calculated from Drude parameters of the ordinary dielectric fit using eq. 3.6. The value is in good agreement with the conductivity measured from the Van der Pauw method (cf. sec. 3.3.1) that ranges from 260-

290 S/cm for films on varied substrates. The above results are in good agreement with the available literature[42].

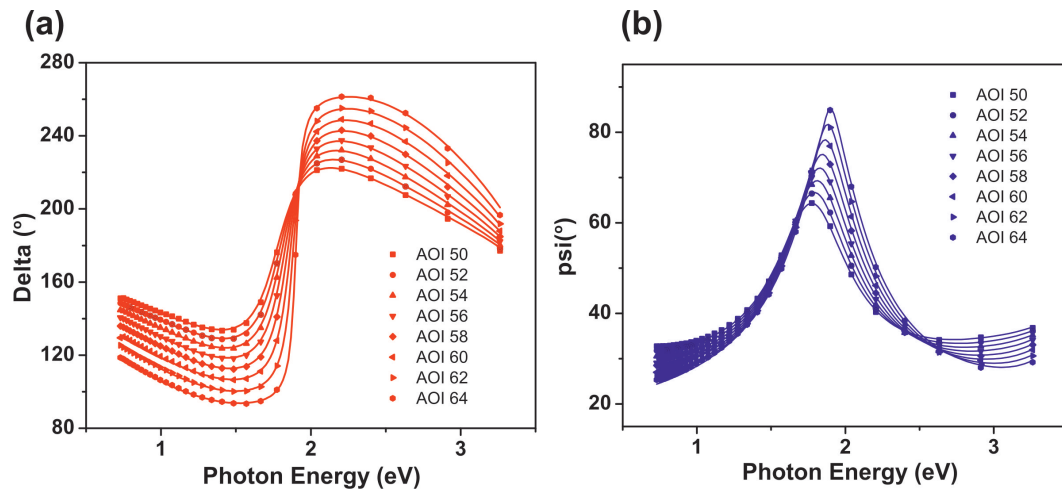


FIGURE 3.9: VASE spectra of the PEDOT:PSS sample spin coated on Si/SiO<sub>2</sub> substrate at room temperature in air ambient. The scatter points represent the measured data at varied angle of incidence (AOI50 to AOI64) and the solid lines represent the best fit of the TLD model. (a) Ellipsometric angle  $\Delta$ , (b) Ellipsometric angle  $\Psi$ .

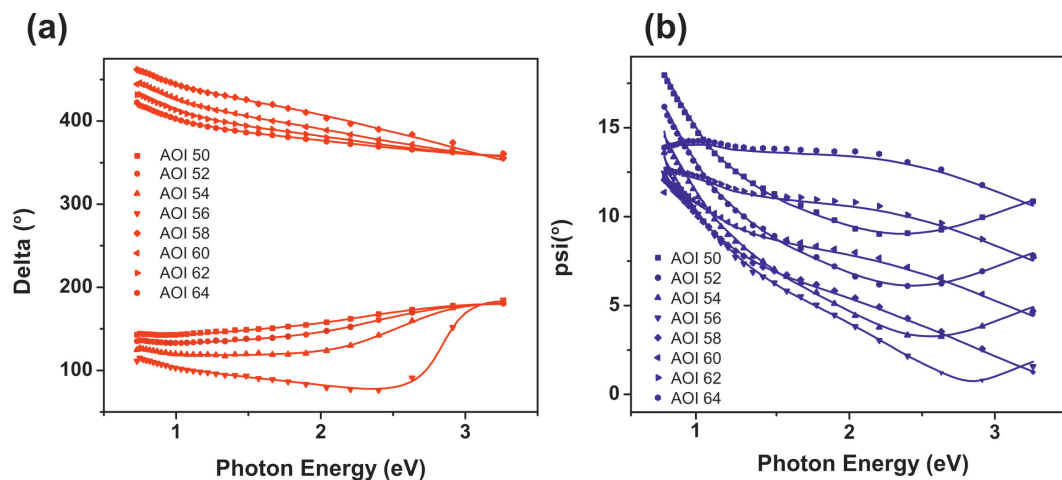


FIGURE 3.10: VASE spectra of the PEDOT:PSS sample spin coated on quartz substrate at room temperature in air ambient. The scatter points represent the measured data at varied angle of incidence (AOI50 to AOI64) and the solid lines represent the best fit of the TLD model. (a) Ellipsometric angle  $\Delta$ , (b) Ellipsometric angle  $\Psi$ .

Fig. 3.12 represents the anisotropic TLD model fitted to the measured ellipsometric angles  $\Psi$  and  $\Delta$ , measured for the film in contact with the electrolyte (0.1 M KCL(aq)). Here, the stratified layers in the Fresnel's optical model are changed according to fig. 3.5. The ambient layer used is quartz due to the quartz prism

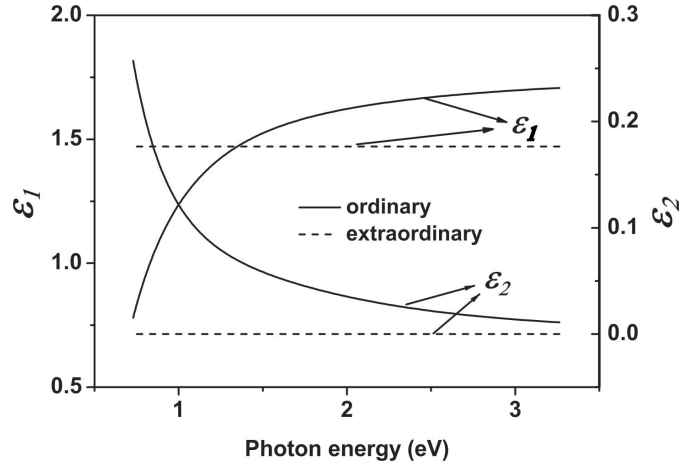


FIGURE 3.11: Complex ordinary and extraordinary dielectric dispersion derived from the uniaxially anisotropic TLD model simultaneously fitted to the ellipsometric data presented in fig 3.9 and 3.10

TABLE 3.2: The best fit parameters of the ordinary TLD of the uniaxially anisotropic dielectric function (cf. eqs.3.3-3.5); DC conductivity ( $\sigma_{DC}$ ) calculated from the Drude term (cf. eq.3.6) ; film thickness ( $d$ ) obtained from the fit and measured from AFM . All fit parameters are obtained by fitting the VASE spectra ( $\Psi, \Delta$  vs  $E$ ) in air.

Fit Parameters	Value
$\epsilon_{\infty}$	1.76 ( $\pm 0.01$ )
$A_D$ (eV <sup>2</sup> )	0.51 ( $\pm 0.02$ )
$\Gamma_D$ (eV)	0.16 ( $\pm 0.01$ )
$E_{OTL}$ (eV)	1.77 ( $\pm 0.07$ )
$A_{TL}$ (eV <sup>2</sup> )	0.07 ( $\pm 0.16$ )
$\Gamma_{TL}$ (eV)	2.59 ( $\pm 0.11$ )
$E_g$ (eV)	0.00 ( $\pm 0.06$ )
$\sigma_{DC}$ (S $\text{cm}^{-1}$ )	258.56 ( $\pm 0.70$ )
Film thickness on Si/SiO <sub>2</sub>	
$d_{Fit}$ (nm)	62.2 ( $\pm 0.6$ )
$d_{AFM}$ (nm)	66.7 ( $\pm 1.4$ )
Film thickness on Quartz	
$d_{Fit}$ (nm)	57.6 ( $\pm 0.4$ )
$d_{AFM}$ (nm)	54.5 ( $\pm 1.2$ )
RMSE	0.784



and quartz substrate at the top, while the substrate layer is water. The best fitted TLD model for the film is presented in the fig. 3.13. Due to the presence of highly hygroscopic PSS in the PEDOT:PSS film, it tends to swell when in contact with electrolytes[20]. Such behavior was observed as an increase in the fitted thickness compared to the dry film. The use of an effective medium model, where water can be explicitly included in the film dielectric function was avoided in order to keep the fit parameters minimal. A 20% increase in thickness was observed due to the swelling, which can be considered as a minor change. All the fitted parameters are tabulated in table 3.3.

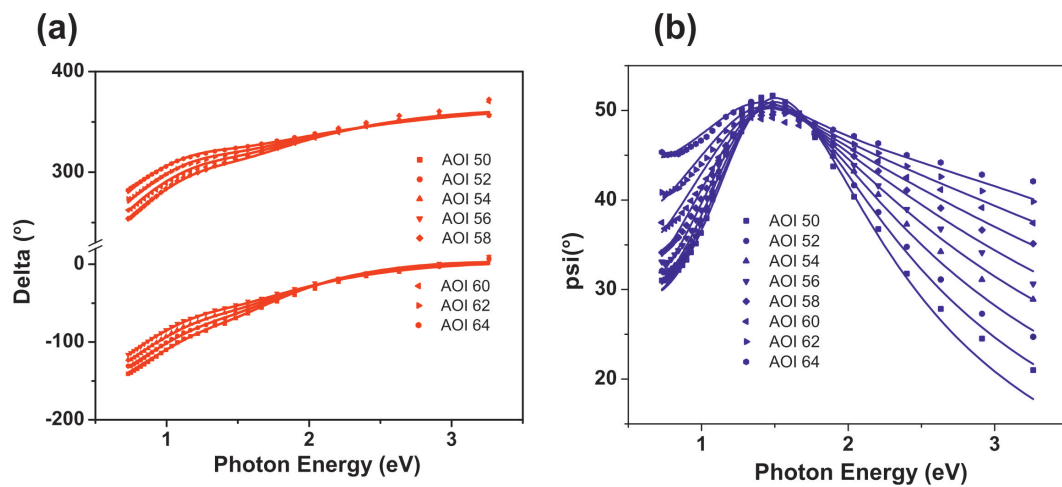


FIGURE 3.12: VASE spectra of the PEDOT:PSS sample spin coated on quartz substrate at room temperature in 0.1 M KCl aqueous solution. The scatter points represent the measured data at varied angle of incidence (AOI, from 50 to 64 degrees) and the solid lines represent the best fit of the TLD model. (a) Ellipsometric angle  $\Delta$ , (b) Ellipsometric angle  $\psi$ .

Fig. 3.13 b shows the comparison between the fitted ordinary and extraordinary complex dielectric functions when in contact with air and with the electrolyte. A parallel shift in the  $\epsilon_{1,o}$  and  $\epsilon_{1,e}$  can be observed, which can be noted in table 3.2 and 3.3, as an increase in  $\epsilon_{\infty}$  in both ordinary and extraordinary directions. This shift can be attributed to the uptake of water by the PEDOT:PSS film. Another clear observation from the comparison is the evolution of an absorption peak at 1.24 eV upon the exposure of the film to the electrolyte. This indicates the emergence of new electronic transitions at lower energies compared to the electronic transition in dry films. This can be explained by the spontaneous reduction of PEDOT:PSS film when it comes in contact with the electrolyte, such that the Fermi level is

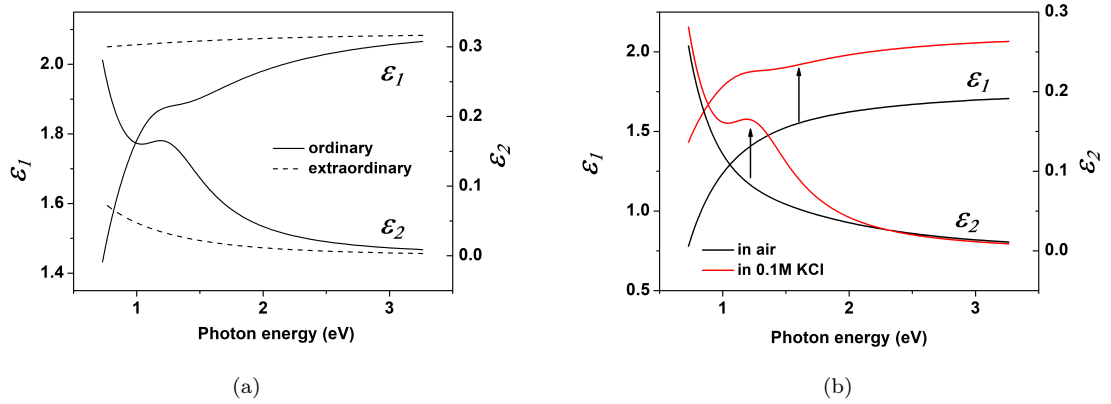


FIGURE 3.13: TLD dielectric model fitted to the ellipsometric angles  $\psi$  and  $\Delta$  measured for the PEDOT:PSS film exposed to 0.1 M KCl (aq) electrolyte. (a) The fitted ordinary and extraordinary dielectric function. (b) comparison of the ordinary dielectric function of the dry and electrolyte exposed PEDOT:PSS film. The arrows represent the parallel shift in the real part( $\epsilon_1$ ) of the dielectric function and the rise of the oscillator at 1.24 eV when exposed to the electrolyte

TABLE 3.3: The best fit parameters of the ordinary TLD and extraordinary Drude term parameters of the uniaxially anisotropic dielectric function (cf. eqs. 3.3-3.5); and DC conductivity ( $\sigma_{DC}$ ) calculated from the Drude term (cf. eq. 3.6) ; film thickness ( $d$ ) obtained from the fit. All fit parameters are obtained by fitting the measured VASE spectra ( $\Psi, \Delta$  vs E) when PEDOT:PSS film is in contact with the electrolyte (0.1 M KCl aqueous solution).

	Ordinary	Extraordinary	
Fit Parameters	Value(+/-)	Value(+/-)	Units
$\epsilon_\infty$	2.11(0.01)	2.09(0.02)	
$A_D$	0.45(0.01)	0.09(0.01)	eV <sup>2</sup>
$\Gamma_D$	0.26(0.07)	1.35(0.00)	eV
$E_{0TL}$	1.24(0.03)	—	eV
$A_{TL}$	0.25(0.01)	—	eV <sup>2</sup>
$\Gamma_{TL}$	0.68(0.12)	—	eV
$E_g$	0.58(0.04)	—	eV
$\sigma_{DC}$	107.53(5.21)	4.7(0.7)	Scm <sup>-1</sup>
	Value(+/-)		Units
$d_{Fit}$	85.4(2.1)		nm
RMSE	1.35		

pushed up towards the conduction band due to the filling of the valence band. Upon doping, the formation of polarons/bipolaron states has been reported in thiophene-based conducting polymers[35]. These energy states are formed just above and below the valence and conduction bands respectively (fig. 3.14). When PEDOT is reduced these states get filled with electrons, thereby decreasing the hole concentration and the energy difference between the valence and conduction band. This is evident from the values of decreased conductivity and the decreased transition energy value of the swollen PEDOT:PSS film as compared to the dry films as listed in table 3.2 and 3.3.

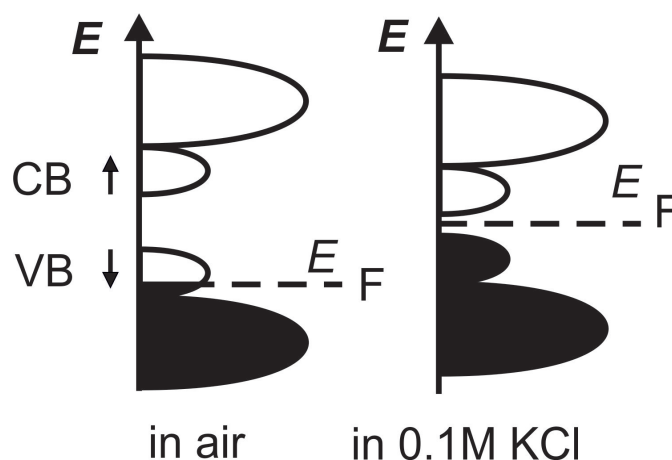


FIGURE 3.14: Scheme depicting the change in position of Fermi level in the band structure of PEDOT, when brought in contact with the electrolyte.

### 3.3.4 Electrochemical variable angle spectroscopic ellipsometry

In the previous section, it was established that the electronic structure of PEDOT:PSS films evolve upon exposure to an electrolyte. In this section, the study is focused on the evolution of this electronic structure by applying an electrochemical bias between PEDOT:PSS (W.E) and Pt (C.E) electrode with respect to the Ag/AgCl, 0.1 M KCl reference. At electrochemical equilibrium (zero W.E-C.E current), the PEDOT:PSS electrode has a potential drop with respect to Ag/AgCl electrode, this potential is termed as open circuit potential (OCP) in electrochemistry, which in our case is found to be 0.1V. The OCP is proportional to the

position of the Fermi level in the band structure of PEDOT[107, 108]. Thus, by applying an external potential at Au/PEDOT:PSS with respect to Ag/AgCl R.E the Fermi level of PEDOT can be tuned[24, 109]. The same is done by performing cyclic voltammetry in the 3-electrode electrochemical cell. In the CV as shown in fig. 3.15 three different regions can be observed. Between -0.2 to + 0.2 V, a capacitive behavior (charge separation region) was observed, where almost no faradic current was generated. In the forward cycle, the anodic current begins to rise after +0.2 V with a small peak at 0.25 V and a broader peak centered at 0.5 V, and the faradic current increased further till 0.8 V. In the reverse sweep, no significant reversible cathodic current is observed at positive potentials. However, a cathodic current increases below -0.25 V with decreasing potential and similarly no reversible anodic current is observed when the scan is reversed. The voltammogram exhibits the characteristics similar to that of a semiconductor electrode, where the reduction and oxidation of valance and conduction bands, respectively, are irreversible due to their opposite charge carrier concentrations[107].

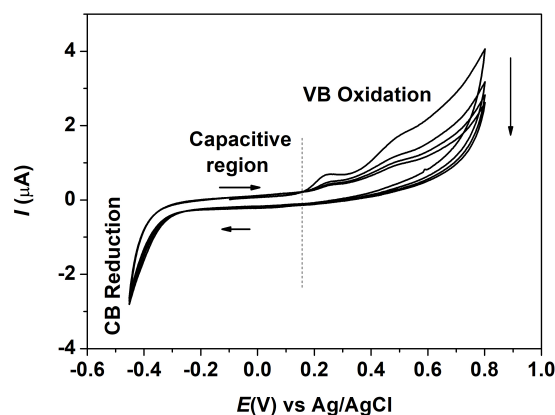


FIGURE 3.15: Cyclic voltammogram measured for the PEDOT:PSS WE vs. Ag/AgCl in 0.1 M KCl, in the three-electrode cell (cf. fig. 3.6), at scan rate  $0.01 \text{ Vs}^{-1}$ . The horizontal arrows denotes the direction of potential sweep, the vertical arrow denotes the temporal evolution of cycles.

In the forward cycle, when the Fermi level sweeps the valence band, there is a high concentration of electrons that can be extracted during the oxidation of PEDOT. However, when the potential scan is reversed, the number of holes in the valence band (VB) is too low to cause any significant current, *i.e.*, when the Fermi level moves towards the conduction band (CB). The opposite is true for

the reduction of CB. In the backward scan, when the Fermi level sweeps the CB, there is a high concentration of empty states to reduce PEDOT. However, when the scan is reversed the number of electrons is low to cause any significant anodic current. The three regions in the CV show three processes which can be used to modulate the conductivity of PEDOT:PSS films upon the application of the electrochemical potential. In the charge separation region, at the application of electrochemical bias, the ions penetrate inside the PEDOT:PSS matrix and disrupt the flow of charge carrier in the PEDOT:PSS film. This process is frequently utilized in the electrolyte gated thin film transistors[86, 90]. Here, no change in the carrier concentration of the film takes place, but the change in mobility of the carriers affects the conductivity. However, in the anodic and cathodic regions, due to the oxidation and reduction of the polymer film the carrier concentration of the semiconductor changes, causing the conductivity to vary. In order to study all the three regions, the EVASE measurements were conducted by placing the electrochemical potential of W.E to a constant value in these regions (until the W.E to C.E current becomes  $\approx$  zero), such that no redox takes place, and the system is in equilibrium under the applied load during the EVASE measurement.

The fitted dielectric function for the EVASE measurements in the potential range of +0.6 V to -0.2 V (-0.1 V step) are presented in fig. 3.16 (corresponding  $\Psi$  and  $\Delta$  fits are presented in appendix B ). The corresponding parameters are tabulated in table 3.4. Similar to the measurements in the absence of any electrochemical bias, the significant magnitude of the Tauc-Lorentz oscillator (inter-band transition) and the Drude charge carriers (inter- band transitions) are observed only in the ordinary direction of the dielectric function. Whereas, the extraordinary dielectric function shows the behavior of an insulator with a relatively constant dielectric function. The low conductivity of PEDOT:PSS in extraordinary direction is reported to be caused by nearest neighbor hopping mechanism[44, 110]. In the extraordinary direction, the PEDOT rich sites in the polymer matrix are separated by thick PSS lamellae, causing a barrier to the charge carriers. which limits the hopping to only nearest neighbor sites [56]. However, in the lateral (ordinary) direction the PEDOT rich sites are likely to have very thin or no barrier

at all, thereby allowing a non-near neighbor hopping (3D-VRH) conduction and therefore a higher conductivity. Fig. 3.17 a represents the trends in the ordinary DC conductivity (calculated from eq. 3.6) and the ordinary inter-band transition energy ( $E_{TL}$ ) with respect to the applied potential.

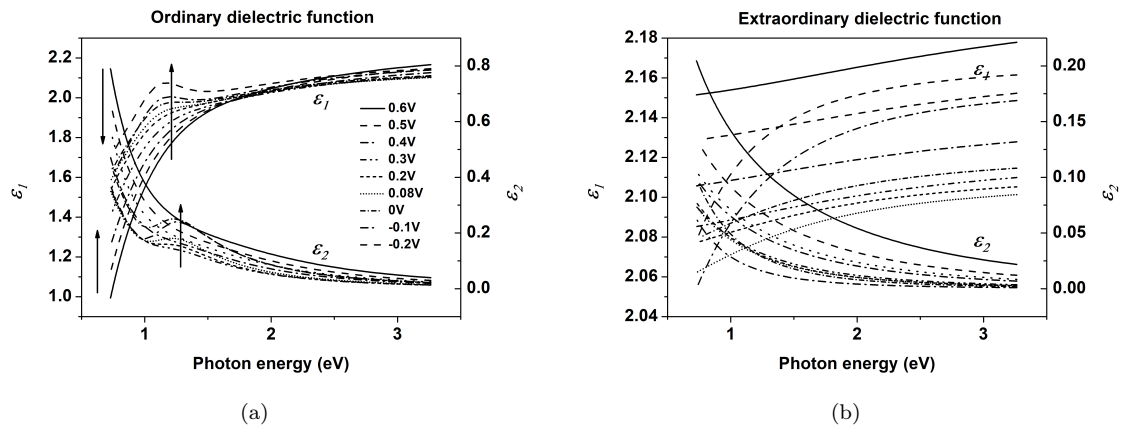


FIGURE 3.16: Uniaxially anisotropic complex TLD dielectric function model fitted to the ellipsometric angles  $\psi$  and  $\Delta$  measured for the PEDOT:PSS film exposed to 0.1 M KCl (aq) electrolyte at varied electrochemical bias. (a) The fitted complex ordinary dielectric function. The arrows represent the rising TL oscillator and decreasing Drude tail with decreasing electrochemical bias (b) The fitted complex extraordinary dielectric function.

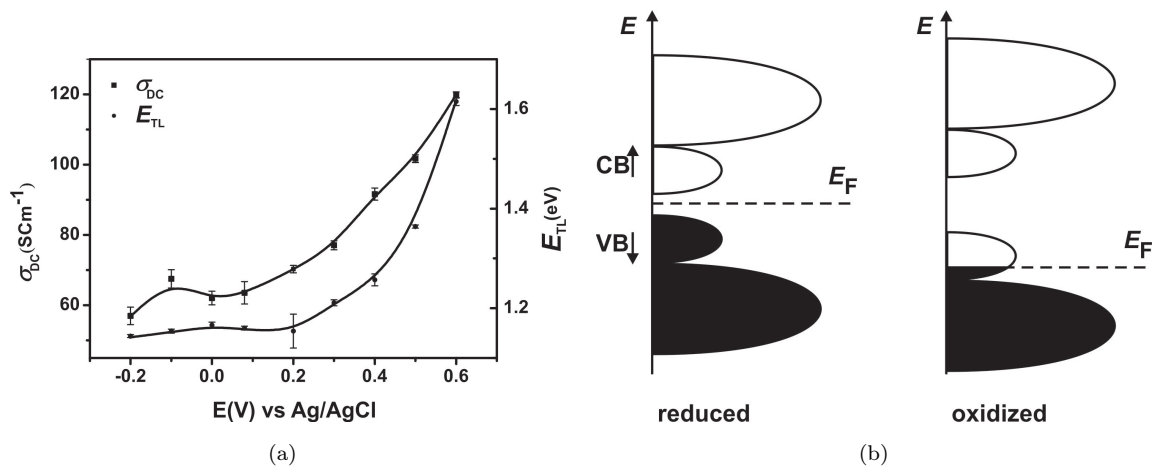


FIGURE 3.17: . (a) The DC conductivity calculated from the Drude parameters (left axis) fitted from the EVASE data under varied equilibrium electric potentials at the PEDOT:PSS electrode, in the range +0.6 to -0.2 V vs Ag/AgCl in 0.1 M KCl (pH $\approx$ 7), and the corresponding Tauc-Lorentz resonance energy (right axis). The error bars represent the confidence of the fitted parameters, lines serve to guide the eye. (b) The scheme representing the evolution of the electronic structure of PEDOT:PSS upon increase of the positive electric bias (redox doping).

TABLE 3.4: The best fit parameters of the ordinary TLD and extraordinary Drude term parameters of the uniaxially anisotropic dielectric function (cf. eqs.3.3-3.5); and DC conductivity ( $\sigma_{DC}$ ) calculated from the Drude term (cf. eq.3.6) ; film thickness (d) obtained from the fit . All fit parameters are obtained by fitting the EVASE spectra ( $\psi, \Delta$  vs Photon energy) , under varied equilibrium electric potentials (EMF) at the PEDOT:PSS electrode, in the range +0.6 to -0.2 V vs Ag/AgCl in 0.1 M KCl (pH  $\approx$  7).

EMF vs Ag/AgCl (V)	Ordinary										Extraordinary				
	$\epsilon_\infty$	$E_{0TL}$ (eV)	$A_{TL}$ (eV) <sup>2</sup>	$\Gamma_{TL}$ (eV)	$E_g$ (eV)	$A_D$ (eV) <sup>2</sup>	$\Gamma_D$ (eV)	$\sigma_{DC}$ (SCm <sup>-1</sup> )	$\epsilon_\infty$	$A_D$ (eV) <sup>2</sup>	$\Gamma_D$ (eV)	$\sigma_{DC}$ (SCm <sup>-1</sup> )	d (nm)	RMSE	
0.6	2.23	1.61	0.34	1.98	0.55	0.84	0.42	119.8	2.16	0.39	2.73	8.8	53.3	0.851	
0.5	2.19	1.36	0.42	1.44	0.80	0.70	0.42	101.7	2.13	0.20	2.25	5.3	61.9	0.788	
0.4	2.17	1.25	0.46	1.20	0.85	0.62	0.42	91.6	2.12	0.14	2.04	4.3	68.1	0.651	
0.3	2.15	1.21	0.46	0.99	0.85	0.52	0.42	77.0	2.10	0.13	1.92	4.5	77.7	1.211	
0.2	2.16	1.15	0.52	0.74	0.87	0.46	0.41	70.3	2.11	0.12	1.53	4.4	83.3	0.770	
0.08	2.15	1.16	0.59	0.63	0.88	0.44	0.43	63.5	2.11	0.10	1.38	4.6	85.4	0.589	
0.0	2.16	1.16	0.70	0.60	0.87	0.43	0.43	62.1	2.12	0.10	1.30	4.1	82.1	1.122	
-0.1	2.20	1.15	1.16	0.55	0.90	0.52	0.47	67.5	2.15	0.10	0.60	10.7	67.7	0.564	
-0.2	2.20	1.14	1.37	0.55	0.92	0.40	0.43	57.0	2.15	0.05	0.40	7.7	75.0	0.880	

These trends can be seen in light of the schematic of PEDOT band structure shown in fig. 3.17 b, where the Fermi level is tuned by the application of external potential. The  $E_{\text{TL}}$  is found to be fairly constant at 1.15 eV in the charge separation regime of the applied voltage (-0.2 V to +0.2 V). Whereas, a steep increase at the onset of +0.2 V is observed in  $E_{\text{TL}}$ .

Since only one Tauc oscillator is used in the model, it can be assumed that  $E_{\text{TL}}$  is the most abundant inter-band transition in the measured energy range. Hence, the constant transition energy in the charge separation regime suggests that the Fermi level in this potential range is found roughly in the band gap region, while the observed transition in this range can be either of the allowed bipolaron transitions of the mid-gap states ( $\pi \rightarrow \text{bipolaron}$ , or  $\pi \rightarrow \text{bipolaron}^*$ ) (c.f. sec. 2.2), as observed in other literature[33, 35]. After the threshold of +0.2 V however, the Fermi level starts to sink below the valence band, causing the transition energy to increase. This is because the energy difference between the conduction band and the HOMO has increased. Also, when the Fermi level sinks inside the VB (oxidation of PEDOT), there are free states available inside the VB for the charge carriers, *i.e.*, the number of holes has increased. This can be observed as a sharp increase in the DC conductivity of the film (fig. 3.17 a) above +0.2 V. A slight increase in conductivity is also observed in the charge separation region, which can be attributed the change in mobility caused by the field effect of ions penetrating the polymer upon the application of EMF in that voltage range. The strength of inter-band absorption( $A_{\text{TL}}$ ) in the ordinary dielectric function is inversely proportional to the applied potential, with the decreasing applied potential (0.6 V to -0.2 V) the strength of the  $E_{\text{TL}}$  increases (shown by the up arrow in fig. 3.16(a) with the strongest and sharpest transition at the lowest investigated potential (-0.2 V) with  $A_{\text{TL}} = 1.14$  eV. Another noteworthy observation from the table 3.4 is that at the potential of 0.08V (OCP) the  $E_{\text{TL}}$  value of 1.16 eV is close to the one obtained by fitting the in-situ measurement without any applied potential (1.24 eV). Also, upon application of 0.6 V, the intraband transition is fitted to be 1.61 eV, which is close to the value fitted for the dry sample (1.77 eV). These observations indicate that, while by the application of an external voltage or by mere bringing the CP



in contact with the electrolyte the doping level is varied, it can be recovered to its pristine state by tuning the Fermi level with applied electrochemical potential. The Tauc gap in the whole potential range is more or less constant, except for 0.6 V, where it abruptly drops to 0.55 eV from 0.8 eV. Since at this potential the Fermi level resides below the exciton level, the gap energy can be attributed to the energy difference between the HOMO and the exciton energy level.

The potential range in the aqueous electrolyte is limited to lower values due to some parasite reactions like the oxidation of water at higher potentials. Therefore, a control experiment is repeated in an inert electrolyte solution of 0.1 M LiClO<sub>4</sub> in acetonitrile, and fig. 3.18 represents the CV of PEDOT:PSS in the voltage range of -0.8 V - +0.8 V. The three distinct regions showing capacitive, oxidation and reduction behavior as in the above case are observed in this experiment as well. This result confirms the attribution of the current peaks in the CV to the oxidation and reduction of the PEDOT W.E and not any dissolved species in the electrolyte. The slight differences in the potentials at which those peaks occur should not be related to the PEDOT band structure, but to the fact that both the working and the reference electrodes, behave differently in those two media in terms of the ion exchange equilibria and electrostatic conditions at electrode surfaces. In acetonitrile, it can be observed that the absolute current is by order of magnitude larger than in aqueous medium. However, this is due to a higher conductivity of the electrolyte solution and is not related to the film conductivity.

The CV presented in fig. 3.18 shows the characteristics of a conventional semiconductor [24, 111, 112]. The cathodic current peak represents the reduction of the conduction band (CB), and the anodic peak is the oxidation of the valence band. One can observe that the cathodic current peak is somewhat smaller compared to the anodic one. Thus, compared with the VB oxidation, the rate constant for the CB reduction is less.

EVASE experiments were conducted in LiClO<sub>4</sub> electrolyte in the EMF range from 0.0V to +1V. The fitted dielectric models for different EC potentials are presented in fig. 3.19. The fitted parameter is tabulated in table 3.5. For the EVASE

TABLE 3.5: The best fit parameters of the ordinary TLD and extraordinary Drude term parameters of the uniaxially anisotropic dielectric function (cf. eqs.3.3-3.5); and DC conductivity ( $\sigma_{DC}$ ) calculated from the Drude term (cf. eq.3.6) ; film thickness ( $d$ ) obtained from the fit . All fit parameters are obtained by fitting the EVASE spectra ( $\psi, \Delta$  vs Photon energy), under varied electromotive force (EMF) at the PEDOT:PSS electrode, in the range +0.0 V to 1.0 V vs Ag/AgCl in 0.1 M LiClO<sub>4</sub>.

EMF vs Ag/AgCl (V)	Ordinary							Extraordinary						
	$\epsilon_\infty$	$E_{0TL}$ (eV)	$A_{TL}$ (eV) <sup>2</sup>	$\Gamma_{TL}$ (eV)	$E_g$ (eV)	$A_D$ (eV) <sup>2</sup>	$I_D$ (eV)	$\sigma_{DC}$ (SCm <sup>-1</sup> )	$\epsilon_\infty$	$A_D$ (eV) <sup>2</sup>	$I_D$ (eV)	$\sigma_{DC}$ (SCm <sup>-1</sup> )	$d$ (nm)	RMSE
0.0	2.21	1.16	0.99	0.53	0.85	0.52	0.32	99.5	2.17	0.05	0.36	8.5	91.3	1.100
0.15	2.169	1.17	0.61	0.65	0.81	0.51	0.32	99.7	2.12	0.11	2.10	3.3	102.0	1.324
0.3	2.2	1.21	0.60	0.83	0.80	0.69	0.38	111.6	2.14	0.15	1.72	5.3	83.9	0.773
0.4	2.38	1.19	1.04	0.91	0.87	1.32	0.27	277.8	2.30	0.13	2.90	2.6	43.2	0.629
0.5	2.20	1.36	0.32	1.077	0.81	0.80	0.30	159.6	2.15	0.15	1.43	6.5	74.3	0.539
0.7	2.14	1.52	0.20	1.354	0.80	0.67	0.32	130.1	2.10	0.15	2.02	4.8	85.3	1.021
0.8	2.14	1.57	0.15	1.28	0.82	0.66	0.34	121.4	2.08	0.13	1.60	5.3	86.6	0.760
0.9	2.14	1.56	0.17	1.355	0.85	0.67	0.34	122.4	2.09	0.15	2.05	4.7	84.7	0.895
1.0	2.14	1.6	0.13	1.29	0.82	0.69	0.40	110.1	2.07	0.14	1.40	6.4	84.2	0.342

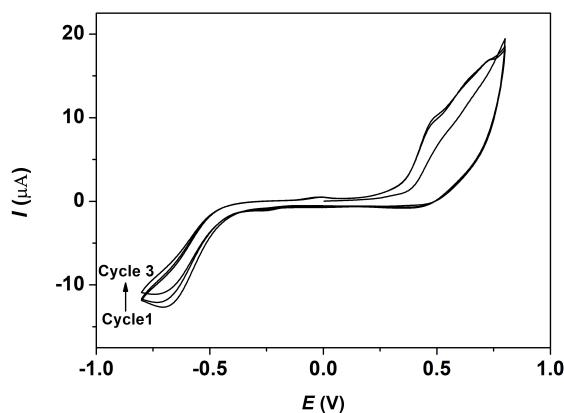


FIGURE 3.18: Cyclic voltammogram measured for the PEDOT:PSS WE vs. Ag/AgCl in 0.1 M LiClO<sub>4</sub>, in acetonitrile, at scan rate 0.01 Vs<sup>-1</sup>.

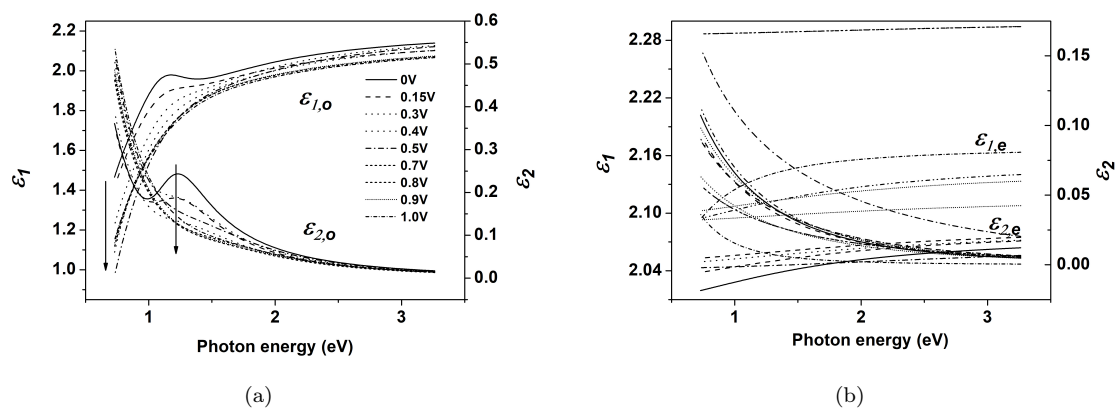


FIGURE 3.19: Uniaxially anisotropic complex TLD dielectric function model fitted to the ellipsometric angles  $\psi$  and  $\Delta$  measured for the PEDOT:PSS film exposed to 0.1 M LiClO<sub>4</sub> in acetonitrile electrolyte at varied electrochemical bias. (a) The fitted complex ordinary dielectric function. The arrows represent the lowering TL oscillator value and increasing Drude tail with increasing electrochemical bias (b) The fitted complex extraordinary dielectric function.

experiment in 0.1 M KCl (aq) electrolyte, the ellipsometry measurement was performed within the backward cycle of the potential scan (+0.6 V to -0.2 V). On the other hand, in the case of 0.1 M LiClO<sub>4</sub> in ACN electrolyte, the EVASE was performed in the forward direction of the potential scan (0 V to 1 V). It can be observed that in the forward direction the conductivity increases until 0.4 V vs. Ag/AgCl and then suddenly drops. This trend is also detectable in other parameters like  $E_{TL}$  and  $E_G$  and can be explained by the degradation PEDOT:PSS due to overoxidation[113]. When scanning the potential in the forward cycle, the

polymer is doped with holes, thereby increasing the hole conductivity. However, overoxidation causes the dissolution of PEDOT:PSS film and hence decreases the conductivity[114]. If the experiment is performed in the backward direction, the previously overoxidized PEDOT becomes reduced, and the conductivity of the already overoxidized PEDOT drops continuously.

### 3.4 Electrochemical impedance spectroscopy

Electrochemical impedance spectroscopy (EIS) measurements were conducted to gain understanding about the impedance behavior of PEDOT:PSS films in different electrochemical potential regions. The Nyquist and Bode plots are presented in fig. 3.20 a and b respectively. Here, the scatter points are the measured data, and the solid lines represent the fits from the equivalent circuit model. A minimalist approach was used to fit the measured impedance data, where a polynomial regression tool was used to fit the equivalent circuit (represented in fig. 3.21). The regression providing the smallest  $\chi^2$  value is automatically selected by the software. To achieve a good fit, first a small data window at higher frequency range is selected (where the sudden shift in the impedance values is observed in the Nyquist plot) and a Parallel RC circuit is fitted. Then the other half of the of the data is fitted with another parallel R,CPE circuit (since a RC circuit produced with a high  $\chi^2$  value). A circuit with a parallel Warburg element was also tried, but it did not provide a better fit compared to the parallel R,CPE model. After fitting this two data windows separately, the whole set of data was fitted with a equivalent circuit model that consisted three blocks; a resistor, parallel RC circuit, and a parallel R(CPE) circuit, where the three blocks are connected in series. The series resistor is usually considered as the solution resistance. The initial values of the elements in the whole data fit were taken from the previous partial data fits. The corresponding values of the circuit components are tabulated in table 3.6. The circuit consists of a series resistor  $R_s$  represents the resistance of the electrolyte(or solution resistance), The first RC circuit,  $R_1C$ , represents the electrical double layer at the PEDOT:PSS|electrolyte interface and the third  $R_2(CPE)$

circuit represents the bulk PEDOT:PSS film itself. It can be observed in the Fig. 3.20 that a good fit is achieved using this equivalent circuit.

The experiment was repeated for multiple potentials, and the measured data were fitted using the same circuit. It was observed from fig. 3.20 that the Nyquist plot for voltages between -0.1 V to +0.2 V almost coincide with each other and show a highly capacitive behavior. On the other hand, at the potentials above +0.2 V and below -0.1 V, the imaginary part of the impedance decreases and the real part increases with decreasing frequencies. This is an indication of an increased rate of Faradic charge transfer at the PEDOT:PSS electrode. The same can be observed in the Bode plot, that while  $Z$  increases at the outer and inner potential window, the phase decreases at these potentials, indicating that the resistive behavior is predominant in this region compared to the capacitive behavior. These results are in line with the cyclic voltammograms (c.f. fig. 3.15).

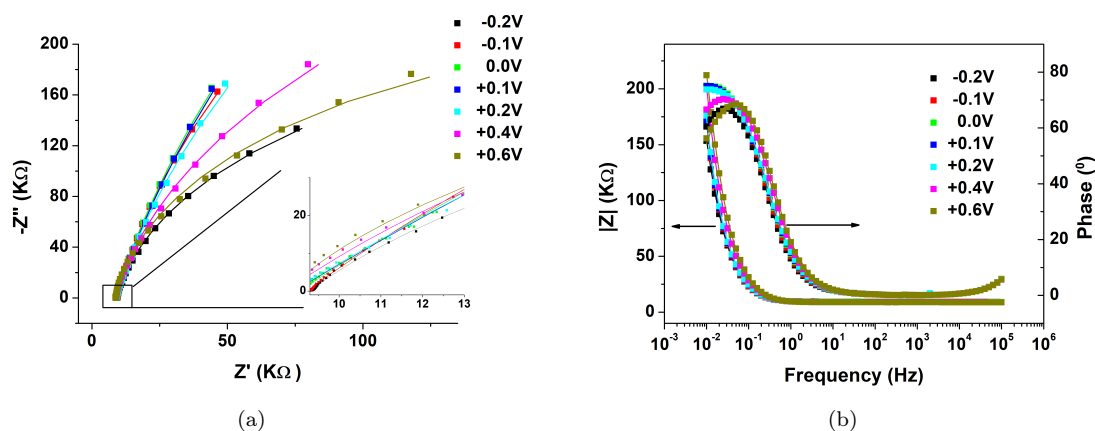


FIGURE 3.20: (a) Nyquist plots for the from the EIS measurements performed on PEDOT:PSS electrodes at varied electrochemical potentials, the solid lines are the equivalent circuit fitted to individual measurements (b) Bode and phase pots of the same as above.

The solution resistance  $R_s$  in the equivalent circuit fit is almost constant at all the applied potentials.  $R_s$  is mainly dependent on the ionic concentration of the electrolytes, the distance between W.E and C.E and the dimensions of the electrodes. Since the electrodes' dimension and distance are constant, it can be concluded that during the capacitive or redox process no significant change in the ionic concentration was observed. The other two series components of the

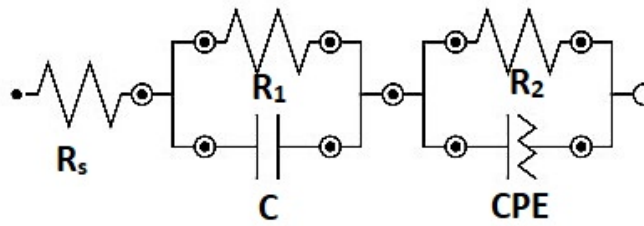


FIGURE 3.21: Equivalent circuit fitted to the Nyquist , Bode and phase plots. The corresponding values of the parameters are presented in Table 3.5

TABLE 3.6: Fit parameters of the equivalent circuit fitted to the EIS measurements at varied applied potential

Voltage (V)	$R_s$ (k $\Omega$ )	$R_1$ ( $\Omega$ )	$C$ (fF)	$R_2$ (k $\Omega$ )	CPE		$\chi^2$	$C_{CPE}$ (Fcm $^{-3}$ )
					$Y_0$ ( $\mu$ Ss $^N$ )	$N$		
-0.2	8.98	314	900	428	77.6	0.926	0.002	11.2
-0.1	8.94	290	900	1590	75.2	0.922	0.001	10.8
0.0	8.85	202	900	2230	72.5	0.913	0.002	10.3
0.1	8.80	143	900	2410	71.8	0.906	0.002	10.2
0.2	8.78	123	900	1730	70.5	0.908	0.002	9.9
0.3	8.73	78.0	900	1120	64.5	0.914	0.003	9.1
0.4	8.70	45.3	900	763	59.9	0.920	0.006	8.4
0.5	8.68	25.4	900	591	56.9	0.925	0.010	7.9
0.6	8.70	40.3	900	436	54.4	0.943	0.007	7.7

equivalent circuits are a parallel  $R_1 - C$  circuit and another parallel  $R_2 - CPE$  circuit. In the  $R_1 - C$  circuit, a very small value of capacitance independent of the applied voltage is observed. This can be seen as a electric double layer (EDL) capacitance between the electrolyte and the PEDOT:PSS film [29]. The thickness of the EDL and hence its capacitance is mainly dependent on the concentration of ions in the electrolyte [107], and since we established that there is no significant change in the concentration of ions, the EDL capacitance remains constant throughout the measured voltage range.  $R_1$  however, decreases continuously with increasing potential, with the exception of 0.6 V. In a parallel RC circuit, the resistor R dictates the time required for the capacitor to get fully charged. Since  $R_1$  decreases with increasing applied voltage, it means that with increasing voltage the EDL charges faster. This can be due to the porous nature of the PEDOT:PSS electrode. Unlike in the metal(solid state) /electrolyte interface, the ions do not stay at the

top surface on PEDOT:PSS electrode but infuse inside the porous structure of the polymer matrix. Since infusion and diffusion of ions is reported to be a slow process[115], it might be possible that the EDL does not discharge completely when the experiment at the particular potential is stopped. Therefore, when the experiment at a different potential is started, the EDL might already be charged to a certain value, making the double layer capacitor to charge faster. A slight increase of  $R_1$  at 0.6 V can be attributed to dissolution of PEDOT:PSS due to overoxidation.

The  $R_2||CPE$  circuit represents the Au|PEDOT:PSS interface. Here the resistor  $R_2$  can be attributed to the charge transfer from PEDOT:PSS to Au and the CPE to the capacitance of PEDOT:PSS (since the exponent  $N$  in CPE  $\approx 1$ ). The capacitance from the CPE parameters can be calculated using Eq. 3.10 and the equivalent volumetric capacitance is calculated by dividing the value by the film dimensions.

$$C_{CPE} = \left[ \frac{(Y_0 \cdot R_s \cdot R_2)}{R_s + R_2} \right]^{1/N} \cdot \left[ \frac{R_s + R_2}{R_s \cdot R_2} \right] \quad (3.9)$$

Where  $C_{CPE}$  is the capacitance of a parallel CPE and R circuit.

The volumetric capacitance values tabulated in table 3.6 show a supercapacitive behaviour. While there is not much variation in the capacitance of the film with the increasing potential. The value slightly decreases with the increasing potential. There is an increase in the value of  $R_2$  as the potential is scanned from -0.2V to +0.1V. Above +0.1 V  $R_2$  begins to decrease again. Comparing this behaviour with the CV measurements, one can draw a parallel in this behaviour, where in the oxidation and reduction regimes of the CV, PEDOT:PSS becomes more conductive and in the capacitive range the conduction drops.

### 3.5 Summary and conclusion

The variable angle spectroscopic ellipsometry technique was used to characterize the dielectric properties of dry PEDOT:PSS films spin-coated from an aqueous solution containing DMSO as co-solvent and (3-glycidoxypropyl)trimethoxysilane (GOPS) as cross-linker. An anisotropic model was used to fit the measured ellipsometric data. The Tauc-Lorentz-Drude model was shown as optimal for fitting the ordinary dielectric function, while the extraordinary function exhibited only a weak dispersion. The measurements were extended to electrochemical variable angle spectroscopic ellipsometry (EVASE) technique for *in-situ* measurements. Upon exposure to the aqueous electrolyte, the film undergoes a ca 20 % thickness increase caused by swelling. The latter is accompanied by a change in the oxidation state and consequently change in the dielectric function is observed in both the ordinary and extraordinary dielectric functions. The semiconducting behavior of the PEDOT:PSS film is observed in the cyclic voltammograms, where the applied potential is cycled between the valence band and the conduction band. The oxidation (above +0.2 V Vs Ag/AgCl), reduction (below -0.2 V vs Ag/AgCl) and the charge separation (between -0.2 V and +0.2 V) regimes can be distinguished in the CV. EVASE measurements were conducted and all three regimes. The electron transition energy of the ordinary dielectric function in the charge separation regime of the CV is almost constant, indicating that the Fermi level resides in the band gap region of the PEDOT:PSS semiconductor. Therefore, it can be said that the change in conductivity in this voltage range is purely due to the capacitive/electrostatic effects caused by the infusion of ions into the polymer matrix and no redox doping takes place. On the other hand, in the oxidation regime of the CV a blue shift in the transition energy is observed, and consequently, the calculated DC conductivity from the Drude parameters show a steep increase in conductivity. This is an indication of oxidative doping of the PEDOT, *i.e.*; the Fermi level sinks into the valence band causing p-type doping in PEDOT.

The electrochemical nature of PEDOT:PSS electrodes were studied with electrochemical impedance spectroscopy at varied applied potential. The measured data



was fitted with two Randles circuit, where one circuit ( $R_1||C$ ) indicated the formation of a double layer with a minimal capacitance value. However, the second Randles circuit ( $R_2||CPE$ ) indicates a supercapacitive behavior, similar to the behavior observed in CVs. This behavior of PEDOT:PSS films was found to be almost the same in the whole investigated potential range. The charge transfer behavior, however, followed the trend of EVASE and CV measurements, where the conductivity is found to be higher in oxidation and reduction regime compared to the charge separation regimes.

From the above measurements, it can be established that PEDOT:PSS based electrodes operate in two different regimes. In the charge separation regime, the conductivity is almost constant, while electric field generated in the film is accompanied by the infusion of ions into the polymer matrix. In the redox regime the polymer can be doped/dedoped to change the carrier concentration and hence its conductivity.

## Chapter 4

# Understanding the transport mechanism in poly(3,4-ethylenedioxythiophene): poly(styrene- sulfonate) based organic electrochemical transistors

In the past three decades, the research in organic electronics has significantly grown due to the numerous desirable properties that organic semiconductors provide [74, 116, 117]. These properties include low cost, tenability through synthetic chemistry, ease of processing and mechanically flexible electronics [118]. These semiconductors possess the ability to conduct ionic as well as electronic carriers, and this property can be utilized to prepare various organic electronic devices such as solar cells, light-emitting diodes (LEDs) or transistors, etc. [119, 120]. The organic electrochemical transistors (OECTs) are of particular importance due to its possible applications in various chemical and biological sensor devices. These can operate under aqueous environments and have the potential to be integrated with the microfluidic-based technology to prepare lab-on-chip devices [121] or for detection of various biological and chemical analytes [122]. Also, OECTs are simple

and easy to fabricate and have low operational voltage. Therefore, these devices are excellent candidates for various sensing applications and will play an essential role in the bioelectronic devices based on organic materials [123]. In the mid-1980s, OECT was first reported by Wrighton and colleagues [85]. As explained in section 2.4 an OECT is composed of a semiconductor thin film in contact with an electrolyte in which the gate electrode is immersed, where the drain current is controlled by the doping state of the channel material, which in turn is controlled by the gate. The OECTs exploit the principle of electrochemical gating which prevents the necessity of placing the gate electrode at a small distance from the channel material (separated by a dielectric). This enables fabrication of planar devices whose architecture and component positioning can be varied independently [119]. The channel material of OECT is generally made up of highly doped semiconducting polymers (a.k.a conducting polymers), such as polypyrrole or PEDOT which are doped by polyanions that are p-type dopants [124, 125]. The channel material is prepared through vapor phase deposition, solution-based coating or electrochemical polymerization methods [17, 115, 126]. Due to the commercial availability in the form of aqueous dispersions, biocompatibility and stability in a variety of conditions, poly(3,4-ethylenedioxythiophene) doped with poly(styrene sulfonate) (PEDOT:PSS) have been used in the present study. Moreover, this conducting polymer has been considered as the standard material for fabricating OECT biosensors [127, 128]. The PEDOT:PSS dispersions are prepared by polymerizing PEDOT in the presence of PSS, making PEDOT:PSS is a p-type doped semiconductor with PSS as a dopant. Highly conducting films of PEDOT:PSS can be produced by the addition of surfactants and co-solvents [129], which enhances the device performance.

PEDOT:PSS based OECTs usually work in depletion mode of operation, *i.e.*, When there is no gate voltage, the hole current flows in the semiconducting channel, and this is referred to ON state. Once a positive gate voltage is applied, the positive ions from the electrolyte get transferred into the semiconducting channel, and this leads to compensation or recombination with the anions [70, 75]. The ion compensation/recombination leads to the decrease in the number of holes in the

channel causing de-doping of the thin semiconducting film. This is because the holes that are removed at the drain are not recharged at the source, which eventually leads to a reduction in the drain current, and the device attains OFF state. However, in the case of accumulation mode, the OECTs are normally in OFF state as the number of charge carriers [130], *i.e.*, holes, is very low in the channel. When the negative bias is applied, it injects negative ions into the channel which leads to accumulation of the holes causing ON state of the transistor. The OECTs can, therefore, act as switches or amplifiers[131]. In the case of the switch, the gate voltage controls the drain current. However, when used as an amplifier, the power of the input(gate) signal is amplified at the output (source-drain).

The OECT relies on the electrochemical doping of the channel material, *i.e.*, on the application of an electrochemical bias, the electronic conductivity of the channel material changes. One can modulate the conductivity of a conducting polymer by applying a polarizing electric field produced by the ionic double layer formed on the polymer/electrolyte or polymer/bulk interface due to an applied electrochemical bias between the channel and a counter (working) electrode . Devices which utilize such properties are termed as electrochemically gated field effect transistors (EGOFET)[132]. On the other hand, the polymer film can also be oxidized or reduced by the application of an electrochemical bias. The oxidation or reduction causes the change in the charge carrier concentration in the polymer film , which in turn affects the conductivity of the channel material. While the device characteristic from a solid state physics point of view can be explained by both mechanisms, the mechanistic functionality of an electrochemical transistor is fundamentally different from that of a solid state device and is still unclear. Due to the presence of both electrochemical and solid state elements in this system, it becomes difficult to differentiate one from the other. In this chapter, our motivation is to differentiate the functioning of PEDOT:PSS based OECT while operating in the capacitive (or field effect) regime from the redox regime.

## 4.1 Experimental part

### 4.1.1 Sample preparation

For the preparation of the PEDOT:PSS film, 20 mL of an aqueous dispersion (Clevios PH- 1000 from Heraeus Holding GmbH, details at [www.clevios.com](http://www.clevios.com)) was prepared by mixing 5 mL of ethylene glycol, 1 drop of dodecyl benzene sulfonic acid (DBSA), and 1 wt% of (3-Glycidyloxypropyl) trimethoxysilane (GOPS). The resulting dispersion was later spin-coated onto quartz substrates during the device fabrication process. Ethylene glycol is added in order to enhance the conductivity of PEDOT:PSS, while DBSA is a surfactant which helps to adjust the surface tension between the PEDOT:PSS suspension and the glass substrate, which helps to avoid the agglomeration of the dispersion and thus improves the coating properties [133]. GOPS is commonly used to promote surface adhesion. It also acts as a polymer cross-linking agent and enhances the stability of PEDOT:PSS films in aqueous environments.

### 4.1.2 Device fabrication

The fabrication process includes the deposition and patterning of metal, parylene-C, and PEDOT:PSS. Quartz slides are cleaned by ultra-sonication in diluted industrial cleaner Micro-90 and subsequently in an acetone/isopropanol solution. Shipley 1813 photoresist is spin coated on the clean substrate (fig. 4.1a), the sample is then loaded in the mask aligner of the photolithography setup SUSS MBJ4. The mask is aligned on top of the sample such that, when exposed to UV light the parts where metal contacts shall be formed are exposed. The sample is exposed to UV light and then developed using MF-26 developer. The developed sample has empty grooves where metal electrodes shall be formed, and the other parts are covered with the photoresist (fig. 4.1b). This is followed by the deposition of a thin chromium seed layer and 100 nm of gold using a metal evaporator (fig. 4.1c). Lift-off is performed to remove the unwanted photoresist and metal deposited on

top of photoresist, this is done by immersion of the samples in acetone and cleaning with isopropanol (fig. 4.1d). The patterned metal electrodes are insulated by the deposition of 2  $\mu\text{m}$  parylene-C layer deposited using an SCS Labcoater 2. 3-(trimethoxysilyl)propyl methacrylate (A-174 Silane) is used as an adhesion promoter of the parylene-C coating on the metal- patterned substrate.

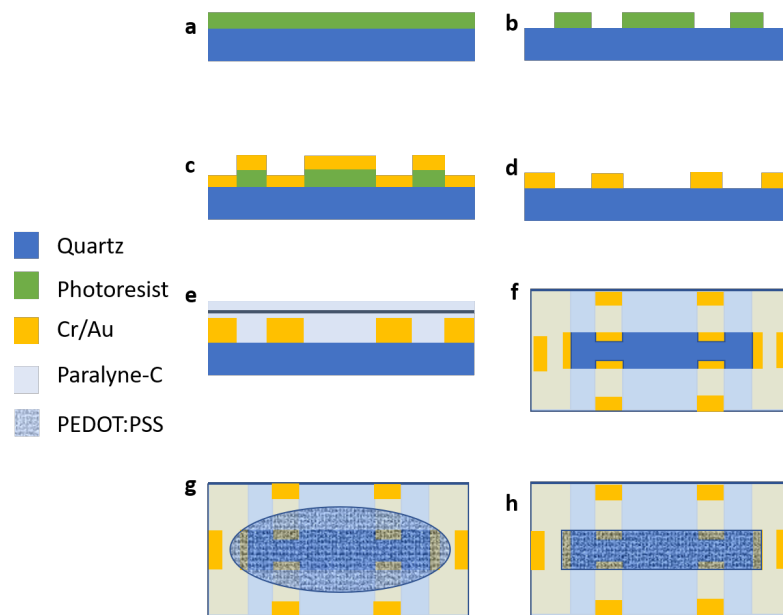


FIGURE 4.1: Scheme of the device fabrication steps with photolithography technique. (a) Photoresist layer is coated on the substrate with spin coating, (b) the photoresist is etched using photolithography (c) Cr/Au metal is deposited using a thermal evaporator (d) lift off is performed (e) Paralyne insulation and sacrificial layers are deposited (f) Channel is patterned by depositing another photoresist and performing another lithography step and reactive ion etching (g) PEDOT:PSS is spin coated (h) the sacrificial paralyne-C layer is removed

A dilute solution of industrial cleaner (Micro-90), which acts as an anti adhesive, in this case, is spin coated on top of the sample and another 2  $\mu\text{m}$  parylene-C is coated (fig. 4.1e), this parylene layer is called the sacrificial layer. The as-prepared sample is then subjected to another photolithography step, where the opening for the channel and contact pads is patterned by spin coating AZ9260 photoresist, exposure with UV light and AZ developer (AZ Electronic Materials). The insulating paralyne-C layers below the opening are etched using reactive ion etching with an  $\text{O}_2/\text{CHF}_3$  plasma using an Oxford 80 Plasmalab plus (fig. 4.1f). PEDOT:PSS

solution is then spin coated on top of the sample (fig. 4.1g). Finally, the sacrificial parylene layer is peeled-off leaving behind the intact transistor structure (fig. 4.1h). Devices are hard baked at 140°C for 1 h and then immersed in de-ionized water to remove any excess of low molecular weight compounds. Fig. 4.1 summarizes the steps involved in the fabrication of the device. Fig. 4.2 shows the image of the final device after peel off, where the PEDOT:PSS channel can be seen in good contact with gold electrodes.

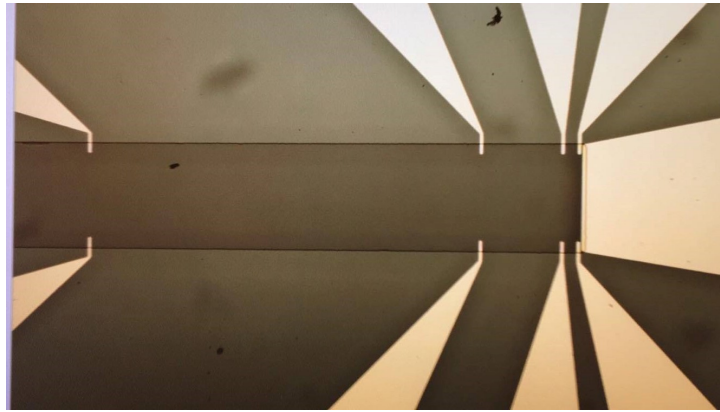


FIGURE 4.2: Photograph of the the device with electrodes

### 4.1.3 Variable angle spectroscopic ellipsometry

The as fabricated OECT devices were subjected to variable angle spectroscopic ellipsometric (VASE) measurements in their dry state. The dry channel of the device was placed on the ellipsometer stage, and a region of interest (ROI) in the channel was selected. The ROI was selected carefully such that only the ellipsometric data from PEDOT:PSS is recorded in the measurement, avoiding the reflections from the Cr/Au electrodes. VASE was performed at 8 different angles of incidence between 50-64 degrees with a step size of 2 degrees. For each spectrum, 30 data points were measured in the wavelength range of 400-1700 nm. Accurion EP4 spectroscopic nulling ellipsometer was used to conduct the VASE measurements.

#### 4.1.4 Electrical resistivity measurements

The electrical conductivity of dry PEDOT:PSS channel in air is measured using four point probe method at room temperature conditions. A constant current is passed through the channel by connecting a current source between the source and drain electrodes. The potential difference between the voltage probes  $V_A$  and  $V_B$  is measured using a high impedance voltmeter. The scheme of the measurement technique is shown in fig.4.3. The dimensions of the channel are defined by the device fabrication design. The resistance of the film between the voltage probe  $V_A$  and  $V_B$  is calculated using Ohm's law, and the resistivity is calculated using the equation:

$$\rho = \frac{V_{AB}}{I_{SD}} \cdot \frac{w \cdot d}{l} \quad (4.1)$$

Where  $\rho$  is the resistivity of the channel material,  $V_{AB}$  is the voltage drop between the voltage probes  $V_A$  and  $V_B$ ,  $I_{SD}$  is the current through the channel,  $w$  is the width of the channel,  $d$  is the thickness of the spin coated channel which is measured using Bruker nanoscope AFM with a silicon tip on a nitride lever in contact mode and  $l$  is the length between the voltage probes  $V_A$  and  $V_B$ .

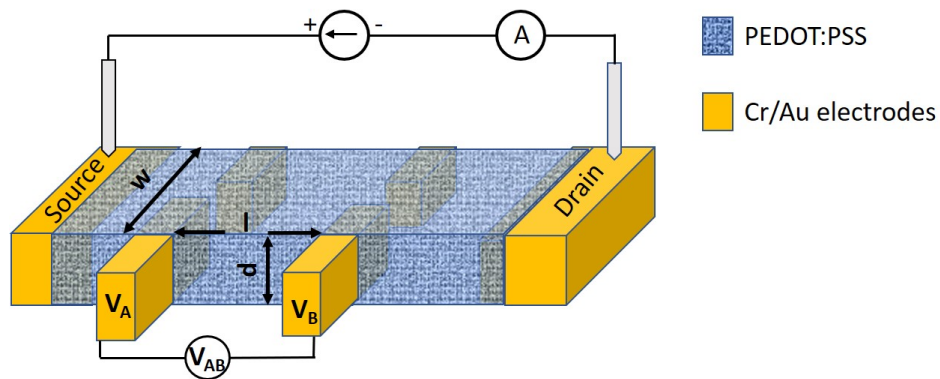


FIGURE 4.3: Scheme of four point probe measurement

The four probe measurement is then repeated in the Kretschmann cell setup (fig 4.4). The device is sandwiched between the cell and a quartz prism, the cell is filled with 0.1 M KCl (aq) such that the channel is in contact with the electrolyte. Four



probe resistivity measurements are performed and the resistivity of the channel is calculated when in contact with the electrolyte.

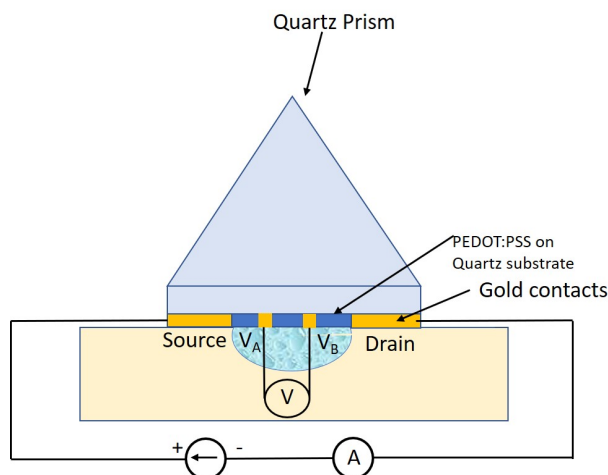


FIGURE 4.4: Scheme of the Krestchmann cell setup where four point probe electrical measurements are performed when the device is in contact with the electrolyte (0.1 M KCl). The source and drain electrode are connected to a current source through an ammeter and the voltage probes are connected to a voltmeter

#### 4.1.5 Cyclic voltammetry

The electrochemical cell setup was connected to Autolab PGSTAT128 potentiometer as shown in fig. 4.5. A cyclic voltammogram is recorded in the potential range from -0.65 V to +0.80 V with PEDOT:PSS/Au as working electrode, Pt rod as counter electrode and Ag/AgCl wire as the reference electrode in 0.1 M aqueous KCl solution. The voltammogram is cycled 5 times (*i.e.*, until the full cycle is found reversible).

#### 4.1.6 Electrochemical variable angle spectroscopic ellipsometry and electrical conductivity measurement

The capacitive (charge separation), anodic and cathodic potential windows of the semiconducting channel are determined from the voltammogram, and the electrochemical variable angle spectroscopic ellipsometry (EVASE) measurements are

performed accordingly in those windows/potential ranges. The EVASE measurements are conducted using the Accurion EP4 spectroscopic imaging ellipsometer. A CV is performed prior to conducting an EVASE measurement to reproduce a reversible full CV cycle. The CV is then paused at particular potential. After the current reached a constant value, where the W.E does not undergo any electrochemical reaction, the EVASE is conducted at a selected regions of interest (ROI) in the PEDOT:PSS channel. This was repeated for 8 different angles of incidence between 50-64 degrees with a step size of 2 degrees. The correction factor in the angle of incidence depending on the refracting index of the prism is applied in the calculations.

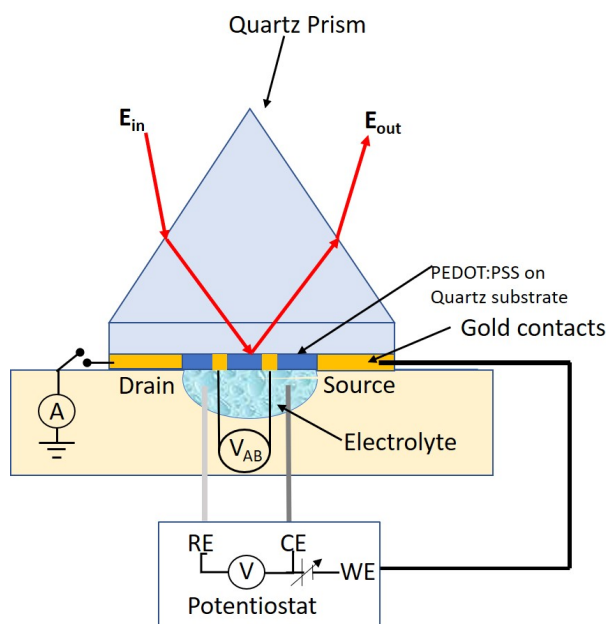


FIGURE 4.5: Scheme of the Krestchmann electrochemical cell where EVASE and electrical measurements (under electrochemical bias) are performed. The source electrode of the device is connected as a working electrode of the potentiostat, the Pt counter electrode immersed in the electrolyte is used as gate to the device, the drain electrode is connected to the ground of the potentiostat through an ammeter and the  $V_A$  and  $V_B$  electrodes of the device are connected to a voltmeter.

After the EVASE measurement at a fixed electrochemical potential, the incoming light is blocked by closing the shutter. This is done to ensure that at this point no photocurrent is generated in PEDOT:PSS channel. The drain electrode

is connected to ground, and the source-drain current for the paused W.E potential is recorded. The potential difference between the voltage probes  $V_A$  and  $V_B$  is measured using a high impedance voltmeter. The electrical resistivity of the PEDOT:PSS films at a particular electrochemical potential is calculated using eq. 4.1.

The EVASE data for 8 angle of incidences is simultaneously fitted using Tauc-Lorentz-Drude model (c.f. sec 3.2), Accurion EP4 model software is used for fitting the measured ellipsometric data. The DC conductivity is calculated using Drude parameters using eq. 3.5. The experiment is repeated for six electrochemical potentials.

#### 4.1.7 Device characterization

In order to measure the device characteristics of the PEDOT:PSS OECT device, two separately controllable current and voltage sources are used, such that the (i) drain characteristics ( $I_D$  vs.  $V_{SD}$ ) at varied gated voltage (ii) and the transfer characteristics ( $I_D$  vs.  $V_G$ ), can be recorded. A hollow cylindrical glass container is sealed on top of the channel using poly(dimethylsiloxane) (PDMS). PDMS is spread on the bottom of the container and placed on the substrate, such that the channel of the device is enclosed in the cylinder and the contact pads stay out of it. The device is kept on the hot plate at 100°C for 30 minutes for the PDMS to cure and seal. The cylinder is filled with 0.1 M KCl (aq) solution. An Ag/AgCl wire is dipped into the solution and is used as a gate electrode in the OECT setup. A Keithley dual-sourcemeter 2612A is used to supply voltage to the gate, to apply a potential across the source-drain electrodes ( $V_{SD}$ ) and to measure the corresponding currents, using a custom Labview software. The figure of merit of the OECT device can be estimated by calculating the transconductance  $g_m$  from the transfer characteristics, using the equation:

$$g_m = \frac{\Delta I_D}{\Delta V_G} \quad (4.2)$$

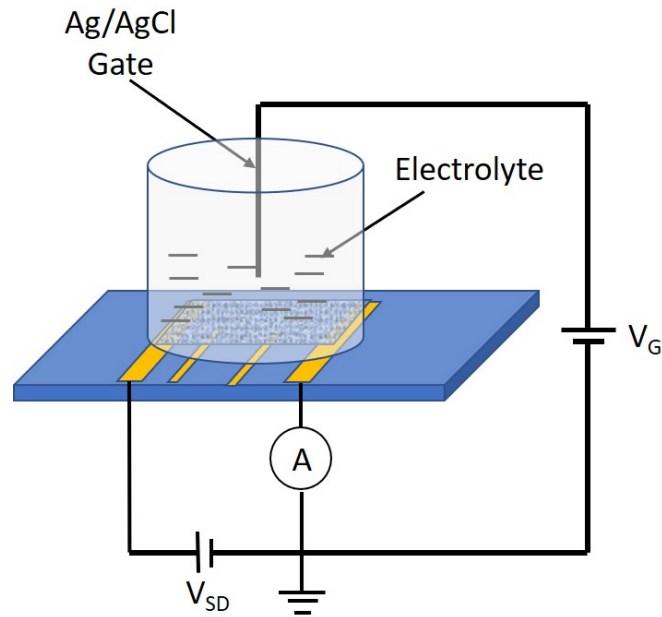


FIGURE 4.6: Schematic of the setup for device characterization measurements. The gate electrode used is Ag/AgCl wire 0.1 M KCl electrolyte. The source and drain electrodes are connected to a voltage source through an ammeter and an additional voltage source is connected to the gate electrode.

## 4.2 Results and discussions

### 4.2.1 Variable angle spectroscopic ellipsometry

The dry channel of PEDOT:PSS device was subjected to variable angle spectroscopic ellipsometry (VASE) measurements. The dielectric dispersion obtained from the TLD model fitted to the measured ellipsometric angles  $\Psi$  and  $\Delta$  is presented in fig. 4.7. The fitted dielectric dispersion is uniaxially anisotropic, with a constant dielectric in the extraordinary direction ( $\epsilon_{1,e} = 1.7$ ,  $\epsilon_{2,e} = 0$ ). It can be observed from fig. 4.7 that the film absorbs weakly in the visible range of electromagnetic spectrum, making the film almost transparent for visible range of the electromagnetic radiation (EMR), however the absorption increases in the NIR range with the appearance of a Drude tail. The energy of the main optical transition of the dry film is found to be at 1.62 eV, which is a slight shift to lower energies compared to the film (PEDOT:PSS + DMSO) used in chapter 3

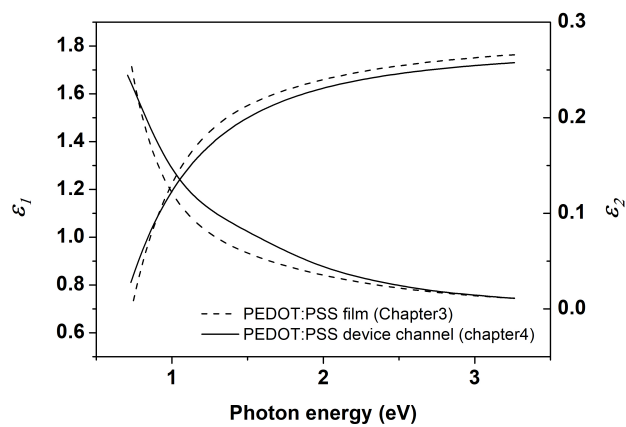


FIGURE 4.7: Ordinary, real ( $\epsilon_1$ ) and imaginary( $\epsilon_2$ ) dielectric dispersion of the dry PEDOT:PSS channel of the device obtained by fitting the ellipsometric angles  $\Psi$  and  $\Delta$  measured by VASE. The dashed line are the Ordinary, real ( $\epsilon_1$ ) and imaginary( $\epsilon_2$ ) dielectric dispersion of the dry PEDOT:PSS used in Chapter 3 and the solid line is from the PEDOT:PSS channel in the current study

(1.77 eV). The comparison of the dielectric functions for both the films is shown in fig. 4.7. This indicates that the Fermi level of the PEDOT:PSS +EG film is at slightly higher energy compared to the PEDOT:PSS +DMSO film, hence the energy difference between the HOMO and LUMO is less in the current study (c.f. fig. 3.14). Solvent treatment of PEDOT:PSS is reported to cause structural modifications in the PEDOT:PSS matrix as discussed in the previous section, which in turn generates additional doping sites in PEDOT:PSS matrix. These additional redox states created by the conformational changes in the PEDOT:PSS matrix can rejuvenate the "dead" charge carriers (in terms of electrochemical activity) in the polymer complex. Park *et al.* reported that for DMSO treated PEDOT:PSS the redox active charge carriers are 2.5 times more in number compared to the pristine PEDOT:PSS [134]. This generation of new redox states shifts the reduction potential of PEDOT to a lower values, thereby creating the "mid band states" states in the band structure at lower energy levels compared to the pristine state. Therefore the main transition energy is shifted to higher values by the addition of DMSO. Such results are inline with the previously reported absorption spectra of PEDOT:PSS thin films , with and without the DMSO treatment [135]. The DC conductivity enhancement by EG treatment however, is lower compared to DMSO treatment. Therefore , based on the above argument we can justify the low value

of the transition energy compared to the one observed on the DMSO treated sample. The DC conductivity of PEDOT:PSS+EG calculated using eq. 3.6 is  $190.2 \text{ Scm}^{-1}$ . This is in close agreement with the value ( $205.4 \text{ Scm}^{-1}$ ) calculated from four probe measurements (section 4.2.2).

These experimental results, namely the observed optical anisotropy, points to the conclusion that the channel behaves as an insulator in the direction normal to the substrate plane and as a semi-metal in the direction parallel to the substrate. This is an essential aspect from a device perspective. In device fabrication, the geometry of the contacts plays an important role, depending on the functioning of the device [44, 119, 136]. For example, in OLED devices, the vertical conduction has more importance compared to the lateral one. However, the opposite is true for OFET or OECT devices.

The VASE measurements are repeated when the channel is brought in contact with the electrolyte (fig. 4.5). Ellipsometric angles are fitted using a TLD model. The fitted parameters are tabulated in table 4.1. Unsurprisingly, a red shift in the transition energy ( $E_{OTL}$ ) is observed. This is due to the spontaneous reduction of the channel as explained in section 4.2.1, where the electrical conductivity is found to be reduced when the channel is brought in contact with the electrolyte [137]. The DC conductivity calculated from the Drude parameters was found to be  $96.7 \text{ S/cm}$ . This is inline with the electrical measurements (c.a sec. 4.2.1), where the electrical conductivity is found to be  $82.6 \text{ S/cm}$ .

## 4.2.2 Electrical Measurements

The four probe measurements for the dry PEDOT:PSS device in air was conducted, and the potential difference between the voltage probes  $V_A$  and  $V_B$  was found to be  $3.54 \text{ V}$  upon passage of a constant current of  $0.1 \text{ mA}$ . The dimensions of the device were defined during the lithography process and are depicted in fig. 4.8. An AFM scan on a separate device was conducted, the channel of the device is scratched to create a step with respect to the substrate, and the scan is performed

across the step (fig. 4.9). Considering that the two devices were prepared with the same parameters and with the same spin speed (for spin coating of PEDOT:PSS), it can be assumed that they have the same thickness. The thickness of  $52.6 \pm 1.5$  nm was calculated from the AFM scans performed at three spots around the step of the PEDOT:PSS channel.

The above values were used to calculate the resistivity of dry PEDOT:PSS channel using eq. 4.1, from which the electrical conductivity ( $\sigma_{ele}$ ) is obtained as:

$$\sigma_{ele} = \frac{1}{\rho} = 205.4 S cm^{-1} \quad (4.3)$$

The Conductivity of the dry PEDOT:PSS used as the channel material in the OECT device is found to be lower compared to the PEDOT:PSS films used in Chapter 3. It shall be noted that the composition of co-solvents used in the devices is different from the one used in the PEDOT:PSS films in the previous chapter.

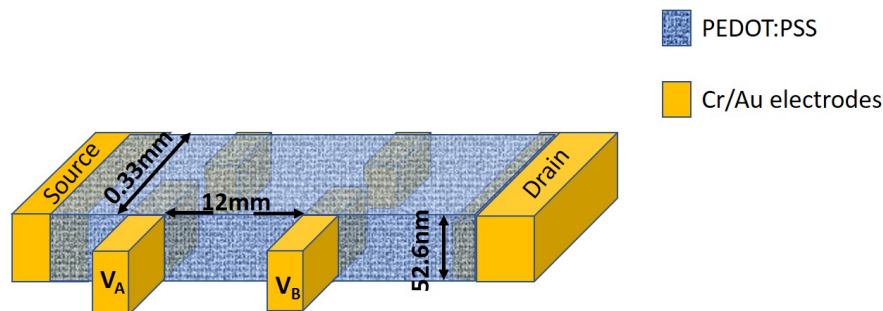


FIGURE 4.8: Schematic representation of the thin PEDOT:PSS channel representing the dimensions of the film. The length and width of the channel are known from the dimensions of the channel slot defined in the lithography process. The thickness is determined from AFM measurements.

The conductivity enhancer used in the current study is ethylene glycol (EG) while in previous case DMSO was used. While the use of these conductivity enhancers is practiced regularly for the processing of thin conducting films of PEDOT:PSS, the mechanism of conductivity enhancement by the addition of these solvents is still under discussion [134, 135]. The primarily accepted viewpoint is the phase separation of insulating PSS from the conducting PEDOT [138], which was evidenced

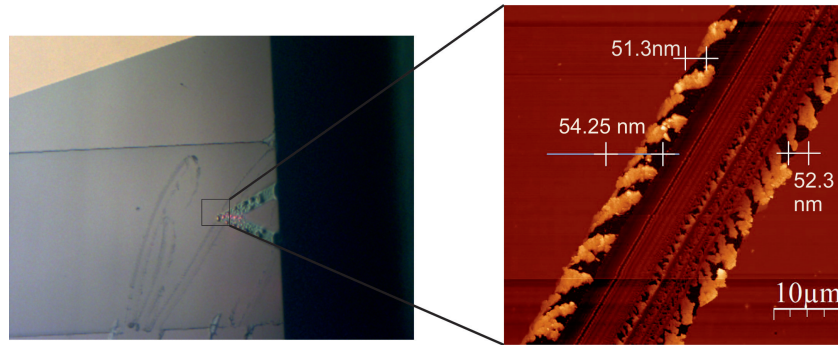


FIGURE 4.9: (Left) Photograph of the scratch on the channel where the AFM scan is performed. (Right) Scanning atomic force micrograph of the PEDOT:PSS channel of device across the scratch. The height profile is measured at three distinct points and the average is considered

by the decrease of S 2p signal intensity, attributed to PSS, in X-ray photoelectron spectroscopy (XPS) studies. Another proposed hypothesis for conductivity enhancements by the addition of co-solvents include a change in the conformation of PEDOT<sup>+</sup> chains [139]. In the pristine state, a coil type conformation is proposed [140, 141], where the plane of the thiophene ring on the PEDOT chain deviates from the plane of its neighboring thiophene, rendering the C<sub>α</sub>-C<sub>α</sub> bond to be more like a  $\sigma$  bond. This structure is a benzoid type, and the conjugated  $\pi$ -electrons in this system are not completely delocalized over the whole PEDOT chain. Hence, the PEDOT:PSS film has a low charge carrier mobility. On the other hand, the co-solvent treated PEDOT:PSS is reported to have an expanded coil conformation. Here, the neighbouring thiophene rings in the PEDOT chains are oriented in almost the same plane. Therefore, the conjugated  $\pi$ -electrons are delocalized over the whole chain [142]. This is a quinoid structure (refer to section 2.2 for details about benzoid and quinoid structures). Both benzoid and quinoid structures maybe present in the untreated PEDOT:PSS film. The benzoid structure may transform into the quinoid after the co-solvent treatment, such that the quinoid is the dominating structure in the high conductivity PEDOT:PSS. It has been reported that redox reaction can also cause these structural transformations [143]. Zhang *et al.* reported that the effect of DMSO on the conductivity enhancement is higher compared to EG, even at very low DMSO concentrations [133]. Therefore, the slight decrease in conductivity measured in PEDOT:PSS channel can be attributed to the use of EG as a conductivity enhancer compared to DMSO. The



reason to use EG is that DMSO is toxic compared to EG to be used in bioelectronics devices.

The conductivity of the same channel in contact with a 0.1 M aqueous solution of KCl, determined in the same manner as above amounts to  $82.6 \text{ Scm}^{-1}$ . The drop in conductivity of PEDOT:PSS channel observed when it is brought in contact with the electrolyte (0.1 M KCl). This drop can be attributed to two major factors. (i) When the channel is brought in contact with the electrolyte, it can adsorb the solvent and swell, as reported for many conducting polymers. The swelling of the polymer disrupts the conducting pathways by separating the conducting islands (PEDOT<sup>+</sup> in this case) of the composite polymer [144, 145]. (ii) When the semiconducting polymer is brought in contact with the electrolyte the Fermi level of the semiconducting polymer equilibrates itself with respect to the potential applied by the charge separation layer formed at the polymer/electrolyte interface, this process can spontaneously reduce/oxidize the polymer film at the working electrode [137]. It's been reported that with the presence of the crosslinkers like GOPS, the swelling of the film is minimal [137, 146] and therefore we can assume the drop on conductivity in the present case is probably due to the spontaneous reduction of PEDOT:PSS. It shall also be noticed that the change in thickness due to swelling was not considered in the resistivity calculation of the swollen film as a minimal swelling was expected.

### 4.2.3 Cyclic voltammetry and capacitance measurements

The cyclic voltammogram (CV) of the OECT device (as explained in section 4.1.4) is presented in fig. 4.10. Three voltage windows can be observed in the CV, separating the oxidation, reduction and the charge separation (capacitive) regions of the channel (W.E). The charge separation region is marked with vertical lines (roughly between -0.2 V to +0.2 V). Since the variation of current in the charge separation region is minimal (hence the name charge separation region), thus one can assume the channel to behave as a capacitor in this voltage range. The volumetric capacitance ( $C_{Vol}$ ) of the channel in the voltage range -0.2 V to +0.2 V is

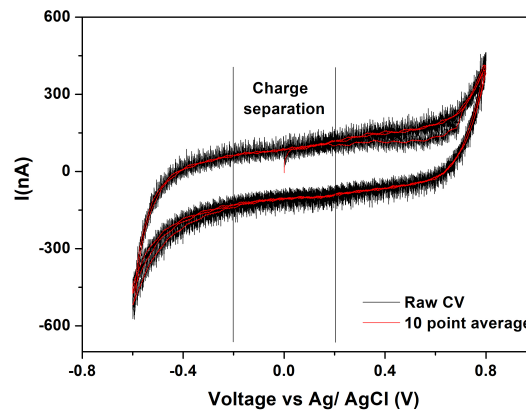


FIGURE 4.10: Cyclic voltammogram of the device. The PEDOT:PSS channel is used as a W.E and Pt rod electrode as an C.E and Ag/AgCl wire is used as a R.E in 0.1 M KCl aqueous solution. the black line is the raw data and the red line (eye guide) represents the 10 point average of the same.

calculated to be  $44 \text{ F cm}^{-3}$  using the equation 4.4.

$$C_{Vol} = \frac{1}{Vol \cdot (V_2 - V_1) \cdot \nu} \cdot \int_{V_1}^{V_2} IdV \quad (4.4)$$

The volume (Vol.) is calculated from the dimensions of the channel depicted in fig. 4.8,  $V_2$  and  $V_1$  are the potential limits of the charge separation region;  $I$  is the current and  $\nu$  is the scan rate of the CV. The calculated ( $C_{Vol}$ ) is in close agreement with values reported by Voklov et. al. ( $34 \text{ F cm}^{-3}$ ) and Rivnay et. al. ( $39 \text{ F cm}^{-3}$ ) [29, 147], however an order of magnitude smaller than the ( $C_{Vol}$ ) reported by Kurra et.al. ( $327 \text{ F cm}^{-3}$ ) [148]. The increased capacitance in the latter case could be due to the acid treatment of PEDOT:PSS performed in that study.

Charge separation in an electrochemical capacitor occurs by the formation of a double layer at the electrode-electrolyte interface. The capacitance of an electrochemical double layer (EDL) capacitor is directly proportional to the surface area of the electrode. In case of non-Porous channel materials, the ions accumulate only on the top surface of the channel, therefore causing a "two dimensional" capacitive effect. This property is efficiently utilized in electrolyte gated solid state

transistors [84]. However, in electrodes made of porous conducting polymer materials like PEDOT:PSS, a high value of capacitance can be achieved due to their large surface area to volume ratio, compared to their solid state counterparts. The observed high capacitance of PEDOT:PSS in the charge separation region of the CV is clear evidence of the supercapacitive behaviour of the PEDOT:PSS film in this study. This supercapacitive behaviour of PEDOT:PSS films can be utilized in the organic electrochemical transistor (OECT) devices [29], where due to the high capacitance of these films a large number of ions can be infused in the polymer film, which in turn can modulate the conductivity of the polymer channel in the transistor, by affecting the mobility of its electronic charge carriers. This effect can be readily used in applications where the large surface area is a constraint, *e.g.* biomedical applications [84, 149].

The capacitance of the channel material of an OECT plays a determinant role in the response time needed to turn the OECT OFF/ON [150]. The  $C_{Vol}$  of the channel governs the redistribution of ions in the CP, which are being infused from the electrolyte. Thus the transconductance and hence the device performance can be tuned by carefully adjusting the ( $C_{Vol}$ ).

A Faradic response can be observed outside the charge separation region of the CV. The shape of the CV represents a typical behaviour of semiconductor electrodes, where at the positive potentials the rise in the positive current is due to the oxidation of the valance band of PEDOT and at the negative potentials the conduction band gets filled with electrons (reduction), giving rise to a negative current. The detailed explanation of this behaviour of a semiconductor electrode is explained in section 3.3.4. An OECT uses this behaviour to its advantage, by oxidation/reduction of the channel materials the the conductivity of the channel can be modulated. This process is termed as doping/de-doping. Thus it is clear from the CV that depending on the applied electrochemical potential both capacitive, and redox processes can be used to modulate the conductivity of the channel in an OECT.

#### 4.2.4 Electrochemical variable angle spectroscopic ellipsometry

The EVASE measurements are performed by conducting a VASE in parallel with an application of an electrochemical bias to the channel (c.f. sec. 4.1.5). The  $\Psi$  and  $\Delta$  measured from the EVASE measurements are fitted with the TLD model. The EVASE fit at E.M.F = 0.024 V vs Ag/AgCl is presented in fig. 4.11 as a representation of the fit. All the  $\Psi$  and  $\Delta$  fits for varied EMFs (as indicated in table 4.1) are presented in Appendix B.

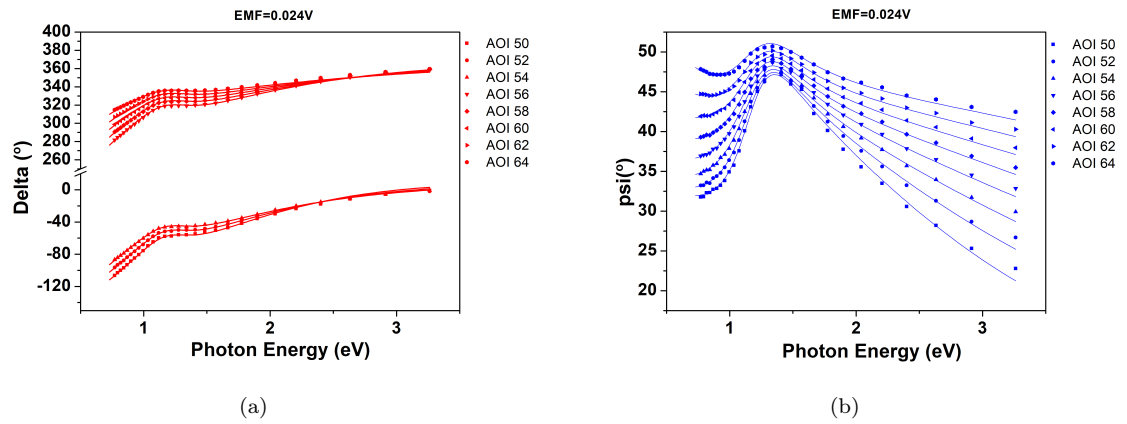


FIGURE 4.11: EVASE spectra of the PEDOT:PSS channel in the OECT device at room temperature in 0.1 M KCl aqueous solution at an electrochemical bias of 0.024 V vs Ag/AgCl. The scatter points represent the measured data at varied angle of incidence (AOI, from 50 to 64 degrees with the step size of 2 degrees) and the solid lines represent the best fit of the TLD model. (a) Ellipsometric angle  $\Delta$ , (b) Ellipsometric angle  $\Psi$ .

The ordinary real ( $\epsilon_{1,o}$ ) and imaginary ( $\epsilon_{2,o}$ ) dielectric functions, extracted from the TLD models fitted to the EVASE measurements for varied applied EC (gate) potential are presented in fig. 4.12.

Similar to the VASE measurements in contact with the electrolyte (without any electrochemical bias), the extraordinary dielectric functions were found to be constant. The parameters for the fitted models are tabulated in table 4.1. Conductivity calculated from the Drude parameters ( $\sigma_{DC}$ ) and measured from electrical four probe measurements ( $\sigma_{ele}$ ) is also tabulated for comparison.

TABLE 4.1: The best fit parameters of the ordinary TLD parameters of the ordinary dielectric function (cf. eqs.3.3-3.5); and DC conductivity ( $\sigma_{DC}$ ) calculated from the Drude term (cf. eq.3.6) ; film thickness (d) obtained from the fit; the electrical conductivity measured by means of the four probe measurements . All fit parameters are obtained by fitting the EVASE spectra ( $\Psi, \Delta$  vs  $E$ ) , under varied equilibrium electric potentials at the PEDOT:PSS electrode, in the range -0.1 to +0.75 V vs Ag/AgCl in 0.1 M KCl (pH  $\approx$ 7).

EMF vs Ag/AgCl (V)	$\epsilon_\infty$	$E_{0TL}$ (eV)	$A_{TL}$ (eV) <sup>2</sup>	$\Gamma_{TL}$ (eV)	$E_g$ (eV)	$A_D$ (eV) <sup>2</sup>	$\Gamma_D$ (eV)	$d$ (nm)	$\sigma_{DC}$ (S $\text{cm}^{-1}$ )	$\sigma_{ele}$ (S $\text{cm}^{-1}$ )	RMSE
-0.1	2.16	1.20	0.77	0.56	0.83	0.55	0.38	81.3	91.2	80.4	0.92
0.02(OCP)	2.14	1.23	0.38	0.69	0.72	0.52	0.34	90.1	96.7	82.6	0.71
0.1	2.15	1.24	0.32	0.92	0.57	0.62	0.27	82.8	145.0	111.0	1.20
0.2	2.18	1.30	0.34	1.11	0.56	0.73	0.30	72.3	156.0	136.7	0.84
0.4	2.20	1.40	0.32	1.55	0.50	0.82	0.28	65.8	178.2	158.9	0.77
0.75	2.13	1.74	0.08	1.15	0.90	0.78	0.71	79.2	69.0	73.1	1.13

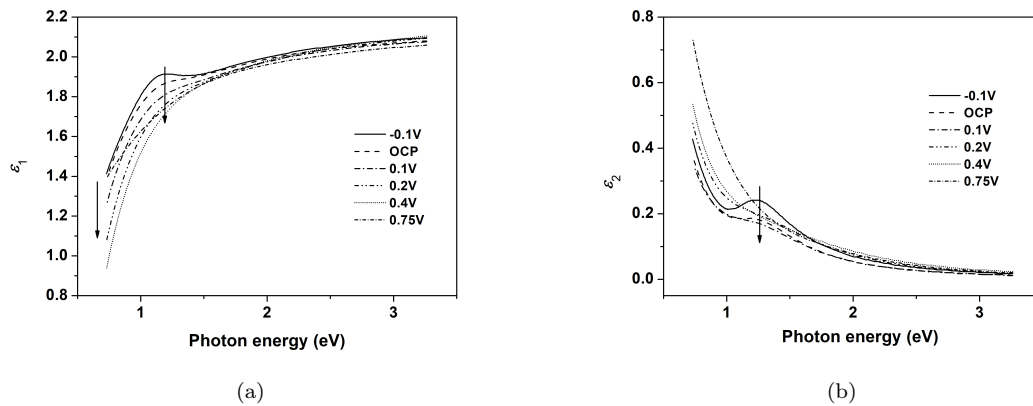


FIGURE 4.12: Ordinary, (a) real ( $\epsilon_1$ ) and (b) imaginary ( $\epsilon_2$ ) dielectric dispersion of the PEDOT:PSS channel of the device obtained by fitting the ellipsometric angles  $\Psi$  and  $\Delta$  measured from EVASE. The arrows in the real and imaginary plots represent that the strength of the main optical transition decreases with a parallel increase in Drude tail when the potential is applied from negative to positive Vs Ag/AgCl in 0.1 M KCl at room temperature conditions.

It can be observed that the DC conductivity ( $91.1 \pm 2.3$  S/cm) for negative applied voltage (-0.1 V) was the lowest. However, as the voltage increased, the conductivity increased. Maximum being  $178.17 \pm 1.8$  S/cm for  $V = 0.4$  V. Moreover, the conductivity corresponding to 0.75 V input voltage was lower than that of  $V = 0.4$  V. The least value of conductivity at -0.1 V can be attributed to the reduction of PEDOT at this potential, as the voltage value fall in the reduction regime of the CV. Similarly the highest value of conductivity can be attributed to the oxidation of PEDOT. On the other hand, the decreased channel conductivity at 0.75 V can be suspected due to the degradation of PEDOT:PSS due to its overoxidation [151]. A slight variation in thickness is also observed with the varying electrochemical potential. This swelling and de-swelling of conducting polymers due to the insertion and de-insertion of ions in the CP matrix have been reported by many authors [23, 152, 153]. This electro-mechanical response of PEDOT:PSS mimics the functioning of a muscle or skin, thus making it a potential candidate for bionic applications [154]. However, due to the usage of a crosslinker (GOPS) in the PEDOT:PSS solution this effect is minimal in this study.

In fig.4.12, one can observe the a peak, in both  $\epsilon_{1,o}$  and  $\epsilon_{2,o}$  at around 1.2 eV (depicted by arrows in the figure). This peak represents the main optical transition

from the valance band to the conduction band of PEDOT. After continuous doping (oxidation) of PEDOT, the peak diminishes with a monotonic increase in the NIR range, indicating the increased number of free charge carriers in the semiconductor in comparison to the localized electrons/holes. Similar results have been reported in other spectro-electrochemical studies [32, 33]. These experimental result can be explained in the same view as in case of the PEDOT:PSS + DMSO film doping in the previous chapter. The electrochemical doping of PEDOT:PSS polymer occurs by the application of positive C.E voltage (gate voltage). At lower voltage ranges, *i.e.* in the capacitive region the transition energy remains almost constant at 1.2 eV, whereas, when the applied voltage pushed Fermi level into the valence band, the transition energy increases. However, the strength of the transition energy oscillator is low, depicting a lower number of transitions in comparison to the non-doped state, but a higher strength for the Drude parameter, indicating a increased free charge carrier absorption, due to the increased number of holes in the valence band (c.f. fig.3.17b) [137]. The experimental observation of decreasing band upon doping is also inline with the theoretical prediction of J.L. Bredas [132]. As explained in chapter 2, the doping or oxidizing of PEDOT causes the formation of more quinoid structures in the PEDOT chain. In order to adopt the quinoid structure, the polymer chain geometry will tend to distort locally around the charges on the chain while pushing the highest occupied band to shift up in energy and parallely and shifting the lowest occupied band lower in energy by a similar amount [35, 132].

In comparison to the large PEDOT:PSS films in Chapter 3, the ordinary dielectric parameters of the PEDOT:PSS used in the current study are very similar. The difference in conductivity due to the use of different cosolvents have been explained in section 4.2.2. However, there is a significant difference in the extraordinary dielectric functions in the two PEDOT:PSS formulations, *i.e.* while a very low conductivity has been found in the PEDOT:PSS+DMSO (chapter 3) formulation, the PEDOT:PSS+EG (Chapter4) formulation is found to be completely insulating in the extraordinary direction. From this observation it can be pointed out the effect of DMSO in decreasing the hopping length in ordinary as

well as extraordinary direction, thereby increasing the conductivity of the CP in both directions, compared to its pristine state. PEDOT:PSS+EG formulation, on the other hand, enhances the conductivity (compared to pristine PEDOT:PSS) only in the ordinary direction as no significant conductivity is observed in the extraordinary direction.

It shall be noted that in the optical measurements only a small illuminated area of the polymer film ( the region of interest selected from the CCD software) can be studied, and not the whole channel. Therefore, parameters like, the defects in the film or doping in different regions of the film cannot be accounted for. Such parameters are important for an OECT device, as they can significantly vary the response and the quality factor of the device. Therefore, a device shall be characterized by the device's drain and transfer characteristics , which takes into account the conduction through the whole channel and the properties like transconductance ( $g_m$ ) can be studied. In the next section we try to explore these characteristics.

#### 4.2.5 Device characteristics

In principle, OECTs can function in accumulation or depletion mode [115, 130]. However, since the channel material in this work is in its conducting (ON) state at room temperature conditions, we conducted the device characterization in depletion mode. That is, at the application of a positive gate voltage the device turns from conducting (ON) to insulating state(OFF). The gate voltage is the potential applied at the Ag/AgCl gate electrode with respect to ground (not to be confused by the electrochemical cell electrode configuration in previous sections). Ag/AgCl wire is used as a gate electrode to reduce gate polarization, because Ag/AgCl is non-polarizable electrode [107]. At the application of a positive gate voltage, positive ions in the electrolyte penetrate into the polymer matrix of the channel, two possible effects can take place at this application, (i) the ions inside the polymer matrix can mobilize/immobilize the charge carriers of PEDOT which can disrupt the conductivity of the PEDOT:PSS film, (ii) above a certain potential the CP can



reduce/oxidize by replacing the charge carriers by infused ions (c.a. sec.4.2.4). To study this effect,  $I$ - $V$  characteristics (or drain characteristics) of the PEDOT:PSS channel was studied. The source-drain voltage ( $V_{SD}$ ) is scanned from 0 to -0.6V and the drain current ( $I_D$ ) is recorded at varied gate potentials. Measured  $I$ - $V$  characteristics are plotted in fig.4.13. It can be noticed that at 0 gate potential the  $I$ - $V$  characteristics show an almost linear Ohmic behaviour, indicating the ON state of the film. With the subsequent increase in gate potential, the drain current starts to saturate at lower  $V_{SD}$  values. At  $V_G = +0.6V$  there is almost no passage of current through the channel, and therefore the device switches to an OFF state.

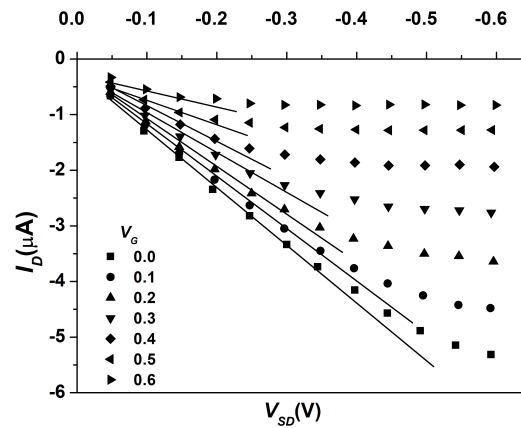


FIGURE 4.13: Drain characteristics of the OECT device at varied gate voltage. The scatter points represent the measured data points and the Solid line is the linear fit in the Ohmic region of the plot

It can be noticed that there are two regions in the drain characteristics plot (fig.4.13). The first region at lower  $V_{SD}$  potentials shows a linear Ohmic behaviour of the PEDOT:PSS channel, while at higher  $V_{SD}$  potentials the current  $I_D$  saturates. This can be explained by the depletion mechanism due to the infused ionic charge carriers [61, 155]. At any given source-drain voltage, the potential at the source electrode is  $V_S$  and at the drain electrode is  $V_d$ . Because potential is a continuous function, the potential at any point on the channel ( $V_{Ch}$ ) changes continuously from drain to source (fig. 4.14). Now at the application of a positive gate potential, when the source electrode is grounded and a negative potential is applied to the drain, the potential difference between the gate and the channel

$(V_{G-Ch})$  changes continuously from drain to source, i.e.  $(V_{G-Ch})$  near the drain electrode will be same as  $(V_{G-D})$  and will decay continuously towards the source electrode. This means that infused ion density will be different along the length of the channel. Such results can be visually observed in the electrochromic moving front experiments [156, 157], where depending on the applied bias the de-doped front of the channel moves from drain to source electrode. However, since the source electrode is grounded and a negative potential is applied at the drain electrode, at any given gate potential, the gate to drain voltage is sufficient for the infusion of cations into the whole polymer film, where the maximum cations infuse near the drain and their density continuously decreases towards the source. By increasing the drain potential (towards negative) at a given positive gate potential, the potential difference between the gate and drain electrode is increased, causing higher densities of ion infusion towards the drain. When the local density of infused cation becomes equal to the intrinsic dopant densities of the channel, it completely de-dopes causing the current to saturate [158], this onset of current saturation is termed as "pinch off". This condition can be mathematically expressed as  $V_G - V_D \geq V_P$ , where  $V_P$  is the pinch off voltage [159]. Therefore, by increasing the gate potential one can decrease the pinch off voltage.

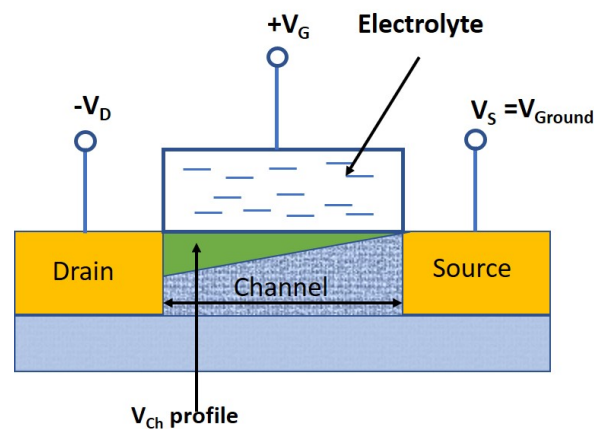


FIGURE 4.14: Sketch of the voltage profile through the channel length.

In the drain characteristics presented in fig.4.13, we can clearly observe the shifting of the pinch off voltage to lower potentials with the increasing gate voltage.

The conductance of the channel in the Ohmic region of the drain characteristics was calculated from slope of the  $I$ - $V$  curve and plotted vs. the gate voltage (fig.4.15). The conductance linearly decreases upto  $V_G=0.4V$  and then starts to saturate. The saturation plateau of the conductance indicates that PEDOT:PSS channel in the OECT device has been highly de-doped at gate potentials above 0.4 V, such that the passage of charge carriers through the channel has been blocked or is minimal. Therefore switching the device OFF.

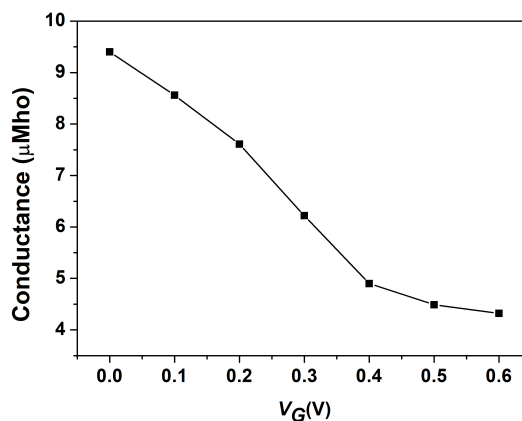


FIGURE 4.15: Gate voltage vs conductance of the OECT device in the ohmic range of the drain characteristics, obtain by calculating the slope of the linear region of the drain characteristics at varied gate voltage

From the CV and EVASE measurements we know that both capacitive and Faradic contributions play part in the modulation of the conductivity of PEDOT:PSS. One cannot quantitatively compare the device characteristics with the electrochemical measurements shown in the section 4.2.4, as the voltage reference in these two cases are ground and Ag/AgCl (in 0.1 M KCl) respectively. Also, one has to keep in mind that the polarities of electrodes in the device transfer characterization experiment are opposite to that of the CV experiment. Therefore, at the application of a positive gate potential, when the channel potential (through drain electrode) is kept negative, PEDOT goes under reduction. Since we know that PEDOT:PSS is a p-type semiconductor, this must be the reduction of the valance band. As the valance band gets filled with electrons, the p-type charge carriers of PEDOT decrease until the Fermi level reaches the band gap (c.a. fig.3.17) [137]. At this

point the conductance of the channel can only be modulated by the capacitive/-field effect as explained in section 4.2.4. The same can be observed in fig.4.15, where the conductance drops steeply from 0-0.4 V of  $V_G$  which can be seen as the reduction of PEDOT, and above 0.4 V the capacitive region takes over. A qualitative comparison of the above explanation can be made to the EVASE measurements, where the conductivity was measured in the capacitive region first and a increase in conductivity was reported upon oxidation of PEDOT.

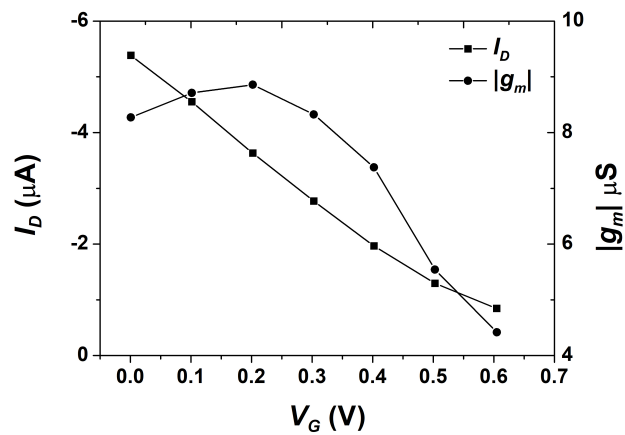


FIGURE 4.16: Transfer characteristics of the OECT device at the source to drain voltage of -0.6V. Left Y axis is the drain current measured at different gate potentials, the right y axis is the transconductance measured by calculating the first derivative of  $I_D$  VS  $V_G$  plot using eq.4.5

The transfer characteristics and the transconductance ( $g_m$ ) of the device at the application of -0.6V of  $V_{SD}$  are plotted in fig.4.16. The transconductance ( $\Delta I/\Delta V_G$ ) at any point i is calculated as:

$$g_{mi} \approx \frac{I_{D(i+1)} - I_{D(i-1)}}{V_{G(i+1)} - V_{G(i-1)}} \quad (4.5)$$

In the transfer characteristics one can observe the switching OFF of the device with the application of increasing gate voltage. The transconductance on the other hand, is the figure of merit of the device. The highest transconductance is observed to be 0.8  $\mu\text{S}/\text{cm}$  at 0.2 V. While much higher transconductances have been reported in the literature for PEDOT:PSS based devices [75, 119], in the current measurement the channel length was significantly large compared to the

reported ones. Since electrochemical doping is a slower process compared to its electrostatic counterpart (OFET, EGOFET), the dimensions of the channel can affect the transconductance significantly.

### 4.3 Summary and conclusions

In the present study, the OECT was fabricated using UV photolithography technique. After preparing the device, it was first kept in dry conditions to measure various electrical parameters such as four probe voltage  $V_{ab}$ , resistivity, source to drain current  $I_{SD}$ , DC conductivity, and dielectric properties of the semiconducting layer were measured.  $V_{ab}$  was measured by passing a current  $I_{SD}$  of 0.1 mA through the channel material and it was found to be 3.54 V. The conductivity of the channel material was found to be 205.4 S/cm in dry condition, which dropped to 82.6 S/cm when brought in contact with the electrolyte. The dielectric and optical properties of the semiconducting channel were measured by using VASE and EVASE. It was found from the graphs that the real part of the ordinary dielectric function in air increased steeply for the lower photon energies, however, it saturated at higher photon energies. The imaginary part was almost zero and increased rapidly on lowering the photon energy. This explains the transparent nature of the PEDOT:PSS polymer films in the visible range of the spectrum of electromagnetic radiation. The extraordinary dielectric function extracted from the fit was constant for all wavelengths, indicating an insulating type behaviour of PEDOT:PSS in the direction normal to the substrate. The DC conductivity values calculated from the fit values were found to be in close agreement with conductivity values obtained from the electrical measurement using the four probe method. From the EVASE measurements it was found that as the voltage increased the electrical conductivity also increased. However for the maximum voltage input, *i.e.*  $V = 0.75$  V, the conductivity measured was very low. The electrochemical gating and transport mechanism was understood by parallel comparison of the electrochemical measurements with the EVASE measurements. The EVASE results indicated the presence of both field effect and redox doping effect in the experiment. It was

found that in capacitive voltage regime of PEDOT (as working electrode) the field effect modulated the conductivity of the channel, whereas, in the redox regime, PEDOT goes through band structure modulation by moving the Fermi level due to applied electrochemical potential and thereby affecting the conductivity.

The characteristic curves of the transistor were also measured and presented. The drain characteristics of the OECT were found to be similar to that of the traditional FET device with the pinch off voltage shifting with every doping cycle. It was observed that at higher positive voltages, the drain current versus drain voltage curve becomes flat. This corresponds to zero current passing through the semiconducting channel and the device takes 'OFF' state. This off state is caused by the reduction in the mobility of the holes in the channel because of the creation of electrostatic field around it, another reason for de-doping can be the electrochemical reduction of PEDOT. The transfer characteristics of the transistor were measured by keeping the drain-source voltage constant and varying the gate-source voltage. The change in drain current was found to be minimal as the gate voltage increased at lower drain voltages. However, the drain current reduced rapidly with at higher gate voltage. The organic electrochemical transistor showed high transconductance for the large channel length. The transconductance could be improved by making the channel length smaller. This is because of the nano-to micro- scale thickness and highly doped nature of the PEDOT:PSS films. The quality factor of the transistors mainly depends on their transconductance which in turn affects the efficiency of the channel to modulate its conductance when external electrical bias is applied across the electrolyte.

In conclusion, the EVASE characterization technique clearly differentiates the field effect from the redox doping mechanism in organic electrochemical transistor devices. However, in this study, this characterization was done while keeping the channel always in ON (conducting) state. On the other hand, in the standard electrical characterization techniques (drain and transfer characterization), one can easily differentiate the OFF state of the device from its ON state and vice-versa, but the mechanism causing these changes in states can't be identified, *i.e.* one can't differentiate the capacitive and redox regimes in these measurements as there is no

electrochemical characterization present in this method. One shall note that the EVASE and electrical characterization experiments conducted on the OECTs in this study are two distinct experiments and shall not be compared in terms of applied voltages. The voltage references in these two cases were different, therefore, in the electrical characterization experiment one can't determine the electrochemical state (capacitive or redox) of the PEDOT:PSS channel at any applied potential. Therefore, in order to gain complete understanding of the mechanistic functioning of the OECTs an electrochemical characterization must be conducted in parallel with the standard device characterization, using an electrochemical voltage reference.

## Chapter 5

### X-Ray reflectivity and near edge

### X-ray absorption fine structure

In comparison to the solid state materials like silicon, the conducting polymers (CPs) exhibit disordered structure [160–163]. CP materials can have varying chain lengths, multiple kind of defects and multiple side chains [164–167]. Most of the CP materials are known to be amorphous, but can also be partially crystalline. In PEDOT based CPs the crystalline order is very low. For example, in PEDOT:tosylate films, the X-ray diffraction (XRD) studies reveal a para-crystalline structure, where the order decreases with distance [168]. PEDOT:PSS films however, were found mostly amorphous, with short range structural order, i.e. a broad diffractive maxima is observed in X-ray diffraction studies[169].

To promote solubility of CPs for easy processing and thin film formation by spin coating, they are often synthesized with flexible polymer side chains [47, 170]. These side chains affect the way the soluble co-polymer is packed in its matrix. The CP macromolecules in a thin film can stack themselves in a lamellar and  $\pi-\pi^*$  interchain stacking arrangement (fig. 5.1). This tightly packed ordered arrangement is distributed in a disordered manner in a conducting polymer film [171, 172]. Siringhaus *et al.* reported XRD studies on poly(3-hexylthiophene) (P3HT), which explore the structural arrangement of these complex microstructures[173]. It was



shown that the ordered microcrystalline domains are embedded in the amorphous polymer matrix in an anisotropic manner. Two different orientation of the microcrystalline P3HT, with respect to the substrate, were identified by the high resolution constant grazing angle XRD measurement for in and out of plane scattering geometry. The in-plane orientation of the crystallites is related to the lamellar layer structure and the out of plane orientation to the  $\pi - \pi^*$  interchain stacking. Such large scale molecular orientation leads to increase the electronic conductivity of the polymer film in the direction of molecular orientation and also explains the absorption of electromagnetic waves in the direction of their polarization. Such structural studies have not been explored in case of PEDOT:PSS, however similar anisotropies are reported in the optical and electrical properties of PEDOT:PSS [42, 174, 175].

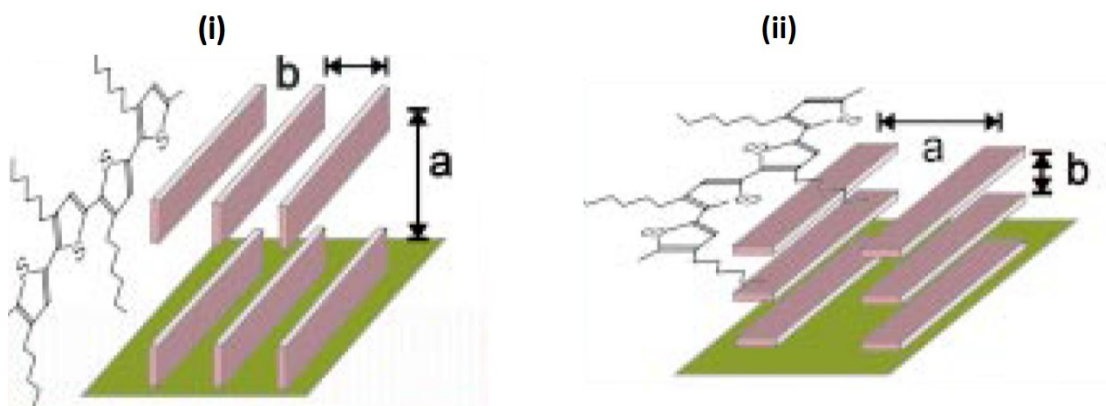


FIGURE 5.1: Schematic representation of the structural arrangement of thiophene molecules in P3HT polymer. (i) lamella oriented perpendicular to the substrate(ii) lamella oriented parallel to the substrate[173]

Orientation of the crystalline domains can be a cause for the optical and electrical anisotropy and the capacitive properties of a CP. However, another widely accepted theory for anisotropy in PEDOT:PSS films is the distribution of PEDOT particles in the PEDOT:PSS matrix at a mesoscopic length scale [174, 176, 177]. According to Nardes *et al.* [174] in the in-plane direction of PEDOT:PSS film the PEDOT rich lamella are separated by a very thin barrier of PSS lamella, providing a higher mobility to the charge carriers in comparison to the direction normal to film, where is a thick PSS barrier between the PEDOT rich lamella (fig. 5.2).

Therefore, regardless of the orientation of the crystallites domains, such systems will be optically and electrically anisotropic.

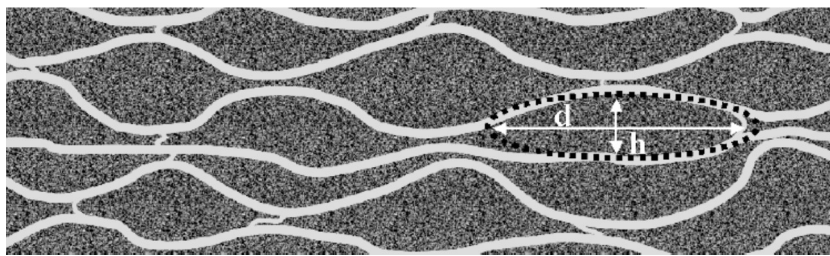


FIGURE 5.2: Sketch of the cross section morphology of a PEDOT:PSS film. The PEDOT rich clusters (dark) are separated by PSS lamellae (light). Image reproduced from [174]

As explained in chapters 3 and 4 the mesoscopic anisotropic behaviour of PEDOT:PSS films can be modeled by variable range hopping mechanism [56]. However, this modelling does not take into account the molecular orientation of EDOT monomers. Therefore, in this chapter, X-ray reflectivity (XRR) and near edge X-ray fine structure (NEXAFS) studies are performed to examine the anisotropy of the conducting polymer PEDOT:PSS at a micromolecular level. While there are many characterization techniques to probe the molecular structuring of conjugated polymers, such as grazing angle X-ray diffraction studies [178], transmission electron microscopy [179], or polarized infrared spectroscopy [180], none of these techniques have the surface sensitivity to exclusively probe the first few nanometers of the thin film. Measuring the absorption of X-rays by the detection of current generated by Auger electrons at different polarizations, NEXAFS is able to achieve the surface sensitivity of  $\leq 3$  nm [181]. With this sensitivity one can exclusively probe the molecular orientation of thin agglomerates of PEDOT. Taking the NEXAFS spectra as a starting point for generating a model XRR spectra in p- and s- polarizations, and comparing them with by using the Fresnel's optical models, and comparing the modelled XRR spectra with the measured data, an attempt is made to understand whether the anisotropy in the given film could come from the preferential orientation of the thiophene molecules in the PEDOT oligomer.

## 5.1 Experimental

### 5.1.1 Sample preparation

PEDOT:PSS thin films were spin coated on Si/SiO<sub>2</sub> substrates, similar to the samples prepared for VASE experiment (see section 3.1). Samples of multiple thicknesses were produced by varying the spin speed and their thicknesses were measured by AFM. The corresponding thicknesses of samples with respect to the spin speed are tabulated in table 5.1. Dimethyl sulfoxide (DMSO) was added in two samples in order to explore its possible effect on the anisotropy.

TABLE 5.1: Samples prepared for XRR and NEXAFS measurements at varied spin speeds to obtain different thickness as measured by AFM.

Sample no.	Spin speed (RPM)	AFM Thickness (nm)	DMSO (%v/v)
1	7000	62	10
2	3000	120	0
3	3000	120	10

### 5.1.2 X-ray reflectivity and NEXAFS

Samples were clipped on the sample holder with screw clips. The top surface of the PEDOT:PSS film was brought in electrical contact with the sample holder with conducting tape. The samples were then loaded into the spectroscopy chamber of the BEAR beamline at the ELETTRA synchrotrone (Trieste, Italy). The samples were aligned with standard alignment procedure described in the BEAR manual [182].

The X-ray reflectivity (XRR) and near edge X-ray absorption fine structure (NEXAFS) spectra were recorded around the carbon K-edge energy range (270-320 eV) in s- and p- polarization of the electromagnetic waves. The measurements were performed at the energy resolution of 0.1 eV and grazing angle of 5°. Firstly, a dark current through the photodiode is measured, with the shutter of the X-Ray

emitter closed. The input intensity of the X-Rays is measured by bringing the photodiode at 180° alignment with the X-Ray emitter. No damage to the CP films was expected due to the incidence of soft X-rays as guided by the previous findings [168].

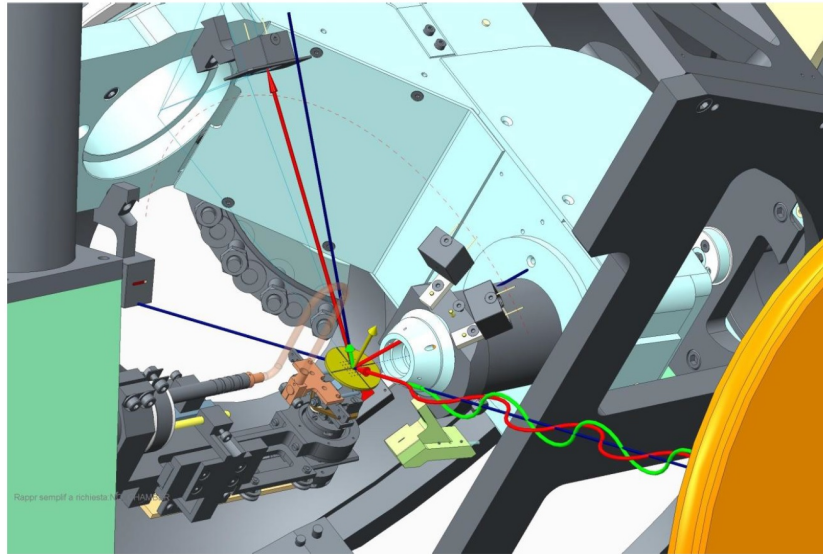


FIGURE 5.3: Schematic diagram of the X-ray reflectivity measurement, the beam of polarized X-ray is incident on the sample and the reflected beam is monitored by the photodiode detector inside the spectroscopy chamber. Image reproduced from [182]

The intensity of the reflected beam was measured by a Keithley 6517A ammeter as the photo-current generated in the photodiode (IRD SXUV-100). The NEXAFS signal was measured as the current that passed through from the PEDOT:PSS film to the sample holder, by another Keithley 6517A ammeter. This current is proportional to the yield of the of the Auger electrons excited through absorption of the polarized X-rays.

The X-ray reflectivity of PEDOT:PSS sample is calculated using the equation below:

$$XRR = \frac{I_R - I_{dark}}{I_{in} - I_{dark}} \quad (5.1)$$

where  $XRR$  is X-ray reflectivity of the sample,  $I_R$  is the intensity of the as reflected X-ray beam,  $I_{dark}$  is the intensity of the dark current detected at the photodiode and  $I_{in}$  is the intensity of the incoming X-ray beam.

The X-ray absorption spectroscopy (XAS) signal measured in NEXAFS is normalized in a similar manner as described above.

$$XAS = \frac{I_A - I_{dark}}{I_{in} - I_{dark}} \quad (5.2)$$

where  $XAS$  is normalized NEXAFS signal,  $I_A$  is the intensity of the current generated by the Auger electrons.

Fresnel's equations were used to model the reflectivities of the PEDOT:PSS films in the energy range of 270 eV-320 eV, by using the measured XAS absorption coefficient as the imaginary part of the dielectric function. For this, it was necessary to calculate the absorption coefficient (in units of the refractive index) from the normalized XAS signal, which is described in the next section. The optical model used was Si/SiO<sub>2</sub>/PEDOT:PSS/Air and the EP4 model software from Accurion GmbH (supplied with the Accurion Ep4 ellipsometer) was used to model the reflectivities. The refractive index dispersion of Si and SiO<sub>2</sub> were obtained from the Henke database [183].

## 5.2 Results and discussion

Normalized X-ray absorption spectrum (XAS) curves obtained from the NEXAFS measurements are presented in fig. 5.4. The curves obtained from p- and s- polarization incidence are presented separately as indicated in the figure captions. Both p- and s- polarization curves present similar features, specially at the dominant structure between 280-285 eV. A slight parallel shift between the p- and -s polarized XAS shall not be considered as an effect of anisotropy, as the XAS signal is presented in arbitrary units and therefore this shift can probably be attributed to the minor errors in the normalization processing of the data.

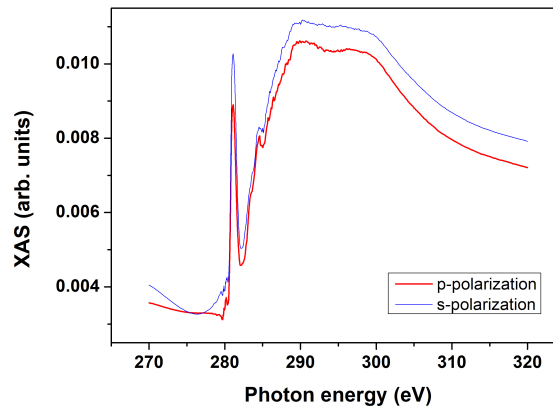


FIGURE 5.4: The normalized XAS spectrum, measured for both p and s polarization, around the C1s edge of the 120nm thick PEDOT:PSS + 10% DMSO film.

The normalised XAS signal is closely related to the absorptivity of the PEDOT:PSS film and hence to the extinction coefficient of the film. However, the so far presented normalized XAS signal is in arbitrary units and shall be rescaled to obtain the values of the extinction coefficient at the unit scale of the refractive index. This was done by first calculating the molecular (EDOT:SS) extinction coefficient from the atomic scattering cross sections according to the molecular formula. The latter were taken from the tables by Henke [184]. The extinction coefficient for the whole film was calculated from the molecular coefficient by taking into account the density of the film as  $1.4 \text{ g/cm}^3$  [185]. The real part of the refractive index is calculated by using Kramers Kronig transformations. The detailed procedure for another example of a film compound (PTDCA) can be found in appendix A of reference [186]. The complex refractive index dispersion calculated from the XAS data for p- and s- polarization in the energy range of 270-320 eV, is presented in fig. 5.5. <sup>1</sup> It can be noticed that the refractive indices extracted from the XAS measured from p- and s- incident EM wave almost coincide with each

<sup>1</sup> This work was done in collaboration with Dr. Luca Pasquali, Professore Associato di Fisica Sperimentale, Dipartimento di Ingegneria 'Enzo Ferrari', Universita' di Modena e Reggio Emilia Via Vivarelli 10 - 41125 Modena (ITALY).

The transformation from the raw data (measured at the BEAR beamline, ELETTRA) which includes the calculation of the: normalized XAS, normalized XRR, conversion of normalised XAS to absorption coefficient and the kramer Kroenig transformation were done by a program written by Dr. Luca Pasquali in the "Igor" data analysis software.

other, indicating an absence of anisotropy in the orientation of ethylenedioxythiophene or styrenesulfonate monomers in the PEDOT:PSS film under study. The same observation was found as valid for the other samples mentioned in table 5.1, *i.e.* the addition of DMSO had no effects on the orientational organization of the molecular subconstituents.

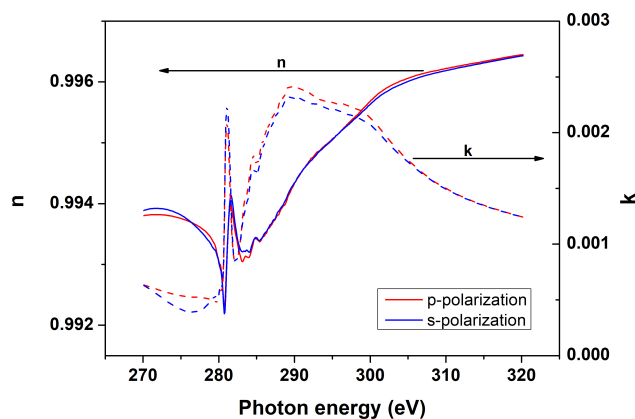


FIGURE 5.5: The complex refractive index dispersion, for both p- and s- polarizations, calculated from the measured XAS data in the C1s edge energy range. The imaginary part ( $k$ ) of the refractive index is calculated from scaling the XAS signal to the molecular (EDOT:SS) scattering cross sections values, whereas the real part ( $n$ ) is calculated using the Kramers-Kronig transformations.

In order to confirm the data processing routine and the extraction of the refractive indices, Fresnel's equations for an isotropic medium were used for modelling XRR (cf. eq. 2.24, 2.25). The thickness of the film was fitted, and a very good accordance of the fitted values with those from table 5.1 were obtained.

Fig. 5.6 and 5.7 shows the comparison between the measured XRR to the one modeled using Fresnel's equations. The model spectrum of both p- and s- reflectivities shows slight shift in energy by ca 1 eV compared to the measured XRR signal, in particular around the prominent C1s peak between 280-285 eV. The C K-edge peaks for various thiophene based molecules reported by Watts *et al.* show a even higher shift (2-3 eV) compared to the peaks described by the Fresnel's model shown above. Nevertheless, the model correctly reproduces all the spectral features expected at the C K-edge of the sample.

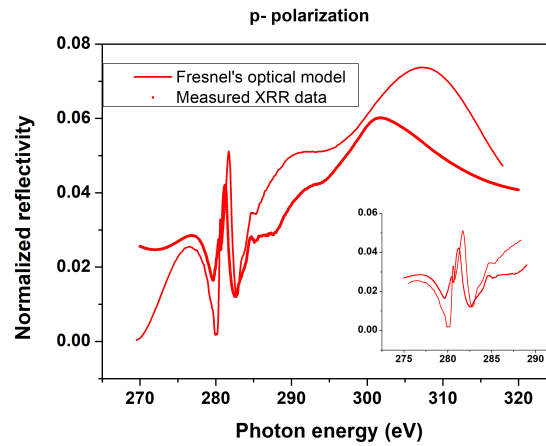


FIGURE 5.6: Measured(dots/thick line) and modeled (solid thin line) XRR signal for p polarization. The model curve was obtained using Fresnel's equations by using the calculated refractive index as shown in fig.5.5.

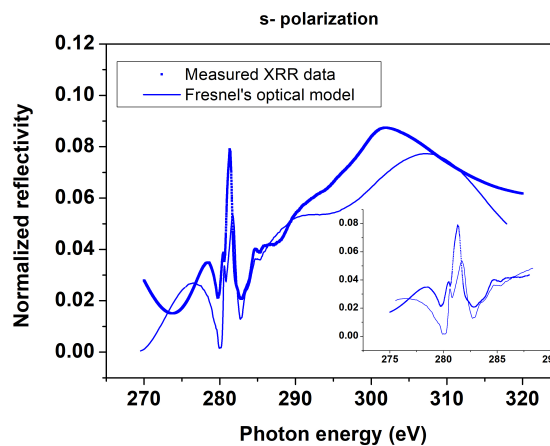


FIGURE 5.7: Measured(dots/thick line) and modeled (solid thin line) XRR signal for s polarization. The model curve was obtained using Fresnel's equations by using the calculated refractive index as shown in fig.5.5.

The source of the discrepancy is not clear and remains an open question, however, a possible explanation could be the mechanical movements of the chamber and the optical components within it, which affect the flux vs energy behaviour of the beamline [187]. Although, a scaling to a standard measurement process is applied to sort this discrepancy in the data analysis, it might be possible that some errors still exist and are the cause of this blue shift.



### 5.3 Summary and conclusions

The X ray resonant reflectivity and Near edge X-Ray absorption fine structure measurements are a useful tool to study the complex structures of conducting polymers. In this chapter, the X-ray reflectivity and absorption in p- and s-polarization of the incident radiation were studied using the BEAR beamline at the ELETTRA synchrotrone facility. In the XAS and XRR spectra, no significant difference was observed between the p- and s-polarizations. The complex refractive index dispersions extracted from the NEXAFS spectra by applying the Kramers-Kronig transformation, for p- and s- polarizations, were found to almost coincide with each other. The refractive index was used to model the reflectivity of the studied films, which showed a very good accordance with the measured XRR spectra. Some discrepancies between the energy of absorption and the maximum reflectivity in the immediate proximity of the C1s edge are observable, which could be caused by the misalignment of the optics in the chamber

In conclusion no effective anisotropy was found at the sub-molecular level in the PEDOT: PSS films, both in presence and absence of DMSO, which was not found to influence the XRR and NEXAFS spectra. Therefore, it can be said that the anisotropy that was detected in other reports and in the spectroscopic ellipsometry measurements presented in previous chapters of this thesis, originates exclusively from the organization of the PEDOT- and PSS- rich domains at the mesoscopic length scale.

# Chapter 6

## Conclusions

The variable angle spectroscopic ellipsometry (VASE) technique was used to characterize the dielectric properties of dry PEDOT:PSS films spin-coated from an aqueous solution containing DMSO as co-solvent and (3-glycidoxypropyl)trimethoxysilane (GOPS) as cross-linker. An anisotropic Tauc-Lorentz-Drude model was used to fit the measured ellipsometric data. The primary transition energy obtained from the fit was 1.77 eV, and the value of conductivity calculated from the Drude parameters was 258.6 S/cm. The conductivity values were found to be in a good match with the electrical conductivity values calculated using the Van-der-Pauw method. The measurements were extended to electrochemical variable angle spectroscopic ellipsometry (EVASE) technique for *in-situ* measurements. It was found that upon exposure to the aqueous electrolyte, the film undergoes a ca 20 % thickness increase, caused by swelling. The latter is accompanied by a change in the oxidation state and consequently a change in the dielectric function is observed in both the ordinary and extraordinary dielectric functions. Cyclic voltammetry is performed on the PEDOT:PSS films, which reveals the capacitive, oxidative and reductive voltage regimes of the experiment. EVASE measurements performed at multiple voltages, in all three regimes, revealed that in the charge separation regime the conductivity can be modulated by the capacitive field effect caused by the formation of capacitive double layer at the electrolyte-PEDOT:PSS (bulk) interface and in the redox regime PEDOT:PSS can be doped/de-doped to change

the carrier concentration and hence change its conductivity. Electrochemical impedance spectroscopy (EIS) measurements confirmed the results obtained from EVASE measurements, indicating a supercapacitive behaviour of PEDOT:PSS in the entire potential range and an electronic charge transfer behaviour in the values above  $\approx +0.2$  V and below  $\approx -0.2$  V vs. Ag/AgCl.

The OECT devices fabricated using UV photolithography technique were characterized using a similar procedure. Electrical and ellipsometric characterization of the PEDOT:PSS channel was found to be in good agreement in terms of the value of conductivity. The conductivity of dry PEDOT:PSS channel was found to be  $190.2 \text{ Scm}^{-1}$  and  $205.4 \text{ Scm}^{-1}$  from ellipsometric and electrical measurements respectively. For the channel immersed in 0.1 M KCl electrolyte, however, the conductivity value dropped to  $96.7 \text{ Scm}^{-1}$  and  $82.6 \text{ Scm}^{-1}$  for ellipsometric and electrical measurements respectively. This drop in conductivity is to be linked with the spontaneous reduction of PEDOT when brought in chemical equilibrium with the electrolyte. The EVASE measurements performed on the PEDOT:PSS devices also show the presence of capacitive and redox regimes in OECT devices. Further characterization performed by standard electrical characterization techniques for devices revealed that at the application of a gate voltage, the OECT could be switched from ON to OFF state by the application of a minimal electrochemical bias ( $\leq 0.6\text{V}$ ). A transconductance of  $0.8 \mu\text{S}/\text{cm}$  was measured from the transfer characteristic curve of the device. While the transconductance is high for the given length of the channel, it is not as good as reported for devices for shorter channel lengths. Therefore, the device performance could be improved by using shorter channel lengths.

For both spin coated PEDOT:PSS films (larger films on substrates with no device architecture) and OECT PEDOT:PSS channels, the dielectric function, and by extension the DC conductivity of PEDOT:PSS was found to be uniaxially anisotropic from ellipsometric measurements. It was investigated if the origin of this anisotropy can be due to molecular orientation of EDOT monomers (thiophene rings). X-ray reflectivity (XRR) and near edge X-Ray absorption fine structure (NEXAFS) measurements were performed at the Carbon K-edge (270-320 eV)

energy range, in both p- and s- polarization of the incident X-ray beam. No significant difference in the absorption (NEXAFS) and reflection (XRR) spectra obtained from the p- and s- polarized incident X-ray was found. The measured NEXAFS spectra in both polarizations was used to extract the complex refractive index of the PEDOT:PSS film. The refractive indices obtained from the p- and s- polarizations of the incident beam was found to nearly coincide with each other, indicating an isotropic orientation of the thiophene rings in the PEDOT:PSS film. This refractive index is then used to model the reflectivities using Fresnel's optical modelling for an isotropic medium. The fitted thickness of the PEDOT:PSS film from the Fresnel's model was found to be in close agreement with the thickness measured using AFM. The isotropic model reflectivities were compared with the measured XRR spectra and a good match was observed, confirming the isotropic behaviour of the crystalline constituents of the PEDOT:PSS film. This indicates that the origin of anisotropy in the uniaxially anisotropic PEDOT:PSS films could be at a mesoscopic or macromolecular level.

In conclusion, the VASE and EVASE measurements revealed that the optoelectronic properties of the PEDOT:PSS films are uniaxially anisotropic, which shall be taken into account for the design of electronic devices utilizing PEDOT:PSS. The swelling of the CP film changes its dielectric function and thus its electronic properties, which was so far neglected in the standard electrical characterization and modelling of devices. Therefore, the characterization of the organic electrochemical transistors must be performed *in-situ*, such that both electrical and electrochemical elements of the device can be taken into account. The proposed EVASE technique for characterizing OECT devices can be used as a benchmark in the field of organic electrochemical transistor devices.

# Bibliography

- [1] C. K. Chiang, C. R. Fincher, Y. W. Park, A. J. Heeger, H. Shirakawa, E. J. Louis, S. C. Gau, and Alan G. MacDiarmid. Electrical conductivity in doped polyacetylene. *Phys. Rev. Lett.*, 39:1098–1101, Oct 1977. doi: 10.1103/PhysRevLett.39.1098. URL <https://link.aps.org/doi/10.1103/PhysRevLett.39.1098>.
- [2] Hideki Shirakawa, Edwin J. Louis, Alan G. MacDiarmid, Chwan K. Chiang, and Alan J. Heeger. Synthesis of electrically conducting organic polymers: halogen derivatives of polyacetylene, (ch). *J. Chem. Soc., Chem. Commun.*, pages 578–580, 1977. doi: 10.1039/C39770000578. URL <http://dx.doi.org/10.1039/C39770000578>.
- [3] J. Foroughi, S. R. Ghorbani, G. Peleckis, G. M. Spinks, G. G. Wallace, X. L. Wang, and S. X. Dou. The mechanical and the electrical properties of conducting polypyrrole fibers. *Journal of Applied Physics*, 107(10):103712, 2010. doi: 10.1063/1.3425793. URL <https://aip.scitation.org/doi/abs/10.1063/1.3425793>.
- [4] G. Gustafsson, Y. Cao, G. M. Treacy, F. Klavetter, N. Colaneri, and A. J. Heeger. Flexible light-emitting diodes made from soluble conducting polymers. *Nature*, 357:477, 1992. doi: 10.1038/357477a0. URL <http://dx.doi.org/10.1038/357477a0>.
- [5] Nanda Gopal Sahoo, Yong Chae Jung, Hye Jin Yoo, and Jae Whan Cho. Influence of carbon nanotubes and polypyrrole on the thermal, mechanical and electroactive shape-memory properties of polyurethane nanocomposites.

- Composites Science and Technology*, 67(9):1920–1929, 2007. ISSN 0266-3538. doi: <https://doi.org/10.1016/j.compscitech.2006.10.013>. URL <http://www.sciencedirect.com/science/article/pii/S0266353806003927>.
- [6] Gang Li, Vishal Shrotriya, Jinsong Huang, Yan Yao, Tom Moriarty, Keith Emery, and Yang Yang. High-efficiency solution processable polymer photovoltaic cells by self-organization of polymer blends. *Nature Materials*, 4: 864, 2005. doi: 10.1038/nmat1500. URL <http://dx.doi.org/10.1038/nmat1500>.
- [7] Suchanun Mounghai, Nikhila Mahadevapuram, Paul Ruchhoeft, and Gila E. Stein. Direct patterning of conductive polymer domains for photovoltaic devices. *ACS Applied Materials Interfaces*, 4(8):4015–4023, 2012. ISSN 1944-8244. doi: 10.1021/am3008328. URL <https://doi.org/10.1021/am3008328>.
- [8] Jonathan Rivnay, Sahika Inal, Brian A. Collins, Michele Sessolo, Eleni Stavrinidou, Xenofon Strakosas, Christopher Tassone, Dean M. De-longchamp, and George G. Malliaras. Structural control of mixed ionic and electronic transport in conducting polymers. *Nature Communications*, 7: 11287, 2016. doi: 10.1038/ncomms11287. URL <https://www.nature.com/articles/ncomms11287#supplementary-information>. URL <http://dx.doi.org/10.1038/ncomms11287>.
- [9] P. N. Bartlett and P. R. Birkin. The application of conducting polymers in biosensors. *Synthetic Metals*, 61(1):15–21, 1993. ISSN 0379-6779. doi: [https://doi.org/10.1016/0379-6779\(93\)91194-7](https://doi.org/10.1016/0379-6779(93)91194-7). URL <http://www.sciencedirect.com/science/article/pii/0379677993911947>.
- [10] Patrick R. Unwin and Allen J. Bard. Scanning electrochemical microscopy. 14. scanning electrochemical microscope induced desorption: a new technique for the measurement of adsorption/desorption kinetics and surface diffusion rates at the solid/liquid interface. *The Journal of Physical Chemistry*, 96(12):5035–5045, 1992. ISSN 0022-3654. doi: 10.1021/j100191a055. URL <https://doi.org/10.1021/j100191a055>.

- [11] A. Kros, R. J. M. Nolte, and N. A. J. M. Sommerdijk. Conducting polymers with confined dimensions: Track-etch membranes for amperometric biosensor applications. *Advanced Materials*, 14(23):1779–1782, 2002. ISSN 0935-9648. doi: 10.1002/1521-4095(20021203)14:23<1779::AID-ADMA1779>3.0.CO;2-T. URL [https://doi.org/10.1002/1521-4095\(20021203\)14:23<1779::AID-ADMA1779>3.0.CO;2-T](https://doi.org/10.1002/1521-4095(20021203)14:23<1779::AID-ADMA1779>3.0.CO;2-T).
- [12] Serge Cosnier. Biomolecule immobilization on electrode surfaces by entrapment or attachment to electrochemically polymerized films. a review. *Biosensors and Bioelectronics*, 14(5):443–456, 1999. ISSN 0956-5663. doi: [https://doi.org/10.1016/S0956-5663\(99\)00024-X](https://doi.org/10.1016/S0956-5663(99)00024-X). URL <http://www.sciencedirect.com/science/article/pii/S095656639900024X>.
- [13] Hui Peng, Lijuan Zhang, Christian Soeller, and Jadranka Travas-Sejdic. Conducting polymers for electrochemical dna sensing. *Biomaterials*, 30(11):2132–2148, 2009. ISSN 0142-9612. doi: <https://doi.org/10.1016/j.biomaterials.2008.12.065>. URL <http://www.sciencedirect.com/science/article/pii/S0142961208010545>.
- [14] Elizabeth W. Paul, Antonio J. Ricco, and Mark S. Wrighton. Resistance of polyaniline films as a function of electrochemical potential and the fabrication of polyaniline-based microelectronic devices. *The Journal of Physical Chemistry*, 89(8):1441–1447, 1985. ISSN 0022-3654. doi: 10.1021/j100254a028. URL <https://doi.org/10.1021/j100254a028>.
- [15] Friedrich Jonas, Werner Krafft, and Bavo Muys. Poly(3, 4-ethylenedioxythiophene): Conductive coatings, technical applications and properties. *Macromolecular Symposia*, 100(1):169–173, 1995. ISSN 1022-1360. doi: 10.1002/masy.19951000128. URL <https://doi.org/10.1002/masy.19951000128>.
- [16] Zifei Wang, Jingkun Xu, Yuanyuan Yao, Long Zhang, Yangping Wen, Haijun Song, and Danhua Zhu. Facile preparation of highly water-stable and flexible pedot:pss organic/inorganic composite materials and their application in electrochemical sensors. *Sensors and Actuators B: Chemical*,

- 196:357–369, 2014. ISSN 0925-4005. doi: <https://doi.org/10.1016/j.snb.2014.02.035>. URL <http://www.sciencedirect.com/science/article/pii/S092540051400183X>.
- [17] Abdelmohsen Benoudjit, Mamoun M. Bader, and Wan Wardatul Amani Wan Salim. Study of electropolymerized pedot:pss transducers for application as electrochemical sensors in aqueous media. *Sensing and Bio-Sensing Research*, 17:18–24, 2018. ISSN 2214-1804. doi: <https://doi.org/10.1016/j.sbsr.2018.01.001>. URL <http://www.sciencedirect.com/science/article/pii/S2214180417301332>.
- [18] A. Elschner and S. Kirchmeyer. *PEDOT-type materials in organic solar cells*. In: *Organic Photovoltaics: Materials, Device Physics, and Manufacturing Technologies*, ed. C. Brabec, V. Dyakonov, and U. Scherf. Weinheim. Wiley-VCH., 2008.
- [19] Gerhard Heywang and Friedrich Jonas. Poly(alkylenedioxythiophene)s<sup>-</sup> new, very stable conducting polymers. *Advanced Materials*, 4(2):116–118, 1992. ISSN 0935-9648. doi: 10.1002/adma.19920040213. URL <https://doi.org/10.1002/adma.19920040213>.
- [20] Bettina Friedel, Panagiotis E. Keivanidis, Thomas J. K. Brenner, Agnese Abrusci, Christopher R. McNeill, Richard H. Friend, and Neil C. Greenham. Effects of layer thickness and annealing of pedot:pss layers in organic photodetectors. *Macromolecules*, 42(17):6741–6747, 2009. ISSN 0024-9297. doi: 10.1021/ma901182u. URL <https://doi.org/10.1021/ma901182u>.
- [21] Lorenz Bießmann, Lucas Philipp Kreuzer, Tobias Widmann, Nuri Hohn, Jean-François Moulin, and Peter Müller-Buschbaum. Monitoring the swelling behavior of pedot:pss electrodes under high humidity conditions. *ACS Applied Materials Interfaces*, 10(11):9865–9872, 2018. ISSN 1944-8244. doi: 10.1021/acsami.8b00446. URL <https://doi.org/10.1021/acsami.8b00446>.



- [22] Krishna C. Persaud. Polymers for chemical sensing. *Materials Today*, 8(4): 38–44, 2005. ISSN 1369-7021. doi: [https://doi.org/10.1016/S1369-7021\(05\)00793-5](https://doi.org/10.1016/S1369-7021(05)00793-5). URL <http://www.sciencedirect.com/science/article/pii/S1369702105007935>.
- [23] Leonardo Lizarraga, Estela Maria Andrade, and Fernando Victor Molina. Swelling and volume changes of polyaniline upon redox switching. *Journal of Electroanalytical Chemistry*, 561:127–135, 2004. ISSN 1572-6657. doi: <https://doi.org/10.1016/j.jelechem.2003.07.026>. URL <http://www.sciencedirect.com/science/article/pii/S0022072803004431>.
- [24] I. N. Hulea, H. B. Brom, A. J. Houtepen, D. Vanmaekelbergh, J. J. Kelly, and E. A. Meulenkaamp. Wide energy-window view on the density of states and hole mobility in poly(*p*-phenylene vinylene). *Phys. Rev. Lett.*, 93:166601, Oct 2004. doi: 10.1103/PhysRevLett.93.166601. URL <https://link.aps.org/doi/10.1103/PhysRevLett.93.166601>.
- [25] Jacob T. Friedlein, Sean E. Shaheen, George G. Malliaras, and Robert R. McLeod. Optical measurements revealing nonuniform hole mobility in organic electrochemical transistors. *Advanced Electronic Materials*, 1(11): 1500189, 2015. ISSN 2199-160X. doi: 10.1002/aelm.201500189. URL <https://doi.org/10.1002/aelm.201500189>.
- [26] Han-Saem Park, Seo-Jin Ko, Jeong-Seok Park, Jin Young Kim, and Hyun-Kon Song. Redox-active charge carriers of conducting polymers as a tuner of conductivity and its potential window. *Scientific Reports*, 3:2454, 2013. doi: 10.1038/srep02454 <https://www.nature.com/articles/srep02454#supplementary-information>. URL <http://dx.doi.org/10.1038/srep02454>.
- [27] T. F. Otero and J. M. Sansiñena. Artificial muscles based on conducting polymers. *Bioelectrochemistry and Bioenergetics*, 38(2):411–414, 1995. ISSN 0302-4598. doi: [https://doi.org/10.1016/0302-4598\(95\)01802-L](https://doi.org/10.1016/0302-4598(95)01802-L). URL <http://www.sciencedirect.com/science/article/pii/030245989501802L>.

- [28] Alan J. Heeger. Nobel lecture: Semiconducting and metallic polymers: The fourth generation of polymeric materials. *Rev. Mod. Phys.*, 73:681–700, Sep 2001. doi: 10.1103/RevModPhys.73.681. URL <https://link.aps.org/doi/10.1103/RevModPhys.73.681>.
- [29] Anton V. Volkov, Kosala Wijeratne, Evangelia Mitraka, Ujwala Ail, Dan Zhao, Klas Tybrandt, Jens Wenzel Andreasen, Magnus Berggren, Xavier Crispin, and Igor V. Zozoulenko. Understanding the capacitance of pedot:pss. *Advanced Functional Materials*, 27(28):1700329, 2017. doi: doi: 10.1002/adfm.201700329. URL <https://onlinelibrary.wiley.com/doi/abs/10.1002/adfm.201700329>.
- [30] Loïg Kergoat, Benoît Piro, Magnus Berggren, Gilles Horowitz, and Minh-Chau Pham. Advances in organic transistor-based biosensors: from organic electrochemical transistors to electrolyte-gated organic field-effect transistors. *Analytical and Bioanalytical Chemistry*, 402(5):1813–1826, 2012. ISSN 1618-2650. doi: 10.1007/s00216-011-5363-y. URL <https://doi.org/10.1007/s00216-011-5363-y>.
- [31] Se Hyun Kim, Kihyon Hong, Wei Xie, Keun Hyung Lee, Sipei Zhang, Timothy P. Lodge, and C. Daniel Frisbie. Electrolyte-gated transistors for organic and printed electronics. *Advanced Materials*, 25(13):1822–1846, 2012. ISSN 0935-9648. doi: 10.1002/adma.201202790. URL <https://doi.org/10.1002/adma.201202790>.
- [32] P. Damlin, C. Kvarnström, and A. Ivaska. Electrochemical synthesis and in situ spectroelectrochemical characterization of poly(3,4-ethylenedioxythiophene) (pedot) in room temperature ionic liquids. *Journal of Electroanalytical Chemistry*, 570(1):113–122, 2004. ISSN 1572-6657. doi: <https://doi.org/10.1016/j.jelechem.2004.03.023>. URL <http://www.sciencedirect.com/science/article/pii/S0022072804001780>.
- [33] J. Yamamoto and Y. Furukawa. Electronic and vibrational spectra of positive polarons and bipolarons in regioregular poly(3-hexylthiophene) doped

- with ferric chloride. *Journal of Physical Chemistry B*, 119(13):4788–4794, 2015. ISSN 1520-6106. doi: 10.1021/jp512654b. URL [GotoISI://WOS:000352329300025](https://doi.org/10.1021/jp512654b).
- [34] L. Groenendaal, G. Zotti, P. H. Aubert, S. M. Waybright, and J. R. Reynolds. Electrochemistry of poly(3,4-alkylenedioxythiophene) derivatives. *Advanced Materials*, 15(11):855–879, 2003. ISSN 1521-4095.
- [35] Jean Luc Bredas and G. Bryan Street. Polarons, bipolarons, and solitons in conducting polymers. *Accounts of Chemical Research*, 18(10):309–315, 1985. ISSN 0001-4842. doi: 10.1021/ar00118a005. URL <https://doi.org/10.1021/ar00118a005>.
- [36] C. Taliani, G. Ruani, R. Zamboni, A. Bolognesi, M. Catellani, S. Destri, W. Porzio, and P. Ostojia. Optical properties of a low energy gap conducting polymer: Polydithieno[3,4-b:,4-d]thiophene. *Synthetic Metals*, 28(1):507–514, 1989. ISSN 0379-6779. doi: [https://doi.org/10.1016/0379-6779\(89\)90566-3](https://doi.org/10.1016/0379-6779(89)90566-3). URL <http://www.sciencedirect.com/science/article/pii/0379677989905663>.
- [37] Uladzimir Zhokhavets, Gerhard Gobsch, Harald Hoppe, and Niyazi Serdar Sariciftci. A systematic study of the anisotropic optical properties of thin poly(3-octylthiophene)-films in dependence on growth parameters. *Thin Solid Films*, 451-452:69–73, 2004. ISSN 0040-6090. doi: <https://doi.org/10.1016/j.tsf.2003.11.042>. URL <http://www.sciencedirect.com/science/article/pii/S0040609003015839>.
- [38] T. J. Prosa, M. J. Winokur, Jeff Moulton, Paul Smith, and A. J. Heeger. X-ray structural studies of poly(3-alkylthiophenes): an example of an inverse comb. *Macromolecules*, 25(17):4364–4372, 1992. ISSN 0024-9297. doi: 10.1021/ma00043a019. URL <https://doi.org/10.1021/ma00043a019>.
- [39] M. Schubert, C. Bundesmann, G. Jakopic, H. Maresch, H. Arwin, N. C. Persson, F. Zhang, and O. Inganäs. Infrared ellipsometry characterization

- of conducting thin organic films. *Thin Solid Films*, 455-456:295–300, 5 2004. ISSN 0040-6090. doi: 10.1016/j.tsf.2003.11.194.
- [40] Jacek Gasiorowski, Kurt Hingerl, Reghu Menon, Thomas Plach, Helmut Neugebauer, Karin Wiesauer, Cigdem Yumusak, and Niyazi S. Sariçiftci. Dielectric function of undoped and doped poly[2-methoxy-5-(3,7-dimethyloctyloxy)-1,4-phenylene-vinylene] by ellipsometry in a wide spectral range. *The Journal of Physical Chemistry C*, 117(42):22010–22016, 2013. ISSN 1932-7447. doi: 10.1021/jp4061957. URL <https://doi.org/10.1021/jp4061957>.
- [41] Hans Arwin and Roger Jansson. Line-shape analysis of ellipsometric spectra on thin conducting polymer films. *Electrochimica Acta*, 39(2):211–215, 1994. ISSN 0013-4686. doi: [https://doi.org/10.1016/0013-4686\(94\)80056-1](https://doi.org/10.1016/0013-4686(94)80056-1). URL <http://www.sciencedirect.com/science/article/pii/S0013468694800561>.
- [42] Leif A. A. Pettersson, Fredrik Carlsson, Olle Inganäs, and Hans Arwin. Spectroscopic ellipsometry studies of the optical properties of doped poly(3, 4-ethylenedioxythiophene): an anisotropic metal. *Thin Solid Films*, 313 (Supplement C):356–361, 1998. ISSN 0040-6090. doi: [https://doi.org/10.1016/S0040-6090\(97\)00846-8](https://doi.org/10.1016/S0040-6090(97)00846-8).
- [43] A. Laskarakis, P. G. Karagiannidis, D. Georgiou, D. M. Nikolaidou, and S. Logothetidis. Optical investigations of the effect of solvent and thermal annealing on the optoelectronic properties of poly(3, 4-ethylenedioxythiophene): poly(styrenesulfonate) films. *Thin Solid Films*, 541(Supplement C):102–106, 2013. ISSN 0040-6090.
- [44] A. M. Nardes, M. Kemerink, R. A. J. Janssen, J. A. M. Bastiaansen, N. M. M. Kiggen, B. M. W. Langeveld, A. J. J. M. van Breemen, and M. M. de Kok. Microscopic understanding of the anisotropic conductivity of PEDOT:PSS thin films. *Advanced Materials*, 19(9):1196–1200, 2007. doi: [doi:10.1002/adma.200602575](https://doi.org/10.1002/adma.200602575). URL <https://onlinelibrary.wiley.com/doi/abs/10.1002/adma.200602575>.

- [45] Jun Liu, Jong-Beom Baek, and Liming Dai. *Conjugated Polymer Synthesis*, pages 1–7. Springer Berlin Heidelberg, Berlin, Heidelberg, 2021. ISBN 978-3-642-36199-9. doi: 10.1007/978-3-642-36199-9\_273-1. URL [https://doi.org/10.1007/978-3-642-36199-9\\_273-1](https://doi.org/10.1007/978-3-642-36199-9_273-1).
- [46] Johannes Thiele. Zur kenntniss der ungesättigten verbindungen. theorie der ungesättigten und aromatischen verbindungen. *Justus Liebigs Annalen der Chemie*, 306(1-2):87–142, 1899. ISSN 0075-4617. doi: 10.1002/jlac.18993060107. URL <https://doi.org/10.1002/jlac.18993060107>.
- [47] Terje A. Skotheim and John Reynolds. *Conjugated polymers: theory, synthesis, properties, and characterization*. 2006.
- [48] Charles Kittel. *Introduction to Solid State Physics*. John Wiley & Sons, Inc., New York, 6th edition, 1986.
- [49] Rudolf Ernst Peierls. More surprises in theoretical physics. *Princeton series in physics*, Princeton University Press, Princeton, N.J, 1991.
- [50] Miklos Kertesz, Cheol Ho Choi, and Shujiang Yang. Conjugated polymers and aromaticity. *Chemical Reviews*, 105(10):3448–3481, 2005. ISSN 0009-2665. doi: 10.1021/cr990357p. URL <https://doi.org/10.1021/cr990357p>.
- [51] W. R. Salaneck, R. H. Friend, and J. L. Brédas. Electronic structure of conjugated polymers: consequences of electron–lattice coupling. *Physics Reports*, 319(6):231–251, 1999. ISSN 0370-1573.
- [52] G. Harbeke, D. Baeriswyl, H. Kiess, and W. Kobel. Polarons and bipolarons in doped polythiophenes. *Physica Scripta*, 1986(T13):302, 1986. ISSN 1402-4896. URL <http://stacks.iop.org/1402-4896/1986/i=T13/a=049>.
- [53] A. J. Heeger, S. Kivelson, J. R. Schrieffer, and W. P. Su. Solitons in conducting polymers. *Rev. Mod. Phys.*, 60:781–850, Jul 1988. doi: 10.1103/RevModPhys.60.781. URL <https://link.aps.org/doi/10.1103/RevModPhys.60.781>.

- [54] J. L. Brédas, F. Wudl, and A. J. Heeger. Polarons and bipolarons in doped polythiophene: A theoretical investigation. *Solid State Communications*, 63(7):577–580, 1987. ISSN 0038-1098. doi: [https://doi.org/10.1016/0038-1098\(87\)90856-8](https://doi.org/10.1016/0038-1098(87)90856-8). URL <http://www.sciencedirect.com/science/article/pii/0038109887908568>.
- [55] J. Cornil, D. Beljonne, and J. L. Brédas. Nature of optical transitions in conjugated oligomers. I. theoretical characterization of neutral and doped oligo(phenylenevinylene)s. *The Journal of Chemical Physics*, 103(2):834–841, 1995. ISSN 0021-9606. doi: 10.1063/1.470116. URL <https://doi.org/10.1063/1.470116>.
- [56] N. F. Mott. Conduction in non-crystalline materials. *The Philosophical Magazine: A Journal of Theoretical Experimental and Applied Physics*, 19(160):835–852, 1969. ISSN 0031-8086. doi: 10.1080/14786436908216338. URL <https://doi.org/10.1080/14786436908216338>.
- [57] György Inzelt. Conducting polymers: A new era in electrochemistry. *Springer-Verlag Berlin Heidelberg*, 2012.
- [58] Alan G. MacDiarmid and Arthur J. Epstein. Secondary doping in polyaniline. *Synthetic Metals*, 69(1):85–92, 1995. ISSN 0379-6779. doi: [https://doi.org/10.1016/0379-6779\(94\)02374-8](https://doi.org/10.1016/0379-6779(94)02374-8). URL <http://www.sciencedirect.com/science/article/pii/0379677994023748>.
- [59] Nicolas Massonnet, Alexandre Carella, Arnaud de Geyer, Jérôme Faure-Vincent, and Jean-Pierre Simonato. Metallic behaviour of acid doped highly conductive polymers. *Chemical Science*, 6(1):412–417, 2015. ISSN 2041-6520. doi: 10.1039/C4SC02463J. URL <http://dx.doi.org/10.1039/C4SC02463J>.
- [60] Jianyong Ouyang. “secondary doping” methods to significantly enhance the conductivity of pedot:pss for its application as transparent electrode

- of optoelectronic devices. *Displays*, 34(5):423–436, 2013. ISSN 0141-9382. doi: <https://doi.org/10.1016/j.displa.2013.08.007>. URL <http://www.sciencedirect.com/science/article/pii/S0141938213000668>.
- [61] A. B. Kaiser. Electronic transport properties of conducting polymers and carbon nanotubes. *Reports on Progress in Physics*, 64(1):1, 2001. ISSN 0034-4885. URL <http://stacks.iop.org/0034-4885/64/i=1/a=201>.
- [62] A. J. Epstein, H. Rommelmann, R. Bigelow, H. W. Gibson, D. M. Hoffmann, and D. B. Tanner. Role of solitons in nearly metallic polyacetylene. *Phys. Rev. Lett.*, 50:1866–1869, Jun 1983. doi: 10.1103/PhysRevLett.50.1866. URL <https://link.aps.org/doi/10.1103/PhysRevLett.50.1866>.
- [63] C. K. Chiang, M. A. Druy, S. C. Gau, A. J. Heeger, E. J. Louis, A. G. MacDiarmid, Y. W. Park, and H. Shirakawa. Synthesis of highly conducting films of derivatives of polyacetylene, (ch)<sub>x</sub>. *Journal of the American Chemical Society*, 100(3):1013–1015, 1978. ISSN 0002-7863. doi: 10.1021/ja00471a081. URL <https://doi.org/10.1021/ja00471a081>.
- [64] Paul J. Nigrey, Alan G. MacDiarmid, and Alan J. Heeger. Electrochemistry of polyacetylene, (ch): electrochemical doping of (ch) films to the metallic state. *Journal of the Chemical Society, Chemical Communications*, (14): 594–595, 1979. ISSN 0022-4936. doi: 10.1039/C39790000594. URL <http://dx.doi.org/10.1039/C39790000594>.
- [65] J. H. Burroughes, D. D. C. Bradley, A. R. Brown, R. N. Marks, K. Mackay, R. H. Friend, P. L. Burns, and A. B. Holmes. Light-emitting diodes based on conjugated polymers. *Nature*, 347:539, 1990. doi: 10.1038/347539a0. URL <http://dx.doi.org/10.1038/347539a0>.
- [66] Akichika Kumatani, Yun Li, Peter Darmawan, Takeo Minari, and Kazuhito Tsukagoshi. On practical charge injection at the metal/organic semiconductor interface. *Scientific Reports*, 3:1026, 2013. doi: 10.1038/srep01026. URL <http://www.nature.com/articles/srep01026#supplementary-information>. URL <http://dx.doi.org/10.1038/srep01026>.

- [67] I. D. Parker. Carrier tunneling and device characteristics in polymer light-emitting diodes. *Journal of Applied Physics*, 75(3):1656–1666, 1994. ISSN 0021-8979. doi: 10.1063/1.356350. URL <https://doi.org/10.1063/1.356350>.
- [68] Tatsuhiro Horii, Hanae Hikawa, Masato Katsunuma, and Hidenori Okuzaki. Synthesis of highly conductive pedot:pss and correlation with hierarchical structure. *Polymer*, 140:33–38, 2018. ISSN 0032-3861. doi: <https://doi.org/10.1016/j.polymer.2018.02.034>. URL <http://www.sciencedirect.com/science/article/pii/S0032386118301587>.
- [69] Melda Sezen-Edmonds and Yueh-Lin Loo. Beyond doping and charge balancing: How polymer acid templates impact the properties of conducting polymer complexes. *The Journal of Physical Chemistry Letters*, 8(18):4530–4539, 2017. ISSN 1948-7185. doi: 10.1021/acs.jpcllett.7b01785. URL <https://doi.org/10.1021/acs.jpcllett.7b01785>.
- [70] Kirchmeyer S. Lovenich W. Merker U. Reuter K. Elschner, A. *PEDOT: Principles and Applications of an Intrinsically Conductive Polymers*, pages 69–70. CRC press, 2010. ISBN 9781420069129.
- [71] Tatsuhiro Horii, Yuechen Li, Yusaku Mori, and Hidenori Okuzaki. Correlation between the hierarchical structure and electrical conductivity of pedot/pss. *Polymer Journal*, 47:695, 2015. doi: 10.1038/pj.2015.48. URL <http://dx.doi.org/10.1038/pj.2015.48>.
- [72] Thomas Stöcker, Anna Köhler, and Ralf Moos. Why does the electrical conductivity in pedot:pss decrease with pss content? a study combining thermoelectric measurements with impedance spectroscopy. *Journal of Polymer Science Part B: Polymer Physics*, 50(14):976–983, 2012. ISSN 0887-6266. doi: 10.1002/polb.23089. URL <https://doi.org/10.1002/polb.23089>.
- [73] S. Timpanaro, M. Kemerink, F. J. Touwslager, M. M. De Kok, and S. Schrader. Morphology and conductivity of pedot/pss films studied



- by scanning-tunneling microscopy. *Chemical Physics Letters*, 394(4):339–343, 2004. ISSN 0009-2614. doi: <https://doi.org/10.1016/j.cplett.2004.07.035>. URL <http://www.sciencedirect.com/science/article/pii/S000926140401070X>.
- [74] Jonathan Rivnay, Sahika Inal, Alberto Salleo, Róisín M. Owens, Magnus Berggren, and George G. Malliaras. Organic electrochemical transistors. *Nature Reviews Materials*, 3:17086, 2018. doi: 10.1038/natrevmats.2017.86. URL <http://dx.doi.org/10.1038/natrevmats.2017.86>.
- [75] Dion Khodagholy, Jonathan Rivnay, Michele Sessolo, Moshe Gurfinkel, Pierre Leleux, Leslie H. Jimison, Eleni Stavriniidou, Thierry Herve, Sébastien Sanaur, Róisín M. Owens, and George G. Malliaras. High transconductance organic electrochemical transistors. *Nature Communications*, 4: 2133, 2013. doi: 10.1038/ncomms3133 <https://www.nature.com/articles/ncomms3133#supplementary-information>. URL <http://dx.doi.org/10.1038/ncomms3133>.
- [76] Matteo Ghittorelli, Leona Lingstedt, Paolo Romele, N. Irina Crăciun, Zsolt Miklós Kovács-Vajna, Paul W. M. Blom, and Fabrizio Torricelli. High-sensitivity ion detection at low voltages with current-driven organic electrochemical transistors. *Nature Communications*, 9(1):1441, 2018. ISSN 2041-1723. doi: 10.1038/s41467-018-03932-3. URL <https://doi.org/10.1038/s41467-018-03932-3>.
- [77] D. A Bernards and G. G Malliaras. Steady-state and transient behavior of organic electrochemical transistors. *Advanced Functional Materials*, 17(17): 3538–3544, 2007. ISSN 1616-301X. doi: 10.1002/adfm.200601239. URL <https://doi.org/10.1002/adfm.200601239>.
- [78] Christopher M. Proctor, Jonathan Rivnay, and George G. Malliaras. Understanding volumetric capacitance in conducting polymers. *Journal of Polymer Science Part B: Polymer Physics*, 54(15):1433–1436, 2016. ISSN 0887-6266. doi: 10.1002/polb.24038. URL <https://doi.org/10.1002/polb.24038>.

- [79] John David Jackson. *Classical electrodynamics*. Wiley, New York, NY, 3rd ed. edition, 1999. ISBN 9780471309321. URL <http://cdsweb.cern.ch/record/490457>.
- [80] David J Griffiths. *Introduction to electrodynamics; 4th ed.* Pearson, Boston, MA, 2013. URL <https://cds.cern.ch/record/1492149>. Re-published by Cambridge University Press in 2017.
- [81] Hiroyuki Fujiwara. *Spectroscopic ellipsometry: principles and applications*. John Wiley Sons, 2007. ISBN 0470060182.
- [82] R.M.A. Azzam and N.M. Bashara. *Ellipsometry and Polarized Light*, pages 75–80. North-Holland Personal Library, 1999. ISBN 0444870164.
- [83] R.M.A. Azzam and N.M. Bashara. *Ellipsometry and Polarized Light*, pages Ch4 269–360. North-Holland Personal Library, 1999. ISBN 0444870164.
- [84] P. Bergveld. Development of an ion-sensitive solid-state device for neurophysiological measurements. *IEEE Transactions on Biomedical Engineering*, BME-17(1):70–71, 1970. ISSN 0018-9294. doi: 10.1109/TBME.1970.4502688.
- [85] Henry S. White, Gregg P. Kittlesen, and Mark S. Wrighton. Chemical derivatization of an array of three gold microelectrodes with polypyrrole: fabrication of a molecule-based transistor. *Journal of the American Chemical Society*, 106(18):5375–5377, 1984. ISSN 0002-7863. doi: 10.1021/ja00330a070. URL <http://dx.doi.org/10.1021/ja00330a070>.
- [86] Martin Weisheit, Sebastian Fähler, Alain Marty, Yves Souche, Christiane Poinsignon, and Dominique Givord. Electric field-induced modification of magnetism in thin-film ferromagnets. *Science*, 315(5810):349, 2007. URL <http://science.sciencemag.org/content/315/5810/349.abstract>.
- [87] Per-Olof Svensson, David Nilsson, Robert Forchheimer, and Magnus Berggren. A sensor circuit using reference-based conductance switching in organic electrochemical transistors. *Applied Physics Letters*, 93(20):203301,

2008. doi: 10.1063/1.2975377. URL <http://aip.scitation.org/doi/abs/10.1063/1.2975377>.
- [88] Michele Sessolo, Jonathan Rivnay, Enrico Bandiello, George G. Malliaras, and Henk J. Bolink. Ion-selective organic electrochemical transistors. *Advanced Materials*, 26(28):4803–4807, 2014. ISSN 1521-4095. doi: 10.1002/adma.201400731. URL <http://dx.doi.org/10.1002/adma.201400731>.
- [89] Na Young Shim, Daniel A. Bernards, Daniel J. Macaya, John A. DeFranco, Maria Nikolou, Róisín M. Owens, and George G. Malliaras. All-plastic electrochemical transistor for glucose sensing using a ferrocene mediator. *Sensors (Basel, Switzerland)*, 9(12):9896–9902, 2009. ISSN 1424-8220. doi: 10.3390/s91209896. URL <http://www.ncbi.nlm.nih.gov/pmc/articles/PMC3267201/>.
- [90] M. J Panzer and C. D Frisbie. High carrier density and metallic conductivity in poly(3-hexylthiophene) achieved by electrostatic charge injection. *Advanced Functional Materials*, 16(8):1051–1056, 2006. ISSN 1616-301X. doi: 10.1002/adfm.200600111. URL <https://doi.org/10.1002/adfm.200600111>.
- [91] Jonathan D. Yuen, Anoop S. Dhoot, Ebinazar B. Namdas, Nelson E. Coates, Martin Heeney, Iain McCulloch, Daniel Moses, and Alan J. Heeger. Electrochemical doping in electrolyte-gated polymer transistors. *Journal of the American Chemical Society*, 129(46):14367–14371, 2007. ISSN 0002-7863. doi: 10.1021/ja0749845. URL <https://doi.org/10.1021/ja0749845>.
- [92] Anoop S. Dhoot, Jonathan D. Yuen, Martin Heeney, Iain McCulloch, Daniel Moses, and Alan J. Heeger. Beyond the metal-insulator transition in polymer electrolyte gated polymer field-effect transistors. *Proceedings of the National Academy of Sciences*, 103(32):11834–11837, 2006. doi: 10.1073/pnas.0605033103. URL <http://www.pnas.org/content/pnas/103/32/11834.full.pdf>.

- [93] Elias Said, Xavier Crispin, Lars Herlogsson, Sami Elhag, Nathaniel D. Robinson, and Magnus Berggren. Polymer field-effect transistor gated via a poly(styrenesulfonic acid) thin film. *Applied Physics Letters*, 89(14):143507, 2006. doi: 10.1063/1.2358315. URL <https://aip.scitation.org/doi/abs/10.1063/1.2358315>.
- [94] D. Tu, L. Herlogsson, L. Kergoat, X. Crispin, M. Berggren, and R. Forchheimer. A static model for electrolyte-gated organic field-effect transistors. *IEEE Transactions on Electron Devices*, 58(10):3574–3582, 2011. ISSN 0018-9383. doi: 10.1109/TED.2011.2162648.
- [95] Alan Graham MacDiarmid, R. J. Mammone, R. B. Kaner, Lord Porter, R. Pethig, A. J. Heeger, D. R. Rosseinsky, Ronald James Gillespie, and Peter Day. The concept of doping of conducting polymers: the role of reduction potentials. *Philosophical Transactions of the Royal Society of London. Series A, Mathematical and Physical Sciences*, 314(1528):3–15, 1985. doi: doi:10.1098/rsta.1985.0004. URL <https://royalsocietypublishing.org/doi/abs/10.1098/rsta.1985.0004>.
- [96] Varun Vohra and Takuya Anzai. Molecular orientation of conjugated polymer chains in nanostructures and thin films: Review of processes and application to optoelectronics. *Journal of Nanomaterials*, 2017:18, 2017. doi: 10.1155/2017/3624750. URL <https://doi.org/10.1155/2017/3624750>.
- [97] Yuta Mochizuki, Tatsuhiko Horii, and Hidenori Okuzaki. Effect of ph on structure and conductivity of pedot/pss. *Transactions of the Materials Research Society of Japan*, 37(2):307–310, 2012. doi: 10.14723/tmrj.37.307.
- [98] L. J. van der Pauw. A method of measuring the resistivity and hall coefficient on lamellae of arbitrary shape. *Philips Technical Review*, 20(8):220–224, 1958.

- [99] Hiroyuki Fujiwara and Michio Kondo. Effects of carrier concentration on the dielectric function of  $\text{ZnO:Ga}$  and  $\text{In}_2\text{O}_3:\text{Sn}$  studied by spectroscopic ellipsometry: Analysis of free-carrier and band-edge absorption. *Physical Review B*, 71(7):075109, 2005.
- [100] A. S. Ferlauto, G. M. Ferreira, Joshua M. Pearce, C. R. Wronski, R. W. Collins, Xunming Deng, and Gautam Ganguly. Analytical model for the optical functions of amorphous semiconductors from the near-infrared to ultraviolet: Applications in thin film photovoltaics. *Journal of Applied Physics*, 92(5):2424–2436, 2002. ISSN 0021-8979.
- [101] Peter Y. Yu and Manuel Cardona. *Fundamentals of semiconductors: physics and materials properties*. Springer-Verlag Berlin Heidelberg, 2010. ISBN 978-3-642-00710-1. doi: <https://doi.org/10.1007/978-3-642-00710-1>.
- [102] A. Laskarakis, P. G. Karagiannidis, D. Georgiou, D. M. Nikolaidou, and S. Logothetidis. Optical investigations of the effect of solvent and thermal annealing on the optoelectronic properties of poly (3, 4-ethylenedioxythiophene): poly (styrenesulfonate) films. *Thin Solid Films*, 541(Supplement C):102–106, 2013. ISSN 0040-6090.
- [103] Ting Ji, Licheng Tan, Xiaotian Hu, Yanfeng Dai, and Yiwang Chen. A comprehensive study of sulfonated carbon materials as conductive composites for polymer solar cells. *Physical Chemistry Chemical Physics*, 17(6):4137–4145, 2015. ISSN 1463-9076. doi: 10.1039/C4CP04965A. URL <http://dx.doi.org/10.1039/C4CP04965A>.
- [104] Changbong Yeon, Jin Yun Sun, Jumi Kim, and Wook Lim Jung. PEDOT:PSS films with greatly enhanced conductivity via nitric acid treatment at room temperature and their application as Pt/TCO-free counter electrodes in dye-sensitized solar cells. *Advanced Electronic Materials*, 1(10):1500121, 2015. ISSN 2199-160X. doi: 10.1002/aelm.201500121. URL <https://doi.org/10.1002/aelm.201500121>.

- [105] A. S. M. Iftexhar Uddin, Usman Yaqoob, and Gwi-y-Sang Chung. Improving the working efficiency of a triboelectric nanogenerator by the semimetallic pedot:pss hole transport layer and its application in self-powered active acetylene gas sensing. *ACS Applied Materials Interfaces*, 8(44):30079–30089, 2016. ISSN 1944-8244. doi: 10.1021/acsami.6b08002. URL <https://doi.org/10.1021/acsami.6b08002>.
- [106] R. Sirko and D. L. Mills. Infrared absorption in the drude tail of doped semiconductors: The effect of finite electron densities. *Phys. Rev. B*, 18:4373–4389, Oct 1978. doi: 10.1103/PhysRevB.18.4373. URL <https://link.aps.org/doi/10.1103/PhysRevB.18.4373>.
- [107] Allen J. Bard, Larry R. Faulkner, Johna Leddy, and Cynthia G. Zoski. *Electrochemical methods: fundamentals and applications*, volume 2. wiley New York, 1980.
- [108] Mary L. Rosenbluth and Nathan S. Lewis. "ideal" behavior of the open circuit voltage of semiconductor/liquid junctions. *The Journal of Physical Chemistry*, 93(9):3735–3740, 1989. ISSN 0022-3654. doi: 10.1021/j100346a072. URL <https://doi.org/10.1021/j100346a072>.
- [109] Masoud Baghernejad, Xiaotao Zhao, Kristian Baruël Ørnsø, Michael Füeg, Pavel Moreno-García, Alexander V. Rudnev, Veerabhadrarao Kaliginedi, Soma Vesztergom, Cancan Huang, Wenjing Hong, Peter Broekmann, Thomas Wandlowski, Kristian S. Thygesen, and Martin R. Bryce. Electrochemical control of single-molecule conductance by fermi-level tuning and conjugation switching. *Journal of the American Chemical Society*, 136(52):17922–17925, 2014. ISSN 0002-7863. doi: 10.1021/ja510335z. URL <https://doi.org/10.1021/ja510335z>.
- [110] R. H. Baughman and L. W. Shacklette. Conductivity as a function of conjugation length: Theory and experiment for conducting polymer complexes. *Phys. Rev. B*, 39:5872–5886, Mar 1989. doi: 10.1103/PhysRevB.39.5872. URL <https://link.aps.org/doi/10.1103/PhysRevB.39.5872>.

- [111] R. Cernini, X. C. Li, G. W. C. Spencer, A. B. Holmes, S. C. Moratti, and R. H. Friend. Electrochemical and optical studies of ppv derivatives and poly(aromatic oxadiazoles). *Synthetic Metals*, 84(1):359–360, 1997. ISSN 0379-6779. doi: [https://doi.org/10.1016/S0379-6779\(97\)80781-3](https://doi.org/10.1016/S0379-6779(97)80781-3). URL <http://www.sciencedirect.com/science/article/pii/S0379677997807813>.
- [112] Kenneth L. Hardee and Allen J. Bard. Semiconductor electrodes: X . photoelectrochemical behavior of several polycrystalline metal oxide electrodes in aqueous solutions. *Journal of The Electrochemical Society*, 124(2):215–224, 1977. doi: 10.1149/1.2133269. URL <http://jes.ecsdl.org/content/124/2/215.abstract>.
- [113] Harri J. Ahonen, Jukka Lukkari, and Jouko Kankare. n- and p-doped poly(3,4-ethylenedioxythiophene): two electronically conducting states of the polymer. *Macromolecules*, 33(18):6787–6793, 2000. ISSN 0024-9297. doi: 10.1021/ma0004312. URL <https://doi.org/10.1021/ma0004312>.
- [114] Payman Tehrani, Anna Kanciurzevska, Xavier Crispin, Nathaniel D. Robinson, Mats Fahlman, and Magnus Berggren. The effect of ph on the electrochemical over-oxidation in pedot:pss films. *Solid State Ionics*, 177(39):3521–3527, 2007. ISSN 0167-2738. doi: <https://doi.org/10.1016/j.ssi.2006.10.008>. URL <http://www.sciencedirect.com/science/article/pii/S0167273806005959>.
- [115] Alexander Giovannitti, Dan-Tiberiu Sbircea, Sahika Inal, Christian B. Nielsen, Enrico Bandiello, David A. Hanifi, Michele Sessolo, George G. Malliaras, Iain McCulloch, and Jonathan Rivnay. Controlling the mode of operation of organic transistors through side-chain engineering. *Proceedings of the National Academy of Sciences*, 113(43):12017–12022, 2016. doi: 10.1073/pnas.1608780113. URL <http://www.pnas.org/content/pnas/113/43/12017.full.pdf>.

- [116] Klas Tybrandt, Suresh Babu Kollipara, and Magnus Berggren. Organic electrochemical transistors for signal amplification in fast scan cyclic voltammetry. *Sensors and Actuators B: Chemical*, 195:651–656, 2014. ISSN 0925-4005. doi: <https://doi.org/10.1016/j.snb.2014.01.097>. URL <http://www.sciencedirect.com/science/article/pii/S0925400514001142>.
- [117] Christian B. Nielsen, Alexander Giovannitti, Dan-Tiberiu Sbircea, Enrico Bandiello, Muhammad R. Niazi, David A. Hanifi, Michele Sessolo, Aram Amassian, George G. Malliaras, Jonathan Rivnay, and Iain McCulloch. Molecular design of semiconducting polymers for high-performance organic electrochemical transistors. *Journal of the American Chemical Society*, 138(32):10252–10259, 2016. ISSN 0002-7863. doi: 10.1021/jacs.6b05280. URL <https://doi.org/10.1021/jacs.6b05280>.
- [118] George Malliaras and Richard Friend. An organic electronics primer. *Physics Today*, 58(5):53–58, 2005. doi: 10.1063/1.1995748. URL <http://physicstoday.scitation.org/doi/abs/10.1063/1.1995748>.
- [119] Fabio Cicoira, Michele Sessolo, Omid Yaghmazadeh, John A. DeFranco, Sang Yoon Yang, and George G. Malliaras. Influence of device geometry on sensor characteristics of planar organic electrochemical transistors. *Advanced Materials*, 22(9):1012–1016, 2010. ISSN 1521-4095. doi: 10.1002/adma.200902329. URL <http://dx.doi.org/10.1002/adma.200902329>.
- [120] J. M Leger. Organic electronics: The ions have it. *Advanced Materials*, 20(4):837–841, 2008. ISSN 1521-4095. doi: 10.1002/adma.200701874. URL <http://dx.doi.org/10.1002/adma.200701874>.
- [121] Jeffrey T. Mabeck, John A. DeFranco, Daniel A. Bernards, George G. Malliaras, Sandrine Hocdé, and Christopher J. Chase. Microfluidic gating of an organic electrochemical transistor. *Applied Physics Letters*, 87(1):013503, 2005. doi: 10.1063/1.1991979. URL <http://aip.scitation.org/doi/abs/10.1063/1.1991979>.



- [122] A Kumar and J Sinha. Electrochemical transistors for applications in chemical and biological sensing. in: Bernardis d.a., malliaras g.g., owens r.m. (eds) organic semiconductors in sensor applications. materials science. *Springer, Berlin, Heidelberg*, 102:245–261, 2008.
- [123] ] M. Berggren;A. Richter-Dahlfors. *Advance materials*, 19(320), 2007.
- [124] Benoît Piro, Giorgio Mattana, Samia Zrig, Guillaume Anquetin, Nicolas Battaglini, Dany Capitaio, Antoine Maurin, and Steeve Reisberg. Fabrication and use of organic electrochemical transistors for sensing of metabolites in aqueous media. *Applied Sciences*, 8(6), 2018. ISSN 2076-3417. doi: 10.3390/app8060928.
- [125] Yuedan Wang, Xing Qing, Quan Zhou, Yang Zhang, Qiongzhen Liu, Ke Liu, Wenwen Wang, Mufang Li, Zhentan Lu, Yuanli Chen, and Dong Wang. The woven fiber organic electrochemical transistors based on polypyrrole nanowires/reduced graphene oxide composites for glucose sensing. *Biosensors and Bioelectronics*, 95:138–145, 2017. ISSN 0956-5663. doi: <https://doi.org/10.1016/j.bios.2017.04.018>. URL <http://www.sciencedirect.com/science/article/pii/S0956566317302658>.
- [126] Yajie Yang, Shibin Li, Luning Zhang, Jianhua Xu, Wen Yao Yang, and Yadong Jiang. Vapor phase polymerization deposition of conducting polymer/graphene nanocomposites as high performance electrode materials. *ACS Applied Materials Interfaces*, 5(10):4350–4355, 2013. ISSN 1944-8244. doi: 10.1021/am4003815. URL <https://doi.org/10.1021/am4003815>.
- [127] Stephan Kirchmeyer and Knud Reuter. Scientific importance, properties and growing applications of poly(3,4-ethylenedioxythiophene). *Journal of Materials Chemistry*, 15(21):2077–2088, 2005. ISSN 0959-9428. doi: 10.1039/B417803N. URL <http://dx.doi.org/10.1039/B417803N>.

- [128] Shruti Badhwar and K. S. Narayan. Optimum design of organic electrochemical type transistors for applications in biochemical sensing. *Journal of Sensors*, 2008:5, 2008. doi: 10.1155/2008/702161. URL <http://dx.doi.org/10.1155/2008/702161>.
- [129] Jonathan Rivnay, Sahika Inal, Alberto Salleo, Róisín M. Owens, Magnus Berggren, and George G. Malliaras. Organic electrochemical transistors. *Nature Reviews Materials*, 3:17086, 2018. doi: 10.1038/natrevmats.2017.86. URL <http://dx.doi.org/10.1038/natrevmats.2017.86>.
- [130] Sahika Inal, Jonathan Rivnay, Pierre Leleux, Marc Ferro, Marc Ramuz, Johannes C. Brendel, Martina M. Schmidt, Mukundan Thelakkat, and George G. Malliaras. A high transconductance accumulation mode electrochemical transistor. *Advanced Materials*, 26(44):7450–7455, 2014. ISSN 0935-9648. doi: 10.1002/adma.201403150. URL <https://doi.org/10.1002/adma.201403150>.
- [131] Marcel Braendlein, Thomas Lonjaret, Pierre Leleux, Jean-Michel Badier, and George G. Malliaras. Voltage amplifier based on organic electrochemical transistor. *Advanced Science*, 4(1):1600247, 2017. ISSN 2198-3844. doi: 10.1002/advs.201600247. URL <http://www.ncbi.nlm.nih.gov/pmc/articles/PMC5238735/>.
- [132] J. L. Brédas. Relationship between band gap and bond length alternation in organic conjugated polymers. *The Journal of Chemical Physics*, 82(8):3808–3811, 1985. ISSN 0021-9606. doi: 10.1063/1.448868. URL <https://doi.org/10.1063/1.448868>.
- [133] Shiming Zhang, Prajwal Kumar, Amel Sarah Nouas, Laurie Fontaine, Hao Tang, and Fabio Cicoira. Solvent-induced changes in pedot:pss films for organic electrochemical transistors. *APL Materials*, 3(1):014911, 2015. doi: 10.1063/1.4905154. URL <https://aip.scitation.org/doi/abs/10.1063/1.4905154>.

- [134] Sung Won Park, Tae Hwan Oh, Jun Sung Hwang, and Young Jae Lee. Effect of solvent and blended polymer on electrical conductivity of pedot:pss/polymer blended nanofibers. *Fibers and Polymers*, 17(8):1171–1174, 2016. ISSN 1875-0052. doi: 10.1007/s12221-016-6468-x. URL <https://doi.org/10.1007/s12221-016-6468-x>.
- [135] Jacek Gasiorowski, Reghu Menon, Kurt Hingerl, Marko Dachev, and Niyazi Serdar Sariciftci. Surface morphology, optical properties and conductivity changes of poly(3,4-ethylenedioxythiophene):poly(styrenesulfonate) by using additives. *Thin Solid Films*, 536:211–215, 2013. ISSN 0040-6090. doi: <https://doi.org/10.1016/j.tsf.2013.03.124>. URL <http://www.sciencedirect.com/science/article/pii/S0040609013005841>.
- [136] Bin Dong, Nan Lu, Marc Zelsmann, Nikolaos Kehagias, Harald Fuchs, Sotomayor Torres, and L. F. Chi. Fabrication of high-density, large-area conducting-polymer nanostructures. *Advanced Functional Materials*, 16(15):1937–1942, 2006. ISSN 1616-3028.
- [137] Gaurav Pathak, Zofia Krasnińska-Krawet, Lilianna Szyk-Warszyńska, and Duško Čakara. Doping of poly(3,4-ethylenedioxythiophene):poly(styrenesulfonate) films studied by means of electrochemical variable angle spectroscopic ellipsometry. *Thin Solid Films*, 651:31–38, 2018. ISSN 0040-6090. doi: <https://doi.org/10.1016/j.tsf.2018.01.049>. URL <http://www.sciencedirect.com/science/article/pii/S0040609018300658>.
- [138] Liangqi Ouyang, Chiara Musumeci, Mohammad J. Jafari, Thomas Ederth, and Olle Inganäs. Imaging the phase separation between pedot and polyelectrolytes during processing of highly conductive pedot:pss films. *ACS Applied Materials Interfaces*, 7(35):19764–19773, 2015. ISSN 1944-8244. doi: 10.1021/acsami.5b05439. URL <https://doi.org/10.1021/acsami.5b05439>.

- [139] J. Ouyang, C.-W. Chu, F.-C. Chen, Q. Xu, and Y. Yang. High-conductivity poly(3,4-ethylenedioxythiophene):poly(styrene sulfonate) film and its application in polymer optoelectronic devices. *Advanced Functional Materials*, 15(2):203–208, 2005. doi: doi:10.1002/adfm.200400016. URL <https://onlinelibrary.wiley.com/doi/abs/10.1002/adfm.200400016>.
- [140] A. Dkhissi, F. Louwet, L. Groenendaal, D. Beljonne, R. Lazzaroni, and J. L. Brédas. Theoretical investigation of the nature of the ground state in the low-bandgap conjugated polymer, poly(3,4-ethylenedioxythiophene). *Chemical Physics Letters*, 359(5):466–472, 2002. ISSN 0009-2614. doi: [https://doi.org/10.1016/S0009-2614\(02\)00651-6](https://doi.org/10.1016/S0009-2614(02)00651-6). URL <http://www.sciencedirect.com/science/article/pii/S0009261402006516>.
- [141] Annika Lenz, Hans Kariis, Anna Pohl, Petter Persson, and Lars Ojamäe. The electronic structure and reflectivity of pedot:pss from density functional theory. *Chemical Physics*, 384(1):44–51, 2011. ISSN 0301-0104. doi: <https://doi.org/10.1016/j.chemphys.2011.05.003>. URL <http://www.sciencedirect.com/science/article/pii/S0301010411001571>.
- [142] Ouyang J., Chu C.-W., Chen F.-C., Xu Q., and Yang Y. High-conductivity poly(3,4-ethylenedioxythiophene):poly(styrene sulfonate) film and its application in polymer optoelectronic devices. *Advanced Functional Materials*, 15(2):203–208, 2005. doi: doi:10.1002/adfm.200400016. URL <https://onlinelibrary.wiley.com/doi/abs/10.1002/adfm.200400016>.
- [143] S. Garreau, J. L. Duvail, and G. Louarn. Spectroelectrochemical studies of poly(3,4-ethylenedioxythiophene) in aqueous medium. *Synthetic Metals*, 125(3):325–329, 2001. ISSN 0379-6779. doi: [https://doi.org/10.1016/S0379-6779\(01\)00397-6](https://doi.org/10.1016/S0379-6779(01)00397-6). URL <http://www.sciencedirect.com/science/article/pii/S0379677901003976>.
- [144] Naiwei Gao, Xinyue Zhang, Shenglong Liao, Hanyu Jia, and Yapei Wang. Polymer swelling induced conductive wrinkles for an ultrasensitive pressure sensor. *ACS Macro Letters*, 5(7):823–827, 2016. doi: 10.1021/acsmacrolett.6b00338. URL <https://doi.org/10.1021/acsmacrolett.6b00338>.

- [145] M. P. Eastman, R. C. Hughes, G. Yelton, A. J. Ricco, S. V. Patel, and M. W. Jenkins. Application of the solubility parameter concept to the design of chemiresistor arrays. *Journal of The Electrochemical Society*, 146(10): 3907–3913, 1999. doi: 10.1149/1.1392571. URL <http://jes.ecsdl.org/content/146/10/3907.abstract>.
- [146] ElMahmoudy Mohammed, Inal Sahika, Charrier Anne, Uguz Ilke, Malliaras George G., and Sanaur Sébastien. Tailoring the electrochemical and mechanical properties of pedot:pss films for bioelectronics. *Macromolecular Materials and Engineering*, 302(5):1600497, 2017. doi: 10.1002/mame.201600497. URL <https://onlinelibrary.wiley.com/doi/abs/10.1002/mame.201600497>.
- [147] Jonathan Rivnay, Pierre Leleux, Marc Ferro, Michele Sessolo, Adam Williamson, Dimitrios A. Koutsouras, Dion Khodagholy, Marc Ramuz, Xenofon Strakosas, Roisin M. Owens, Christian Benar, Jean-Michel Badier, Christophe Bernard, and George G. Malliaras. High-performance transistors for bioelectronics through tuning of channel thickness. *Science Advances*, 1(4), 2015. doi: 10.1126/sciadv.1400251. URL <http://advances.sciencemag.org/content/advances/1/4/e1400251.full.pdf>.
- [148] Narendra Kurra, Jihoon Park, and H. N. Alshareef. A conducting polymer nucleation scheme for efficient solid-state supercapacitors on paper. *Journal of Materials Chemistry A*, 2(40):17058–17065, 2014. ISSN 2050-7488. doi: 10.1039/C4TA03603D. URL <http://dx.doi.org/10.1039/C4TA03603D>.
- [149] Xenofon Strakosas, Manuelle Bongo, and Róisín M. Owens. The organic electrochemical transistor for biological applications. *Journal of Applied Polymer Science*, 132(15), 2015. ISSN 0021-8995. doi: 10.1002/app.41735. URL <https://doi.org/10.1002/app.41735>.
- [150] Jonathan Rivnay, Pierre Leleux, Marc Ferro, Michele Sessolo, Adam Williamson, Dimitrios A. Koutsouras, Dion Khodagholy, Marc Ramuz, Xenofon Strakosas, Roisin M. Owens, Christian Benar, Jean-Michel Badier,

- Christophe Bernard, and George G. Malliaras. High-performance transistors for bioelectronics through tuning of channel thickness. *Science Advances*, 1(4):e1400251, 2015. ISSN 2375-2548. doi: 10.1126/sciadv.1400251. URL <http://www.ncbi.nlm.nih.gov/pmc/articles/PMC4640642/>.
- [151] Alexander Giovannitti, Christian B. Nielsen, Dan-Tiberiu Sbircea, Sahika Inal, Mary Donahue, Muhammad R. Niazi, David A. Hanifi, Aram Amasian, George G. Malliaras, Jonathan Rivnay, and Iain McCulloch. N-type organic electrochemical transistors with stability in water. *Nature Communications*, 7:13066, 2016. doi: 10.1038/ncomms13066 <https://www.nature.com/articles/ncomms13066#supplementary-information>. URL <http://dx.doi.org/10.1038/ncomms13066>.
- [152] Qibing Pei and Olle Inganaes. Electrochemical applications of the bending beam method. 1. mass transport and volume changes in polypyrrole during redox. *The Journal of Physical Chemistry*, 96(25):10507–10514, 1992. ISSN 0022-3654. doi: 10.1021/j100204a071. URL <https://doi.org/10.1021/j100204a071>.
- [153] T. F. Otero, E. Angulo, J. Rodríguez, and C. Santamaría. Electrochemomechanical properties from a bilayer: polypyrrole / non-conducting and flexible material — artificial muscle. *Journal of Electroanalytical Chemistry*, 341(1):369–375, 1992. ISSN 1572-6657. doi: [https://doi.org/10.1016/0022-0728\(92\)80495-P](https://doi.org/10.1016/0022-0728(92)80495-P). URL <http://www.sciencedirect.com/science/article/pii/S002207289280495P>.
- [154] R. H. Baughman. Conducting polymer artificial muscles. *Synthetic Metals*, 78(3):339–353, 1996. ISSN 0379-6779. doi: [https://doi.org/10.1016/0379-6779\(96\)80158-5](https://doi.org/10.1016/0379-6779(96)80158-5). URL <http://www.sciencedirect.com/science/article/pii/S0379677996801585>.
- [155] Christopher R. Newman, C. Daniel Frisbie, Demetrio A. da Silva Filho, Jean-Luc Brédas, Paul C. Ewbank, and Kent R. Mann. Introduction to organic thin film transistors and design of n-channel organic semiconductors.

- Chemistry of Materials*, 16(23):4436–4451, 2004. ISSN 0897-4756. doi: 10.1021/cm049391x. URL <https://doi.org/10.1021/cm049391x>.
- [156] Sahika Inal, George G. Malliaras, and Jonathan Rivnay. Optical study of electrochromic moving fronts for the investigation of ion transport in conducting polymers. *Journal of Materials Chemistry C*, 4(18):3942–3947, 2016. ISSN 2050-7526. doi: 10.1039/C5TC04354A. URL <http://dx.doi.org/10.1039/C5TC04354A>.
- [157] Eleni Stavrinidou, Michele Sessolo, Bjorn Winther-Jensen, Sébastien Sanaur, and George G. Malliaras. A physical interpretation of impedance at conducting polymer/electrolyte junctions. *AIP Advances*, 4(1):017127, 2014. doi: 10.1063/1.4863297. URL <https://doi.org/10.1063/1.4863297>.
- [158] A. M. Nardes, M. Kemerink, and R. A. J. Janssen. Anisotropic hopping conduction in spin-coated pedot:pss thin films. *Phys. Rev. B*, 76:085208, Aug 2007. doi: 10.1103/PhysRevB.76.085208. URL <https://link.aps.org/doi/10.1103/PhysRevB.76.085208>.
- [159] Luisa Torsi, Maria Magliulo, Kyriaki Manoli, and Gerardo Palazzo. Organic field-effect transistor sensors: a tutorial review. *Chemical Society Reviews*, 42(22):8612–8628, 2013. ISSN 0306-0012. doi: 10.1039/C3CS60127G. URL <http://dx.doi.org/10.1039/C3CS60127G>.
- [160] D. Kumar and R. C. Sharma. Advances in conductive polymers. *European Polymer Journal*, 34(8):1053–1060, 1998. ISSN 0014-3057. doi: [https://doi.org/10.1016/S0014-3057\(97\)00204-8](https://doi.org/10.1016/S0014-3057(97)00204-8). URL <http://www.sciencedirect.com/science/article/pii/S0014305797002048>.
- [161] Alan J. Heeger. Semiconducting and metallic polymers: The fourth generation of polymeric materials (nobel lecture). *Angewandte Chemie International Edition*, 40(14):2591–2611, 2001. ISSN 1433-7851. doi: 10.1002/1521-3773(20010716)40:14<2591::AID-ANIE2591>3.0.CO;2-0. URL [https://doi.org/10.1002/1521-3773\(20010716\)40:14<2591::AID-ANIE2591>3.0.CO;2-0](https://doi.org/10.1002/1521-3773(20010716)40:14<2591::AID-ANIE2591>3.0.CO;2-0).

- [162] A. B. Kaiser. Systematic conductivity behavior in conducting polymers: Effects of heterogeneous disorder. *Advanced Materials*, 13(12-13): 927–941, 2001. ISSN 0935-9648. doi: 10.1002/1521-4095(200107)13:12/13<927::AID-ADMA927>3.0.CO;2-B. URL [https://doi.org/10.1002/1521-4095\(200107\)13:12/13<927::AID-ADMA927>3.0.CO;2-B](https://doi.org/10.1002/1521-4095(200107)13:12/13<927::AID-ADMA927>3.0.CO;2-B).
- [163] Rodrigo Noriega, Jonathan Rivnay, Koen Vandewal, Felix P. V. Koch, Natalie Stingelin, Paul Smith, Michael F. Toney, and Alberto Salleo. A general relationship between disorder, aggregation and charge transport in conjugated polymers. *Nature Materials*, 12:1038, 2013. doi: 10.1038/nmat3722<https://www.nature.com/articles/nmat3722#supplementary-information>. URL <http://dx.doi.org/10.1038/nmat3722>.
- [164] Kohsuke Kawabata, Masahiko Saito, Noriko Takemura, Itaru Osaka, and Kazuo Takimiya. Effects of branching position of alkyl side chains on ordering structure and charge transport property in thienothiophenedione and quinacridone-based semiconducting polymers. *Polymer Journal*, 49: 169, 2016. doi: 10.1038/pj.2016.103<https://www.nature.com/articles/pj2016103#supplementary-information>. URL <http://dx.doi.org/10.1038/pj.2016.103>.
- [165] Alexander Giovannitti, Iuliana P. Maria, David Hanifi, Mary J. Donahue, Daniel Bryant, Katrina J. Barth, Beatrice E. Makdah, Achilleas Savva, Davide Moia, Matyáš Zetek, Piers R. F. Barnes, Obadiah G. Reid, Sahika Inal, Garry Rumbles, George G. Malliaras, Jenny Nelson, Jonathan Rivnay, and Iain McCulloch. The role of the side chain on the performance of n-type conjugated polymers in aqueous electrolytes. *Chemistry of Materials*, 30(9): 2945–2953, 2018. ISSN 0897-4756. doi: 10.1021/acs.chemmater.8b00321. URL <https://doi.org/10.1021/acs.chemmater.8b00321>.
- [166] Marcin Procek, Kinga Kepska, and Agnieszka Stolarczyk. A study on the impact of poly(3-hexylthiophene) chain length and other applied side-chains on the no2 sensing properties of conducting graft copolymers. *Sensors*, 18(3), 2018. ISSN 1424-8220. doi: 10.3390/s18030928.



- [167] D. S. Wallace, A. M. Stoneham, W. Hayes, A. J. Fisher, and A. Testa. Theory of defects in conducting polymers. ii. application to polyacetylene. *Journal of Physics: Condensed Matter*, 3(22):3905, 1991. ISSN 0953-8984. URL <http://stacks.iop.org/0953-8984/3/i=22/a=003>.
- [168] K. E. Aasmundtveit, E. J. Samuelsen, L. A. A. Pettersson, O. Inganäs, T. Johansson, and R. Feidenhans'l. Structure of thin films of poly(3,4-ethylenedioxythiophene). *Synthetic Metals*, 101(1):561–564, 1999. ISSN 0379-6779. doi: [https://doi.org/10.1016/S0379-6779\(98\)00315-4](https://doi.org/10.1016/S0379-6779(98)00315-4). URL <http://www.sciencedirect.com/science/article/pii/S0379677998003154>.
- [169] Brett D. Martin, Nikolay Nikolov, Steven K. Pollack, Alexey Sapirgin, R. Shashidhar, Fan Zhang, and Paul A. Heiney. Hydroxylated secondary dopants for surface resistance enhancement in transparent poly(3,4-ethylenedioxythiophene)–poly(styrenesulfonate) thin films. *Synthetic Metals*, 142(1):187–193, 2004. ISSN 0379-6779. doi: <https://doi.org/10.1016/j.synthmet.2003.09.005>. URL <http://www.sciencedirect.com/science/article/pii/S0379677903004715>.
- [170] Kyeongwoon Chung, Andrew McAllister, David Bilby, Bong-Gi Kim, Min Sang Kwon, Emmanouil Kioupakis, and Jinsang Kim. Designing interchain and intrachain properties of conjugated polymers for latent optical information encoding. *Chemical Science*, 6(12):6980–6985, 2015. ISSN 2041-6520. doi: [10.1039/C5SC02403J](https://doi.org/10.1039/C5SC02403J). URL <http://dx.doi.org/10.1039/C5SC02403J>.
- [171] Ioan Botiz and Natalie Stingelin. Influence of molecular conformations and microstructure on the optoelectronic properties of conjugated polymers. *Materials*, 7(3):2273, 2014. ISSN 1996-1944. URL <http://www.mdpi.com/1996-1944/7/3/2273>.
- [172] Adam D. Printz and Darren J. Lipomi. Competition between deformability and charge transport in semiconducting polymers for flexible and stretchable

- electronics. *Applied Physics Reviews*, 3(2):021302, 2016. doi: 10.1063/1.4947428. URL <https://doi.org/10.1063/1.4947428>.
- [173] H. Sirringhaus, P. J. Brown, R. H. Friend, M. M. Nielsen, K. Bechgaard, B. M. W. Langeveld-Voss, A. J. H. Spiering, R. A. J. Janssen, E. W. Meijer, P. Herwig, and D. M. de Leeuw. Two-dimensional charge transport in self-organized, high-mobility conjugated polymers. *Nature*, 401:685, 1999. doi: 10.1038/44359. URL <http://dx.doi.org/10.1038/44359>.
- [174] A. M. Nardes, M. Kemerink, and R. A. J. Janssen. Anisotropic hopping conduction in spin-coated PEDOT:PSS thin films. *Phys. Rev. B*, 76:085208, Aug 2007. doi: 10.1103/PhysRevB.76.085208. URL <https://link.aps.org/doi/10.1103/PhysRevB.76.085208>.
- [175] Leif A. A. Pettersson, Soumyadeb Ghosh, and Olle Inganäs. Optical anisotropy in thin films of poly(3,4-ethylenedioxythiophene)-poly(4-styrenesulfonate). *Organic Electronics*, 3(3):143–148, 2002. ISSN 1566-1199.
- [176] Takumi Takano, Hiroyasu Masunaga, Akihiko Fujiwara, Hidenori Okuzaki, and Takahiko Sasaki. Pedot nanocrystal in highly conductive pedot:pss polymer films. *Macromolecules*, 45(9):3859–3865, 2012. ISSN 0024-9297. doi: 10.1021/ma300120g. URL <https://doi.org/10.1021/ma300120g>.
- [177] Hui Shi, Congcong Liu, Qinglin Jiang, and Jingkun Xu. Effective approaches to improve the electrical conductivity of pedot:pss: A review. *Advanced Electronic Materials*, 1(4):1500017, 2015. ISSN 2199-160X. doi: 10.1002/aelm.201500017. URL <https://doi.org/10.1002/aelm.201500017>.
- [178] T. Erb, U. Zhokhavets, G. Gobsch, S. Raleva, B. Stühn, P. Schilinsky, C. Waldauf, and C. J Brabec. Correlation between structural and optical properties of composite polymer/fullerene films for organic solar cells. *Advanced Functional Materials*, 15(7):1193–1196, 2005. ISSN 1616-301X. doi: 10.1002/adfm.200400521. URL <https://doi.org/10.1002/adfm.200400521>.

- [179] Martin Brinkmann and Patrice Rannou. Molecular weight dependence of chain packing and semicrystalline structure in oriented films of regioregular poly(3-hexylthiophene) revealed by high-resolution transmission electron microscopy. *Macromolecules*, 42(4):1125–1130, 2009. ISSN 0024-9297. doi: 10.1021/ma8023415. URL <https://doi.org/10.1021/ma8023415>.
- [180] Jun Liu, Yuehe Lin, Liang Liang, James A. Voigt, Dale L. Huber, Zhengrong R. Tian, Eric Coker, Bonnie McKenzie, and Matthew J. McDermott. Templateless assembly of molecularly aligned conductive polymer nanowires: A new approach for oriented nanostructures. *Chemistry – A European Journal*, 9(3):604–611, 2003. ISSN 0947-6539. doi: 10.1002/chem.200390064. URL <https://doi.org/10.1002/chem.200390064>.
- [181] Joachim Stöhr. *NEXAFS Spectroscopy*. Springer-Verlag Berlin Heidelberg, 1992. ISBN 978-3-642-08113-2.
- [182] *Sample alignment and reflectivity*, 2017 (accessed October 3, 2017). <https://www.elettra.trieste.it/lightsources/elettra/elettra-beamlines/bear/the-manuals.html>.
- [183] *X-Ray Interactions With Matter, Index of refraction*, 2018 (accessed October 24, 2018). [http://henke.lbl.gov/optical\\_constants/](http://henke.lbl.gov/optical_constants/).
- [184] B. L. Henke, E. M. Gullikson, and J. C. Davis. X-ray interactions: Photoabsorption, scattering, transmission, and reflection at  $E = 50\text{--}30,000$  eV,  $Z = 1\text{--}92$ . *Atomic Data and Nuclear Data Tables*, 54(2):181–342, 1993. ISSN 0092-640X. doi: <https://doi.org/10.1006/adnd.1993.1013>. URL <http://www.sciencedirect.com/science/article/pii/S0092640X83710132>.
- [185] Sung Won Park, Tae Hwan Oh, Jun Sung Hwang, and Young Jae Lee. Effect of solvent and blended polymer on electrical conductivity of PEDOT:PSS/polymer blended nanofibers. *Fibers and Polymers*, 17(8):1171–1174, 2016. ISSN 1875-0052. doi: 10.1007/s12221-016-6468-x. URL <https://doi.org/10.1007/s12221-016-6468-x>.

- [186] R. Capelli, N. Mahne, K. Koshmak, A. Giglia, B. P. Doyle, S. Mukherjee, S. Nannarone, and L. Pasquali. Quantitative resonant soft x-ray reflectivity of ultrathin anisotropic organic layers: Simulation and experiment of PTCDA on Au. *The Journal of Chemical Physics*, 145(2):024201, 2016. ISSN 0021-9606. doi: 10.1063/1.4956452. URL <https://doi.org/10.1063/1.4956452>.
- [187] Subhrangsu Mukherjee. *NEXAFS data normalization tutorial*, 2018. <http://www.saha.ac.in/surf/manabendra.mukherjee/>.

# Appendix A

## Measurement of ellipsometric parameters $\Psi$ and $\Delta$

Since the advent of ellipsometry in the late 1800s, many instrumentation techniques have appeared to measure the ellipsometric parameters of a thin film. Among them are rotating analyzer ellipsometer (RAE), rotating compensator ellipsometer (RCE), phase modulation ellipsometer (PME) and nulling ellipsometer. This appendix will focus only on the techniques of nulling ellipsometer, since it was the instrument used in the presented thesis.

In a nulling ellipsometer, the incoming light beam passes through a polarizer and compensator, which then strikes the sample and reflects, the reflected beam of light passes through an analyzer and finally to the light detector. The polarizer and analyzer are rotated such that the light at the detector has zero intensity, hence the name nulling ellipsometer. In the whole process the compensator angle is kept constant (usually at  $45^\circ$  or  $-45^\circ$ ). Fig. A.1 gives depicts the arrangement of the optical elements in a typical nulling ellipsometer.

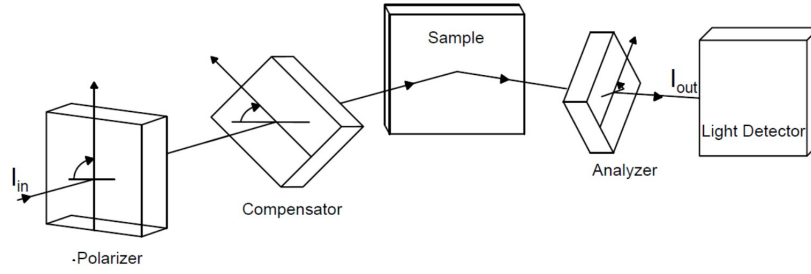


FIGURE A.1: Schematic illustration of a typical nulling ellipsometer with their optical elements.

The optical arrangement as in fig. A.1 can be expressed mathematically in a Jones matrix formulation as below:

$$I_{out} = AR(A)SR(-C)CR(C)R(-P)PI_{in} \quad (\text{A.1})$$

Where,  $I_{out}$  is the output intensity of light  $AR(A)$ ,  $S$ ,  $R(-C)CR(C)$  and  $R(-P)P$  is the Jones matrix expressions for the optical components analyzer, compensator and polarizer with their respective rotation angle  $R(X)$  ( $X$  is the optical component). Equation A.1 can be further expanded into its equivalent matrix formulation:

$$\begin{bmatrix} E_A \\ 0 \end{bmatrix} = \begin{bmatrix} 1 & 0 \\ 0 & 0 \end{bmatrix} \begin{bmatrix} \cos A & \sin A \\ -\sin A & \cos A \end{bmatrix} \begin{bmatrix} \rho_p & 0 \\ 0 & \rho_s \end{bmatrix} \begin{bmatrix} \cos C & -\sin C \\ \sin C & \cos C \end{bmatrix} \begin{bmatrix} 1 & 0 \\ 0 & e^{-i\delta} \end{bmatrix} \begin{bmatrix} \cos C & \sin C \\ -\sin C & \cos C \end{bmatrix} \\ X \begin{bmatrix} \cos P & -\sin P \\ \sin P & \cos P \end{bmatrix} \begin{bmatrix} 1 & 0 \\ 0 & 0 \end{bmatrix} \begin{bmatrix} 1 \\ 0 \end{bmatrix} \quad (\text{A.2})$$

The above matrix can be simplified into:

$$E_A = \rho_p \cos A [\cos C \cos (P - C) - \gamma_c \sin C \sin (P - C)] \\ + \rho_s \sin A [\sin C \cos (P - C) + \gamma_c \cos C \sin (P - C)] \quad (\text{A.3})$$

Where,  $\gamma_c = e^{-\iota\delta}$  and  $\delta$  is the phase shift of the compensator,  $\rho_p$  and  $\rho_s$  are the p and s reflection coefficients of the sample. As explained above, in a nulling ellipsometer the measurement conditions are satisfied when the output intensity of light is zero, i.e.  $E_A = 0$ . The rotation angle and the phase shift of the compensator are generally kept fixed at  $45^\circ$  and  $90^\circ$  respectively. Substitution these values in equation A.3, yields:

$$\begin{aligned} \frac{\rho_p}{\rho_s} &= \tan A \frac{1 - \iota \tan (P - 45^\circ)}{1 + \iota \tan (P - 45^\circ)} \\ &= \tan (-A) e^{\iota(-2P+90^\circ)} \end{aligned} \quad (\text{A.4})$$

and since,

$$\frac{\rho_p}{\rho_s} = \tan \psi e^{\iota\Delta} \quad (\text{A.5})$$

Comparing equation A.5 and A.4, the values of the ellipsometric parameters  $\psi$  and  $\Delta$  can be calculated by the measuring the polarizer and analyzer angles as:

$$\begin{aligned} \psi &= -A \\ \Delta &= -2P + 90^\circ \end{aligned} \quad (\text{A.6})$$

In summary, the polarizer in a nulling ellipsometer is rotated such that the light after reflection from the sample becomes a linearly polarized light. The analyzer is rotated such that the transmission axis of the analyzer is perpendicular to the polarization of the reflected light, so that the output intensity is zero.

# Appendix B

## $\Psi$ and $\Delta$ fitting of EVASE measurements

The fitting of the ellipsometric parameters  $\Psi$  and  $\Delta$  obtained from EVASE measurements in this study is based on the optical models derived from Fresnel's equations (c.f. sec. 2.5). The optical models used in the VASE and EVASE measurements can be depicted from fig.B.1.

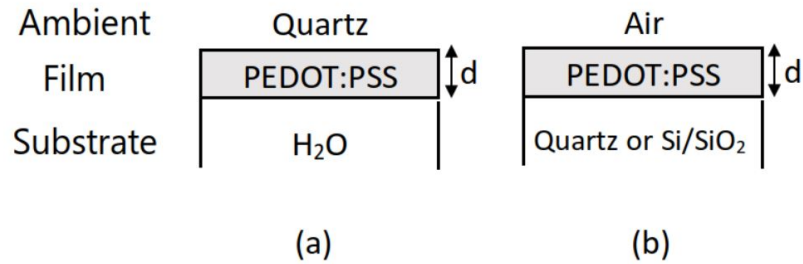


FIGURE B.1: Schematic representation of the optical model used in (a)EVASE and (b) VASE measurements

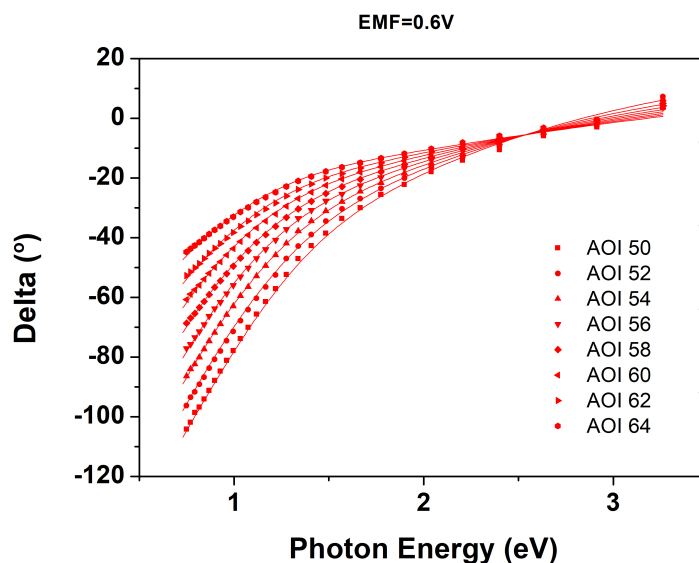
In fig.B.1 two optical models are considered. For VASE (fig.B.1b) measurements optical model with three stratified layers, where, , air is taken as the ambient layer, the PEDOT:PSS film is modeled using the TLD model defined in section 3.2 and the substrate is Quartz or Si/SiO<sub>2</sub> . For *in-situ* VASE and EVASE measurements, where the PEDOT:PSS film is sandwiched between the electrolyte and



quartz substrate (and prism) (c.f. fig. 3.5), the stratified layer model (fig.B.1a) is taken with quartz as the ambient, PEDOT:PSS film (TLD model) as the sandwiched layer and water ( $\text{H}_2\text{O}$ ) as the substrate layer. The dielectric dispersion of Quartz, air and water is obtained from the available literature. A model  $\Psi$  and  $\Delta$  dispersion in the given wavelength range can be obtained using the above model and by employing a linear regression analysis (Levenberg–Marquardt method) the model is fitted to the measured  $\Psi$  and  $\Delta$ . By following the steps described in fig.2.11, the optical constants are obtained. However, Ellipsometry is an analytical tool, therefore, due to the cross-correlations of the fitting parameters, multiple solutions to the fits are possible. Thus the cross-correlation of parameters in case of the VASE fitting of the dry PEDOT:PSS film is reduced by simultaneously fitting SE measurements at 8 different AOIs on both Si/SiO<sub>2</sub> and quartz substrates with the same TLD model. These steps reduced the cross correlation significantly and a unique dielectric dispersion for dry PEDOT:PSS film could be obtained. The fitted thickness was compared to the thickness of the sample measured using AFM. Since linear regression analysis depends greatly on the initial values used in the regression, the fit parameters obtained for the dry film were taken as the initial values in the regression analysis of *in-situ* VASE measurements. The swelling of the PEDOT:PSS film determined from the simultaneous fit of 8 AOIs was confirmed with the QCM-D analysis (not shown here, presented in the publication mentioned chapter 3). Once this analysis method is confirmed and established, the fittings for the EVASE measurements can be performed in the similar fashion where the initial values for the regression analysis is always taken from the parameters obtained from the fit of preceding EMF's ellipsometric measurements. The  $\Psi$  and  $\Delta$  fits for all the EMF values shown in table 3.4 and 4.1 are presented below from fig.B.2-B.15

## B.1 $\Psi$ and $\Delta$ fits of EVASE measurements of PEDOT:PSS thin films used in chapter 3

(a)



(b)

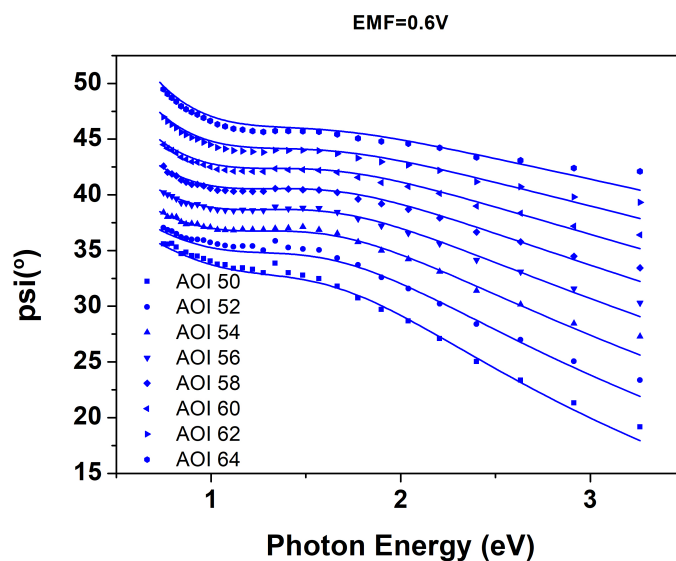
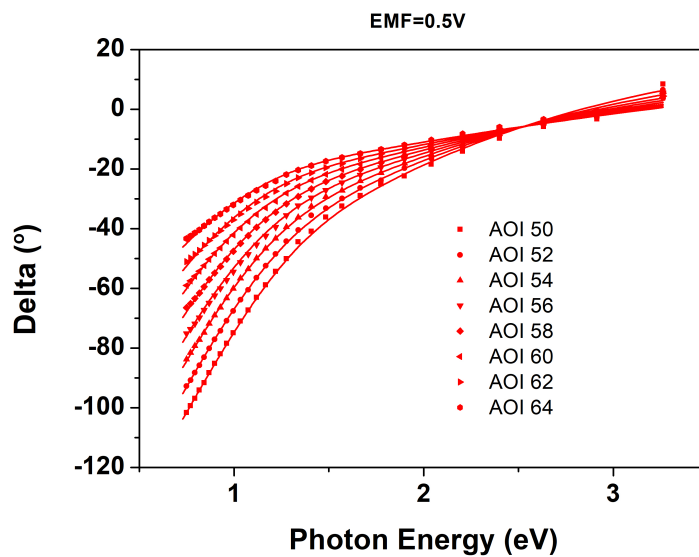


FIGURE B.2: EVASE spectra of the PEDOT:PSS sample spin coated on quartz substrate at room temperature in 0.1 M KCl aqueous solution at an electrochemical bias of 0.6 V vs Ag/AgCl. The scatter points represent the measured data at varied angle of incidence (AOI, from 50 to 64 degrees with the step size of 2 degrees) and the solid lines represent the best fit of the TLD model. (a) Ellipsometric angle  $\Delta$ , (b) Ellipsometric angle  $\Psi$ .

(a)



(b)

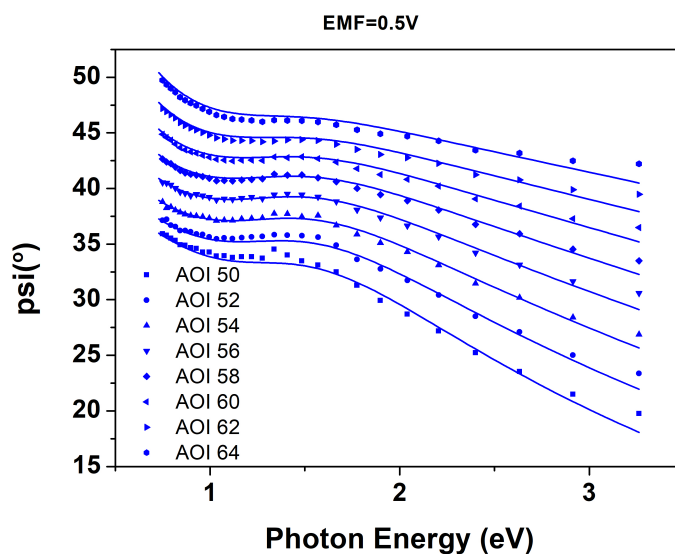
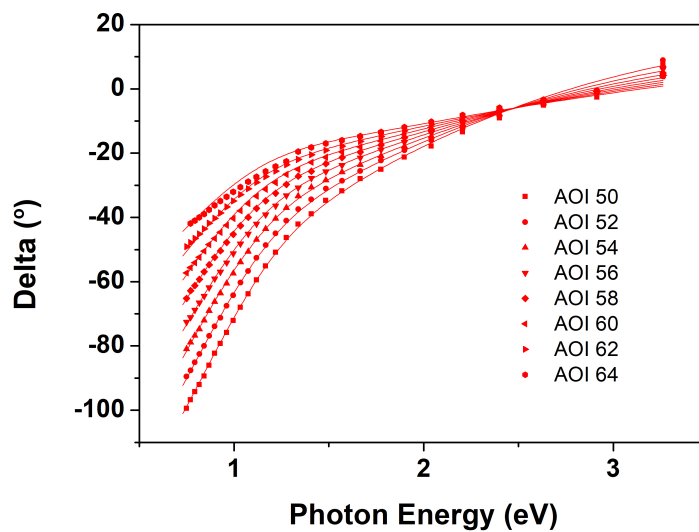


FIGURE B.3: EVASE spectra of the PEDOT:PSS sample spin coated on quartz substrate at room temperature in 0.1 M KCl aqueous solution at an electrochemical bias of 0.5 V vs Ag/AgCl. The scatter points represent the measured data at varied angle of incidence (AOI, from 50 to 64 degrees with the step size of 2 degrees) and the solid lines represent the best fit of the TLD model. (a) Ellipsometric angle  $\Delta$ , (b) Ellipsometric angle  $\Psi$ .

(a)



(b)

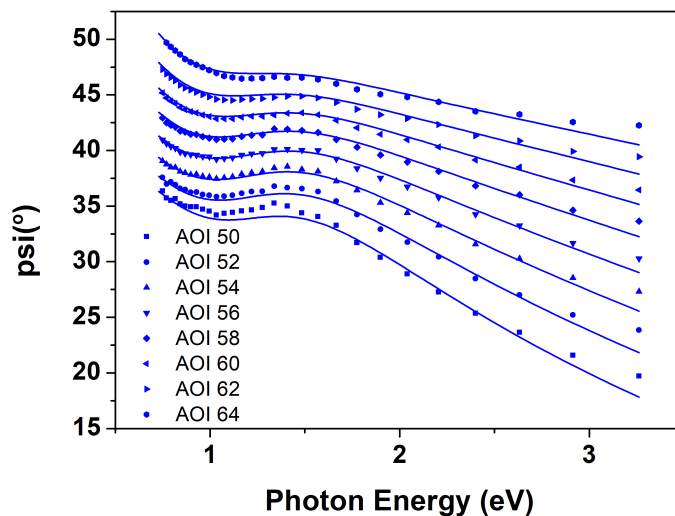
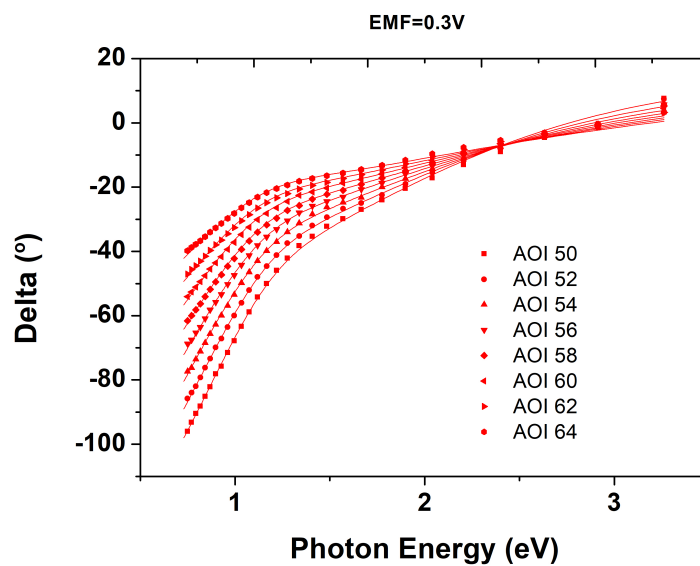


FIGURE B.4: EVASE spectra of the PEDOT:PSS sample spin coated on quartz substrate at room temperature in 0.1 M KCl aqueous solution at an electrochemical bias of 0.4 V vs Ag/AgCl. The scatter points represent the measured data at varied angle of incidence (AOI, from 50 to 64 degrees with the step size of 2 degrees) and the solid lines represent the best fit of the TLD model. (a) Ellipsometric angle  $\Delta$ , (b) Ellipsometric angle  $\Psi$ .

(a)



(b)

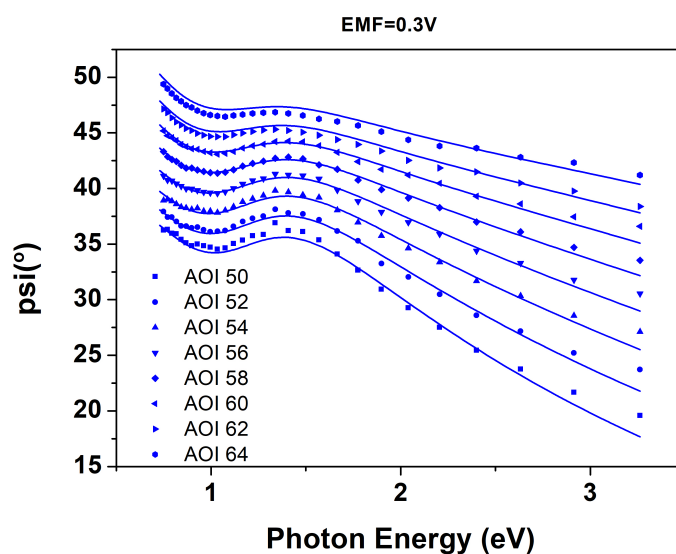
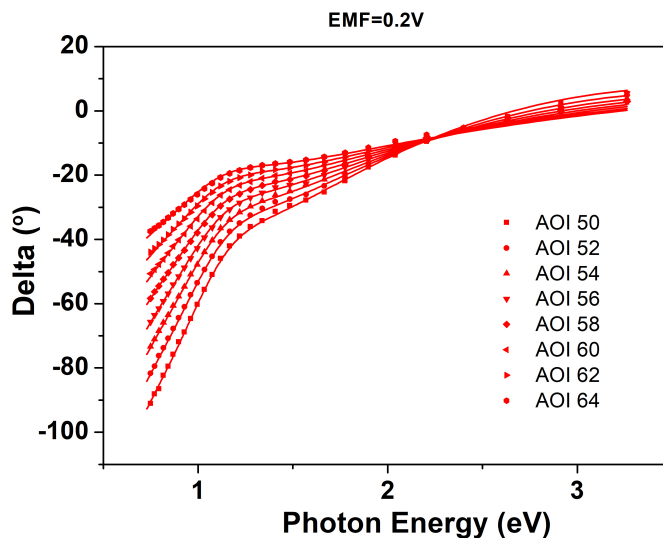


FIGURE B.5: EVASE spectra of the PEDOT:PSS sample spin coated on quartz substrate at room temperature in 0.1 M KCl aqueous solution at an electrochemical bias of 0.3 V vs Ag/AgCl. The scatter points represent the measured data at varied angle of incidence (AOI, from 50 to 64 degrees with the step size of 2 degrees) and the solid lines represent the best fit of the TLD model. (a) Ellipsometric angle  $\Delta$ , (b) Ellipsometric angle  $\Psi$ .

(a)



(b)

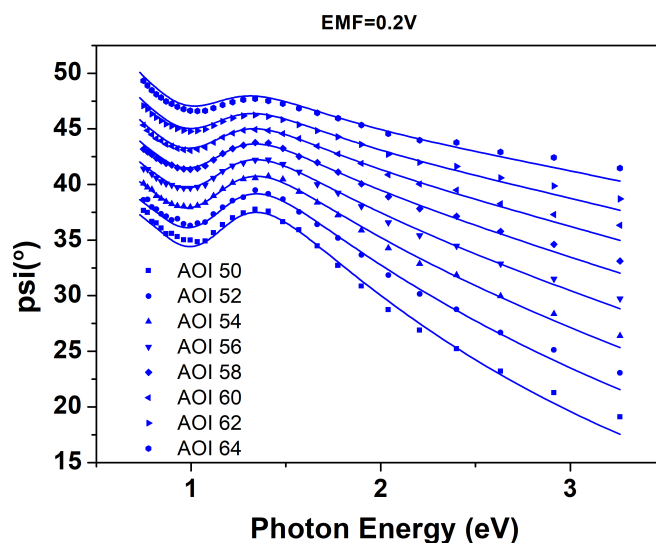
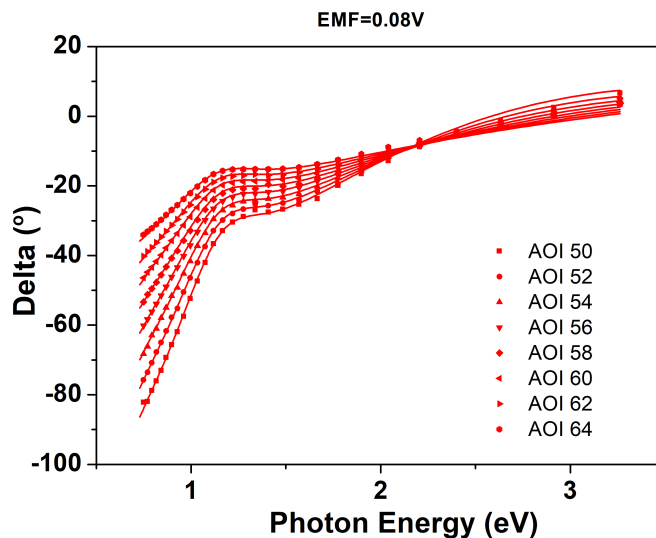


FIGURE B.6: EVASE spectra of the PEDOT:PSS sample spin coated on quartz substrate at room temperature in 0.1 M KCl aqueous solution at an electrochemical bias of 0.2 V vs Ag/AgCl. The scatter points represent the measured data at varied angle of incidence (AOI, from 50 to 64 degrees with the step size of 2 degrees) and the solid lines represent the best fit of the TLD model. (a) Ellipsometric angle  $\Delta$ , (b) Ellipsometric angle  $\Psi$ .

(a)



(b)

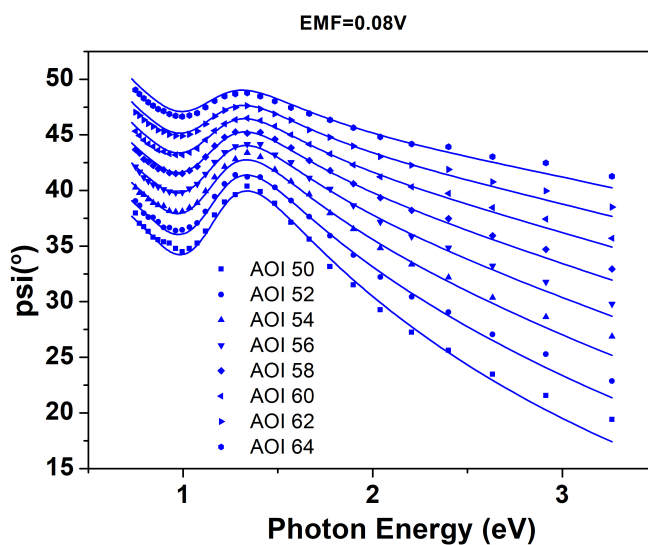
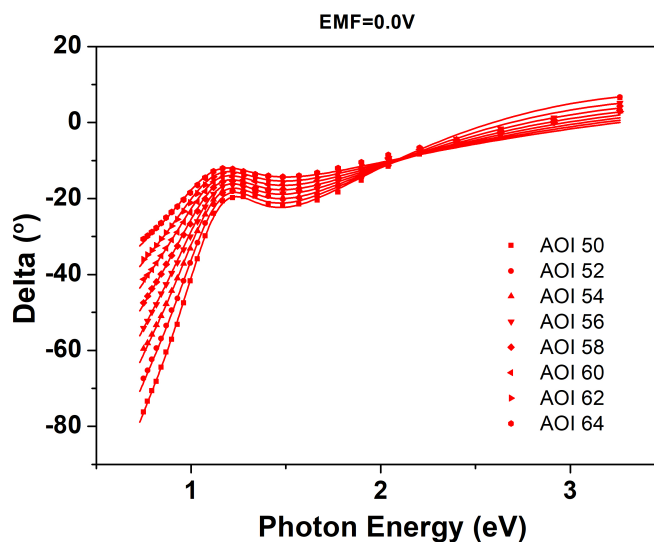


FIGURE B.7: EVASE spectra of the PEDOT:PSS sample spin coated on quartz substrate at room temperature in 0.1 M KCl aqueous solution at an electrochemical bias of 0.08 V vs Ag/AgCl. The scatter points represent the measured data at varied angle of incidence (AOI, from 50 to 64 degrees with the step size of 2 degrees) and the solid lines represent the best fit of the TLD model. (a) Ellipsometric angle  $\Delta$ , (b) Ellipsometric angle  $\Psi$ .

(a)



(b)

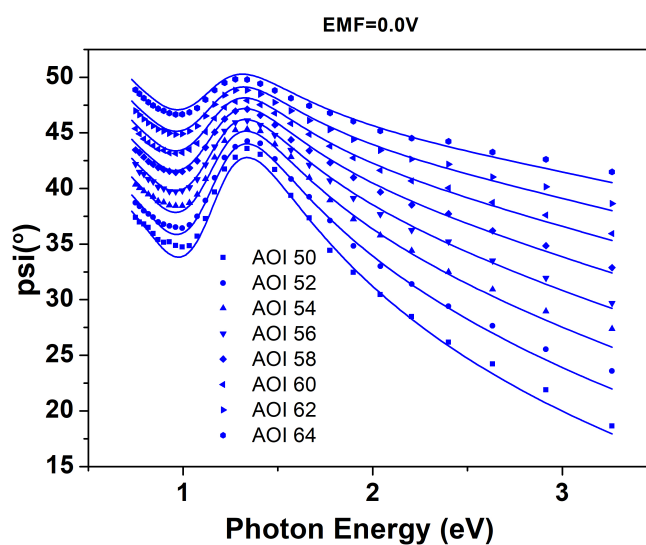
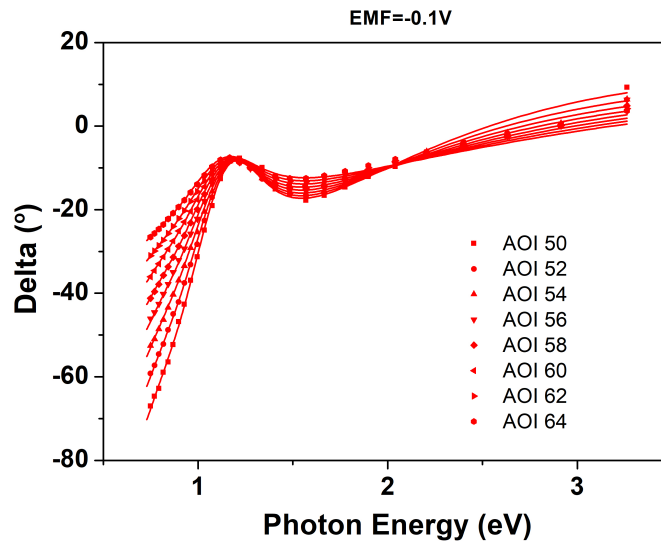


FIGURE B.8: EVASE spectra of the PEDOT:PSS sample spin coated on quartz substrate at room temperature in 0.1 M KCl aqueous solution at an electrochemical bias of 0.0 V vs Ag/AgCl. The scatter points represent the measured data at varied angle of incidence (AOI, from 50 to 64 degrees with the step size of 2 degrees) and the solid lines represent the best fit of the TLD model. (a) Ellipsometric angle  $\Delta$ , (b) Ellipsometric angle  $\Psi$ .



(a)



(b)

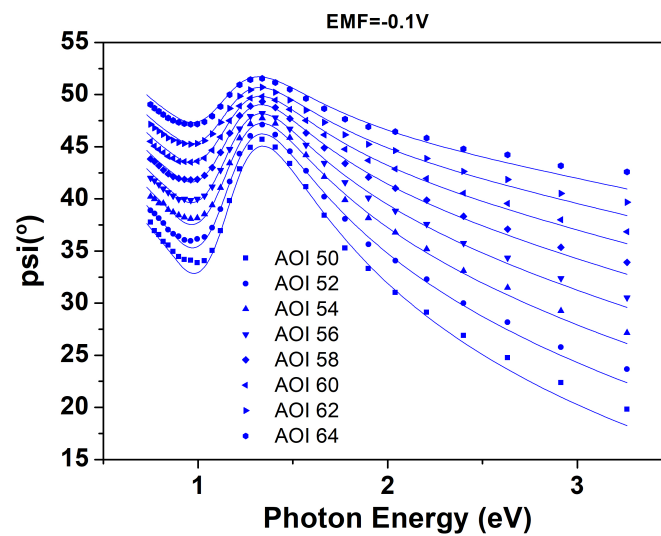
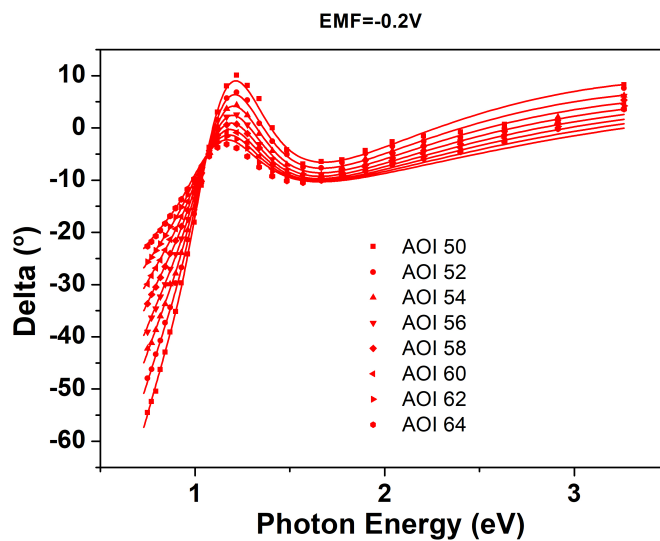


FIGURE B.9: EVASE spectra of the PEDOT:PSS sample spin coated on quartz substrate at room temperature in 0.1 M KCl aqueous solution at an electrochemical bias of -0.1 V vs Ag/AgCl. The scatter points represent the measured data at varied angle of incidence (AOI, from 50 to 64 degrees with the step size of 2 degrees) and the solid lines represent the best fit of the TLD model. (a) Ellipsometric angle  $\Delta$ , (b) Ellipsometric angle  $\Psi$ .

(a)



(b)

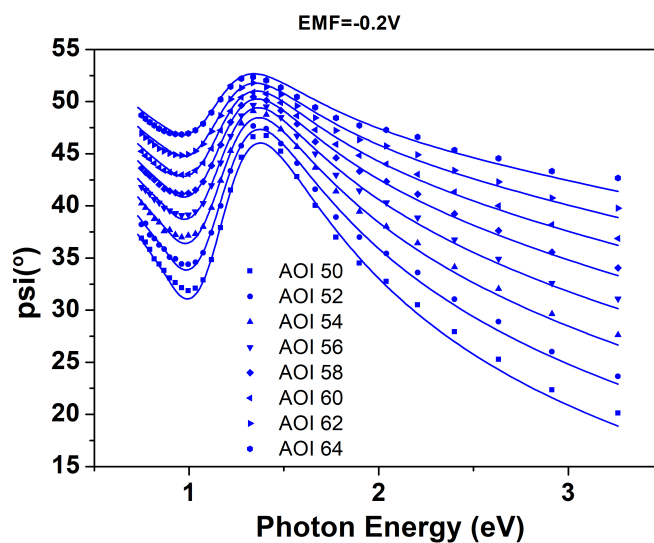
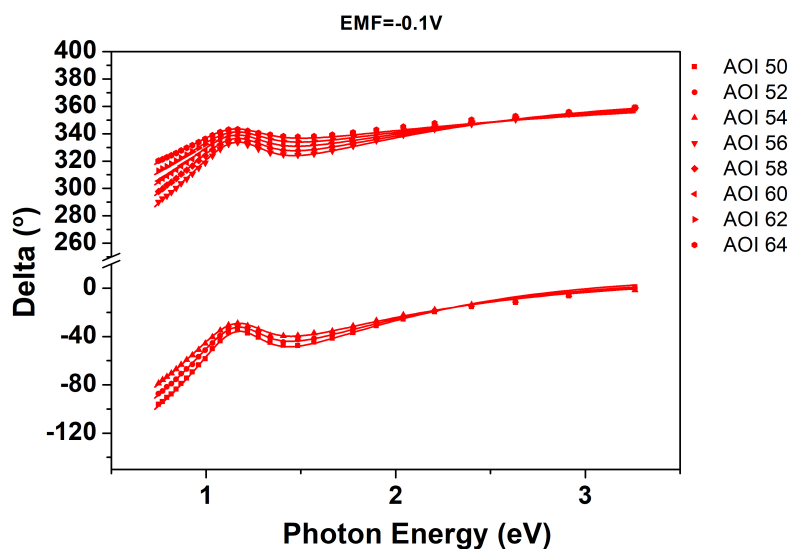


FIGURE B.10: EVASE spectra of the PEDOT:PSS sample spin coated on quartz substrate at room temperature in 0.1 M KCl aqueous solution at an electrochemical bias of -0.2 V vs Ag/AgCl. The scatter points represent the measured data at varied angle of incidence (AOI, from 50 to 64 degrees with the step size of 2 degrees) and the solid lines represent the best fit of the TLD model. (a) Ellipsometric angle  $\Delta$ , (b) Ellipsometric angle  $\Psi$ .

## B.2 $\Psi$ and $\Delta$ fits of EVASE measurements of PEDOT:PSS channel used in chapter 4

(a)



(b)

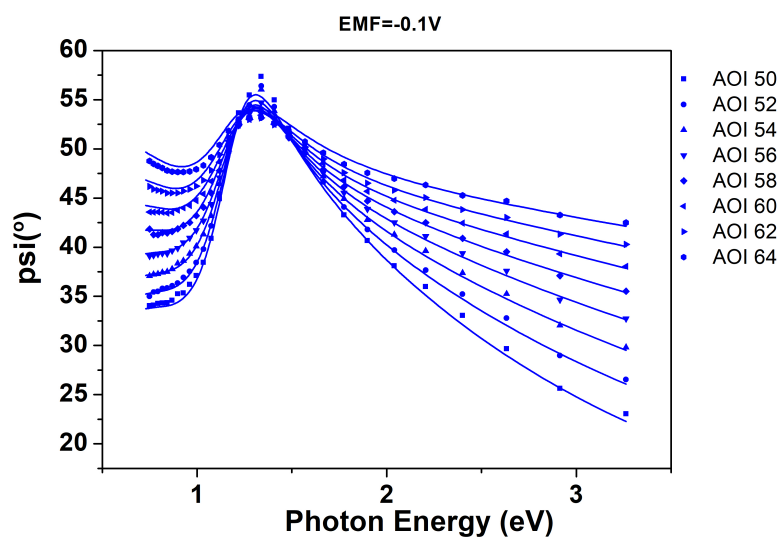
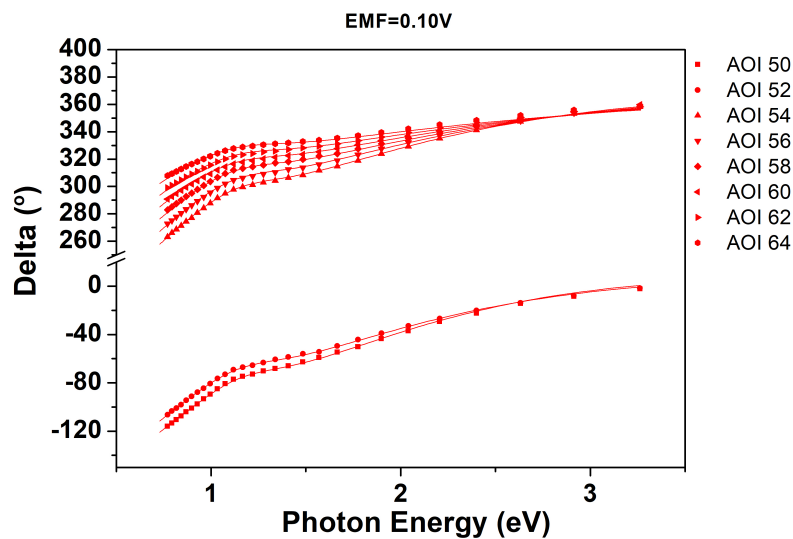


FIGURE B.11: EVASE spectra of the PEDOT:PSS channel in the OECT device at room temperature in 0.1 M KCl aqueous solution at an electrochemical bias of  $-0.1 V$  vs Ag/AgCl. The scatter points represent the measured data at varied angle of incidence (AOI, from 50 to 64 degrees with the step size of 2 degrees) and the solid lines represent the best fit of the TLD model. (a) Ellipsometric angle  $\Delta$ , (b) Ellipsometric angle  $\Psi$ .

(a)



(b)

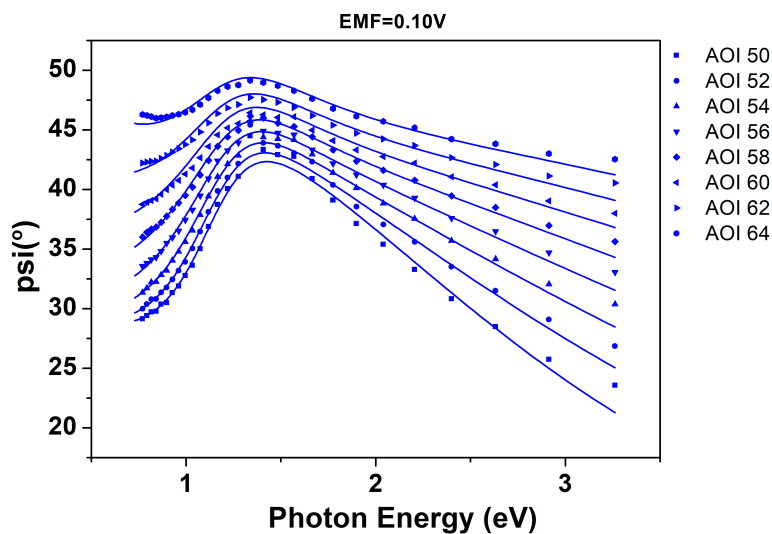
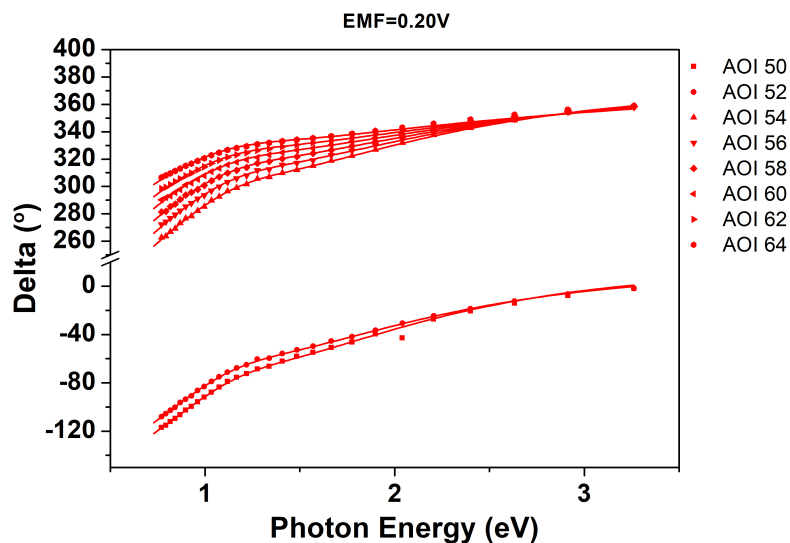


FIGURE B.12: EVASE spectra of the PEDOT:PSS channel in the OECT device at room temperature in 0.1 M KCl aqueous solution at an electrochemical bias of 0.1 V vs Ag/AgCl. The scatter points represent the measured data at varied angle of incidence (AOI, from 50 to 64 degrees with the step size of 2 degrees) and the solid lines represent the best fit of the TLD model. (a) Ellipsometric angle  $\Delta$ , (b) Ellipsometric angle  $\Psi$ .

(a)



(b)

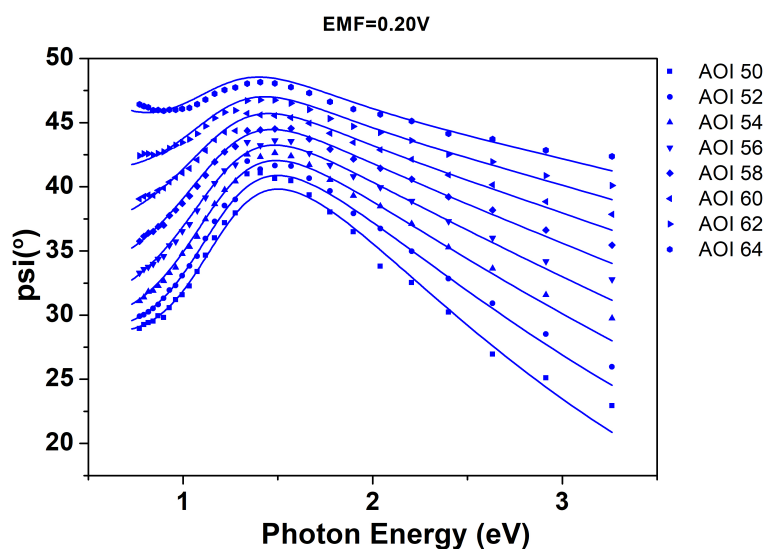
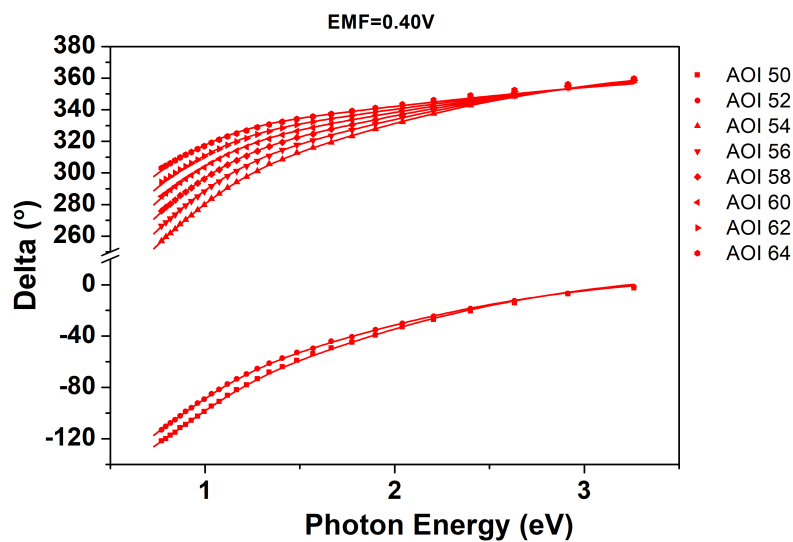


FIGURE B.13: EVASE spectra of the PEDOT:PSS channel in the OECT device at room temperature in 0.1 M KCl aqueous solution at an electrochemical bias of 0.2 V vs Ag/AgCl. The scatter points represent the measured data at varied angle of incidence (AOI, from 50 to 64 degrees with the step size of 2 degrees) and the solid lines represent the best fit of the TLD model. (a) Ellipsometric angle  $\Delta$ , (b) Ellipsometric angle  $\Psi$ .

(a)



(b)

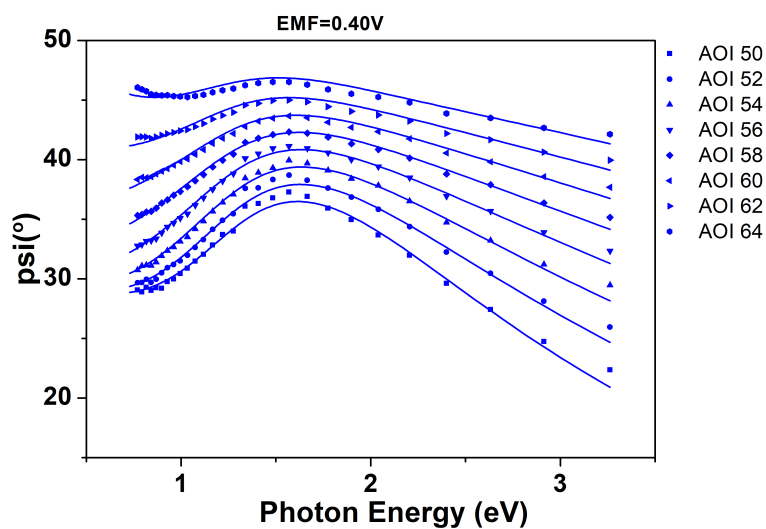
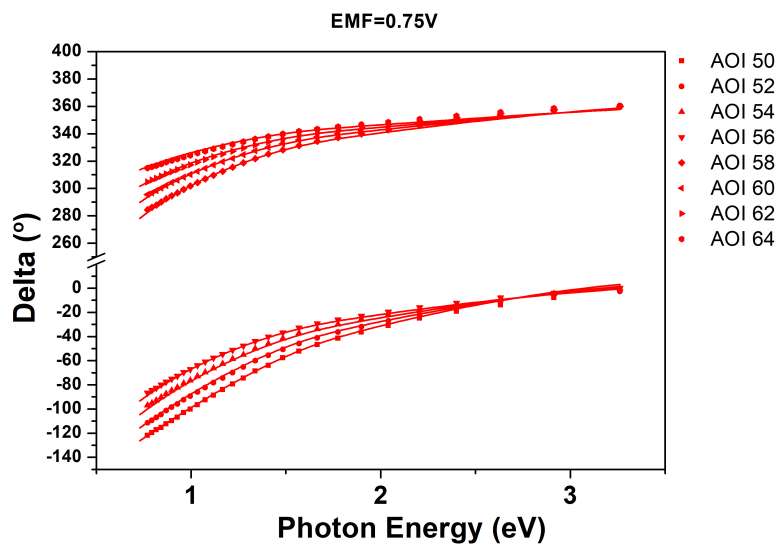


FIGURE B.14: EVASE spectra of the PEDOT:PSS channel in the OECT device at room temperature in 0.1 M KCl aqueous solution at an electrochemical bias of 0.4 V vs Ag/AgCl. The scatter points represent the measured data at varied angle of incidence (AOI, from 50 to 64 degrees with the step size of 2 degrees) and the solid lines represent the best fit of the TLD model. (a) Ellipsometric angle  $\Delta$ , (b) Ellipsometric angle  $\Psi$ .

(a)



(b)

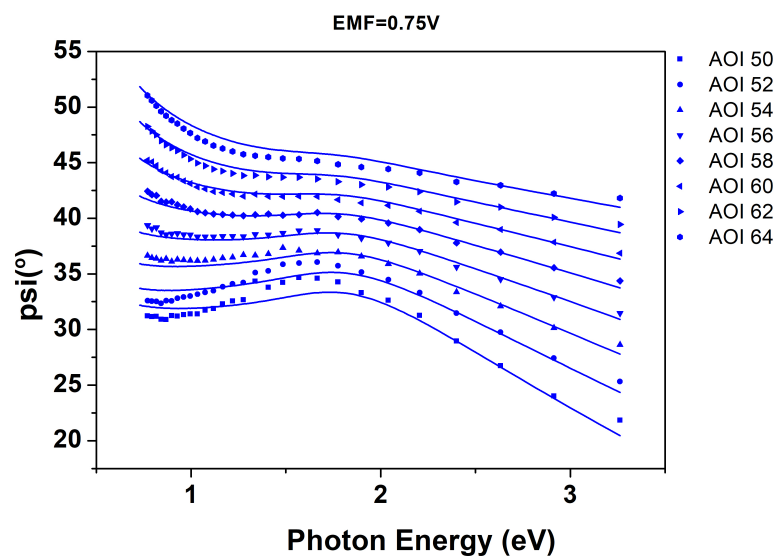


FIGURE B.15: EVASE spectra of the PEDOT:PSS channel in the OECT device at room temperature in 0.1 M KCl aqueous solution at an electrochemical bias of 0.75 V vs Ag/AgCl. The scatter points represent the measured data at varied angle of incidence (AOI, from 50 to 64 degrees with the step size of 2 degrees) and the solid lines represent the best fit of the TLD model. (a) Ellipsometric angle  $\Delta$ , (b) Ellipsometric angle  $\Psi$ .

# Appendix C

## Ion beam deposition

The contact pads on the samples used for electrochemical variable angle ellipsometry (EVASE) measurements were fabricated using ion beam deposition (IBD) technique. IBD is standard deposition process where an ion source, which can be a gas, evaporated solid or a liquid solution, is ionized by the application of high voltages. The ionized beam is then focused on an target material. The target material is sputtered or evaporated by the incidence of the ion beam and a thin layer of the material is deposited on the sample (substrate).

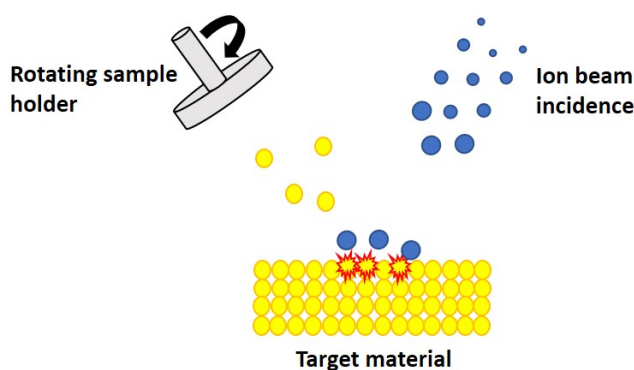


FIGURE C.1: Schematic illustration of a ion beam deposition system. A high energy ion beam strikes the material to be deposited. The material sputters out from the source and gets deposited on the substrate fixed on the rotating sample holder.

IBD is a physical deposition process implemented by the simultaneous bombardment of ion to the source material with an independently controllable beam of



ionic particles. The ion beams can be either inert ( $\text{Ne}^+$ ,  $\text{Ar}^+$  or  $\text{Kr}^+$ ) or reactive ( $\text{N}^+$  or  $\text{O}^+$ ) in nature.

## C.1 Experimental part

A Gatan, Inc's Precision Etching Coating System (PECS)II was used for deposition of Chromium/Gold contacts on the quartz substrate used in EVASE measurements. A thin chromium layer serves as an adhesion layer, which is sandwiched between the quartz substrate and the gold layer.

The quartz substrate was cleaned by ultrasonicing it in acetone for 10 minutes, which was followed by a ultrasonication step in D.I water ( $18 \text{ M}\Omega$ ) to remove any acetone left on the substrate and lastly the substrate was thoroughly rinsed with Isopropyl alcohol to avoid water stains on the substrate. The substrate was then blow dried with 99.8% Argon. After cleaning the substrate, it was masked with carbon tape at the centre. Fig.C.2 depicts the masking process.

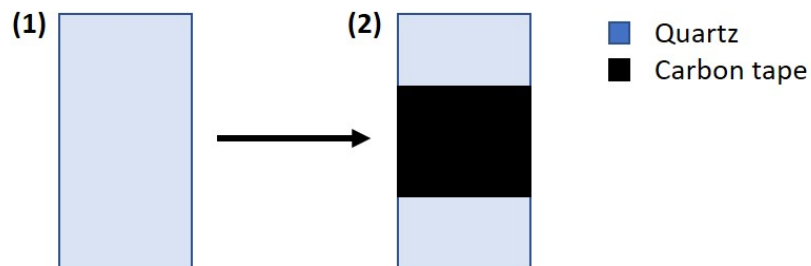


FIGURE C.2: Schematic illustration of masking of a quartz substrate. (1) bare quartz substrate. (2) Quartz substrate masked with Carbon tape.

The as prepared masked substrate is attached to the sample holder by sticking another double sided carbon tape on the back side of the substrate. The height of the sample holder is adjusted in the transfer device (fig.C.3) to obtain a smooth deposition. The sample is then loaded into the IBD vacuum chamber.

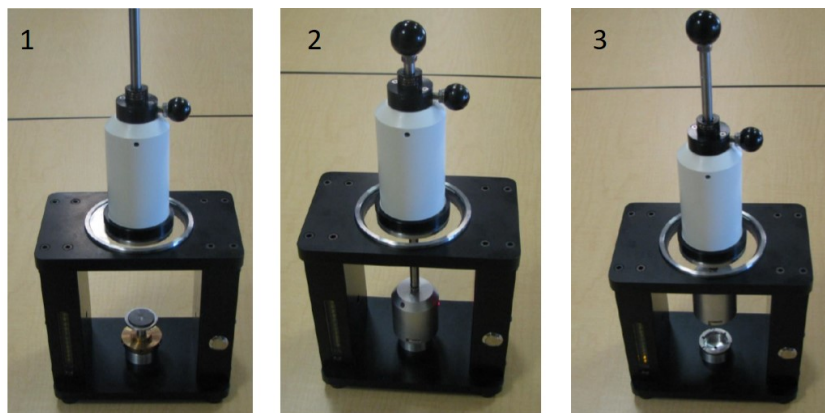


FIGURE C.3: Photograph of the sample transfer device. (1) Sample holder is placed in the transfer device. (2) Sample is attached to the transfer device. (3) Sample is lifted to perform the transfer to the IBD chamber.

After the sample is loaded in the chamber the coating procedure is started. The coating target is manually positioned. In this case the first target was chromium. The target material is conditioned for 20 seconds. While conditioning the shutter above the sample is closed, such that the sputtered material during conditioning does not deposit on the sample. Since the available IBD system was not equipped with a thickness monitor, the deposition was done at a fixed ion beam energy for a given time. The thickness was later measured with AFM. After several trials, the energy and time parameters were kept such that a 10 nm thick chromium layer and a 100 nm thick Au layer can be deposited. Chromium coating was performed at beam energy of 4 KeV and coating was done for 10 minutes. For Gold coating the energy and time parameters were 4 KeV and 30 minutes respectively. The sample holder was constantly rotated at 6 RPM for the whole deposition process.

After both the coats, the sample is taken out from the IBD chamber. The carbon tape is removed (fig.C.4). The sample is cleaned in the same steps as for the bare quartz substrate explained above. This is done to remove any glue left from the tape. The sample is then ready for spin coating of PEDOT:PSS as explained in chapter 3.

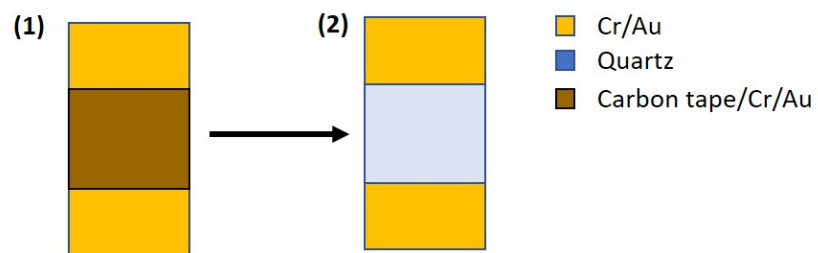


FIGURE C.4: Schematic representation of the sample as taken out from the IBD chamber after deposition. (1) Sample with carbon tape. (2) Sample after removing carbon tape.

# Curriculum vitae

**Gaurav Pathak** (Born in India, 1986) completed his bachelors of science (B.Sc.) degree at St. Joseph's college of Art and science, Bangalore University, Bangalore, (2006-2010). During his B.Sc. Studies he was a visiting student at the Raman Research institute, (R.R.I) Bangalore, where he worked on the theoretical problem of wide field imaging for radio telescopes. After completing his bachelor's degree, he joined the international masters program in solid state physics at the University of Stuttgart ,Germany. During his masters studies he joined Max Planck institute for solid state physics, Stuttgart as a research intern. He earned his master degree in 2012 with a master thesis entitled "Electrical properties of surface modified topological insulators " . In early 2013 he was awarded a Junior research fellowship at the Indian Institute of technology , Delhi, New Delhi, where he worked on studying the magnetic properties of topologically insulating materials using a superconducting quantum interference device magnetometer. He entered a PhD program in biophysics at the university of Zagreb in 2014, while being employed at the university of Rijeka as a Marie Curie ITN fellow. His research work during his PhD was focused on developing a mechanistic understanding of the functioning of organic electrochemical transistors devices which can be used for bioelectronic applications. During his term as a PhD student he published a paper entitled "Doping of poly(3,4-ethylenedioxythiophene):poly(styrenesulfonate) films studied by means of electrochemical variable angle spectroscopic ellipsometry" in a peer reviewed international journal. He attended several international conferences, where he either presented posters or gave oral presentations.

## Publications :

- Gaurav Pathak, Zofia Krasinska-Krawet, Lilianna Szyk- Warszynska, and Duško Čakara. Doping of poly(3,4- ethylenedioxythiophene): poly(styrenesulfonate) films studied by means of electrochemical variable angle spectroscopic ellipsometry. Thin Solid Films, 651:31-38, 2018. ISSN 0040-6090. doi: <https://doi.org/10.1016/j.tsf.2018.01.049>.

Sveučilište u Rijeci

 Razvoj istraživačke infrastrukture na Kampusu Sveučilišta u Rijeci  
 OBRAZAC ZA IZVJEŠĆIVANJE O KORIŠTENJU ZNANSTVENE OPREME

Projekt Sveučilišta u Rijeci „Razvoj istraživačke infrastrukture na Kampusu Sveučilišta u Rijeci“ financiran je iz Europskog fonda za regionalni razvoj (EFRR) u iznosu od 180.182.048,91 kn.

Vrsta rada:	doktorski rad
Datum:	XXX
Institucija/e:	Sveučilište u Rijeci, Centar za mikro i nanoznanosti i tehnologije
Naziv rada (HRV):	Optičko-elektronička svojstva tankih filmova poli(3,4-etilendioksitiofen):polistiren sulfonata pri variranim stanjima dopiranosti
Naziv rada (ENG):	Optoelectronic properties of the poly(3,4-ethylenedioxythiophene):polystyrene sulphonate thin films in varied doping states
Sažetak:	<p>Poly(3,4-ethylenedioxythiophene): polystyrene sulfonate (PEDOT:PSS) has gained considerable attention in the past decade due to its novel applications in the field of flexible electronics. PEDOT:PSS is the leading candidate for the channel material in the organic electrochemical transistor (OECT) devices. While PEDOT:PSS has been reported to provide high values of transconductance in transistor devices, the fundamental physical understanding of electrochemical gating of conducting polymers is still unclear. Whether the effect of gating is electrostatic, electrochemical or both, and how to distinguish them, is still a topic of debate. In this thesis, the optoelectronic properties of PEDOT:PSS thin films are studied using variable angle spectroscopic ellipsometry (VASE). The electrochemical characterization of PEDOT:PSS films is performed in combination with VASE measurements, which is termed as electrochemical variable angle ellipsometry (EVASE). The EVASE measurements were able to successfully differentiate the electrostatic effects on the PEDOT:PSS film from that of the redox effects due to the application of an electrochemical bias. In addition, ellipsometric techniques take into account the anisotropy and the increase in film thickness upon swelling of the film (when immersed in an electrolyte); which are usually neglected in state of the art electrical characterization. The above study was extended to the OECT devices, which provided an optical and electrochemical characterization of OECTs. For the electrical characterization, the drain and transfer characteristics of the device were obtained. A highest transconductance value of the device was found to be 0.8 <math>\mu\text{S}/\text{cm}</math>. X-ray reflectivity (XRR) and near edge X-ray absorption fine structure (NEXAFS) studies were performed to investigate if the origin of anisotropy in these systems could be due to the molecular orientation of their crystalline constituents. No such anisotropy was detected from the above measurements on PEDOT:PSS films. Indicating that the origin of anisotropy in such films could solely be due to the morphological reasons, where the sub-micrometer sized PEDOT-rich domains are separated by PSS lamellae in the horizontal direction.</p>
Ključne riječi (HRV):	PEDOT, elipsometrija, VASE, fleksibilna, elektronika, bioelektronika, organski, tranzistor, anizotropija
Ključne riječi (ENG):	PEDOT, ellipsometry, VASE, flexible, electronics, bioelectronics, organic, transistor, anisotropy
Autor rada:	Gaurav Pathak
Mentor/i:	doc. dr. sc. Duško Čakara
Komentor:	prof. dr. sc. George Malliaras